FY20 STATUS REPORT: SNF INTERIM STORAGE CANISTER CORROSION AND SURFACE ENVIRONMENT INVESTIGATIONS

Spent Fuel and Waste Disposition

Prepared for
US Department of Energy
Spent Fuel and Waste Science and Technology

Rebecca Schaller, Andrew Knight, Charles Bryan, Brendan Nation, Timothy Montoya, Ryan Katona

Sandia National Laboratories

November 11, 2020

M2SF-21SN010207055
National Laboratory Report No. SAND20-12663 R

DISCLAIMER

This information was prepared as an account of work sponsored by an agency of the U.S. Government. Neither the U.S. Government nor any agency thereof, nor any of their employees, makes any warranty, expressed or implied, or assumes any legal liability or responsibility for the accuracy, completeness, or usefulness, of any information, apparatus, product, or process disclosed, or represents that its use would not infringe privately owned rights. References herein to any specific commercial product, process, or service by trade name, trade mark, manufacturer, or otherwise, does not necessarily constitute or imply its endorsement, recommendation, or favoring by the U.S. Government or any agency thereof. The views and opinions of authors expressed herein do not necessarily state or reflect those of the U.S. Government or any agency thereof.

Prepared by
Sandia National Laboratories
Albuquerque, New Mexico 87185 and Livermore, California 94550

Sandia National Laboratories is a multimission laboratory managed and operated by National Technology and Engineering Solutions of Sandia, LLC, a wholly owned subsidiary of Honeywell International, Inc., for the U.S. Department of Energy's National Nuclear Security Administration under contract DE-NA0003525.

SUMMARY

This progress report describes work performed during FY20 at Sandia National Laboratories (SNL) to assess the localized corrosion performance of container/cask materials used in the interim storage of spent nuclear fuel (SNF). Of particular concern is stress corrosion cracking (SCC), by which a through-wall crack could potentially form in a canister outer wall over time intervals that are shorter than possible dry storage times. Work in FY20 further defined our understanding of the potential chemical and physical environment present on canister surfaces, evaluated the relationship between the environment and the resultant corrosion that occurs, and initiated crack growth rate testing under relevant environmental conditions.

In FY20, work to define dry storage canister surface environments included several tasks. First, collection of dust deposition specimens from independent spent fuel storage installation (ISFSI) site locations helped to establish a more complete understanding of the potential chemical environment formed on the canister. Second, the predicted evolution of canister surface relative humidity RH) values was estimated using ISFSI site weather data and the horizontal canister thermal model used by the SNL probabilistic SCC model. These calculations determined that for typical ISFSI weather conditions, sea-salt deliquescence to produce $MgCl_2$-rich brines could occur in less than 20 years at the coolest locations on the canister surface, and, even after nearly 300 years, conditions for NaCl deliquescence (75% RH) are not reached. This work illustrates the importance of understanding the stability of $MgCl_2$-rich brines on the heated canister surface, and the potential impact of brine composition on corrosion processes, including pitting and stress corrosion cracking. In an additional study, the description of the canister surface environment was refined in order to define more realistic corrosion testing environments including diurnal cycles, soluble salt chemistries, and inert mineral particles. The potential impacts of these phenomena on canister corrosion are being evaluated experimentally. Finally, work over the past few years to evaluate the stability of magnesium chloride brines continued in FY20. $MgCl_2$ degassing experiments were carried out, confirming that $MgCl_2$ brines slowly degas HCl on heated surfaces, converting to less deliquescent magnesium hydroxychloride phases and potentially leading to brine dryout.

In FY20, corrosion testing and modeling was performed in more canister relevant environments. Continued evaluation of pitting observed in large scale exposure tests from FY18/19 and comparison of results to pitting in exposures of varied brine compositions helped elucidate influences of the canister surface environment on pit growth, both size and morphology. In addition to enhanced experimentation through testing in more relevant scenarios, FY20 also produced expanded modeling efforts for the maximum pit size model. Efforts focused on accounting for non-static brine/corrosion conditions to better predict pitting and SCC initiation. Two major observations produced from the corrosion work in FY20 are: 1) $MgCl_2$ brines influence the pit morphology towards the formation of more irregular shapes with near surface microcracks and 2) $MgCl_2$ brines influence the controlling cathodic kinetics through dominance of the hydrogen evolution reaction in the cathode and formation of precipitates that lower the predicted maximum pit size. Understanding the potentially opposing roles of these two phenomena on SCC initiation will better enhance our determination of the susceptibility of SNF canisters to SCC. While major advancements with respect to understanding the relationship between canister-relevant brine conditions and corrosion were accomplished in FY20, it is still unknown how cracks, once initiated, will behave under these conditions. To further the study of this, SNL has installed capabilities (four new load frames) and started initial tests of the crack growth rate of stainless steel canister materials in canister-relevant environments. New crack growth rate data will be added to the SNL literature database and compared to the model developed for use in flaw disposition for the ASME code case N-860.

Overall, in FY20, SNL was able to better quantify and model canister-relevant environments present at ISFSI sites. This was applied to inform current and future corrosion tests to explore the effects of relevant brines on corrosion and SCC initiation. Experiments in FY20 elucidated potentially significant

influences of $MgCl_2$-dominated brines on corrosion; these brines may also govern crack initiation and crack growth rates. This will enable better predictions of timing and location of SCC occurrence to minimize risk of exposure, to inform canister inspections, and to develop and apply enhanced repair and mitigation strategies.

ACKNOWLEDGEMENTS

The authors would like to acknowledge the following people for their contributions to the work documented in this report: Sandians Sara Dickens, Luis Jaregui, Jay Taylor, Michael Melia, Greg Koenig, Sam Durbin, Philip Noell, Jake Carpenter, and Makeila Maguire; Paul Plante, Neil Fales, and the M&O team at the Maine Yankee ISFSI; Alana Parey, Jay Srinivasan, Jenifer Locke, and Eric Schindelholz of the Ohio State University; Rob Kelly of the University of Virginia; Scott Gordon of the Colorado School of Mines; John Plumley of the University of New Mexico; and Ned Larson of DOE:NE.

This page is intentionally left blank.

CONTENTS

This page is intentionally left blank.

LIST OF FIGURES

LIST OF TABLES

This page is intentionally left blank.

ACRONYMS

AAO	anodized aluminum oxide
AH	absolute humidity
ANL	Argonne National Laboratory
CFCGR	corrosion fatigue crack growth rate
CGR	crack growth rate
CISCC	chloride-induced stress corrosion cracking
CT	compact tension
DCPD	direct current potential drop
DI	deionized [water]
DIC	dissolved inorganic carbon
DIC	digital image correlation
DLEPR	double loop electrochemical potentiodynamic reactivation
DNV-GL	Det Norske Veritas Group
DOE	US Department of Energy
DPC	dual-purpose canister
DRH	deliquescence relative humidity
EBSD	electron backscatter diffraction
EDM	electrical discharge machining
EDS	energy-dispersive [X-ray] spectroscopy
FTIR	Fourier transform infrared spectroscopy
FY	fiscal year
GTAW	gas tungsten arc welding
HAZ	heat affected zone
HER	hydrogen evolution reaction
HLW	high-level radioactive waste
IC	ion chromatography
INL	Idaho National Laboratory
IRP	[DOE] Integrated Research Project
ISF	interim storage facility
ISFSI	independent spent fuel storage installation
LLW	low-level radioactive waste
LT	longitudinal transverse
NDE	non-destructive evaluation

NEUP	Nuclear Energy University Program
NRC	Nuclear Regulatory Commission
OP	optical profilometry
ORNL	Oak Ridge National Laboratory
ORR	oxygen reduction reaction
PNNL	Pacific Northwest National Laboratories
PTFE	polytetrafluoroethylene
RD	rolling direction
RH	relative humidity
SAW	submerged-arc welding
SCC	stress corrosion cracking
SEM	scanning electron microscope
SENT	single edge notched tension specimen
SFWST	Spent Fuel and Waste Science and Technology
SNF	spent nuclear fuel
SNL	Sandia National Laboratory
SRNL	Savannah River National Laboratory
ST	short transverse
ToF-SIMS	time-of-flight secondary ion mass spectrometry
UT	ultrasonic phase array
UTS	ultimate tensile strength
UVA	University of Virginia
VCC	vertical concrete canister
WL	water layer
XCT	X-ray computed tomography
XRD	X-ray diffraction
YMP	Yucca Mountain Project
YS	yield strength

SPENT FUEL AND WASTE SCIENCE AND TECHNOLOGY

FY20 STATUS REPORT: SNF INTERIM STORAGE CANISTER CORROSION AND SURFACE ENVIRONMENT INVESTIGATIONS

1. INTRODUCTION

In dry storage, spent nuclear fuel (SNF) is commonly stored in welded stainless steel (SS) canisters enclosed in passively-ventilated overpacks. Over time, dust accumulates on the canister surfaces, and as the SNF cools, salts within that dust will deliquesce to form concentrated brines. If the salts contain aggressive species such as chloride, then the resulting brine can cause localized corrosion, and if sufficient tensile stresses are present in the metal, stress corrosion cracking (SCC) can occur. Over time, SCC cracks could penetrate the canister wall. The risk of corrosion and SCC is greatest in near-marine settings, where chloride-rich sea-salt aerosols are deposited on the canister surface. Developing an improved understanding of the occurrence and risk of SNF storage canister SCC is considered to be critical to demonstrating the safety of long-term dry storage of SNF. For this reason, the Department of Energy (DOE) is funding a large effort to evaluate the occurrence and potential consequences of storage canister stress corrosion cracking as well as to develop prevention, mitigation, and repair technologies for this degradation mechanism, if it should occur. This effort includes work at several different national laboratories and a large DOE-funded effort at universities, as part of the Nuclear Energy University Program (NEUP) (Figure 1).

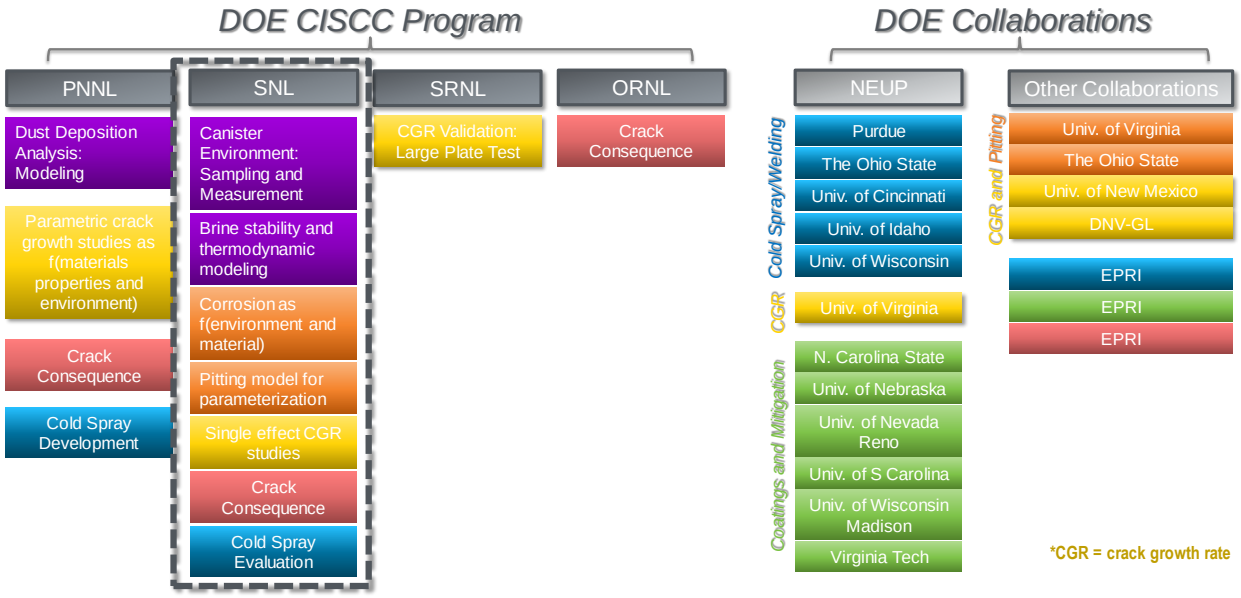

Figure 1. Experimental work on canister SCC currently being carried out by SNL and other national laboratories and collaborators.

Sandia National Laboratory (SNL) plays a main role in this effort, leading work to develop a scientific basis for understanding canister corrosion and SCC initiation and growth, and work to evaluate the potential consequences of canister SCC. This work also involves development of a probabilistic model for canister stress corrosion cracking. Pacific Northwest National Laboratories (PNNL) has a supporting large role in many of these activities. SNL is also performing corrosion experiments to support work to develop cold spray repair technologies at PNNL. Finally, SNL is evaluating potential coatings for prevention and mitigation of canister corrosion and SCC. It should be noted that the DOE has large NEUP efforts in both SCC mitigation and repair and corrosion coating development.

This report documents work done to develop a scientific basis for canister SCC—to define the canister surface environment and corrosion phenomena, including the occurrence and growth of canister pitting and SCC. Other aspects of the SNL program shown in Figure 1 are documented in Spent Fuel and Waste Science and Technology (SFWST) reports.

Over the past few years, Sandia National Laboratories (SNL) has worked to develop a probabilistic model for stress corrosion cracking which utilizes mechanistically-based sub-models to describe individual processes and events that occur during canister aging and that could eventually lead to canister SCC (Figure 2). The current model framework contains numerous assumptions and oversimplifications, many with insufficient scientific basis. Current SCC work at SNL focuses on acquiring data for improved sub-model development, concentrating mostly on determining the underlying mechanisms that govern (1) brine evolution, both before and after initiation of corrosion; (2) the corrosion processes of pitting, SCC crack initiation, and SCC crack growth. This includes developing high-quality data for salt compositions and deposition rates at ISFSI sites and for brine compositions in the evolving canister surface environment, and statistical pitting and SCC initiation and growth data for canister-relevant conditions. By improving sub-model parameterization and validation, this work will reduce uncertainty in our estimates of the timing and occurrence of SCC.

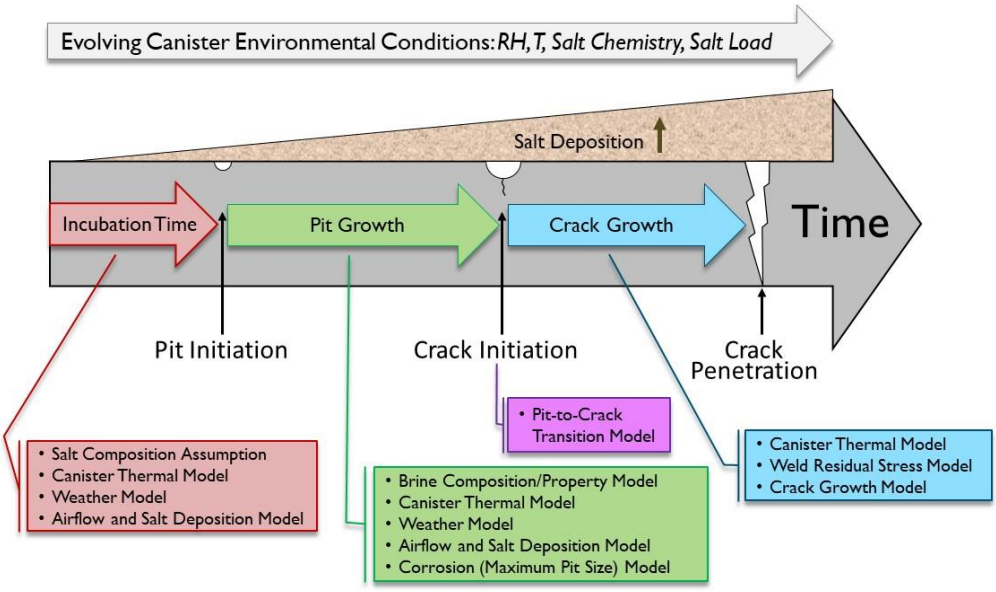

Figure 2. Probabilistic model for SNF dry storage canister stress corrosion cracking.

1.1 Background

A timeline for SCC of spent nuclear fuel canisters in dry storage is shown in Figure 2. Several important events and processes occur during the development of through-wall SCC and understanding the timing of event initiation and the rates of these processes is critical to accurate evaluation of possible SCC penetration times. These parameters are highly dependent upon the evolving physical and chemical environment on the canister surface, and on the canister material properties, including composition, surface finish, and weld-related microstructure and residual stress levels. SNL and several collaborators are working to understand these dependencies, and their effect on potential canister penetration rates by SCC.

Once a canister is placed in a ventilated overpack, dust and salt aerosols begin to be deposited on the canister surface. Determining the composition of those salts is critical to understanding the risk of canister corrosion, and SNL has participated in several dust sampling campaigns over the last several years. Section 2.1 presents the results of the latest campaign, involving dust sampling carried out at the Maine Yankee ISFSI in October 2019. Initially, canister surface temperatures may be too high to permit salt deliquescence or even development of adsorbed water layers on salts, and localized corrosion cannot occur. But as the canister cools, surface relative humidity (RH) values increase; eventually, salts will deliquesce and a brine forms on the metal surface, permitting corrosion to occur. Once a brine is present, corrosion may be delayed for a time, but this period is likely to be insignificant relative to storage time intervals. The period following emplacement and prior to corrosion is known as the incubation period and is a function of the physical environment—the temperature, RH, and salt load on the canister surface. The chemical composition of the deposited salts is also important, as it controls both the corrosiveness of the brine and the RH at which deliquescence occurs. SNL is evaluating the physical conditions and the chemical environment on the canister surface, both prior to and after initiation of corrosion. In Section 2.2 of this report, an in-depth discussion of realistic conditions on canister surfaces is provided, focusing on defining realistic diurnal cycles, salt chemistries, and inert components in the dust, all of which could potentially affect corrosion processes, either beneficially or detrimentally. This information will be used to define realistic testing environments.

One important conclusion in Section 2.2 concerns the prediction of the evolution of canister surface RH values as the canister cools over time. The evaluation presented in Section 2.2.1 shows that, while sea-salt deliquescence may occur relatively soon after canister emplacement, deliquescence of NaCl in the sea salts will not occur for hundreds of years. This means that over time periods relevant to canister corrosion, deliquescent brines will be magnesium chloride rich. Because of this, the long-term stability of $MgCl_2$-rich brines on the heated canister surface, and the effect of atmospheric exchange and corrosion reactions is of particular interest. Experimental and modeling studies of the stability and properties of $MgCl_2$-rich brines are presented in Section 2.3.

Once deliquescence occurs, if the deliquescent brine is chemically aggressive (e.g., chloride-rich), then pitting corrosion will initiate. SNL corrosion research is presented in Section 3. Pitting initiation and pit growth rates, and possible limitations on pit growth, are strongly controlled by environmental factors such as temperature, RH, and salt load, but also by material properties, including composition, surface finish, microstructure, and stress level. SNL has several collaborations with university groups evaluating aspects of pitting initiation and growth as a function of environmental conditions and material properties. SNL is collaborating with the Colorado School of Mines and the University of New Mexico to evaluate the effect of stress on pit growth rates. Because of the dominance of $MgCl_2$ brines during the storage period, SNL is working with Ohio State University (OSU) to evaluate pit initiation and growth on unstrained samples with different surface finishes and in different brine chemistries (e.g., NaCl-rich and $MgCl_2$-rich). SNL is also evaluating the effect of brine composition on the cathodic current generated in the region surrounding the pit, and the anodic current demand due to dissolution within the pit. In the SNL probabilistic SCC model, these values are used to determine the maximum pit size that can occur for a

given set of environmental conditions (Chen and Kelly 2010). This work is being carried out in collaboration with the University of Virginia (UVA) (Section 3.2).

In the presence of tensile stresses, the current assumption is that pits that grow sufficiently large will eventually initiate SCC cracks. Existing models relate pit depth to crack initiation through the calculated crack tip stress intensity factor (e.g., Kondo, 1989; Turnbull et al., 2006). However, this approach must be implemented stochastically, and makes broad assumptions about the shape of the pit. To develop a more realistic relationship between pitting and crack initiation, SNL is working with OSU to experimentally evaluate conditions of pit-to-crack transition under controlled conditions. SNL is also evaluating pitting and crack initiation using large weld samples from a full-diameter canister mockup that SNL used to characterize weld residual stresses (Enos and Bryan, 2016c); this work is described in Section 3.5.

Once a SCC crack initiates, the rate of crack growth will be controlled by the temperature and chemical environment, as well as, possibly, the salt surface load. The tensile stress profile through the metal is also important, as it is combined with the depth of the crack to determine the crack tip stress intensity factor (Newman and Raju, 1981; Newman and Raju, 1979). SNL is working with colleagues at PNNL and SRNL to measure crack initiation and growth rates as a function of canister surface environment (brine composition and temperature). Prior to FY20, SNL's role was largely to define the appropriate environments for testing, and to help interpret test results. However, in FY20, SNL installed load frames, and began its own testing. Most of the experimental work to date has been carried out by Det Norske Veritas Group (DNV-GL), an engineering company that supplied Sandia's load frames, and specializes in SCC testing for both the boiling water reactor and oil and gas industries. However, the load frames at SNL are up and running, and SCC testing will begin early in FY21. Sandia's crack growth measurement work is described in Section 4.

Finally, as industry begins to move towards strategies for mitigation and repair of SCC cracks, should they be observed on SNF dry storage canisters, SNL is supporting work to develop repair strategies. We are working with PNNL to evaluate cold spray repairs for compatibility and corrosion resistance. Moreover, SNL is also working as a collaborator in a NEUP project led by Purdue University to evaluate the corrosion properties of cold-spray repairs. This funding does not come from the SFWST program, but the collaboration will allow us to leverage our funding for both projects.

2. CANISTER SURFACE ENVIRONMENT

In FY20, several efforts focused on understanding the canister surface environment and how it evolves over time. First, a set of analyses were carried out to describe realistic canister surface environments for corrosion testing purposes. Then, field sampling of dusts and soluble salts was performed at the Maine Yankee ISFSI. Finally, experiments and calculations to evaluate $MgCl_2$ stability on heated surfaces were carried out. Each of these efforts is described in the following sections.

2.1 Analysis of Samples Collected from SNF Storage Canister Overpacks at the Maine Yankee ISFSI

On October 15, 2019, the Management and Operations contractor at the Maine Yankee Independent Spent Fuel Storage Installation, located near Wiscasset, Maine provided support to SNL in inspecting and in some cases, removing, witness samples from the inlet and outlet vents of four in-service SNF dry storage systems at the site. The samples consisted of glass coupons for dust and salt collection, and corrosion witness specimens—4-point bend specimens of 304 stainless steel within their fixtures. The samples had been placed within the vents of the overpacks on September 1, 2017 by the Colorado School of Mines, as part of a DOE-funded Integrated Research Project (IRP). Once the project ended, CSU transferred ownership of the emplaced samples to SNL for long-term monitoring. During this campaign, all the inlet and outlet vents were opened, and the samples were removed for inspection. At each location, the glass coupons were collected for analysis at SNL and replaced with fresh coupons. The corrosion specimens were inspected, and the condition recorded they were then placed back into the overpacks. A few samples were collected for more in-depth analysis at SNL.

It is important to note that conditions in the inlet and outlet overpacks do not represent conditions on the canister surfaces. This is true for several reasons. First, the samples in the vents do not reflect waste canister surface temperatures. The air entering the inlet vents will be at ambient temperature and will heat only slightly before entering the main body of the overpack. The air exiting the outlet vents will be somewhat warmer than the air entering the overpack, having been heated by heat exchange with the canister, but will still not reflect canister surface temperatures. Second, although the vents are screened, moisture in the form of fog, rain, or even snow can be drawn into, or blown into the vents and can settle onto the coupons and corrosion samples—there was ample evidence that this occurred, especially at the inlet vents. This cannot happen on the actual canister surface, much deeper in the overpack. Finally, recent PNNL modeling of dust transport and deposition through an overpack indicates that, when large dust particles enter the vents, most of that material is deposited in the vents, and does not reach the canister surface. Hence, the particle size distribution, and the composition of soluble salts (if they vary with particle size) deposited in the inlet vents does not match that on the canister surfaces.

Despite these limitations, the samples do offer useful information. The dust collection coupons provide information on the composition of atmospheric salts at the site, which may differ from the composition on the canister surface, where finer particles are preferentially deposited—salt aerosol compositions commonly vary with particle size. This information is important for establishing the relationship between ambient salt aerosols and canister surface deposits, which is necessary to evaluate the relative risk of canister SCC at the site. As such, this sampling campaign complements one carried out in July of 2018, in which canister surface deposits were sampled (Bryan and Schindelholz, 2018a). Canister surface deposits were sampled in July of 2018. The corrosion test specimens are more difficult to relate directly to canister surface conditions, as they are not heated and will experience higher RH values than the canister surface; the amount and composition of deposited salts may differ as well. They do, however offer a relative assessment of the corrosivity of salt aerosols at the site.

2.1.1 Samples

The four vertical concrete canister (VCC) systems at Maine Yankee into which the samples were placed are designated 18, 37, 42, and 56. These systems were to represent different conditions at the ISFSI—convolutions of hot and cold systems, and systems exposed to prevailing winds vs. systems sheltered by other canisters from prevailing winds. Note that the inlet and outlet vents on each canister face in different directions, and commonly do not have the same wind exposures. The matrix is as follows:

Hot:	VCCs 37 and 42
Cold:	VCCs 18 and 56
Exposed to prevailing winds:	VCCs 18 (inlet), 42 (inlet), and 56 (outlet)
Blocked from prevailing winds:	VCCs 18 (outlet), 37 (inlet and outlet), 42 (outlet) and 56 (inlet)

At each location, witness samples were placed in both inlet and outlet vents. Two sample fixtures were emplaced. The first consisted of one large 4-point bend sample, consisting of a 15″ long fixture, containing a 10″ long, $^{5}/_{8}$″ thick beam with a square cross-section. This sample lay on its side within the vents. Attached to the side of the fixture via a bolted clip and facing upwards was a 2″ × 2″ glass slide to collect dust. The second fixture was a small rack of three small 4-point bend specimens with ¼″ thick beams at different tensions; the surface finish of the beams was the same at any given sample location but varied between locations. An example storage system with witness samples is shown in Figure 3.

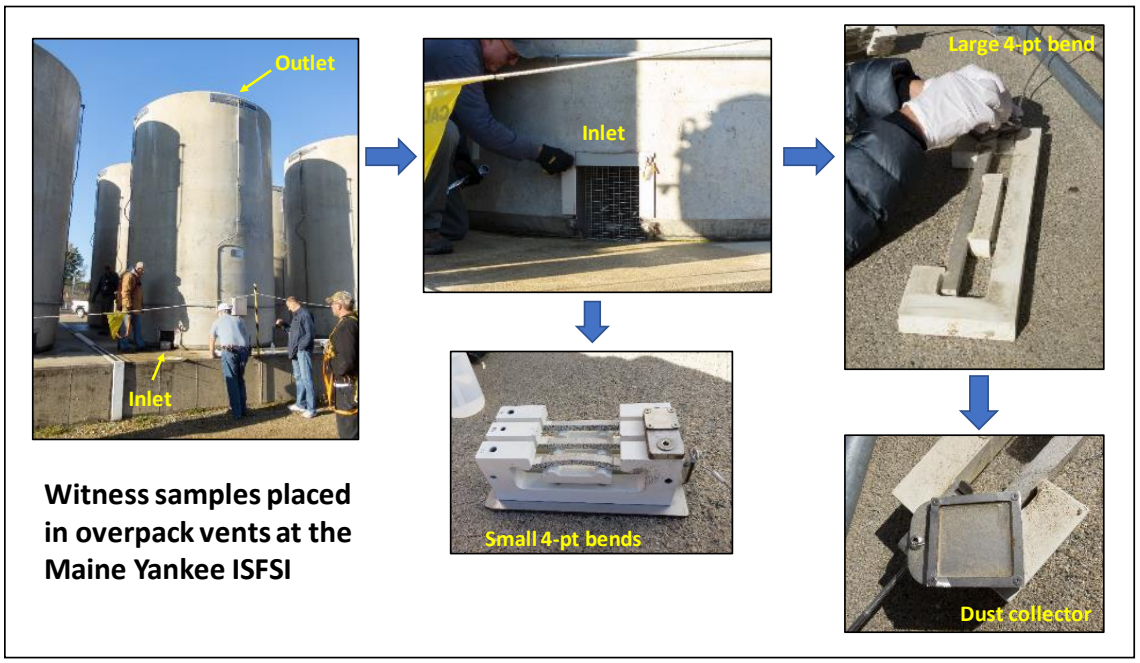

Figure 3. Evaluating witness samples at the Maine Yankee ISFSI.

The large 4-point bend samples were inspected, but none were removed for laboratory analysis. However, each of the attached glass dust collectors was removed and replaced with a clean glass slide. The used slides were taken to SNL for further analyses. The large 4-point bend specimens and a general description of their condition at the time of inspection are listed in Table 1. The smaller 4-point bend specimens were also examined, and two were removed for further study. The condition of the smaller 4-point bend specimens is given in Table 2.

Table 1. List of large 4-point bend specimens placed in overpack vents at Maine Yankee.

VCC	Designation	Material	Surface condition	Load (MPa)	Weld Type	Notes
18 I	MY#I#C#P	304L	36#	250MPa	—	Pitting and corrosion visible on front and top; oxide stains
18 O	MY#O#C#B	304L	36#	250MPa	—	Significant staining on front (may be pits), oxide staining and pitting on top
37 I	MY#I#H#B	304L	Mill	250MPa	—	Thick dust/pollen on sample, stain on top; *dropped*
37 O	MY#O#H#B	304L	Mill	250MPa	—	Oxide stains on front, a few dust particles on top
42 I	MY#I#H#P	Mockup	As-received	250MPa	CW	Stained and dusty
42 O	MY#O#H#B	304L	Polished	250MPa	—	Dusty, no visible corrosion on the front, oxide staining on the top
56 I	MY#I#C#B	Mockup	As-received	250MPa	LW	Oxide staining near weld toe (front), nothing on top
56 O	MY#O#C#P	304H	Polished	250MPa	—	Dusty, no visible corrosion on front or top

Front: refers to the side of the fixture that was facing upwards. Top: refers to the tensioned face of the beam.

MY = Maine Yankee I = inlet O = outlet C = cold H = hot P = exposed to prevailing winds B = blocked from prevailing winds

Table 2. List of small 4-point bend specimens placed in overpack vents at Maine Yankee.

VCC	HCN#	Material	Surface Condition	Load (MPa)	Sample Number	Notes
18 I	MY#I#C#P	304L	Polished	310	3	Yellow with pollen, no visible corrosion.
				240	6	
				150	18	
18 O	MY#O#C#P	304L	Polished	310	10	Oxide staining near paint edge, dust.
				240	15	
				150	19	
37 I	MY#I#H#B	304L	Mill	240	4	Dust, small stains, dark spot on one sample.
				150	8	
				310	23	
37 O	MY#O#H#B	304L	Mill	150	9	Dust, stain patterns, corrosion on scratch (maybe carbon steel in scratch).
				240	16	
				310	24	
42 I	MY#I#H#P	304L	36#	310	1	Oxide staining on all. **Pulled #20 on 10/15/2019.**
				240	13	
				150	20	
42 O	MY#O#H#P	304L	36#	310	12	Oxide staining, dust on all. **Pulled #14 on 10/15/2019.**
				240	14	
				150	21	
56 I	MY#I#C#B	304L	60#	310	2	Minor discoloration. Black spot (insect dropping?) on one sample.
				240	5	
				150	7	
56 O	MY#O#C#B	304L	60#	310	11	Dusty, no visible corrosion, brown spot on paint (not corrosion).
				240	17	
				150	22	

During the inspection, the following general observations were made (Figure 4):

- The test specimens were inserted into the vents but were tethered to the screens with a steel cable, so they were not deep inside the vents. The samples were dirty with wind-blown dust and plant debris.
- Spider webs and other insect debris were common (site personnel frequently clean wasp nests from the outlet vents)
- Inlet samples were in general much dirtier than outlet samples
- There was much lower deposition on vertical surfaces of the fixtures
- Many samples showed evidence of wetting—rain or snow spatter, or possibly condensation or accumulation of wet fog. This was indicated by rings and droplet patterns on the sample surfaces.
- Many of the specimens showed minor oxide staining and corrosion, but major corrosion was not observed.

Figure 4. Witness samples from Maine Yankee, showing heavy dust (a, b); spiderwebs and other insect fragments (c); a heavy coating of yellow pollen (d); and water stains (e, f).

A total of 8 glass coupon dust samples were collected from each of the sample locations. For SEM/EDS and chemical analysis, those samples were designated by the sampling location, as follows:

- VCC-18 inlet
- VCC-18 outlet
- VCC-37 inlet
- VCC-37 outlet
- VCC-42 inlet
- VCC-42 outlet
- VCC-56 inlet
- VCC-56 outlet

2.1.2 Methods

Following photography of the dust collection coupons, the coupons were examined using Scanning Electron Microscope/Energy Dispersive X-ray Spectroscopy (SEM/EDS). Then, coupons were leached to extract the soluble salts for analysis. The following analytical methods were used:

- *SEM imaging and EDS element mapping.* SEM/EDS analysis of the dry dust samples provides textural and mineralogical information of dust and soluble salt species and allows visual identification of organic matter (floral/faunal fragments).
- *Chemical analysis of soluble salts by ion chromatography (IC).* The soluble salts were leached from the Scotch-brite™ pads and glass fiber filters with deionized water. Analysis of the leachate provides soluble salt compositions and concentrations in the samples.

SEM Imaging and EDS Analysis

SEM/EDS analysis of the glass coupon samples provides textural and mineralogical information on the dust, and allows visual identification of organic matter (floral/faunal fragments). Samples retained for SEM analysis were coated with gold/palladium to reduce sample charging during analysis. Imaging and element mapping was done with a Tescan Vega3 SEM, equipped with an EDAX Element® EDS detector. An accelerating voltage of 15 keV was used, and working distances of 9 to 12 mm, with varying degrees of magnification. Images were obtained using both secondary and backscattered electron imaging, and a beam current of 100-200 pA. A somewhat higher beam current (up to 1 nA) was used to produce a high count rate during EDS analysis and to facilitate rapid element mapping.

Chemical Analysis

After leaching, IC analyses were done with a Dionex ICS-1100 RFIC ion chromatograph. Anionic analytes were F^-, Cl^-, Br^-, NO_2^-, NO_3^-, SO_4^{-2}, and $PO_4^{-3;}$ however, signals for Br^- and NO_2^- were not detected in any sample, and those species are not included here. Analyses were done with a 4 mm Dionex Ionpac AS-23 RFIC column and AG-23 guard column, and a Dionex AERS 500 suppressor. Blanks were run after every sample to minimize carryover, but in some cases, a small amount of carryover was observed. Six standards and a blank were made by dilution of stock Dionex IC anion standards. Sample concentrations were estimated using a subset of the standards (never less than three and a blank), excluding those which were higher than necessary to constrain the sample concentration. This was done because the calibration curves were based on the least squares method, which over-weights higher-concentration standards, potentially resulting in larger errors for values in the lower part of the range. Cationic analytes were Li^+, Na^+, NH_4^+, K^+, Mg^{+2}, and Ca^{+2}. IC analyses were done with a Dionex Ionpac CS-12A column and CG-12A guard column, and a CERS 500 suppressor, all 4 mm in diameter. As with the anions, blanks were run after every sample to minimize carryover; in some cases, a small amount of carryover was observed. The standards were made by dilution of stock Dionex IC cation standards. As

with the anions, six standards and a blank were made, but only a bounding subset of the standards (never less than three and a blank) was used to determine the sample concentrations. All standards and eluents were purchased for this analysis and were well within their expiration dates.

2.1.3 Results and Discussion

2.1.3.1 SEM/EDS analysis

The dust was analyzed as deposited, directly on the glass wafer dust collectors (Figure 5). There were no major differences in dust mineralogy between samples. In general, large amounts of organic materials were present, including pollen, stellate trichome (from oak leaves), and other plant fibers. Spiderweb strands were also common, and insect parts were observed occasionally. This was expected based upon the macroscopic visual inspection of the coupons and the obvious presence of yellow pollen and cobwebs. The mineral phases present were dominated by detrital minerals; mainly micas (muscovite, biotite), quartz, and feldspars. In addition to those common minerals, salt phases were also common.

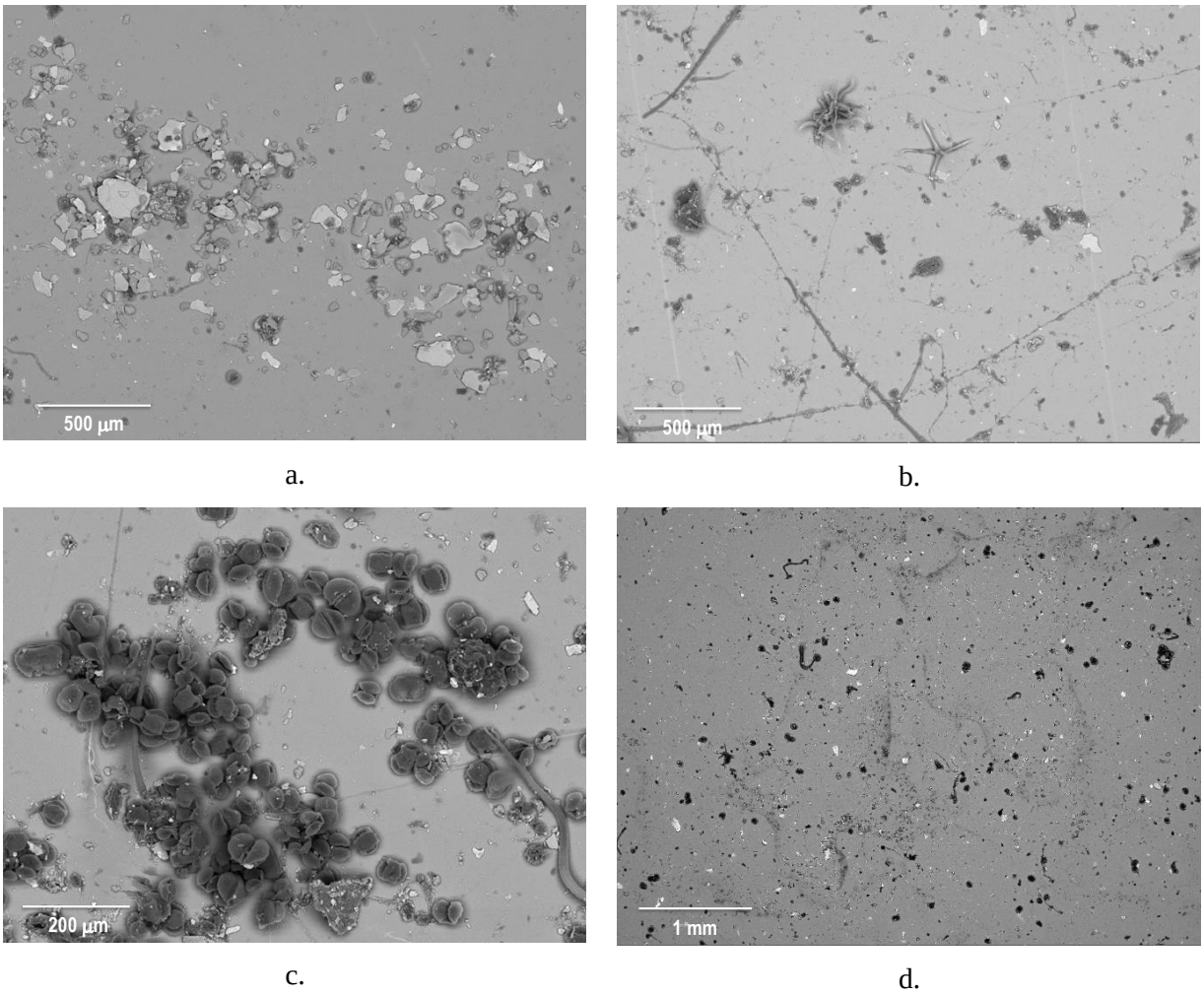

a. b.

c. d.

Figure 5. SEM images of common features in the dust on the Maine Yankee dust collectors. a) Mineral grains, consisting mostly of mica (large flat flakes), and other silicate minerals; b) cobwebs and stellate trichomes; c) pollen and plant fibers; and d) salts, redistributed on the glass surface by moisture.

Salt phases: Composition and distribution

Soluble salts were common on the surface of the glass collectors. They occurred in many different forms. Individual salt aerosols were observed occasionally, as individual salt aerosols (Figure 6a), or more commonly, as tiny chloride particles associated with mineral and pollen grains (Figure 6b). In one case, a dried isolated droplet of seawater (that possibly entered the overpack as a droplet of sea-fog) was present on the glass surface (Figure 6c). These appear to represent individual salt particles that entered the overpack, either in a dry or deliquesced state. Salts are also frequently associated with pollen and plant matter—while in some cases, the salts appear to have been transported into the overpack on the organic particles, more commonly the salts appear to have been wetted on the glass surface and to have wicked up into and onto the organic particles when they dried out (Figure 7). In many cases, salts were redistributed by wetting, forming large areas of continuous salt films on the glass surface, frequently occurring as an apron of fine sulfates, with larger chloride grains distributed throughout (Figure 8).

These observations have significance with respect to discussions of washing dry storage canisters to remove salts. Wetting results in salt redistribution and recrystallization, taking discrete, highly separated chloride salt particles and causing them to coalesce into much larger grains (e.g., Figure 8a); alternatively they might be redistributed into continuous layers on the metal surface (Figure 8c and d). Both could potentially represent a more aggressive environment for corrosion. Because of the potential for salt redistribution, washing canisters with aqueous solutions to remove salts is a cleaning process that should only be undertaken with great care, if at all.

It is notable that, although there is significant nitrate present in the leachate from the glass dust collectors (Section 2.1.3.2), no discrete nitrate phases were observed in the EDS analysis. Therefore, there is some uncertainty regarding the origin and mineralogy of the soluble nitrate in the samples.

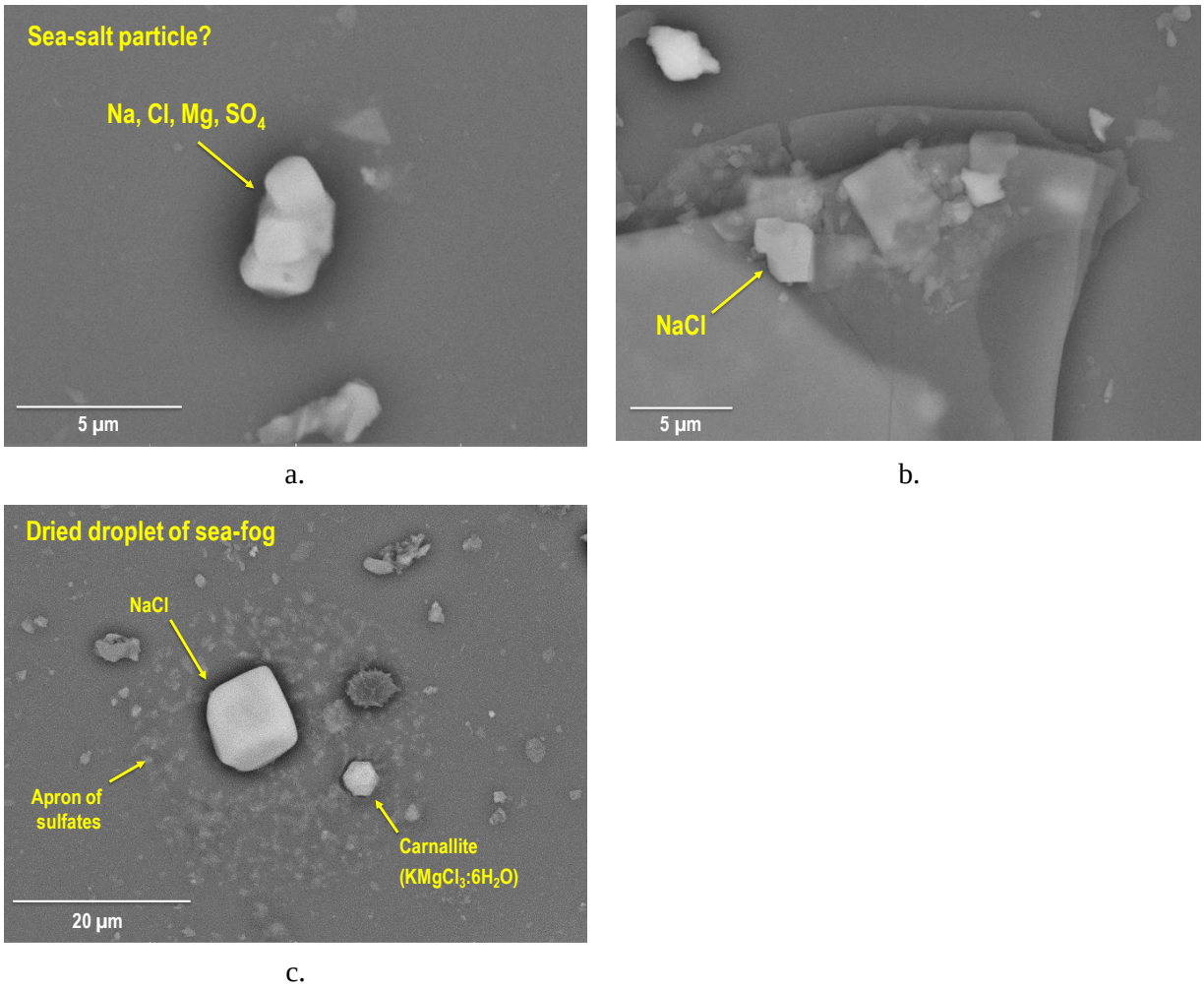

Figure 6. SEM images of soluble salts on the Maine Yankee glass coupons. a) Particle exhibiting the characteristic morphology and composition of a sea-salt aerosol; b) small particle of NaCl attached to a larger mineral grain; c) a precipitated salt assemblage on the glass surface, compositionally consistent with being a dried droplet of seawater.

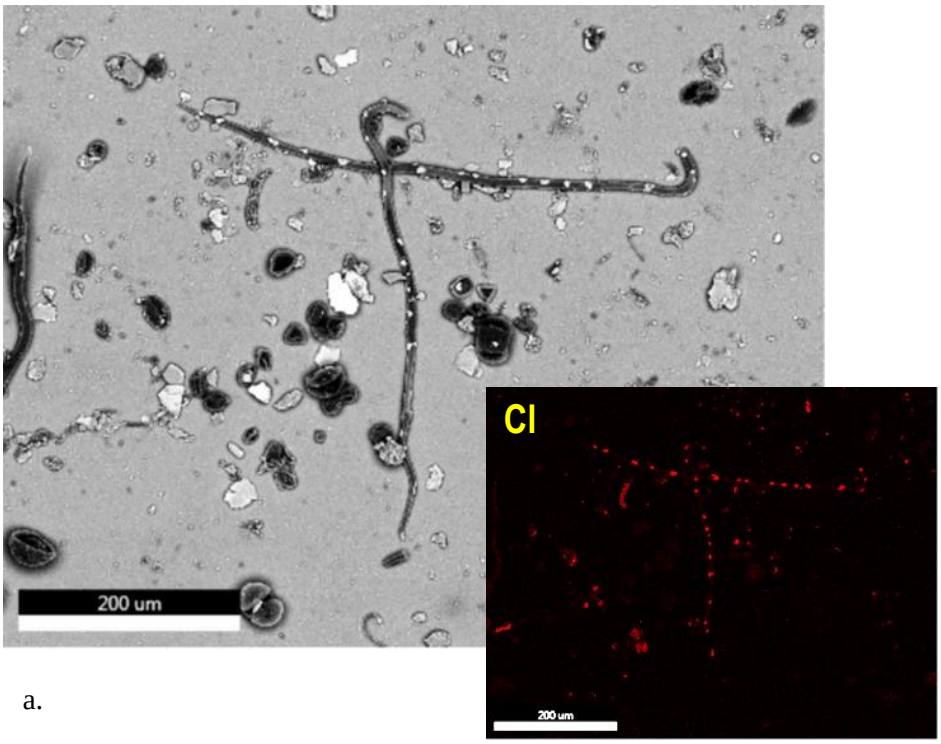

a.

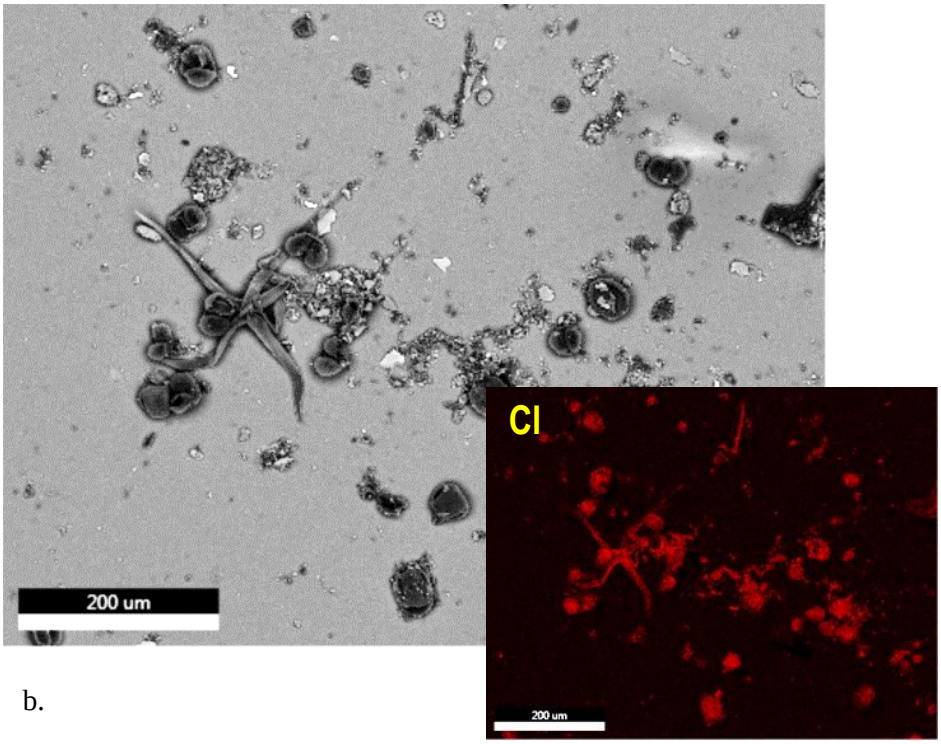

b.

Figure 7. SEM images and EDS chloride maps of soluble salts associated with organic particles on the Maine Yankee glass coupons. a) NaCl grains decorating a stellate trichome; b) chloride associated with pollen, a stellate trichome, and organic fibers.

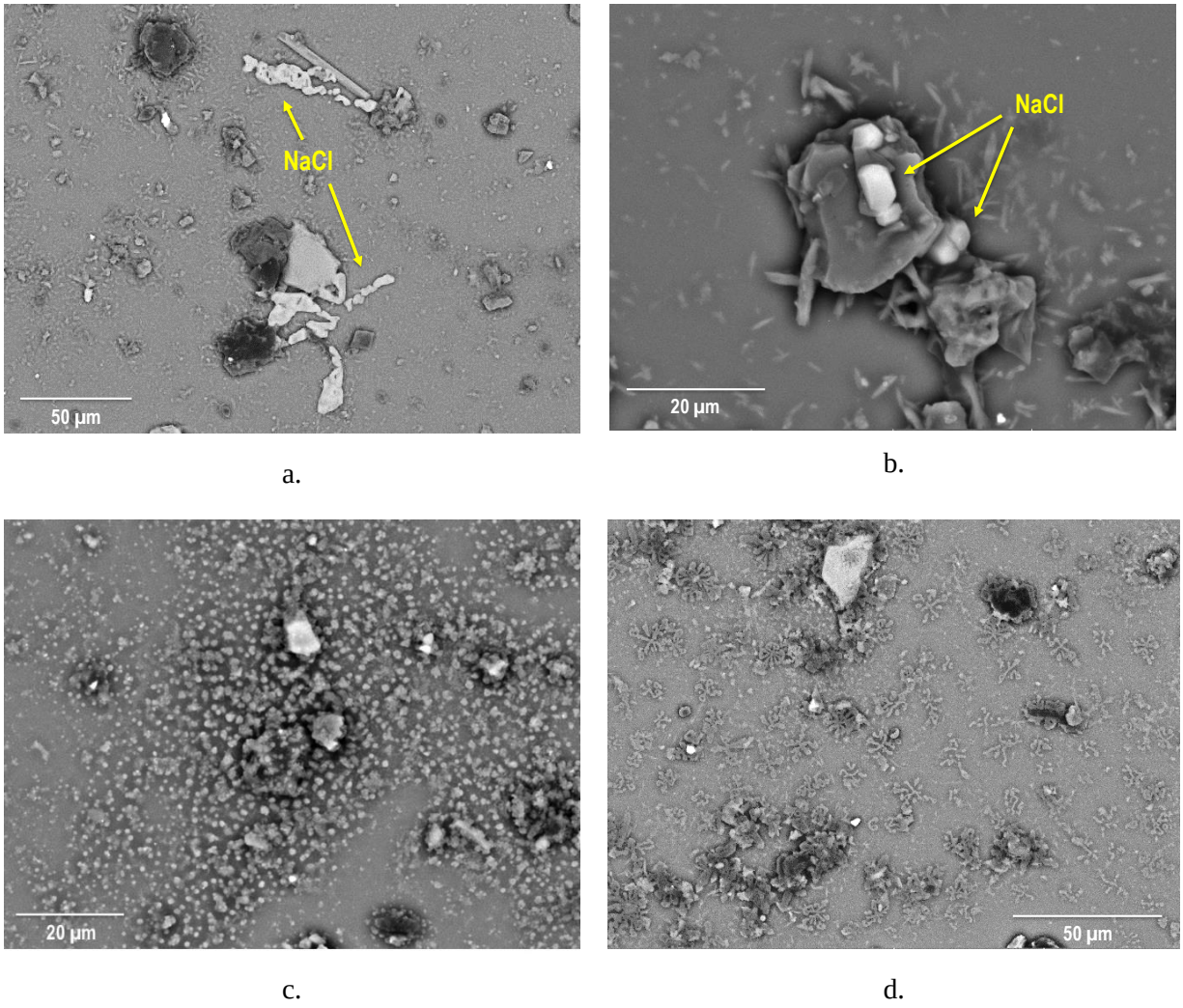

Figure 8. SEM images of soluble salts that have been redistributed by wetting and re-drying on the Maine Yankee glass coupons. a) large NaCl crystals that crystallized out of a continuous water layer on the glass; b) NaCl crystals on a mineral grain, surrounded by an apron of acicular sulfates; c, d) a film of fine-grained sulfates with intermixed fine particles of NaCl.

SEM/EDS Analysis of Small 4-point Bend Samples

In addition to analysis of the dust collectors, the two small 4-point bend samples that were collected were examined by SEM/EDS. These analyses showed the presence of localized corrosion associated with areas of dust. In addition, a few isolated NaCl crystals were observed on sample VCC 42 (Figure 9). However, it is important to note that no evidence of SCC was observed; this is perhaps surprising, given the high tensile stresses to which some of the samples were loaded. Future observations will be important in understanding the relative risk of SCC at this site.

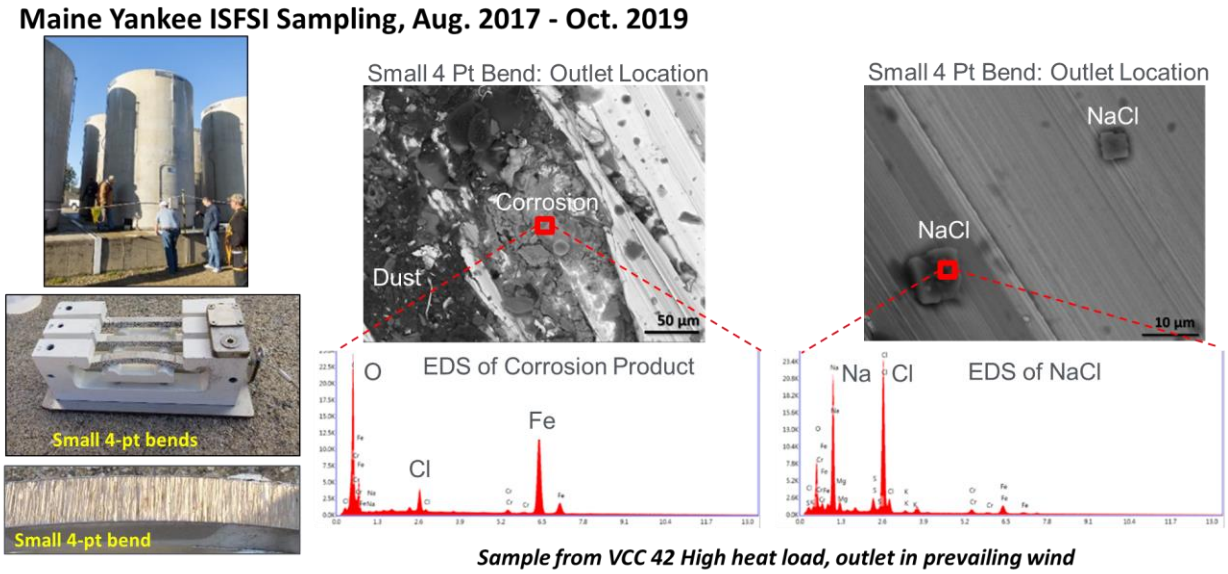

Figure 9. Corrosion products and NaCl on the surface of a 4-point bend sample extracted from an outlet vent at Maine Yankee.

2.1.3.2 Leaching and Chemical Analysis by Ion Chromatography.

Following SEM analysis, the dust collectors were leached with deionized water, and the leachate analyzed by IC to determine the composition of the soluble salts. The soluble ion concentrations are shown in Table 3, and in Figure 10. Measurement uncertainties are generally 5 % or less but may be as high as 20% for values that are near the quantification limits.

Table 3. Composition of soluble salts leached from the Maine Yankee dust collectors (µmoles/sample).

Sample #	Na^+	NH_4^+	K^+	Mg^{+2}	Ca^{+2}	Cl^-	NO_2^-	NO_3^-	PO_4^{-3}	SO_4^{-2}
18 in	1.853	0.021	0.500	0.190	0.478	0.675	0.027	0.273	0.020	0.120
18 out	0.350	0.026	0.080	0.041	0.120	0.969	0.033	0.879	0.007	0.221
37 in	2.368	0.016	0.398	0.232	0.494	0.989		0.364	0.033	0.208
37 out	0.152	0.019	0.029	0.012	0.039	0.178	0.017	0.168		0.065
42 in	0.963	0.016	0.479	0.089	0.263	0.373	0.017	0.128		0.085
42 out	2.339	0.018	1.109	0.183	0.981	0.872	0.033	1.528		0.292
56 in	0.669	0.012	0.500	0.063	0.285	0.272	0.017	0.111		0.077
56 out	0.373	0.018	0.358	0.045	0.334	0.139		0.053		0.027

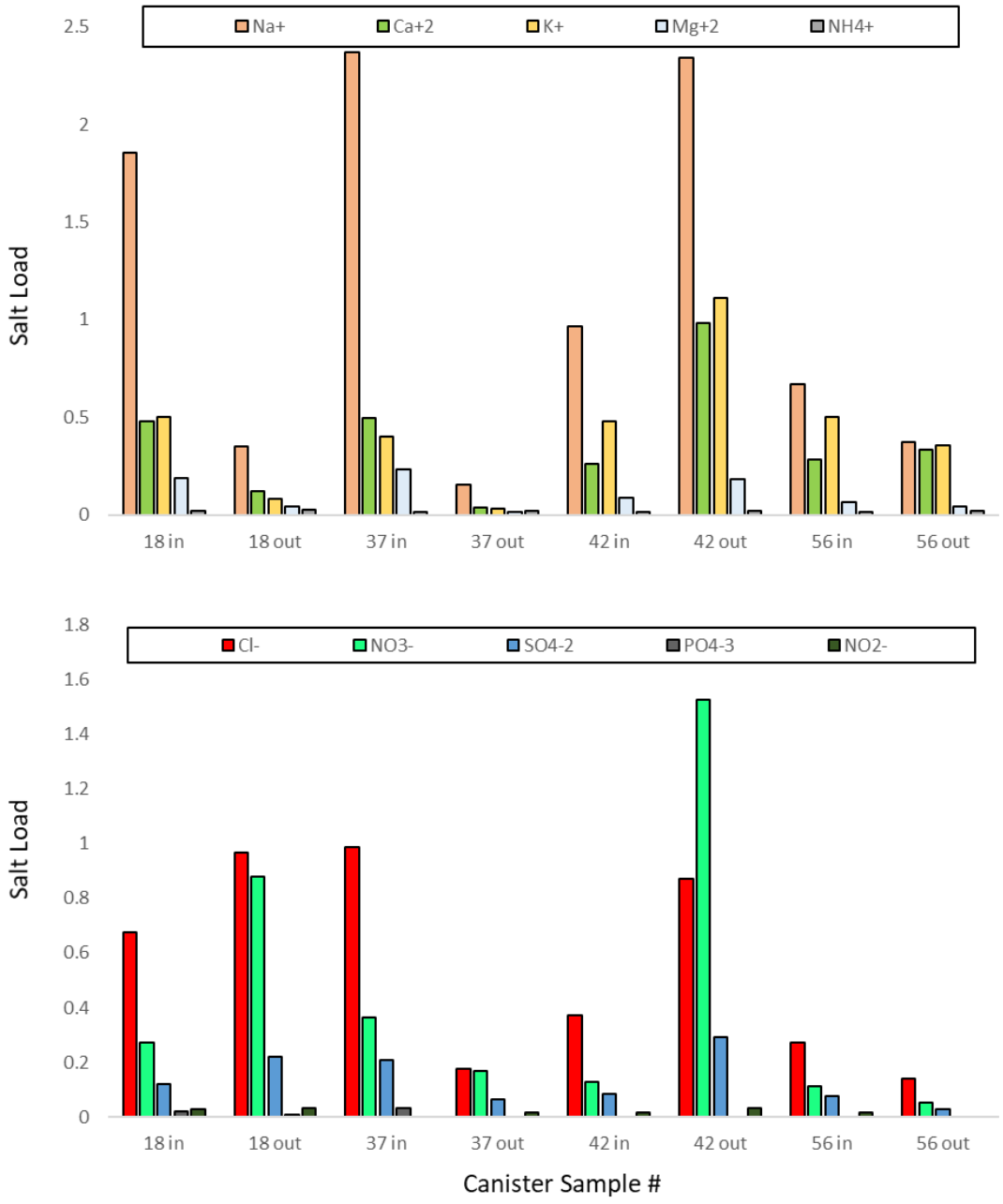

Figure 10. Composition of soluble salts leached from the Maine Yankee dust collectors. Upper: cations. Lower: anions.

Generally, the salt are a mixture of solutes that are marine (Na^+,Cl^-, Mg^{+2}, SO_4^{-2}) and continental (Ca^{2+}, K^+, NO_3^-, and SO_4^{-2}) in origin. Although continental salts are certainly present, very little NH_4^+ was observed. There are a number of reasons why this could be true, NH_4^+ is prone to degassing and could have been lost. This might have occurred during sample transport, handling or leaching. Alternatively, it may have occurred inside the vents, either by degassing from the dry salts, or after wetting; experimental evidence indicates that NH_4^+ salts and brines containing Cl^-or NO_3^- degas readily from even mildly

heated surfaces (Bryan and Schindelholz, 2018b; Schindelholz et al., 2017b). The primary cation present is Na^+, but Ca^{+2} and K^+ are also common and in a few samples are nearly as abundant as Na^+. The Na:Mg ratio suggests that the Mg present is likely from sea-salt aerosols. The primary anions are Cl^- and NO_3^- and to a lesser degree SO_4^{-2}. Chloride is the dominant ion in most of the samples, though a few samples (e.g., *VCC-42 out*) have significant amounts of NO_3^-. Carbonate was not measured directly in these samples, though observed anion deficiencies suggest that carbonate is present and abundant. While carbonate may exist as soluble inorganic salts, it also may be present as a sorbed anionic species on the abundant organic materials. Compared to previous sampling at Maine Yankee where dusts and salts were collected directly from the canister surface, these samples are more chloride-rich. This may indicate that sea-salt aerosols tend to be coarse, and deposit in the vent rather than on the canister surface.

Among the samples, the chemical composition is relatively consistent, the exception being sample *VCC-42 out*, which was significantly more nitrate-rich than samples from the other locations. In general, inlet vents had higher salt loads than outlet vents, although again VCC-42 was an exception, the outlet vent having significantly higher salt loads. The impact of the other variables, such as heat load and exposure to prevailing winds is not clear. VCC 37 and VCC 42 had hotter canisters. While these two VCCs do have the high loadings of Na at one vent location, (37 in and 42 out), the reciprocal vents have fairly low salt loading (37 out and 42 in). With respect to wind exposure, VCC 18 and VCC 42 inlet vents were considered "exposed". While there does not appear to be a strong trend between exposure and salt loading, the outlet vents of these two overpacks, both considered sheltered from the wind, have the highest NO_3^-:Cl^-ratio, with 42 actually having more nitrate than chloride.

2.1.3.3 Summary

In October of 2019, corrosion test specimens were examined and dust coupons were collected from the inlet and outlet vents of four VCC systems of varying heat load and wind exposure. The samples were located close to the vent screens and had heavy loads of dust. The dust consisted mostly of silicate minerals and organic particles—pollen, stellate trichomes, and plant fibers. Soluble salts, as determined by leaching, consisted of a mixture of sea-salts and continental salts; however, salts observed by SEM were chlorides and sulfates, and included a small number of sea-salt particles and sea-salt mineral assemblages that appear to have been deposited wet, possibly as sea-fog droplets. Although nitrate was leached from the coupons, no discrete nitrate phases were observed by SEM, and it may be intimately associated with the organic phases.

An important conclusion from this work is that the salts in the vent dust samples differ from the canister salts, suggesting that salt aerosols collected externally or in the vents may not represent the salts on the canister surface. This suggests that external, or vent, corrosion monitoring may be highly conservative relative to conditions on the canister surface. Also, although the salts of the dust collectors sometimes occurred as discrete grains, frequently, they had been wetted and redistributed, wicking into the organic materials upon drying, forming much coarser NaCl crystals, or forming finely crystalline and widely distributed surface coatings. This suggests there may be some risk associated with washing canisters to remove salts; if it is not done thoroughly, salt redistribution may result in more aggressive corrosion conditions on the canister surface. For this reason, the ASME subcommittee responsible for developing an inspection standard for SNF dry storage canisters has recommended that water not be used to clean the canisters for inspection, nor as a couplant for inspections utilizing ultrasound techniques.

Finally, the lack of observed SCC in the witness specimens, even under high loads, and in the apparently more aggressive environment of the vents, is encouraging. Future sampling will be critical to understand the risk of canister SCC at this site.

2.2 Testing Environments

Four studies were carried out to better understand the canister surface environment and how it evolves over time. First, an existing canister thermal model was combined with ambient weather data from different SIFSIs to calculate the spatial and temporal evolution of RH on the canister surface. Although these calculations are specific to the thermal model used, they do provide insights on the timing and composition of deliquescent brines that are anticipated to form on the canister surface over time, as the heat load decreases and the canister cools. Second, ambient weather data were used to calculate relevant diurnal cycles in T and RH on a heated canister surface, focusing on cycles that would result in large daily changes in brine properties (e.g., dryout) on the metal surface. Cyclic changes in T and RH are generally considered to be more aggressive than constant conditions (Nishikata et al., 1995), and cyclic corrosion testing using the derived conditions is currently in progress at SNL. Third, soluble salt data from field sampling of dusts on in-service SNF dry storage canisters was evaluated to determine relevant brine compositions for testing purposes. Testing to date has been carried out with sea salts or individual salts present in the sea-salt assemblage, but soluble salts sampled from canisters frequently have a significant component that is "continental" in origin (i.e., derived from land use or other anthropogenic processes). These components, such as nitrate and sulfate, may inhibit or promote canister corrosion. Finally, dust collected from in-service canisters was evaluated to determine the size range of detrital mineral grains present. These minerals are anticipated to be chemically inert but may affect corrosion by facilitating brine spreading via capillary processes, or by creating occluded areas on the metal surface that could result in crevice corrosion.

2.2.1 Evolution of Temperature and RH on the Canister Surface Through Time

In order to determine the RH on the canister surface at any given location and point in time, two inputs are required: (1) a thermal model for the canister surface; and (2), the absolute humidity (AH) of the air entering the overpack, which is obtained from site-specific ambient weather data. The probabilistic SCC model developed by Sandia uses estimated storage canister surface temperatures based on computational fluid dynamics modeling of filled storage casks performed by PNNL. There are two models, one for a horizontal storage system, based on a model developed for Transnuclear (now Orano) NUHOMS systems at Calvert Cliffs, and one for a vertical system, based on HOLTEC HI-STORM 100 storage systems at Diablo Canyon. Here, the data from the horizontal system model described in Suffield et al. (2012) are used to illustrate the evolution of the canister surface RH over time. The model was run at different heat loads to simulate different points in time after placement in storage. These correspond to the following:

- 24 kW — 0 years
- 20 kW — 2 years
- 15 kW — 7 years
- 10 kW — 12 years
- 8 kW — 27 years
- 6 kW — 42 years
- 4 kW — 92 years
- 2 kW — 292 years

These models provide temperature maps of the canister surface through time; an example is shown in Figure 35.

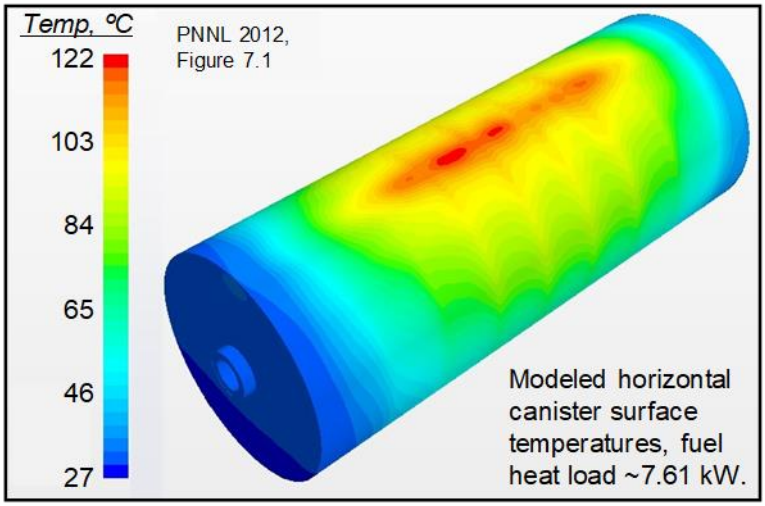

Figure 11. Predicted temperatures on the canister surface for the Calvert Cliffs NUHOMS model, at a heat load of 7.61 kW.

For the SNL probabilistic SCC model, the results of the 8 different heat load models were discretized into thermal maps using 35 different points on the canister surface. The nodes are not evenly spaced longitudinally, but instead were chosen to capture the overall longitudinal and circumferential variations in canister surface temperatures predicted by the models. The nodes are shown in Figure 12, along with an example of the simplified, flattened temperature map made by interpolating between the nodes. Comparison with Figure 11 shows that the overall temperature distribution is captured well.

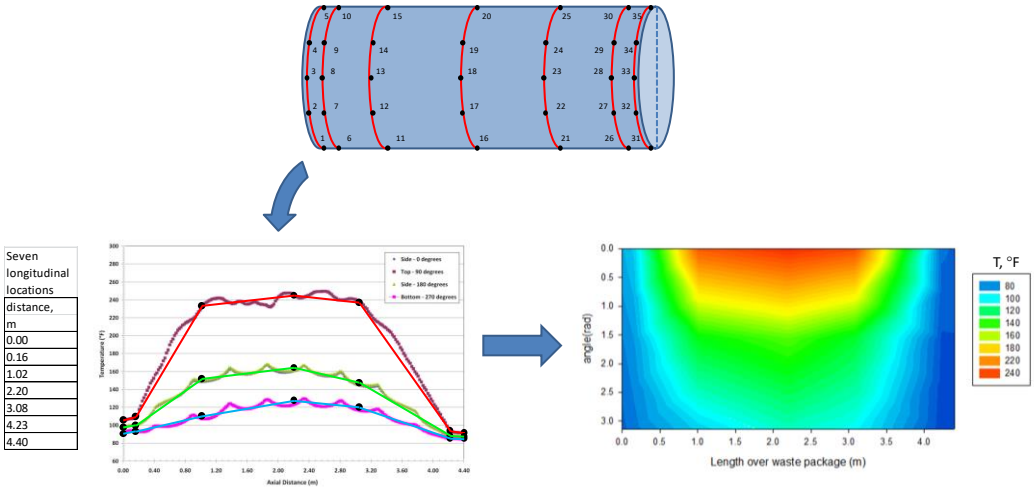

Figure 12. Simplified grid of 35 nodes used to estimate the canister surface temperature at any location over time. An example map derived from the grid data is shown.

The predicted thermal evolution of the canister surface at each of the 35 nodes used in the model, from time = 0 to 292 years, is shown in Figure 3. The assumed ambient air temperature used in the model is 15.5 °C (60 °F). The heat load drops rapidly with time and so do the surface temperatures; in some locations on the canister surface, temperatures below 40 °C are reached in less than 10 years. However, it is important to note that the temperatures everywhere on the whole canister surface remain significantly elevated—at least 7-10 °C above ambient—for hundreds of years.

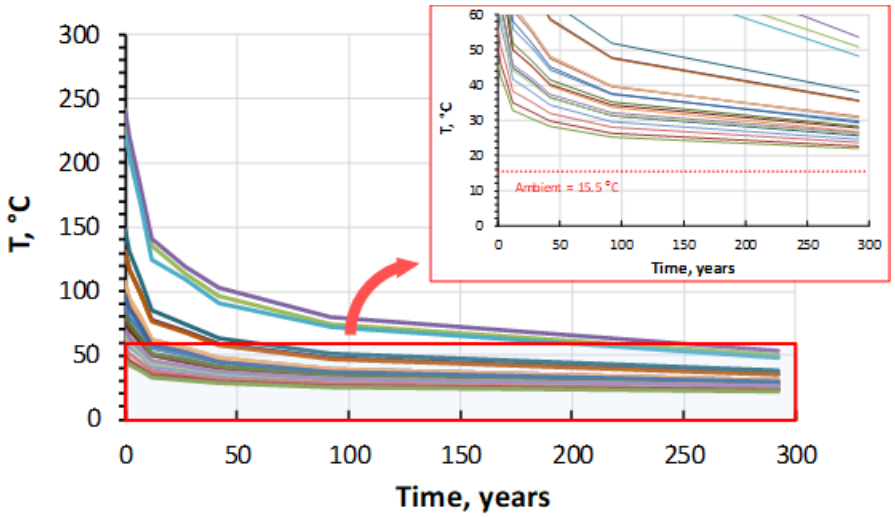

Figure 13. Predicted evolution of canister surface temperatures at 35 nodes on the surface of a spent fuel storage canister, assuming an ambient air temperature of 15.5 °C (60 °F) (see inset).

Given the canister surface temperatures, the RH on the canister surface can be calculated for any given absolute humidity (AH) of the air entering the overpack by using an equation of state for water (Wagner and Pruß, 2002) to correct for the change in temperature. The relationship between RH, AH, and T, is shown in Figure 14, for a range of different AH values. Over time, as the canister cools, the relative humidity represented by any given AH increases.

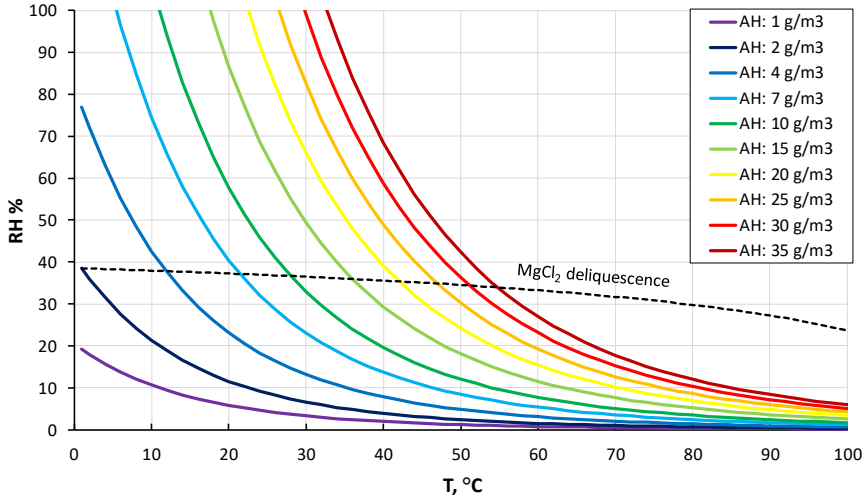

Figure 14. RH as a function of temperature and absolute humidity.

The base case thermal model results in Figure 13 are based on an assumed ambient temperature of 15.5 °C (60 °F). At that temperature, the maximum possible AH is 13.3 g/m^3, the AH at which the air is saturated with water. Using this value as the maximum AH for air entering the overpack, the RH values on the canister surface corresponding to the temperature curves in Figure 13 are shown in Figure 15. RH values can exceed the deliquescence point of bischofite ($MgCl_2$:$6H_2O$), which closely corresponds to the deliquescence RH of sea-salts, in less than 20 years at some locations on the waste package surface

(specifically, the bottom of the canister, near the ends). By 50 years, a significant portion of the canister surface may be cool enough for magnesium chloride deliquescence.

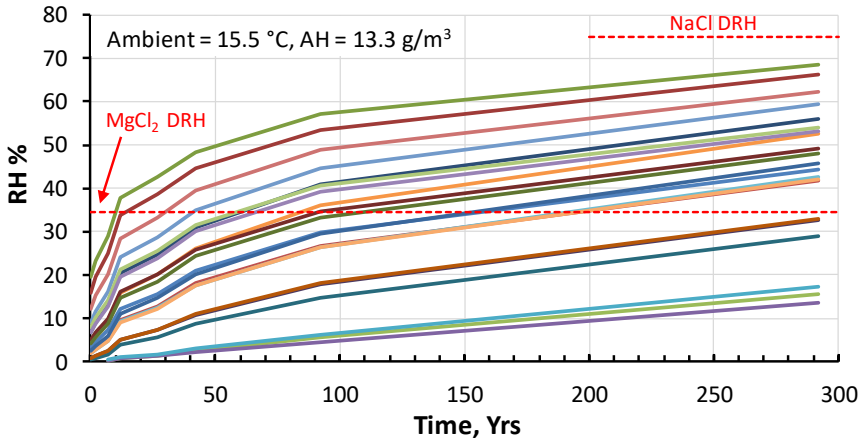

Figure 15. Predicted evolution of RH on the canister surface for the base-case horizontal canister thermal model. Ambient temperature = 15.5 °C, and the AH is assumed to be 13.3 g/m^3, the maximum possible value at that temperature.

What AH values have been observed under natural conditions? SNL has compiled weather data from the airport locations nearest to 64 different ISFSIs across the country, and maximum daily AH values over a calendar year are shown in Figure 16. In this data set, maximum daily dewpoint values frequently exceeded 25 g/m^3 during summer months but exceeded 28 °C (AH = 30 g/m^2) for a combined total of only two days, achieving dewpoint values as high as 29 °C (AH = 31.8 g/m^2). Excluding these rare events, a value of 30 g/m^3 appears to be a reasonable estimate for maximum AH values experienced at a U.S. ISFSI.

The minimum incoming air temperature necessary to achieve an AH of 30 g/m^3 is ~30 °C. Because canister surface temperatures scale linearly with the ambient air temperature, the base-case thermal model can be easily modified to represent an incoming air temperature of 30 °C by simply adding a delta of 14.5 °C (30 °C – 15.5 °C) to the base-case thermal model values. The resulting canister surface temperature curves are shown in Figure 17, and the predicted RH values, in Figure 18.

Comparing the data in Figure 15 and Figure 18 shows that they are remarkably similar. The RH curves using ambient temperatures of 30 °C and an AH value of 30 g/m^3 AH are only a few percent higher than those at the lower ambient temperature and AH. When calculating canister surface RH, the effects of the higher AH are mostly offset by the higher assumed canister surface temperatures.

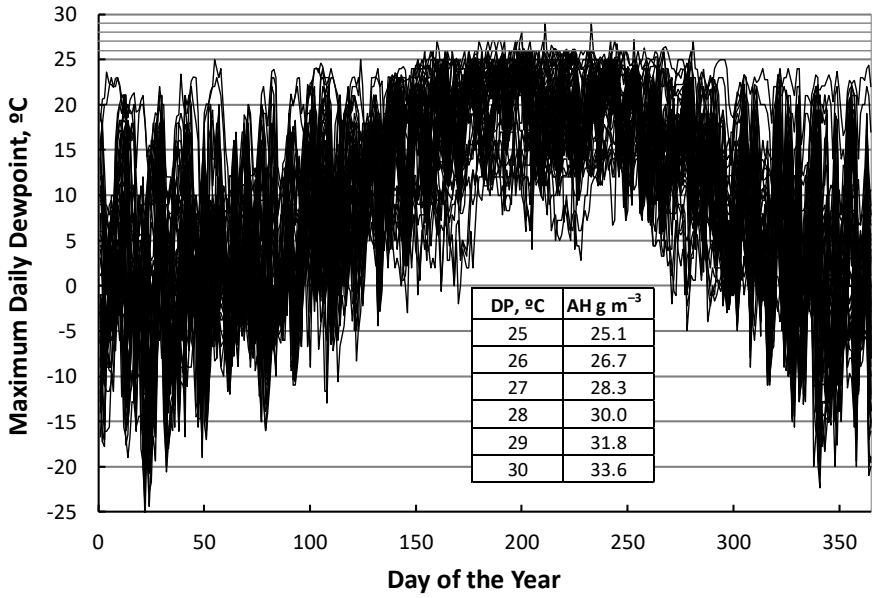

Figure 16. Daily maximum dewpoint data over a year, for 64 ISFSI sites.

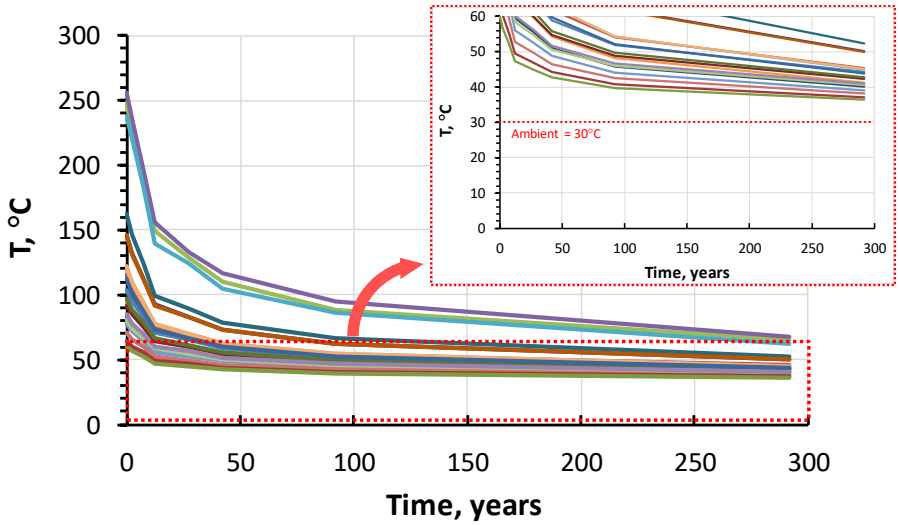

Figure 17. Predicted evolution of canister surface temperatures through time for the horizontal canister thermal model, assuming an ambient air temperature of 30 °C (86 °F).

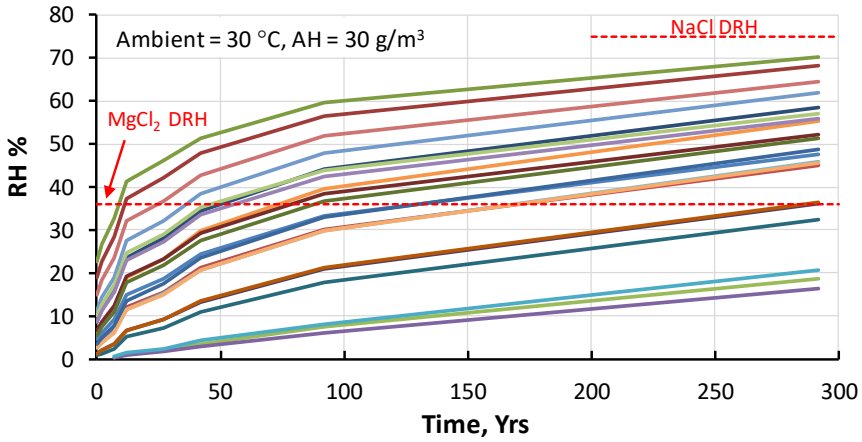

Figure 18. Predicted evolution of canister surface temperatures through time for the horizontal canister thermal model, assuming an ambient air temperature of 30 °C (86 °F).

There are some assumptions in these calculations. The weather data in Figure 16 are only for a single year (2012); however, it is unlikely that additional yearly data will vary significantly. Also, AH values of 30 g/m^3 are probably associated with temperatures above 30 °C; that is, the RH of the incoming air was not 100%. In this case, the canister surface temperature is being underestimated and the surface RH values are being conservatively overestimated. But the calculation shown here is a good approximation.

It is important, also, to remember that corrosion, and even stress corrosion cracking, has been observed in stainless steels at RH values well below the deliquescence RH of bischofite. Fairweather et al. (2008) observed SCC of 304 at 15% RH, in testing at 45 °C and 60 °C; Shirai et al. (2011) observed 304L SCC at 15% RH and 80 °C; and NRC (2014) observed SCC of 304 at RH values between 20% and 30% at temperatures of 60 ° and 80 °C. However, only the Fairweather conditions represent a combination of RH and temperature that are actually achievable on the canister surface.

2.2.2 Diurnal cycles in T and RH

At any ISFSI site, temperature and RH will vary over the course of a day, and over the seasons. These changes are also reflected in the canister surface conditions, and, once conditions for deliquescence have been achieved, these variations will correspond to large daily cycles in the amount and composition of brine on the canister surface which may have either beneficial or detrimental effects with respect to corrosion of the metal. Here, realistic diurnal cycles in T ad RH on canister surfaces are identified, and one cycle has been chosen for use in corrosion testing. Part of the discussion below has been taken from the FY17 status report for this program (Schindelholz et al., 2017a), and is repeated for convenience in this more in-depth discussion of diurnal cycles.

For a SNF dry storage canister within its overpack, surface temperatures vary widely with location due to passive cooling by air flowing up through the overpack. Air entering the overpack through inlet vents near the base flows up and around the canister, becoming hotter as it moves upward. Canister surface temperatures are lowest near the inlet at the base and increase upwards. At any given canister surface location, canister surface temperatures are highest immediately after loading, and decrease over time as the fuel ages and the heat load drops. At any given location and point in time, the temperature is a function of both the heat load and the temperature of the ambient air entering the overpack. Previous thermal modeling of canisters within their overpack indicates that the surface temperature varies nearly linearly with the ambient air temperature; to a reasonable approximation, a 1ºC increase in ambient air temperature equates to a 1ºC increase is canister surface temperature. Moreover, despite the canister thermal mass, the very efficient passive cooling means that canister surface temperatures change rapidly in response to changes in ambient air temperature. Hence, it is reasonable to assume that canister surface temperatures at any given location will track diurnal and seasonal variations of the outside temperature,

maintaining a fixed offset, or delta, due to the heating from the fuel. The RH at any given canister surface location is a function of the surface temperature and absolute humidity (AH), or water content, of the incoming air. It, too, varies diurnally and seasonally, both because of changes in ambient air temperature and corresponding changes in canister surface temperature, and because of diurnal and seasonal changes in the AH of the ambient air.

Hence, canister surface temperatures and RH vary daily and seasonally as the outside air temperature and AH change. This can have major effects on the volume of deliquescent brine present and on the composition of the brine. In the extreme case, daily weather changes may cause the RH at the canister surface to fluctuate above and below the deliquescence RH for the deposited salts, causing the salts to dry out and re-wet on a daily basis. *Note that all SNF canisters, as they cool, will pass through an interval when the periodic dry-out and rewetting of salts will occur in response to ambient weather fluctuations.*

Siegel et al. (2015) suggested that conditions of periodic dry-out are the most aggressive for corrosion initiation and growth, perhaps because of the formation of very concentrated brines as dry-out occurs. Some experimental studies have attempted to evaluate the effects of cyclical changes in RH and periodic dry-out on the extent and rate of corrosion (NRC, 2014; Siegel et al., 2015). However, these experiments did not cycle T and RH in a realistic manner or over a realistic range for field conditions. Under natural conditions, AH varies relatively little over the course of the day; changes in ambient RH are driven largely by changes in T. This means the T and RH correlate indirectly—higher temperatures correspond to lower RH values. On the canister surface, temperatures will be higher than ambient, but the same relationship would hold. Moreover, with increasing canister surface temperature, the maximum possible RH decreases, and the RH swing caused by daily temperature fluctuations narrows. Experimental studies run under cyclic conditions have not captured this relationship. For instance, the NRC (2014) evaluated pitting and SCC initiation under cyclic temperature and RH conditions, but utilized a system design where T and RH covaried directly—higher temperatures corresponded to higher RH values. Moreover, during the cycle, the AH varied by more than 12 g/m^3, a much higher range than is commonly observed in daily fluctuations at natural sites. Siegel et al. (2015) evaluated SCC crack growth in aluminum under cyclic RH conditions, but held the temperature constant and varied the RH from 40% to 90%, corresponding to an AH variation of over 15 g/m^3.

Finally, for both experiments, no attempt was made to ramp temperature and RH at rates that were typical of natural settings. If Siegel is correct that corrosion rate increases as brine concentration increases during the dry-out step, then it is clear that the rate of RH change is a critical parameter, especially if the goal is to compare corrosion rates determined by testing at constant RH with those determined under realistically varying conditions.

The goal of this task is to utilize real ISFSI site-specific weather data to develop a realistic model for coupled diurnal variations in T and RH on a heated canister surface. Specifically, we have identified conditions where the RH fluctuates on a daily cycle above and below the deliquescence RH for sea-salts, potentially resulting in daily dry-out and re-deliquescence. This temperature/RH cycle will be used in corrosion experiments to evaluate the effects of diurnal weather cycles on pitting and SCC.

To determine a realistic diurnal cycle in T and RH, weather data sets representing locations near three different ISFSIs were examined. Airport weather data sets are very complete, with data collected on an hourly schedule. The ISFSIs examined were Arkansas Nuclear 1 in west-central Arkansas; San Onofre on the Pacific coast between Los Angeles and San Diego, California; and Turkey Point, on the Atlantic coast just south of Miami. Comparing these data sets offers assurance that overall diurnal cycling behavior is similar at all sites, and that the conditions chosen for testing are typical.

2.2.2.1 Arkansas Nuclear 1.

The Arkansas Nuclear 1 data set exhibits both a high average AH and large daily temperature swings. A high average AH means that the deliquescence RH is reached at a higher temperature, important experimentally because higher T will speed corrosion and shorten necessary experiment times. Large daily temperature swings are also useful, as they result in larger RH swings, increasing the probability of finding a time interval in which the daily RH fluctuations intersect the deliquescence RH, resulting in dry-out and re-wetting.

Once the data set had been identified, different temperature offsets were applied to the ambient data to represent the heated canister surface, and a new RH was calculated at the higher temperature using the equation of state for water provided by Wagner and Pruß (2002). Examples of the results are in shown in Figure 19. In Figure 19a, the ambient temperature and relative humidity are provided for the entire year of 2013. A large seasonal fluctuation in temperature is obvious, and short-term (daily or day-to-day) fluctuations form a band about 20ºC wide. The range of RH values does not show a significant seasonal dependence, and short-term fluctuations define a broad band, as much as 70% wide. Calculated RH values for a temperature offset of 10ºC are shown in Figure 19b. The width of the T band does not change—it is simply offset 10ºC higher. The RH band is offset to much lower values and is also much narrower, only about 30% wide. Further increasing the temperatures to 20ºC above ambient (Figure 19c) results in lower RH values and an even narrower band of RH values.

The right-hand plots in Figure 19 show the same data sets, zooming in on 20 days in the summer to illustrate daily T, RH, and AH fluctuations. In these data, the indirect correlation between temperature and RH is clear; when temperature rises, RH drops. This occurs because, as seen in the figures, diurnal changes in AH are generally quite small, and for a constant AH, a rise in T results in a drop in RH.

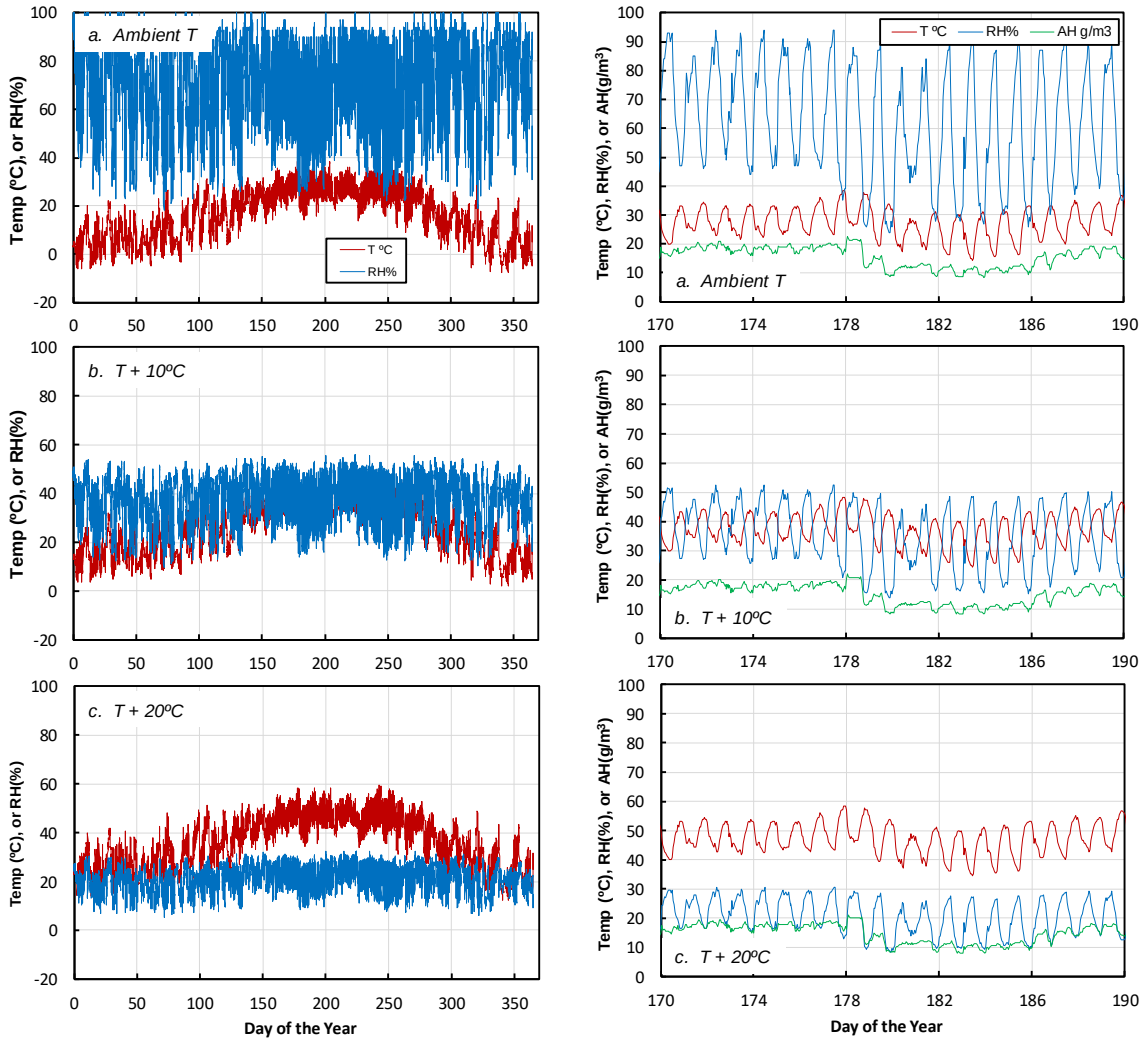

Figure 19. Arkansas Nuclear 1: Effect of increasing canister surface T on surface RH. Yearly data on the left, and an interval during the summer on the right. Top—ambient T; Middle—ambient T+10ºC; Bottom—ambient T+20ºC.

Determining a diurnal fluctuation that crosses the deliquescence RH for bischofite.

For sea-salts, the presence of brine is determined by the deliquescence of bischofite ($MgCl_2$:$6H_2O$), which, at near-ambient temperatures, is 36 % RH; this drops to about 35% RH at 40ºC. The desire is to carry out experiments under representative diurnal conditions, at which the RH varies from above to below the deliquescence RH (DRH) on a daily basis. For the Arkansas Nuclear 1 data set, using the weather data with a 10ºC delta provides some representative conditions that meet this criterion. A one-week section of the weather data with a 10ºC delta, representing the time interval from 170 to 177 days (Figure 19, right), was fitted using Excel Solver with a repeating 24-hour cycle discretized into 2-hour intervals. Temperature and RH cycles were determined independently. The resulting cycles are given in Table 4 and the resulting fits are compared to the actual data in Figure 20. The 24-hour cycle fits the data well. Also shown in Figure 20 are AH values calculated from the paired temperature and RH values for the 24-hour cycle; again, the calculated values are consistent with the actual data.

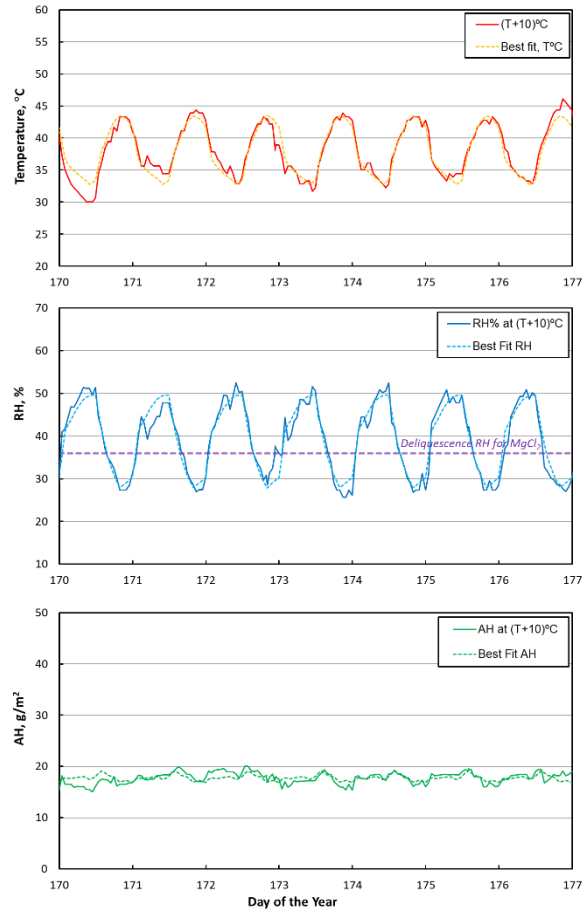

Figure 20. Arkansas Nuclear 1: Comparison of temperature-adjusted weather data with best-fit diurnal cycle that crosses bischofite DRH.

Table 4. Best-fit Arkansas Nuclear 1 diurnal cycle that crosses the bischofite DRH.

Hour	Temp. ºC	RH, %
2	41.68	30.33
4	36.45	41.68
6	35.27	43.92
8	34.35	46.69
10	33.69	48.68
12	32.74	49.54
14	33.44	49.57
16	38.24	40.98
18	40.55	34.62
20	42.69	30.62
22	43.51	27.82
24	42.97	29.15

While independently fitting both T and RH yields the best fit to the data and captures the diurnal variations well over the 7-day period examined, this approach may be difficult to implement in an RH chamber because RH is strongly dependent on T, and varying them both simultaneously may not be possible, or may not yield the desired smooth transition from point to point. Simultaneously changing T and RH was tested at SNL, and occasionally resulted in RH transients for some conditions. However, the cycle given in Table 4 did *not* result in transients.

An alternative approach makes use of the fact that the AH varies little over the 24-hour cycle (b). As illustrated in Figure 21 holding the AH constant at 17.5 g/m^3 while following the 24-hour temperature cycle yields an RH cycle that matches the temperature-adjusted weather data nearly as well as the best-fit RH curve derived by directly fitting the data. The diurnal variations are captured well, and overall shape of the curve matches the slow daily increases and decreases in RH. This is important because the transition periods have been identified as critical times, during which there appears to be an increase in corrosion rate (Siegel et al., 2015). The 24-hour best fit cycle made by varying the temperature while holding the AH constant at 17.5 g/m^3 is given in Table 5. It may be useful for experimentally reproducing the diurnal T and RH cycle in environmental systems where varying T and RH simultaneously results in artifacts.

It should be obvious that many possible T and RH cycles exist that meet the criterion of intersecting the deliquescence RH on a daily basis. The cycle determined here is just one realistic choice, that can be readily implemented, because at least over the time interval evaluated, the day-to-day fluctuations are highly regular and can be duplicated by varying only temperature, while holding AH constant.

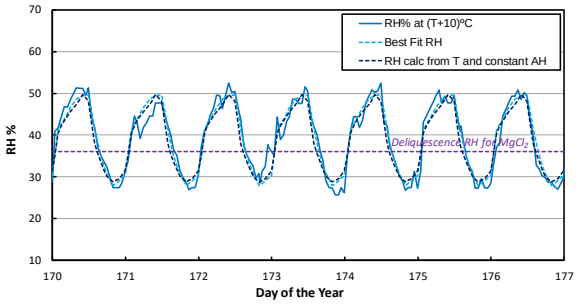

Figure 21. Arkansas Nuclear 1: Comparison of temperature-adjusted weather data with simplified (constant AH) best-fit diurnal cycle that crosses bischofite DRH.

Table 5. Simplified (constant AH) best-fit Arkansas Nuclear 1 diurnal cycle that crosses the bischofite DRH.

Hour	Temp. ºC	AH, g/m^3
2	41.68	17.5
4	36.45	17.5
6	35.27	17.5
8	34.35	17.5
10	33.69	17.5
12	32.74	17.5
14	33.44	17.5
16	38.24	17.5
18	40.55	17.5
20	42.69	17.5
22	43.51	17.5
24	42.97	17.5

Determining a diurnal fluctuation that crosses the deliquescence RH for halite.

Interest in the effects of diurnal variations in temperature and RH on corrosion have largely focused on the region where dry-out occurs, using the logic that it is in that range that the greatest changes in brine properties (concentration, volume, and composition) occur. However, this is not entirely accurate. Below the deliquescence point, the salts dry out. But once deliquescence occurs at around 35% RH, brine properties (concentration and volume) vary only slightly between 35% and 50% RH. A region over which potentially much larger changes in concentration, composition, and volume occur is at the point of NaCl deliquescence (74% RH), where the brine volumes, properties, and composition change markedly. As with the deliquescence point of bischofite, waste packages will eventually cool to the point where diurnal variations in ambient temperature and RH will cause canister surface RH values to fluctuate across 74% on a daily basis. As noted in Section 2.2.1, this may not occur for hundreds of years for heat-generating SNF dry storage canisters. However, for non-heat-generating canisters containing greater-than-class-C (GTCC) waste, such conditions may apply as soon as the waste is emplaced.

Figure 38 shows the weather data from Arkansas Nuclear 1, along with data for temperature deltas of 2 and 5ºC. It is evident that under ambient conditions, the canister surface RH will vary over the NaCl deliquescence RH on a daily basis; no temperature delta is required to achieve this. In fact, even very small temperature deltas shift the RH to values below the deliquescence point of NaCl. Hence, the optimal conditions for evaluating the effect of daily NaCl deliquescence correspond to ambient conditions. Note that these conditions may be difficult to achieve in a laboratory setting, as the minimum daily temperatures will be very close to, or even slightly below, room temperature.

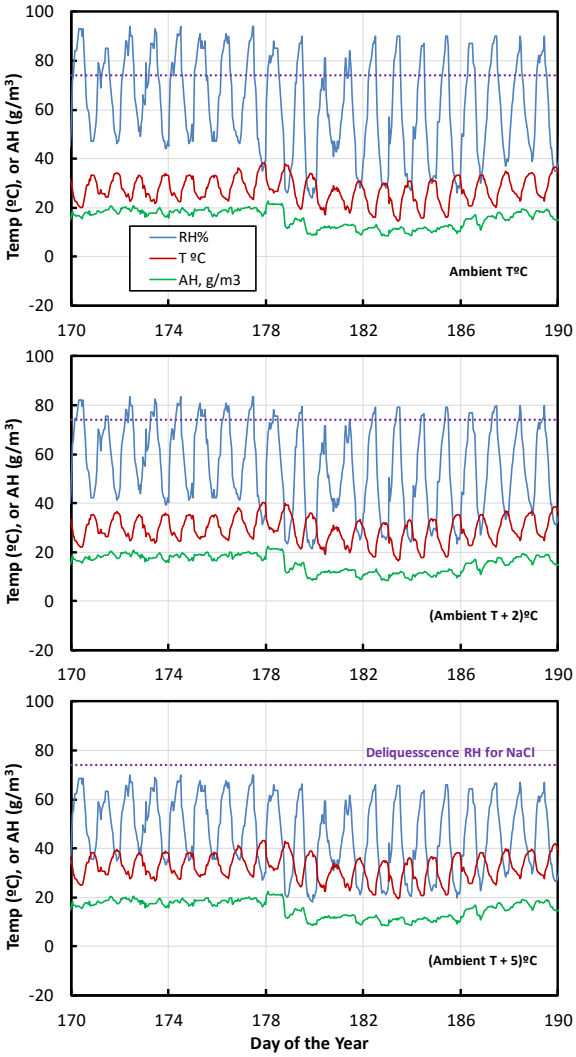

Figure 22. Arkansas Nuclear 1: Effect of increasing T on RH, zooming in on 20 days in the summer. (a) ambient T; (b) ambient T+2ºC; ambient T + 5ºC.

To develop a simplified schedule for duplicating the ambient temperature weather data, the same approach was used as previously. A one-week section of the data, representing the time interval from 170 to 177 days, was fitted using Excel Solver with a repeating 24-hour cycle discretized into 2-hour intervals. Temperature and RH cycles were determined independently. The resulting 24-hour cycle is given in Table 6, and compared to the actual data in Figure 23. The 24-hour cycle fits the data reasonably well. Also shown are AH values calculated from the paired temperature and RH values; again, the calculated values are consistent with the actual data. Note that some of these temperatures are only slightly above room temperature (70ºF or 21ºC), so unless the environmental chamber can be cooled, care must be taken to keep the room temperature below the needed temperatures.

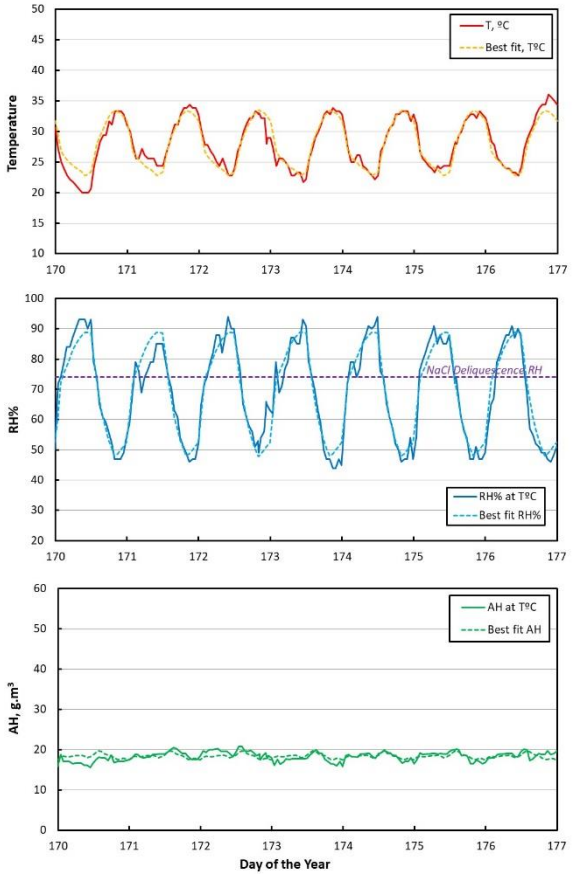

Figure 23. Arkansas Nuclear 1: Comparison of temperature-adjusted weather data with best-fit diurnal cycle that crosses halite DRH.

Table 6. Best-fit Arkansas Nuclear 1 diurnal cycle that crosses the halite DRH.

Hour	Temp. ºC	RH %
2	31.85	51.78
4	26.41	73.67
6	25.28	77.89
8	24.35	83.19
10	23.69	86.97
12	22.74	88.87
14	23.44	88.63
16	28.24	71.72
18	30.55	60.06
20	32.69	52.68
22	33.51	47.70
24	32.98	50.11

As with the previous data set, a simpler approach makes use of the fact the AH varies little over the 24-hour cycle (Figure 23c). As illustrated in Figure 24 holding the AH constant at 18.0 g/m^3 while following the 24-hour temperature cycle yields an RH cycle that matches the weather data nearly as well as the best-fit RH curve derived by directly fitting the data. This possible test cycle is shown in Table 7.

Again, it is important to stress that while conditions for NaCl deliquescence may be of great scientific interest, these conditions are of limited interest to SNF dry storage canister studies. This is because as shown in Figure 22, even very small increases in temperature, corresponding to very low heat loads, make it impossible to reach the deliquescence RH for NaCl of around 74% RH. Hence, only the coolest canisters (for instance, those containing reactor components classified as GTCC waste) will be able to achieve conditions for NaCl deliquescence within time spans relevant to dry storage.

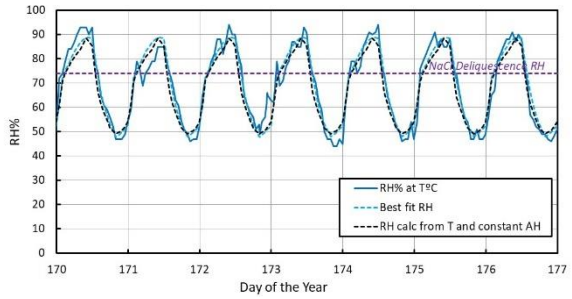

Figure 24. Arkansas Nuclear 1: Comparison of temperature-adjusted weather data with simplified (constant AH) best-fit diurnal cycle that crosses the halite DRH.

Table 7. Simplified (constant AH) best-fit Arkansas Nuclear 1 diurnal cycle that crosses the halite DRH.

Hour	Temp. ºC	AH, g/m^3
2	31.85	18.0
4	26.41	18.0
6	25.28	18.0
8	24.35	18.0
10	23.69	18.0
12	22.74	18.0
14	23.44	18.0
16	28.24	18.0
18	30.55	18.0
20	32.69	18.0
22	33.51	18.0
24	32.98	18.0

In order to demonstrate the representativeness of the trends observed for the Arkansas Nuclear 1 data, two additional sites are evaluated below. These illustrate that the diurnal cycle developed from any single site can be used to represent sites across the complex as a whole.

2.2.2.2 San Onofre.

Weather data for the nearest airport to San Onofre are shown in Figure 25. Compared to Arkansas nuclear one, the weather is more moderate, cooler in the summer, and hotter in the winter. The AH is somewhat lower at Arkansas Nuclear 1 in the summer, probably due to the cooler temperatures. The overall trends observed at Arkansas Nuclear 1 are again seen at San Onofre. Diurnal cycles are regular, especially in the summer, and temperature and RH strongly anti-correlate, while AH shows very little change over daily cycles.

Determining a diurnal fluctuation that crosses the deliquescence RH for bischofite.

For the San Onofre data set, using the weather data with a 13ºC delta provides representative conditions that result in diurnal cycling over the deliquescence RH of $MgCl_2$. A 13-day section of the weather data with a 13ºC delta, representing the time interval from 182 to 197 days, was fitted using Excel Solver with a repeating 24-hour cycle discretized into 2-hour intervals. Temperature and RH cycles were determined independently. The resulting cycles are given in Table 8, and the resulting fits are compared to the actual data in Figure 26. The 24-hour cycle fits the data well. Also shown in Figure 26 are AH values calculated from the paired temperature and RH values for the 24-hour cycle; again, the calculated values are consistent with the actual data. Use of a single daily cycle does not provide as good a fit as for the Arkansas Nuclear 1 site, but it is adequate.

As with the previous data set, the best-fit temperature data can be used with a constant AH to produce a nearly identical solution. This cycle is provided in Table 9, and is illustrated in Figure 27 For San Onofre, a constant AH value of 13.8 g/m^3 is used, significantly lower than that for the Arkansas Nuclear 1 site. This lower AH probably reflects the lower temperatures of the San Onofre site relative to The Arkansas Nuclear 1 site.

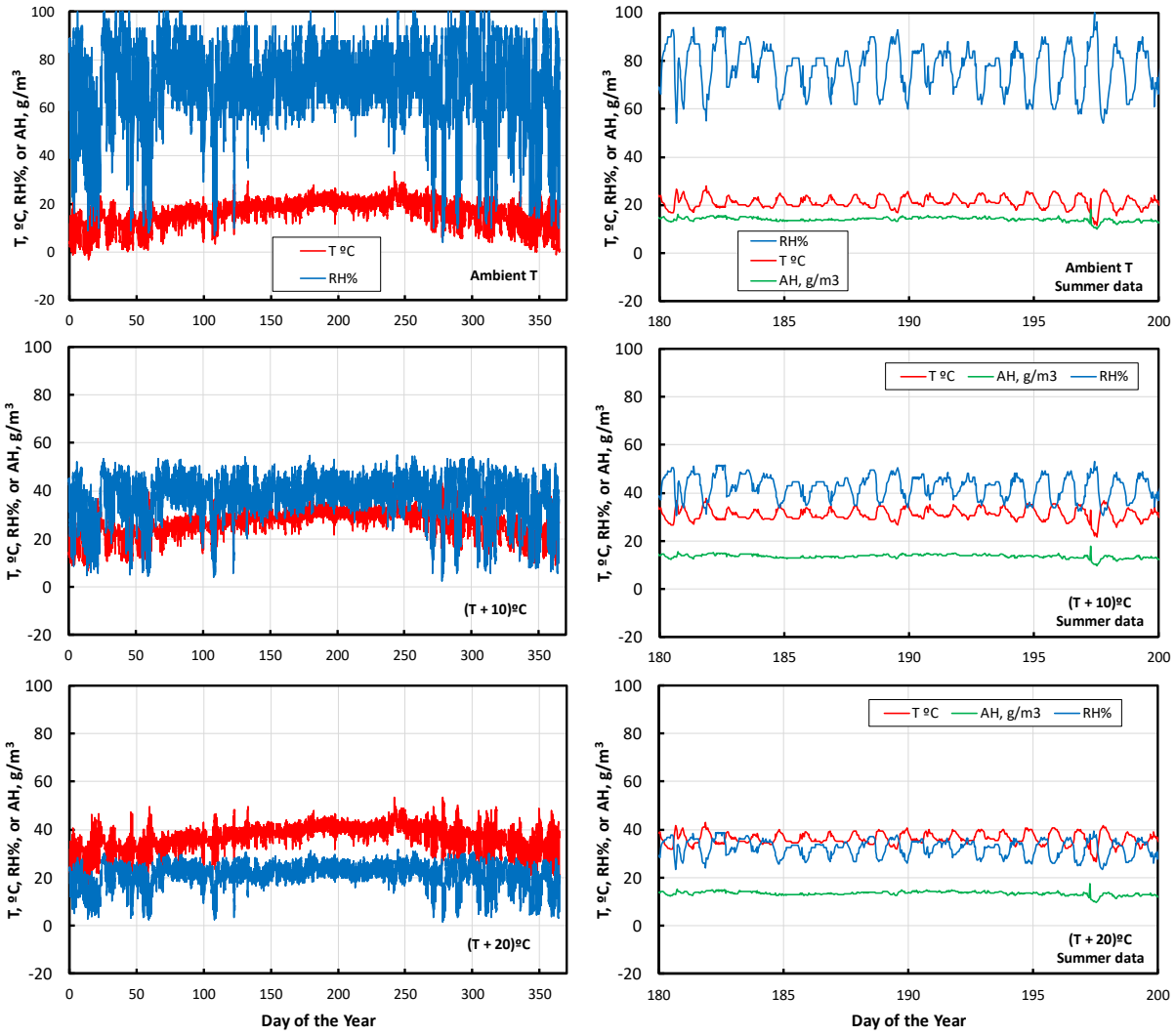

Figure 25. San Onofre: Effect of increasing canister surface T on surface RH. Yearly data on the left, and an interval during the summer on the right. Top—ambient T; Middle—ambient T+10ºC; Bottom—ambient T+20ºC.

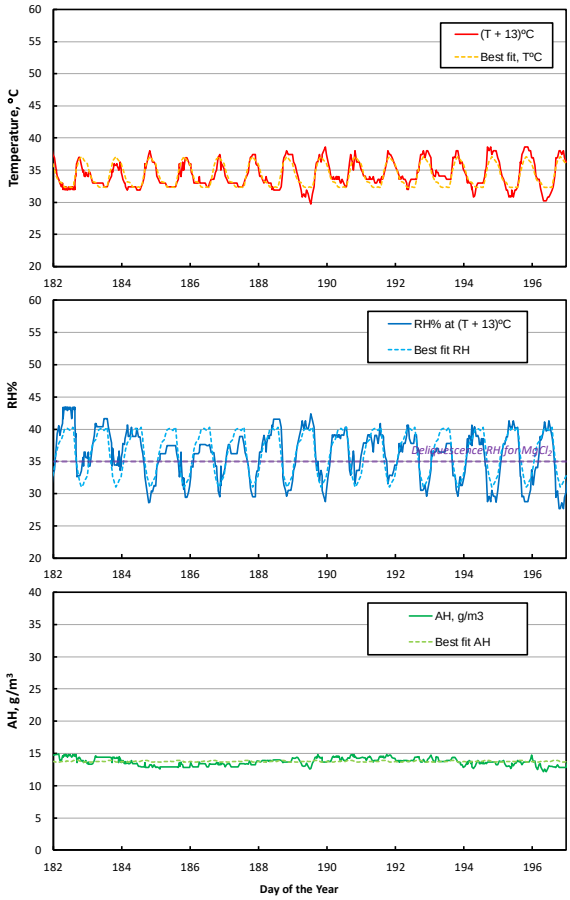

Figure 26. San Onofre: Comparison of temperature-adjusted weather data with best-fit diurnal cycle that crosses bischofite DRH.

Table 8. Best-Fit San Onofre diurnal cycle that crosses the bischofite DRH

Hour	Temp. ºC	RH, %
2	34.23	36.05
4	33.20	37.88
6	33.10	38.46
8	32.33	39.94
10	32.36	40.11
12	32.37	39.79
14	32.33	40.35
16	34.85	35.43
18	36.56	32.43
20	37.11	30.94
22	36.51	31.89
24	36.02	32.87

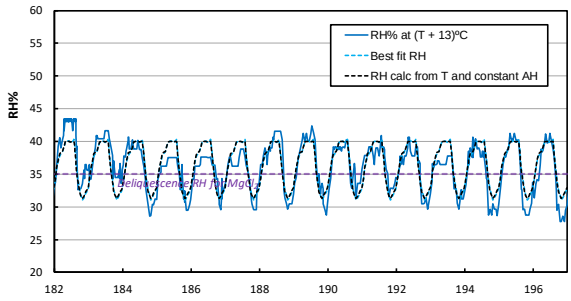

Figure 27. San Onofre: Comparison of temperature-adjusted weather data with simplified (constant AH) best-fit diurnal cycle that crosses the bischofite DRH.

Table 9. Simplified (constant AH) best-fit San Onofre diurnal cycle that crosses the bischofite DRH.

Hour	Temp. ºC	AH, g/m^3
2	34.23	13.8
4	33.20	13.8
6	33.10	13.8
8	32.33	13.8
10	32.36	13.8
12	32.37	13.8
14	32.33	13.8
16	34.85	13.8
18	36.56	13.8
20	37.11	13.8
22	36.51	13.8
24	36.02	13.8

Determining a diurnal fluctuation that crosses the deliquescence RH for halite.

For San Onofre, the only weather condition that shows reliable diurnal fluctuations across the deliquescence point of NaCl is the ambient temperature condition—even a temperature increase of just two degrees above ambient is sufficient to inhibit deliquescence of NaCl. Hence, the ambient condition (Figure 25, top) was fitted to derive the appropriate daily cycle. The best fit cycle is given in Table 10, and compared with the measured temperature data in Figure 28. Fitting with the best-fit T data, and a constant AH of 14.4 g/m^3 (Table 11), yields a nearly identical fit (Figure 29).

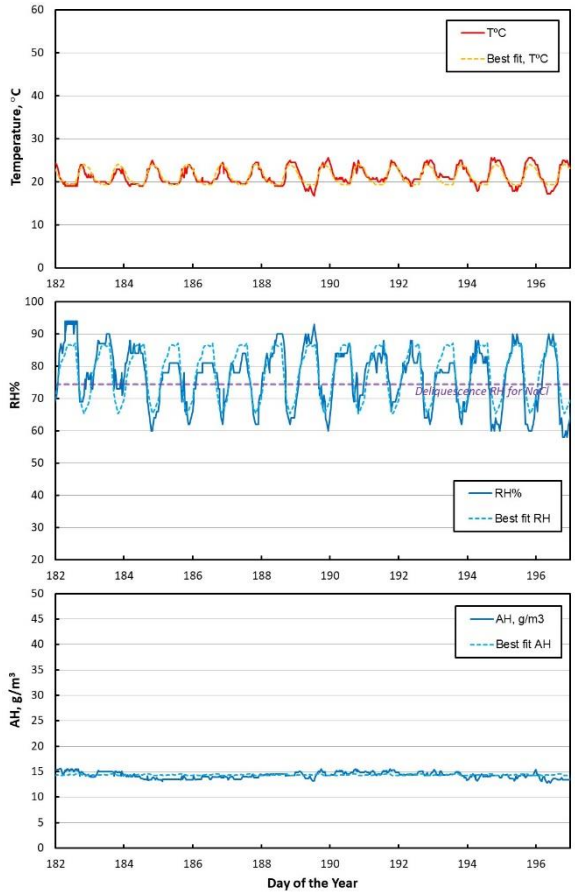

Figure 28. San Onofre: Comparison of temperature-adjusted weather data with best-fit diurnal cycle that crosses the halite DRH.

Table 10. Best-Fit San Onofre diurnal cycle that crosses the halite DRH.

Hour	Temp. °C	RH %
2	21.28	77.04
4	20.18	81.46
6	20.10	82.74
8	19.33	86.34
10	19.37	86.67
12	19.37	86.00
14	19.33	87.18
16	21.85	75.48
18	23.55	68.42
20	24.12	65.07
22	23.50	67.32
24	23.01	69.55

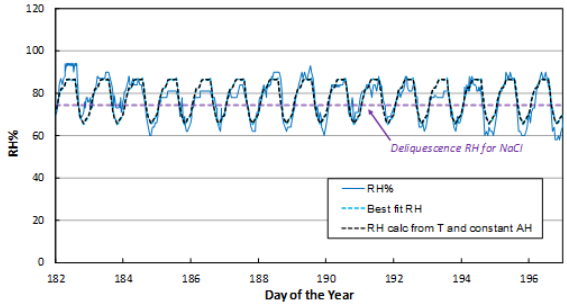

Figure 29. San Onofre: Comparison of temperature-adjusted weather data with simplified (constant AH) best-fit diurnal cycle that crosses the halite DRH.

Table 11. Simplified (constant AH) best-fit San Onofre diurnal cycle that crosses the halite DRH.

Hour	Temp. ºC	AH, g/m^3
2	21.28	14.4
4	20.18	14.4
6	20.10	14.4
8	19.33	14.4
10	19.37	14.4
12	19.37	14.4
14	19.33	14.4
16	21.85	14.4
18	23.55	14.4
20	24.12	14.4
22	23.50	14.4
24	23.01	14.4

2.2.2.3 Turkey Point

Weather data collected near the Turkey Point ISFSI in Florida are shown in Figure 30. Compared to the previous two sites, the weather resembles that of San Onofre. It is more moderate than the Arkansas site—cooler in the summer and hotter in the winter. However, the average AH is actually the highest of the three sites. As with the other sites, temperature and RH inversely correlate, while AH varies little from day to day.

Determining a diurnal fluctuation that crosses the deliquescence RH for bischofite.

For the Turkey Point data set, using the weather data with a 14.75ºC delta provides some representative conditions that meet the criterion with respect to the deliquescence of $MgCl_2$. A 13-day section of the weather data with a 14.75ºC delta, representing the time interval from 175 to 195 days, was fitted using Excel Solver with a repeating 24-hour cycle discretized into 2-hour intervals. Temperature and RH cycles were determined independently. The resulting cycles are given in Table 12, and the resulting fits are compared to the actual data in Figure 31 The 24-hour cycle fits the data well. Also shown in Figure 31 are AH values calculated from the paired temperature and RH values for the 24-hour cycle; again, the calculated values are consistent with the actual data. Use of a single daily cycle does not provide as good a fit as for the Arkansas Nuclear 1 site, but it is adequate.

As with the previous data sets, the best-fit temperature data can be used with a constant AH to produce a nearly identical solution. This cycle is provided in Table 13, and is illustrated in Figure 32. For Turkey Point, a constant AH value of 19.7 g/m^3 is used, significantly larger than that for the San Onofre site, and slightly larger than the value for Arkansas Nuclear 1 site.

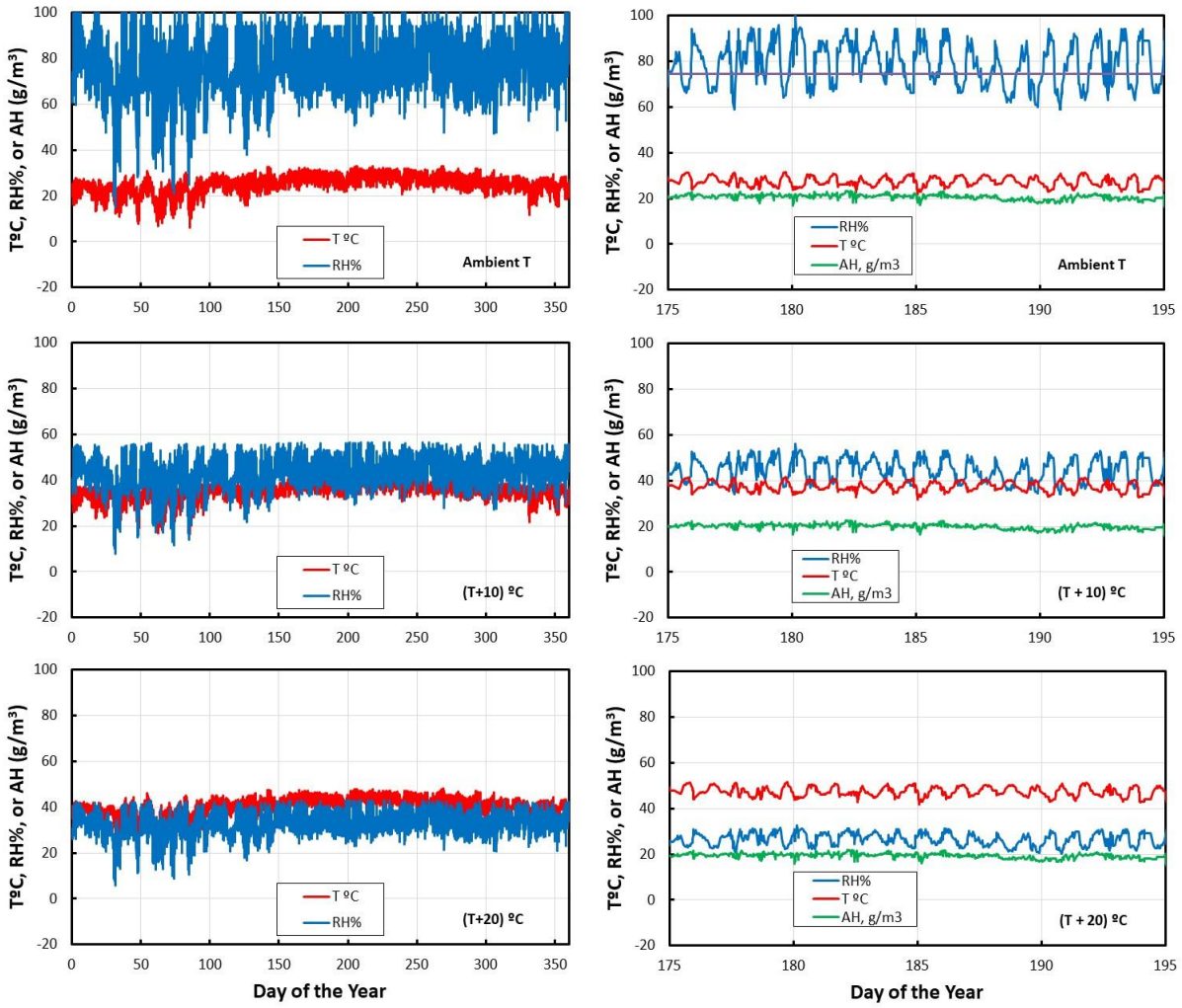

Figure 30. Turkey Point: Effect of increasing canister surface T on surface RH. Yearly data on the left, and an interval during the summer on the right. Top—ambient T; Middle—ambient T+10ºC; Bottom—ambient T+20ºC.

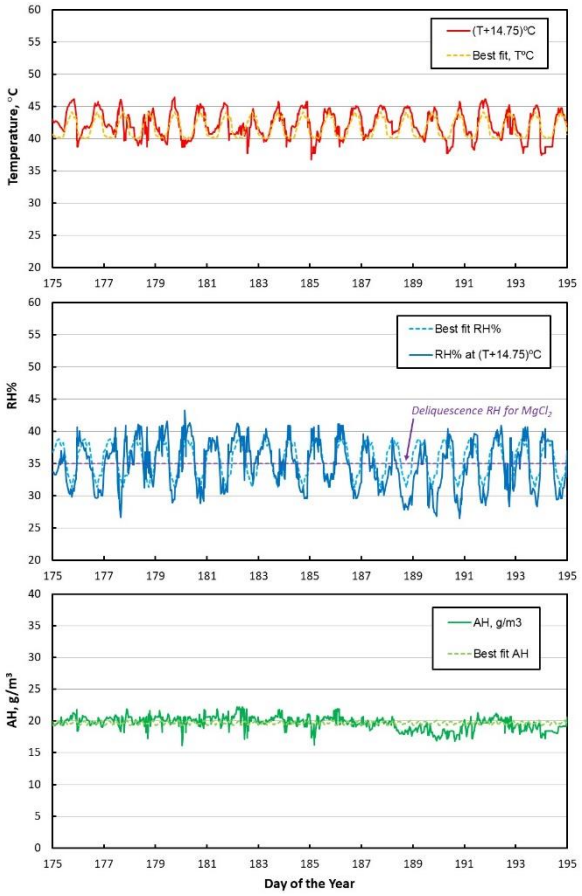

Figure 31. Turkey Point: Comparison of temperature-adjusted weather data with best-fit diurnal cycle that crosses bischofite DRH.

Table 12. Best-Fit Turkey Point diurnal cycle that crosses the bischofite DRH.

Hour	Temp. ºC	RH, %
2	40.36	37.29
4	40.07	38.58
6	40.25	38.78
8	40.03	37.72
10	40.32	38.23
12	41.74	35.79
14	42.58	33.42
16	43.42	32.47
18	44.15	31.26
20	43.21	33.17
22	43.48	33.13
24	40.57	36.81

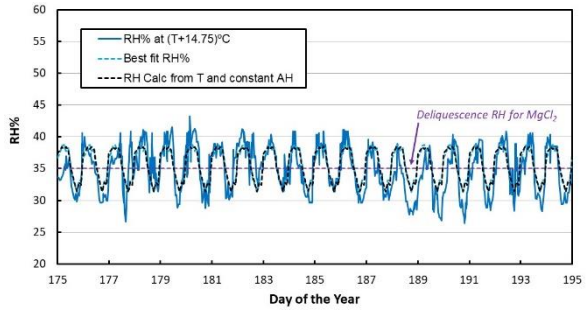

Figure 32. Turkey Point: Comparison of temperature-adjusted weather data with simplified (constant AH) best-fit diurnal cycle that crosses the bischofite DRH.

Table 13. Simplified (constant AH) best-fit Turkey Point diurnal cycle that crosses the bischofite DRH.

Hour	Temp. ºC	AH, g/m^3
2	40.36	19.7
4	40.07	19.7
6	40.25	19.7
8	40.03	19.7
10	40.32	19.7
12	41.74	19.7
14	42.58	19.7
16	43.42	19.7
18	44.15	19.7
20	43.21	19.7
22	43.48	19.7
24	40.57	19.7

Determining a diurnal fluctuation that crosses the deliquescence RH for halite.

For Turkey Creek, the best weather condition to produce reliable diurnal fluctuations across the deliquescence point of NaCl is the ambient temperature condition plus 1ºC. The best fit cycle is given in Table 14, and compared with the measured temperature data, with a delta of 1ºC, in Figure 33. Fitting with the best-fit T data, and a constant AH of 20.6 g/m3 (Table 15), yields a nearly identical fit (Figure 34).

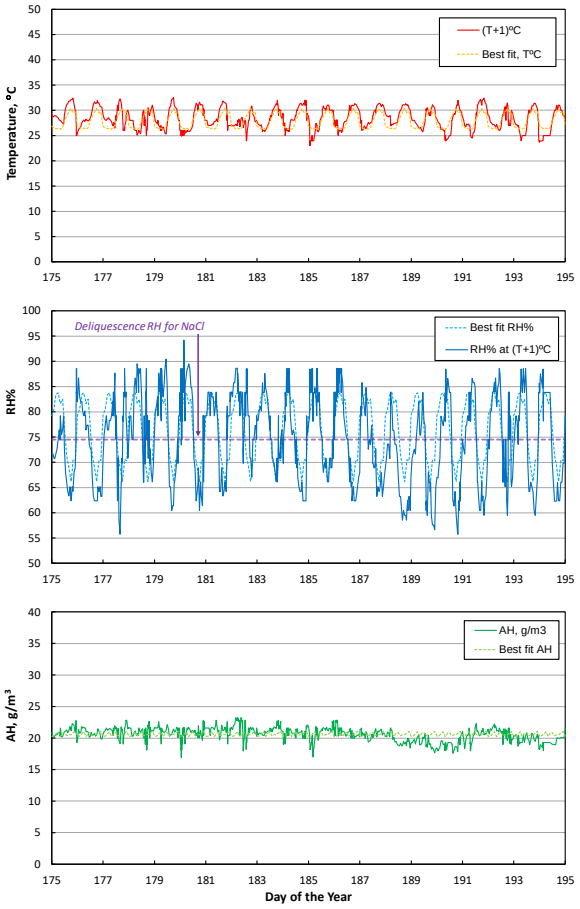

Figure 33. Turkey Point: Comparison of temperature-adjusted weather data with best-fit diurnal cycle that crosses the halite DRH.

Table 14. Best-Fit San Onofre diurnal cycle that crosses the halite DRH.

Hour	Temp. ºC	RH %
2	26.61	80.53
4	26.32	83.45
6	26.50	83.77
8	26.28	81.61
10	26.57	82.56
12	27.99	76.68
14	28.83	71.34
16	29.67	68.97
18	30.40	66.11
20	29.46	70.56
22	29.73	70.31
24	26.82	79.41

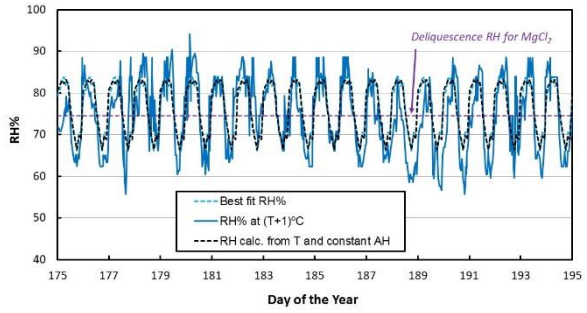

Figure 34. Turkey Point: Comparison of temperature-adjusted weather data with simplified (constant AH) best-fit diurnal cycle that crosses the halite DRH.

Table 15. Simplified (constant AH) best-fit San Onofre diurnal cycle that crosses the halite DRH.

Hour	Temp. ºC	AH, g/m^3
2	26.61	20.6
4	26.32	20.6
6	26.50	20.6
8	26.28	20.6
10	26.57	20.6
12	27.99	20.6
14	28.83	20.6
16	29.67	20.6
18	30.40	20.6
20	29.46	20.6
22	29.73	20.6
24	26.82	20.6

2.2.2.4 Recommended diurnal cycles for testing

Of the three different diurnal cycles provided in this section for daily cycling over the bischofite deliquescence RH, the cycle for Arkansas Nuclear 1 has been chosen for use in testing. This is because it is the cycle with the largest range of RH values, and hence, the cycle that will result in the largest range of possible brine compositions. Therefore, it is the most conservative choice for testing purposes.

Noted in Section 2.2.1, conditions for NaCl deliquescence will not be reached on heated canister surfaces and are of less interest for SNF dry storage considerations. However, if testing is undertaken, then the diurnal cycle presented in Table 14 is recommended, as the temperatures are all well above normal indoor temperatures and would not require a chiller to implement in the lab. Moreover, the higher temperatures make it a more aggressive environment than the other cycles for NaCl.

2.2.3 Realistic Brine Chemistries (Cl/NO_3)

To date, SNL has performed testing with simulated sea-salt brines, and with individual components (NaCl, $MgCl_2$) of those brines, that represent a worst-case scenario for salts on canister surfaces, as they are extremely chloride-rich and do not contain other ions that may inhibit corrosion. Such brines may be relevant to some coastal locations, but sampling and analysis of in-service canister surface dusts has shown that at many East Coast locations, the dusts are actually a mixture of marine salts (Na^+, Cl^-, Mg^{+2}, SO_4^{-2}-rich) and a continental component (Ca^{+2}, K^+, (NH_4^+), NO_3^-, SO_4^{-2}-rich) . In this section, measured salt compositions at two ISFSI sites (Maine Yankee and Hope Creek) are evaluated to determine representative salt compositions for those sites. Of particular interest is the presence of NO_3^-, and how brines containing it change with RH, because nitrate has been shown to inhibit corrosion (Cook et al., 2017). The compositions determined here will be taken into consideration when planning experiments to evaluate the effect of other anions on the corrosivity of canister surface brines.

2.2.3.1 Maine Yankee

Determining a representative composition for the soluble salts

The storage systems at the Maine Yankee ISFSI have been sampled three times. In 2017, a robot was used to enter one overpack, and samples were collected from the top of the shield plug and from shelves near the bottom of the overpack using a damp sponge. The 2017 shelf samples were quite coarse, contained large amounts of concrete efflorescence that fell from the walls of the overpack, and, having been collected robotically, were probably not a quantitative sample of what was on the surface where the sampling occurred. In 2018, samples were collected by hand from the top of one canister (the lid was sufficiently thick to provide shielding), using sponges and a template to quantitatively sample a large area—these are considered to be the best, most representative samples, and they show strong compositional similarities and trends. In 2019, dust collection coupons that had been placed about 2 years earlier were collected from the inlet and outlet vents of 4 different canisters. The coupons were very close to the vents and had high salt and dust loads and abundant organic particles, including pollen, stellate trichomes, and even cobwebs and insect parts. In many cases, they also showed evidence of having been wetted by rain blowing into the vents. These samples differed chemically from the samples from the canister surface, and are not considered representative of deposition on the canister. In the following discussion, we concentrate on samples from the 2018 sampling of the actual canister surface. The results of the other two samplings are shown for comparison, but are not used in calculating possible salt compositions.

The 2018 Maine Yankee soluble salt analyses are given in Table 16, with the blank values subtracted. Because the 2018 samples from Maine Yankee were collected from a large area (6 × 6 cm), soluble salt concentrations were relatively high, and compositions were easy to measure and more accurate than previous attempts from other sites, which used small (3 cm^2) SaltSmart™ pads for sample collection. The measurement accuracy was affected slightly by inadvertent use of much larger sponge pieces than intended, which raised the blank values, but the measured data were sufficiently high that the blanks were still a relatively minor component (Bryan and Schindelholz, 2018a). As is always the case with canister dust analyses, the charge balances are poor, indicating a deficiency of anions. This is largely because carbonate was not included in the analyses, and carbonate phases are frequently seen by SEM. Concrete efflorescence, consisting mostly of calcium carbonate and calcium silicates (which can leach CaOH), was a common phase in the Maine Yankee samples, indicating that the anion deficiency was largely due to the unquantified carbonate and perhaps hydroxide.

The soluble ion concentrations are plotted against Na^+ in Figure 35. With the exception of calcium, the ions form linear trends, intersecting the X and Y axes at or near zero. This suggests that the soluble salt compositions vary little from sample to sample, and that only the amount of salt deposited changes. For calcium, the trend is much more scattered, probably because of the contribution from concrete efflorescence, which falls from the overpack, and is not related to salts in dust aerosols. The analyses

from the 2017 and 2019 sampling episodes are compared to the 2018 data in Figure 36. For some elements, the trends match; in other cases, a different trend appears to be present, or the points are scattered and no trend at all is apparent. Part of the scatter may be because concentrations are low in the 2017 and 2019 samples, and analytical uncertainty is higher, much of the differences in trends may be related to differences in the particle sizes deposited in the different areas sampled; salt aerosol compositional variations with particle size are commonly observed. For this reason, the 2018 data from dusts collected directly from the canister surface will be used to determine the relevant salt compositions.

Table 16. Soluble Ion Concentrations in 2018 Maine Yankee Samples, µmol/sample

Sample #	Na^+	NH_4^+	K^+	Mg^{2+}	Ca^{2+}	F^-	Cl^-	NO_3^-	PO_4^{3-}	SO_4^{2-}
MY-1	7.5	n.d.	2.3	2.2	34.9	0.8	3.7	4.2	0.3	4.2
MY-2	7.3	0.1	2.4	1.7	40.3	1.6	2.9	4.8	0.2	3.9
MY-3	1.2	n.d.	0.1	0.7	8.1	0.7	0.6	0.1	n.d.	0.6
MY-4	1.8	n.d.	0.4	n.d.	5.3	0.6	0.6	1.0	n.d.	0.6
MY-5	5.1	n.d.	1.4	1.8	21.0	1.5	3.2	1.7	n.d.	4.0
MY-6	15.4	n.d.	5.8	4.0	37.3	1.8	7.6	7.8	0.5	9.4

Note: Blank-subtracted values

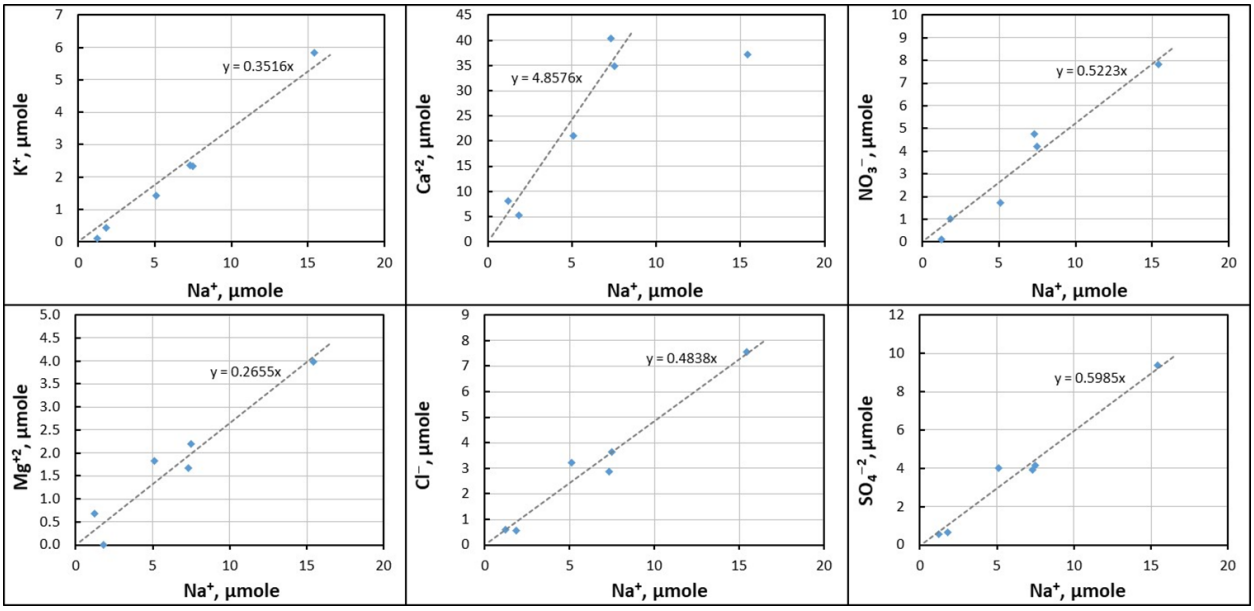

Figure 35. Soluble ion concentrations in Maine Yankee 2018 samples, plotted against Na concentration.

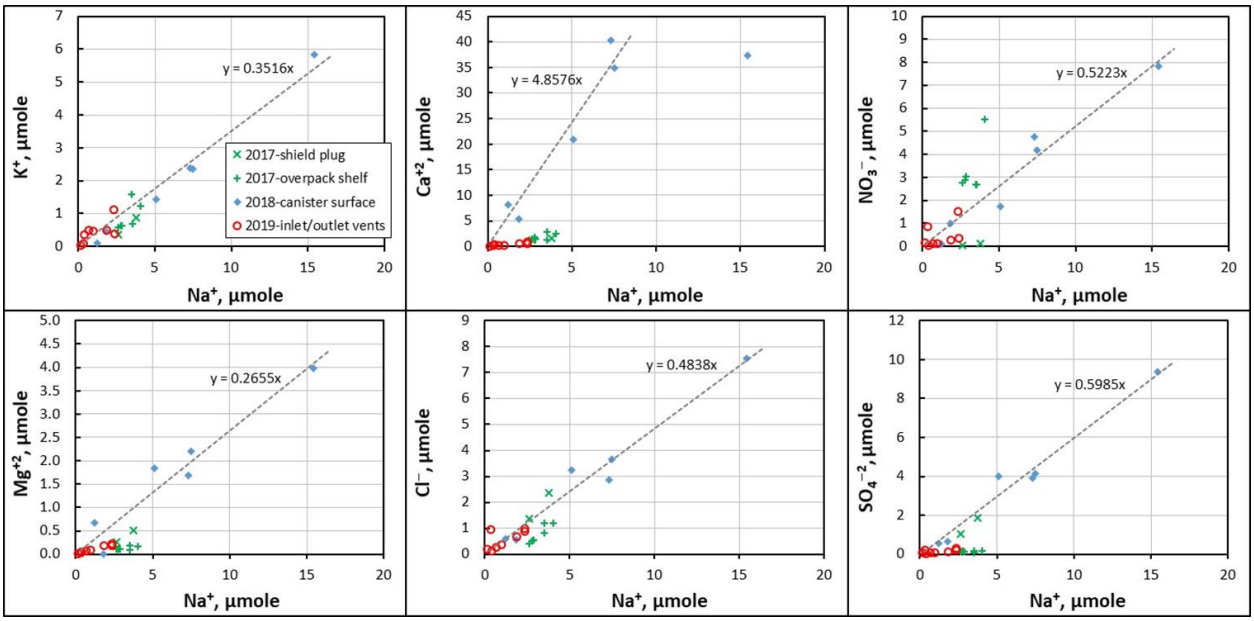

Figure 36. Soluble ion concentrations in Maine Yankee 2017, 2018, and 2019 samples, compared.

In Figure 35, best-fit lines have been fitted to the data, assuming an intercept of (0,0), and the slopes have been used to estimate the bulk composition of the soluble salts that were deposited. Normalized to a Na^+ concentration of 1 µmol, the predicted values are given in Table 17. Bicarbonate was used to charge balance, and that value is also provided in Table 17. The normalized soluble ion composition of the Maine Yankee salts is shown graphically in Figure 37.

Table 17. Composition of soluble salts, based on best-fits to 2018 Main Yankee data

Species	Normalized molar conc.
Na^+	1.0000
K^+	0.3516
Ca^{+2}	4.8576
Mg^{+2}	0.2655
Cl^-	0.4838
NO_3^-	0.5223
SO_4^{-2}	0.5985
HCO_3^-	*9.3947

* Based on charge balance

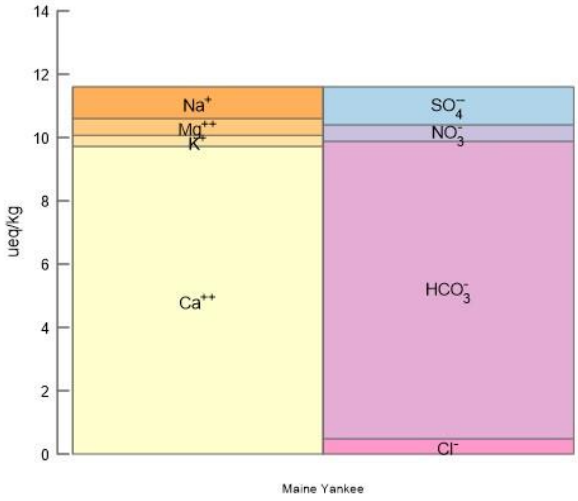

Figure 37. Normalized soluble ion composition of Maine Yankee salts, shown in µeq.

Determining a brine composition to use for salt deposition

The values in Table 17 represent normalized ion concentrations, but cannot be used directly as a solution for depositing salt on test specimens. Such a solution must be relatively concentrated—based on previous work, 0.3-0.5 molal works well for effective salt deposition. If mixed to produce a concentration of 0.5 molal, the composition in Table 2 would be heavily supersaturated with carbonates, and would precipitate out a large mass of material, making deposition impossible.

To determine the composition of an evaporating solution of these salts—and hence, what brines would result from deliquescence of salt phases corresponding to this composition—EQ3/6 was used. To avoid precipitation, the starting solution was taken to be very dilute—the normalized values in Table 17 were input at concentrations of 10^{-5} molal. The results of the calculations are shown in Figure 38. As the solution evaporates, the divalent cations are removed from solution as carbonates and sulfates, and the resulting solution becomes progressively enriched in monovalent ions. Because of the high solubilities of Na and K chlorides and nitrates, these species increase nearly monotonically in the brines as they evaporate, in the same relative abundances as are shown in Table 2. At 66% RH, both halite (NaCl) and niter (KNO_3) begin to precipitate; as the RH drops further, the brine becomes progressively more nitrate-rich, until soda niter ($NaNO_3$) precipitates and the brine dries out. The mineral assemblage that governs the deliquescence properties of the brine is NaCl-KNO_3-$NaNO_3$.

The combination of salts in Table 17 is soluble in water at micromolar levels that correspond to very high RH, but as can be seen in Figure 38b, carbonate saturates and precipitates if these waters are concentrated even slightly. As noted earlier, this is a problem—the salt deposition process requires that the deposited materials be completely dissolved, and a relatively high concentration. A solution concentration around 0.3-0.5 molal would be effective. Here, brine representing an RH of 99%, corresponding to a concentration of about 0.3 molal, was selected as a target.

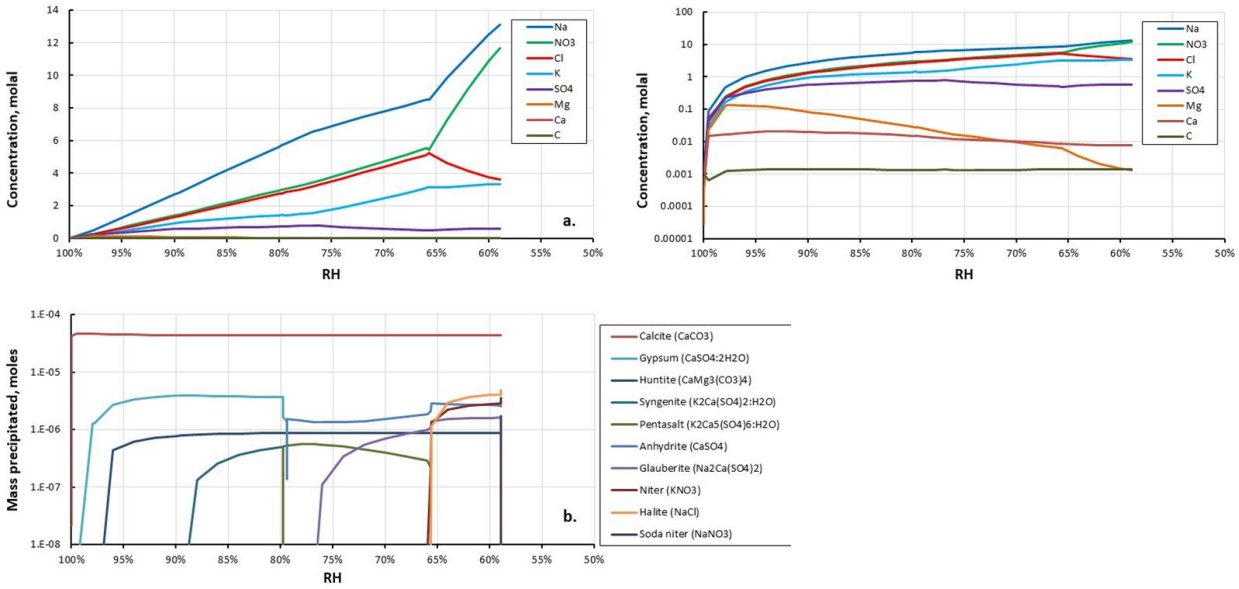

Figure 38. Predicted evaporative evolution of a solution of Maine Yankee salts. a) Brine compositions on a linear scale; b) precipitated minerals.

EQ3/6 modeling was undertaken to determine how brine concentrations could be modified to achieve a similar overall brine evolution, while delaying salt precipitation as long as possible. This proved extremely difficult, because as predicted by chemical divide theory, small changes in the initial brine

compositions resulted in huge changes in the trajectory of the evaporated waters. A few examples of this are given below to illustrate the importance of considering all brine components in developing a brine composition for testing.

Case 1. Remove the salts that precipitate as the brine evaporates to 99% RH. In the base case water (Figure 38), Ca and Mg remain very low as the water evaporates, because they precipitate as carbonates and sulfates. The water evaporates to form a Na-K-NO3-Cl brine, with relatively minor sulfate. Is it possible to simply remove the salts that precipitate out early and use the remaining brine composition? No. Removing 90% of the calcite and gypsum that precipitates out by an RH of 99% has absolutely no effect on the evolving brine chemistry. But removing 100% of those precipitates has an enormous effect on brine chemistry, because a small amount of those minerals back-react with the brine as evaporation continues. This is illustrated in Figure 39, were the brine behavior varies considerably between the base case and the modified composition.

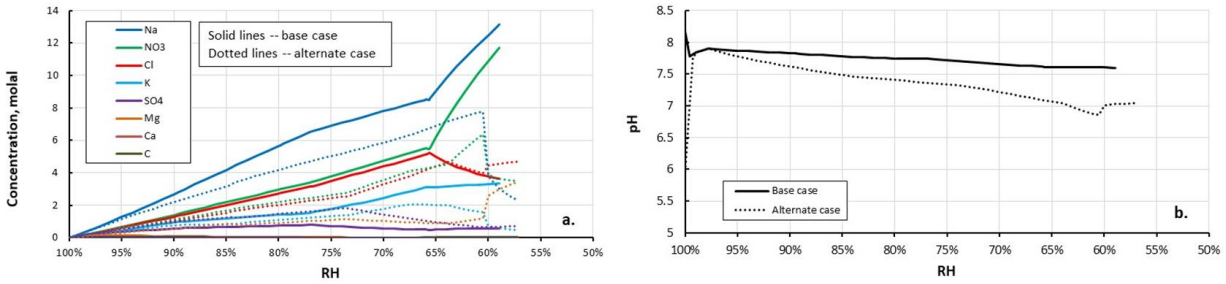

Figure 39. Predicted evaporative evolution of Maine Yankee salts, after subtracting off the calcite and gypsum that precipitates when evaporated to 99%RH. a) composition; b) pH

Case 2. Remove all Ca, Mg, and SO_4, while maintaining charge balance with carbonate. Since the base case water evaporates to form a Na-K-NO_3-Cl brine, with relatively minor sulfate, is it possible to just remove Ca, Mg, and SO_4? Taking out Ca, Mg, and SO_4, rebalancing the charge with carbonate, and evaporating yields a water that follows a very similar compositional evolution, although there is significantly more carbonate in the adjusted brine (Figure 40). However, the pH evolves very differently. In the base case, it stays between pH 7 and 8, while in the Ca-Mg-SO_4-free case, it rapidly increases to pH 10. Because of the potential importance of pH on corrosion reactions, this is deemed unacceptable. Moreover, in current experiments, we have seen that minor components (possibly sulfate) appear to affect the mode and extent of corrosion, so eliminating individual species may have unintended consequences.

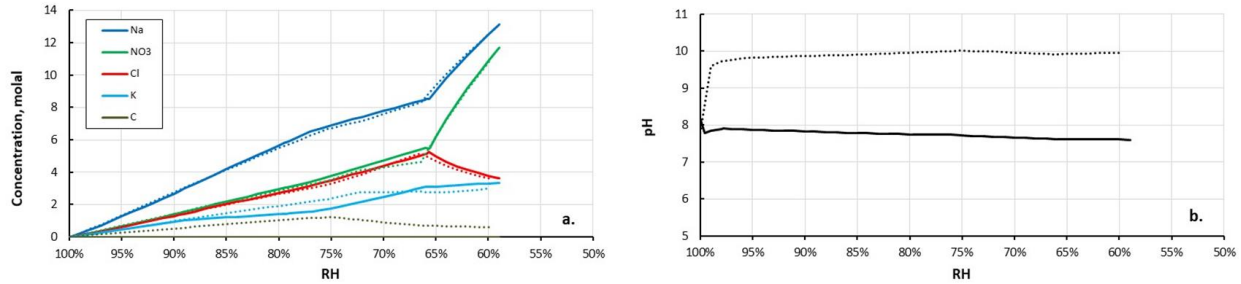

Figure 40. Predicted evaporative evolution of Maine Yankee salts, after eliminating all Ca, Mg, and SO_4, and rebalancing the charge with carbonate. a) composition; b) pH.

Case #3. Subtract off all Ca, Mg, and CO_3, and sufficient SO_4 to achieve charge balance. Note that carbonate is removed from the initial brine, but re-equilibration with the atmosphere results in re-carbonation during the evaporation step. These results are not shown here to save space, but this case results in a similar fit to Case #2 in terms of chemistry, except that the pH decreases to a value of about 5.6, two pH units below the base case. This was also considered unacceptable.

After several other attempts, a brine composition was chosen that corresponded to the base case brine evaporated to 99% RH, with the precipitated solids subtracted out, with Ca and Mg further reduced proportionally by a small amount, and with some SO_4 additional removed as well. The resulting solution is not saturated with any minerals at 99% RH. Evolution of the chosen brine is shown in Figure 41. As can be seen, the major element compositions are captured reasonably well, although the sulfate concentration increases too much with evaporation. The pH remains at near-neutral values, within a half a pH unit of the base case. Ca and CO_3 are initially similar to the base case values, but as the RH drops, become depleted relative to the base case. Mg increases significantly above the base case values as the RH drops, but still only reaches a maximum of about 0.1 molal. The deliquescence-controlling mineral assemblage does not change. The proposed brine composition to deposit is shown in Table 18. A mixing formula is also provided.

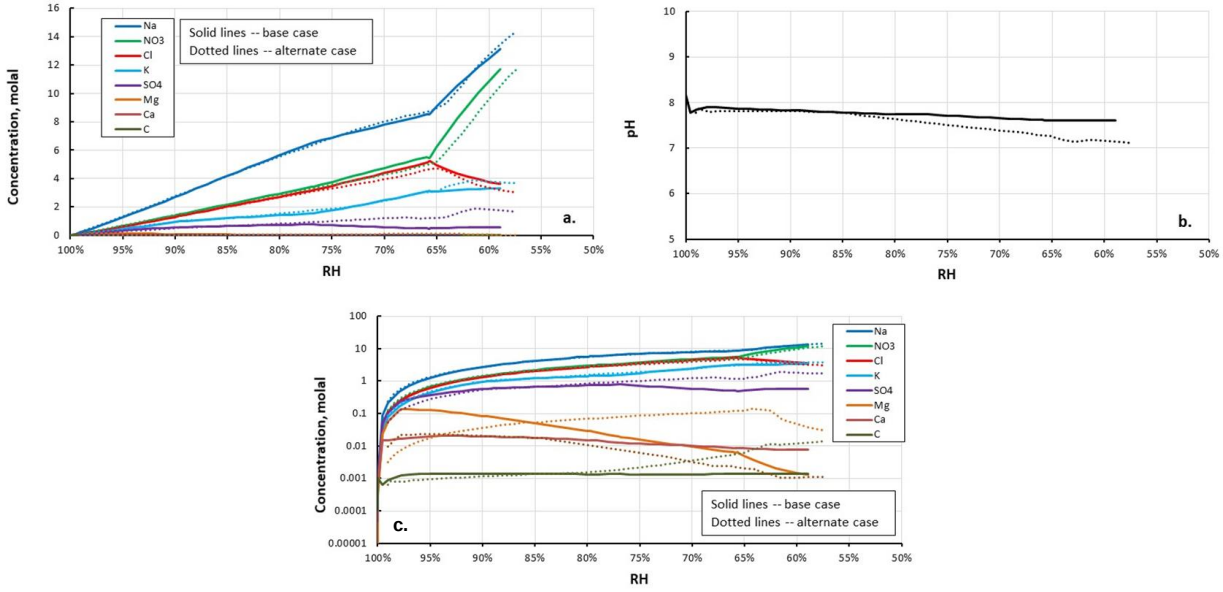

Figure 41. Predicted evaporative evolution of Maine Yankee salts, reducing some components to achieve an unsaturated 99% RH starting solution. a) composition; b) pH; c) composition on log scale to emphasize minor species.

Table 18. Composition of the proposed brine simulant for depositing Main Yankee salts.

Species	Conc., molal	To mix:	
		Salt	Wt, grams
Na^+	2.417E-01	NaCl	5.3590
K^+	8.499E-02	$NaNO_3$	3.5070
Ca^{+2}	9.416E-03	KNO_3	8.5929
Mg^{+2}	3.209E-03	$CaCl_2$	1.0450
Cl^-	1.169E-01	$MgCl_2{:}6H_2O$	0.6524
NO_3^-	1.263E-01	Na_2SO_4	7.6789
SO_4^{-2}	5.406E-02	$NaHCO_3$	0.0543
HCO_3^-	6.467E-04	**SUM**	26.8896

Deliquescence behavior of the Maine Yankee salt assemblage

It is important to know the deliquescence properties of the chosen salt assemblage as a function of temperature, in order to determine the range of possible testing conditions. As stated previously, the deliquescence-controlling minerals for this composition are halite (NaCl), niter (KNO_3), and soda niter ($NaNO_3$). Predicted deliquescence RH values as a function of temperature calculated for both individual salts and for the three-salt assemblage using EQ3/6 and the *data0.ypf.R2* database are given in Figure 42a. However, the simulation using *data0.ypf.R2*, fails for temperatures above 41 °C, and RH values at higher temperatures cannot be calculated. Moreover, shape of the deliquescence curve at lower temperatures is suspect; the *data0.ypf.R2* database used here does not predict the composition of concentrated mixed nitrate-chloride brines well, and these values must be viewed with caution. The previous version of the database, *data0.ypf*, more accurately predicted nitrate mineral solubilities, and may be more accurate for this calculation. Values calculated using *data0.ypf* have also been included in Figure 42a and are preferred here. At 25 °C, the single salts NaCl and $NaNO_3$ each deliquesce at about 75% RH, and KNO_3 at about 94% RH. The deliquescence of a multi-salt assemblage is always lower than that of any single component in the assemblage, and when several relatively deliquescent salts are mixed together, the deliquescence point of the mixture can be much lower than that of the single salts. The three-salt assemblage NaCl-KNO_3-$NaNO_3$ is predicted to deliquesce at about 67% RH at 25 °C. The solubilities of the two nitrate phases increase rapidly with temperature, so their deliquescence RH drops; the deliquescence RH of the three-salt assemblage also drops as the temperature increases.

The predicted brine chemistry as a function of RH at 25 °C, 40 °C, and 60 °C, using the *data0.ypf* database, is shown in Figure 42b. As the temperature increases from 25 °C to 60 °C, the predicted deliquescence RH drops markedly, and the initial deliquescent brine concentration increases greatly, reaching an ionic strength of over 20 molal at 60 °C.

It is apparent that if nitrate is inhibitive, there is sufficient nitrate present even at Maine Yankee, which is a relatively near-marine site, to be beneficial. However, nitrate-chloride mixtures will deliquesce at significantly lower RH values (and hence, higher temperatures) than just chloride mixtures. This is illustrated here for Na and K salts, but is even more true for Ca- and Mg-bearing brines, because individual Ca and Mg nitrates and chlorides are even more deliquescent. Lower deliquescent RH values means that a brine can exist at higher temperatures than for the chloride-only systems. Also, brine volumes will be larger at any given RH, for instance, sea-salt brines show a drastic decrease in volume below 74% RH, when halite is predicted to precipitate. However, for the Maine Yankee brines, the first

nitrate or chloride salt does not precipitate until the RH drops to 66% RH (Figure 38); for the same salt load, a much larger volume of brine would be present between 74 and 66% RH for the Maine Yankee salts than for pure sea-salts. Hence, if nitrate does not prove to be inhibitive, then its presence may be detrimental, as brines could form at higher temperatures, and under many circumstances, a thicker brine layer would be present.

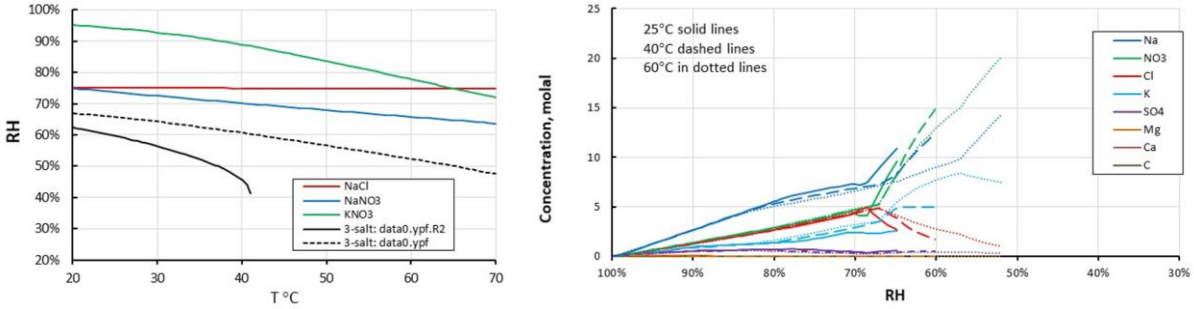

Figure 42. Deliquescence properties of Maine Yankee salt assemblage. a) Predicted deliquescence RH values for NaCl, $NaNO_3$, KNO_3, and the three-salt mixture as a function of temperature. b) Predicted evaporative evolution of Maine Yankee salts at 25 °C, 40 °C and 60 °C.

2.2.3.2 Hope Creek Salts

Determining a representative composition for the soluble salts

At the Hope Creek ISFSI, two canisters were sampled in November 2013. The canisters were vertical canisters, that had been in storage for approximately 10 years. Sampling was done with Scotch-brite™ pads for dust collection and SaltSmart™ pads to measure soluble salts. Dust and salt loads on the sides of the canisters were extremely light, but dust loads on the top of the canisters were much heavier. Table 19 shows the measured soluble ion concentrations as collected from the Salts-marts. Samples were also collected from an unused canister at the site in November 2014, and the results are discussed here as well. Note that these were collected from a cold canister and may not be relevant to heated canisters.

Table 19. Soluble ion concentrations in Hope Creek samples, µmol/sample

Sample #	Na^+	NH_4^+	K^+	Mg^{2+}	Ca^{2+}	F^-	Cl^-	NO_3^-	PO_4^{3-}	SO_4^{2-}
144-008	*5.7E-03*	n.d.	*2.1E-02*	1.5E-02	5.1E-02	n.d.	9.3E-03	2.4E-02	n.d.	3.4E-02
144-009	*4.2E-03*	n.d.	4.3E-02	7.1E-03	7.9E-02	n.d.	8.6E-03	8.3E-02	*4.6E-04*	5.9E-02
144-010	*1.7E-02*	n.d.	3.7E-02	4.0E-03	7.3E-02	n.d.	1.7E-02	6.1E-02	n.d.	3.7E-02
145-006	*2.3E-02*	n.d.	5.6E-02	1.5E-02	7.8E-02	n.d.	4.6E-02	1.1E-01	n.d.	4.1E-02
145-007	*3.0E-02*	6.9E-03	2.7E-02	1.3E-02	2.6E-02	n.d.	4.4E-02	1.5E-02	n.d.	4.7E-02
145-014	*2.6E-02*	2.3E-02	*2.3E-02*	1.9E-02	4.8E-02	n.d.	1.9E-02	2.0E-02	n.d.	8.6E-02
144-013	1.8E+00	n.d.	4.6E-01	1.4E+00	2.5E+00	1.6E-02	*1.0E-01*	2.9E-01	4.0E-02	*9.4E-01*
144-014	5.8E-01	n.d.	1.6E-01	3.2E-01	6.9E-01	1.7E-02	*4.9E-01*	*9.8E-02*	*2.8E-03*	*5.7E-01*
145-013	1.4E+00	7.5E-04	3.8E-01	1.2E+00	2.2E+00	n.d.	*4.7E-02*	2.1E-01	2.6E-02	8.4E-01
145-011		1.5E-02	6.1E-03	2.4E-03	2.4E-02	n.d.	4.6E-03	9.4E-04	n.d.	8.7E-03
144-003		n.d.	1.6E-02	3.8E-03	2.1E-02	n.d.	n.d.	3.4E-02	2.0E-03	1.3E-02
144-004		8.8E-03	8.1E-03	1.3E-02	4.6E-02	n.d.	5.1E-03	9.0E-03	n.d.	9.3E-03
145-002		n.d.	*3.0E-02*	9.9E-03	8.8E-02	n.d.	*2.7E-03*	7.5E-02	n.d.	1.2E-02
SS-Bl-8 min-1		n.d.	n.d.	n.d.	n.d.	n.d.	n.d.	6.4E-03	n.d.	n.d.
SS-Bl-8 min-2		n.d.	n.d.	n.d.	n.d.	n.d.	3.3E-03	-4.6E-03	n.d.	n.d.
SS-Bl-15 min		1.6E-01	n.d.	8.2E-03	4.4E-03	8.3E-03	*2.6E-03*	-1.8E-03	*5.8E-03*	8.8E-03

Note: Blank-subtracted values

Greyed-out numbers indicate that the values were above blank values, but below the limit of quantitation.

Composition of Hope Creek Brines using all the collected data

The soluble ion concentrations are plotted against Ca^{2+}, the most abundant cation in the salts, in Figure 43. As with Maine Yankee, there is generally a linear relationship between the Ca^{2+} concentration and the other soluble ions, passing through (0,0), suggesting that the composition of the soluble salts varies little from sample to sample. However, it should be noted that the trend is dominated by the three samples from the top of the canister; other values are barely above the detection limit for the analysis and are clustered near zero. Note that this plot includes the samples (yellow triangles) collected from the unused canister at Hope Creek in November, 2014, for comparison.

Like the Maine Yankee samples, the data have been fit with best-fit lines assuming an intercept of (0,0), and the slopes have been used to estimate the bulk composition of the soluble salts that were deposited. Using these slopes, the composition was normalized to a Ca^{2+} concentration of 1 µmol, and the normalized salt composition is given in Table 20. Bicarbonate was used to charge balance, and that value is also provided in Table 20. The normalized soluble ion composition of the Hope Creek salts is shown graphically in Figure 44.

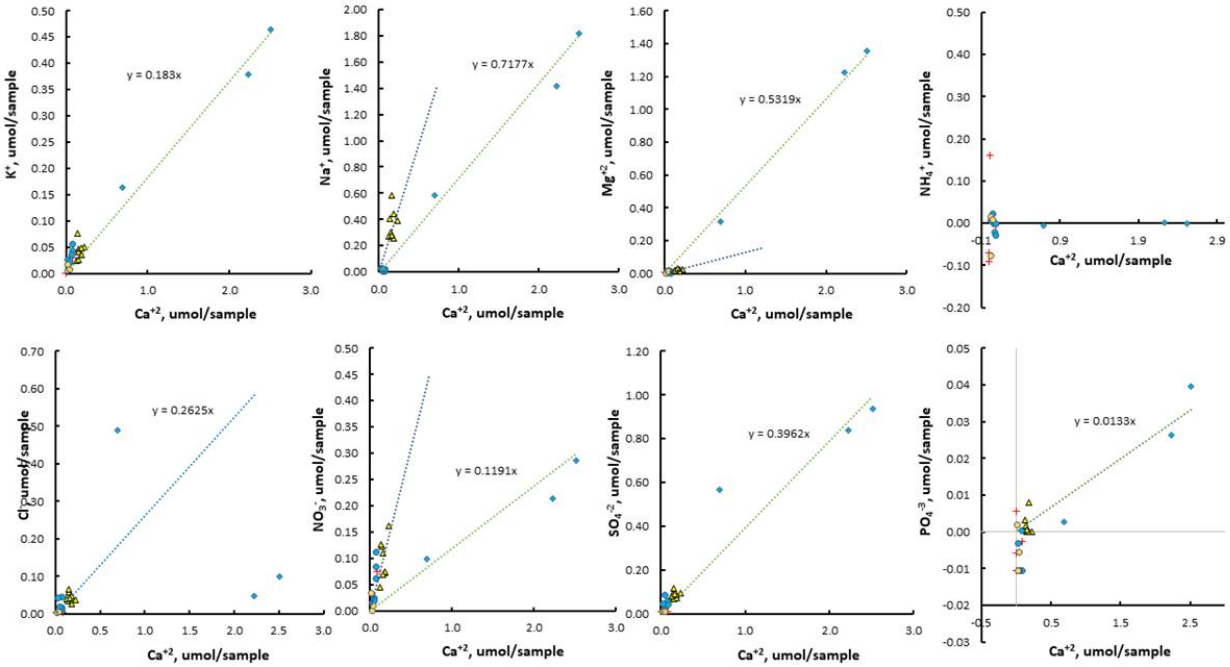

Figure 43. Soluble ion concentrations in all the Hope Creek samples, plotted against Ca^{2+} concentration. (Green lines—fits to all the data; blue lines—fits to the low-concentration subset of the data).

Table 20. Composition of soluble salts, based on best-fits to the Hope Creek data.

Species	Normalized molar conc.
Na^+	0.7170
K^+	0.1830
Ca^{+2}	1.0000
Mg^{+2}	0.5319
Cl^-	0.2625
NO_3^-	0.1191
SO_4^{-2}	0.3962
HCO_3^-	*2.7898

*Based on charge balance

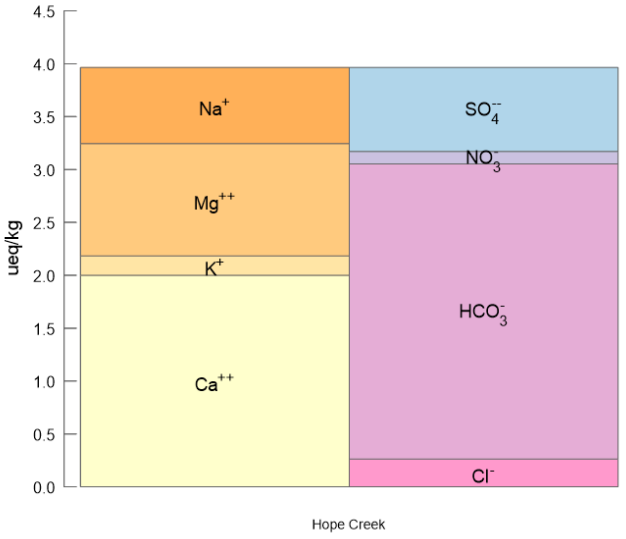

Figure 44. Normalized soluble ion composition of Hope Creek salts, shown in μeq.

Composition of Hope Creek brines excluding the highest concentration samples

For some elements, the trend formed by the whole sample set, dominated by the high concentration samples from the top of the canister, appears to differ from the trend defined by the majority of the samples, which are lower concentration. Excluding the samples from the top of the canister results in a significantly different fit (Figure 45), suggesting much higher Na concentrations relative to the data in Figure 43. However, these fits are highly scattered, and rely heavily on the data collected from the unused canister at the site, which may not be relevant to a heated canister. Moreover, the concentrations are so low that analytical uncertainties are high. Given these limitations, the fits calculated including the higher-concentration samples will be used for the rest of this analysis.

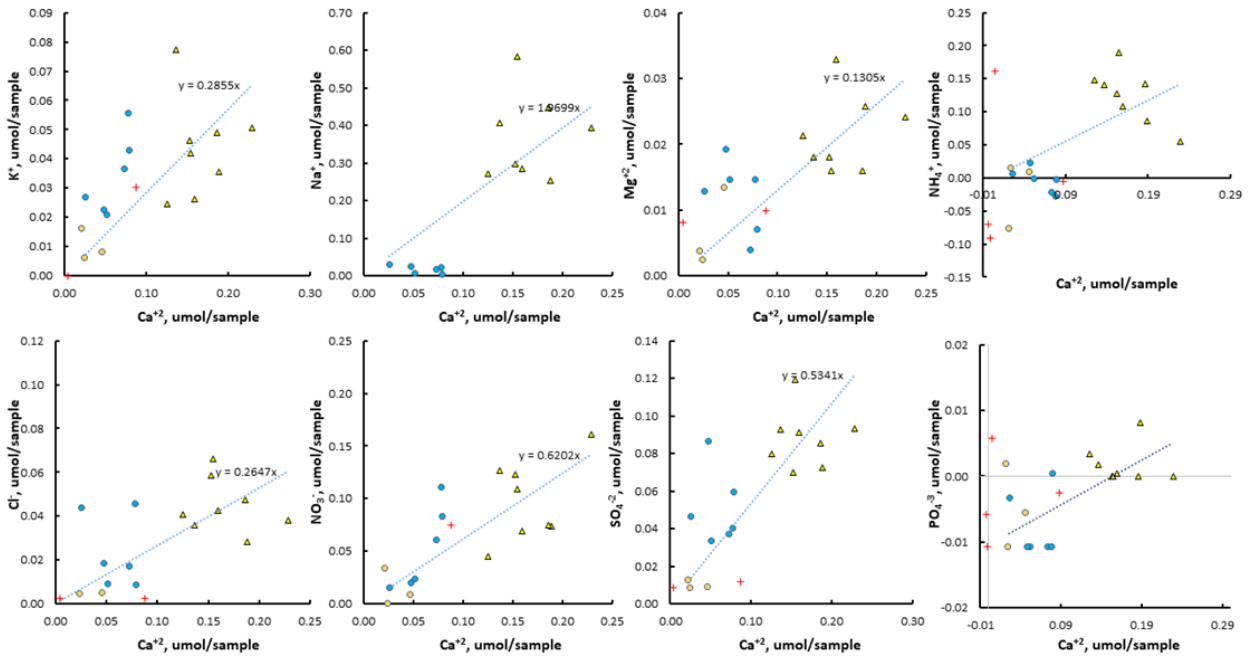

Figure 45. Soluble ion concentrations in the Hope Creek samples when the high concentration canister top samples are excluded, plotted against Ca concentration.

Determining a Hope Creek-based brine composition to use for salt deposition

As with the Maine Yankee salts, the values in Table 20 represent normalized ion concentrations, and cannot be used for depositing salt on test specimens because they are oversaturated. For corrosion testing, solutions must be 0.3-0.5 molal for effective salt deposition. If mixed to those brine compositions, these solutions would precipitate out, and would precipitate out a large mass of material, making deposition impossible. The methodology to create a representative brine composition for Hope Creek was the same as for Maine Yankee, where EQ3/6 was used to generate a dilute starting solution with a composition reflecting the normalized values in Table 20. The concentration of the initial solution was 10^{-5} molal.

The results of the calculations using the normalized concentrations of the Hope Creek samples from Table 20 are shown in Figure 46. As the solution evaporates, the divalent cations are removed from solution as carbonates and sulfates, and the resulting solution becomes progressively enriched in monovalent ions.

Because of the high solubilities of Na^+ and K^+ chlorides and nitrates, these species increase nearly monotonically in the brines as they evaporate. Due to a slightly higher Cl^- content in the Hope Creek salts compared to the samples from Maine Yankee, halite (NaCl) precipitates at around 70%, and niter (KNO_3) at about 66% (these minerals simultaneously precipitate at 66% RH for the Maine Yankee composition). Following the precipitation of NaCl, and as the RH continues to decrease, the brine becomes progressively more nitrate- and sulfate-rich until it precipitates thernadite (Na_2SO_4), and finally, at 67% RH, niter (KNO_3). The mineral assemblage that governs the deliquescence properties of the Hope Creek brine (including all the samples) is NaCl-Na_2SO_4-KNO_3.

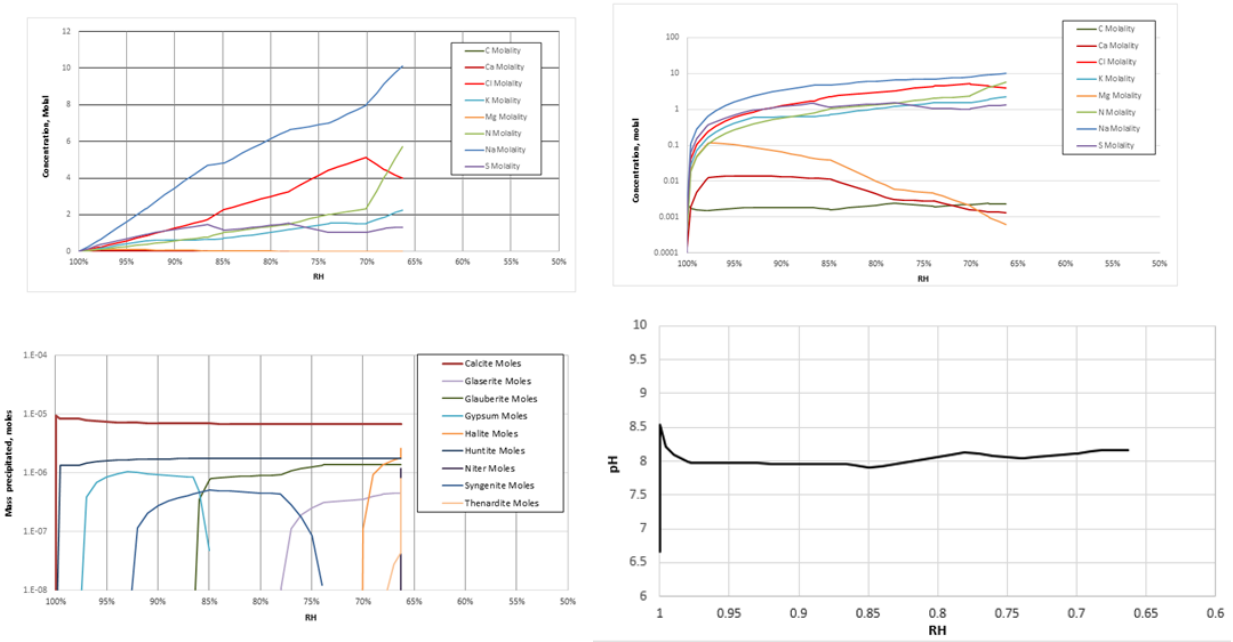

Figure 46. Predicted evaporative evolution of all Hope Creek salts. a) Brine compositions on a linear scale; b) brine composition on a log scale; c) precipitated minerals; d) solution pH.

Calculation of a Hope Creek representative brine for corrosion testing

To use the composition of the normalized Hope Creek brine for testing, adjustments are needed to allow mixing of a stable, more concentrated brine for deposition onto corrosion samples. Saturation of divalent carbonate and sulfate salts at low degrees of evaporation (corresponding to high RH), as seen in Figure 46c, prevents using this solution without modification. As noted earlier, the salt deposition process requires that the deposited materials be completely dissolved and relatively high concentration. A solution concentration around 0.3-0.5 molal would be effective. Here, brine representing an RH of 99%, corresponding to a concentration of about 0.3 molal, was selected as a target.

As discussed for the Maine Yankee soluble salts, the composition of the brine was modified to delay the precipitation of salts as long as possible and produce a brine of ~0.3-0.5 molal, that shared the same evolution behavior as the initial system. As Figure 46 shows, calcite ($CaCO_3$), huntite ($Mg_3Ca(CO_3)_4$), and various sulfate containing salts are the first salts to precipitate, therefore modifications to Ca^{2+}, Mg^{2+}, HCO_3^{2-}, and SO_4^{2-} were made to try to achieve a more concentrated representative brine. Many attempts were made to achieve a more concentrated brine without any precipitation, and as for the Maine Yankee samples, the predicted evolution of the initial brine, especially the pH, proved difficult to match. The final, successful attempt resulted in a concentrated brine (~0.3 molal) without precipitation and was achieved by reducing Ca by 100x relative to the initial solution, reducing both Mg^{2+} and HCO_3^- by 500x,

and charge balancing with SO_4^{2-}. The composition of this brine as a function of RH during evaporation is shown in Figure 47. Reducing the Ca^{2+}, Mg^{2+}, and HCO_3^- allowed for the brine to reach an RH ~ 99% before calcite precipitated – corresponding to a brine of ~0.3 molal. The composition of the major ions (Na^+, Cl^-, NO_3^-, K^+, and SO_4^{2-}) matched very well in the adjusted brine versus the original Hope Creek composition. Additionally, the minor ions (Mg^{2+}, Ca^{2+}, HCO_3^-) trace the composition of the original brine well. Mg^{2+} is a bit reduced in high RH (early stages of evaporation), however it converges at lower RH values. Also, the contribution of these ions to the overall composition is minimal, and therefore their changes in concentration are not likely to impact the overall chemical behavior of the brine very much. The pH of the alternative system matches the original system very well, and never deviates by more than 0.3 pH units during the evaporation process (Figure 47). The deliquescence-controlling mineral assemblage does not change between the adjusted and original composition. The proposed brine composition for deposition onto corrosion samples is shown in Table 21, along with the mixing formula.

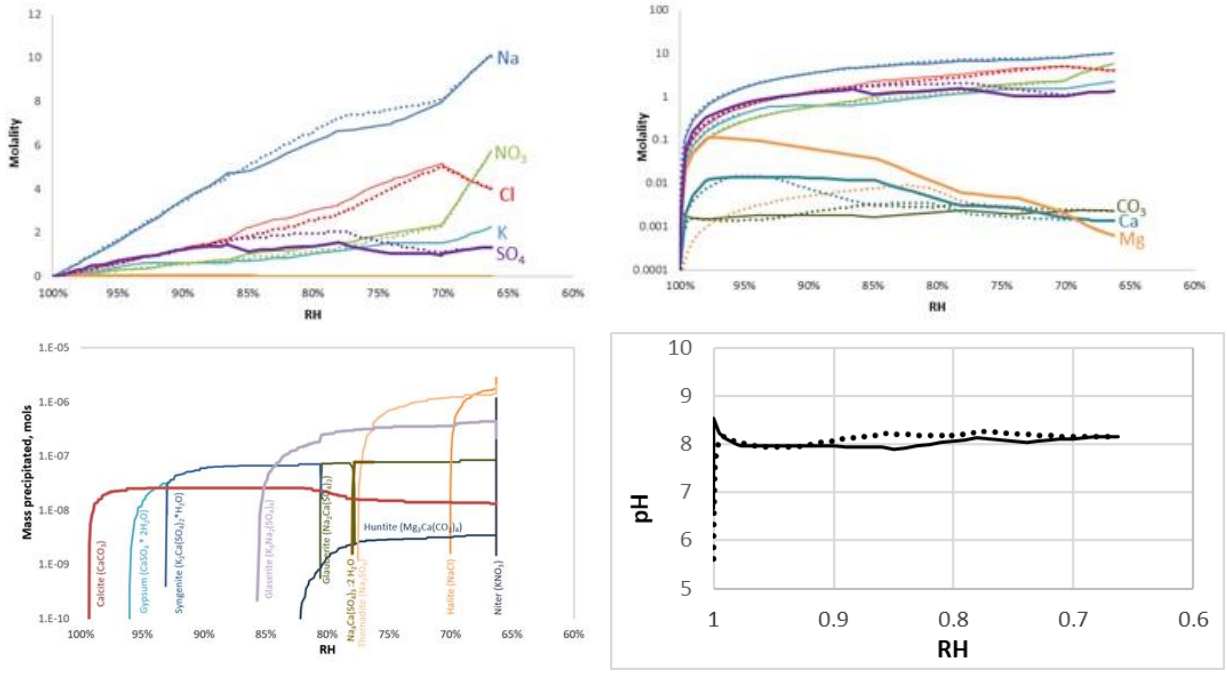

Figure 47. Predicted evaporative evolution of Hope Creek salts adjusted to prepare a solution of ~0.3 molal. a) Brine compositions on a linear scale; b) brine composition on a log scale; c) precipitated minerals; d) solution pH.

Table 21. Composition of Proposed brine simulant for depositing Hope Creek salts.

Species	Conc., molal	To mix:	
		Salt	Wt, grams
Na^+	1.815E-01	NaCl	0.1171
K^+	4.633E-02	$NaNO_3$	1.2131
Ca^{+2}	2.532E-03	KNO_3	1.0608
Mg^{+2}	2.693E-04	KCl	2.2686
Cl^-	6.646E-02	$CaCl_2$	0.2810
NO_3^-	3.018E-02	$MgCl_2{:}6H_2O$	0.0548
SO_4^{-2}	1.393E-03	Na_2SO_4	9.6193
HCO_3^-	1.393E-04	$NaHCO_3$	0.1171
		SUM	16.9402

Deliquescence behavior of the Hope Creek salt assemblage

In contrast to Maine Yankee, where the deliquescence-controlling minerals were halite (NaCl), niter (KNO_3), and soda niter ($NaNO_3$), for the Hope Creek composition, the brine dries out before soda niter can form, and therefore the mineral assemblage is controlled by NaCl, KNO_3, and thernadite (Na_2SO_4). The predicted deliquescence RH values as a function of temperature calculated for both individual salts and for the three-salt assemblage using EQ3/6 and the *data0.ypf.R2* database are given in Figure 48. Once again, the resulting deliquescence of a multi-salt assemblage is lower than that of any single component in the assemblage. At 25 °C, the deliquesce of the NaCl-KNO_3-Na_2SO_4 assemblage is predicted at about 66% RH, while the single salts deliquescence for NaCl takes place at about 75% RH, KNO_3 at about 95% RH, and Na_2SO_4 at about 90% RH. As a reminder, because the solubilities of nitrates increase considerably with temperature, the deliquescence RH for KNO_3 is strongly temperature dependent. Like the Maine Yankee 3-salt assemblage, the deliquescence RH of the three-salt assemblage drops as the temperature increases; and once again the simulation fails prior to achieving temperatures above 51 °C. This calculation was done in both Geochemist's Workbench and Eq3/6. In contrast to Maine Yankee, where the shape of the deliquescence curve at lower temperatures was suspect, the deliquescence behavior of the 3-salt assemblage for Hope Creek appears to behave more realistically. This could be due to less of a dependence to predict chloride-nitrate brines, as the nitrate composition is much lower.

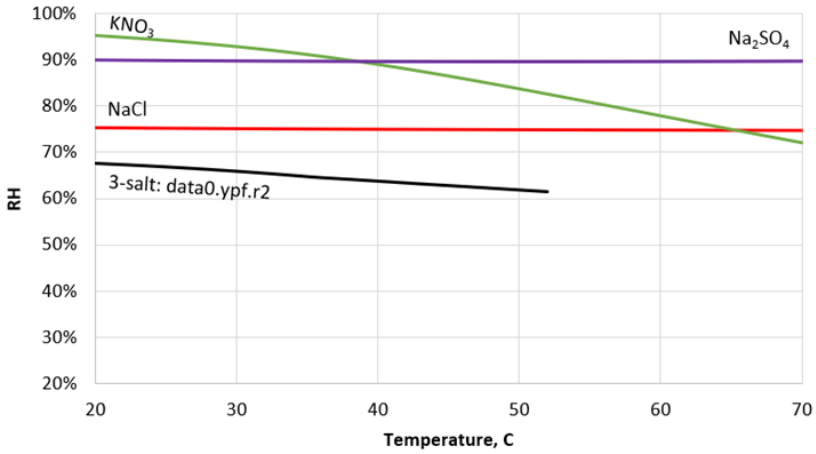

Figure 48. Predicted deliquescence RH values for NaCl, $NaSO_4$, KNO_3, and the three-salt mixture, as a function of temperature. Predicted values for the three-salt mixture were calculated using data0.ypf.R2.

The predicted Hope Creek brine chemistry using *data0.ypf.R2* at 25 °C, 40 °C, and 60 °C is shown in Figure 49. The predicted deliquescence RH dropped only slightly from 25 °C to 40 °C. The 60 °C simulation did not go to completion and began to display unusual behavior prior to stopping; it is unlikely that it is accurate. This calculation was performed with the *data0.ypf.R2* database, and as discussed previously, that database does not describe highly concentrated nitrate-rich solutions well.

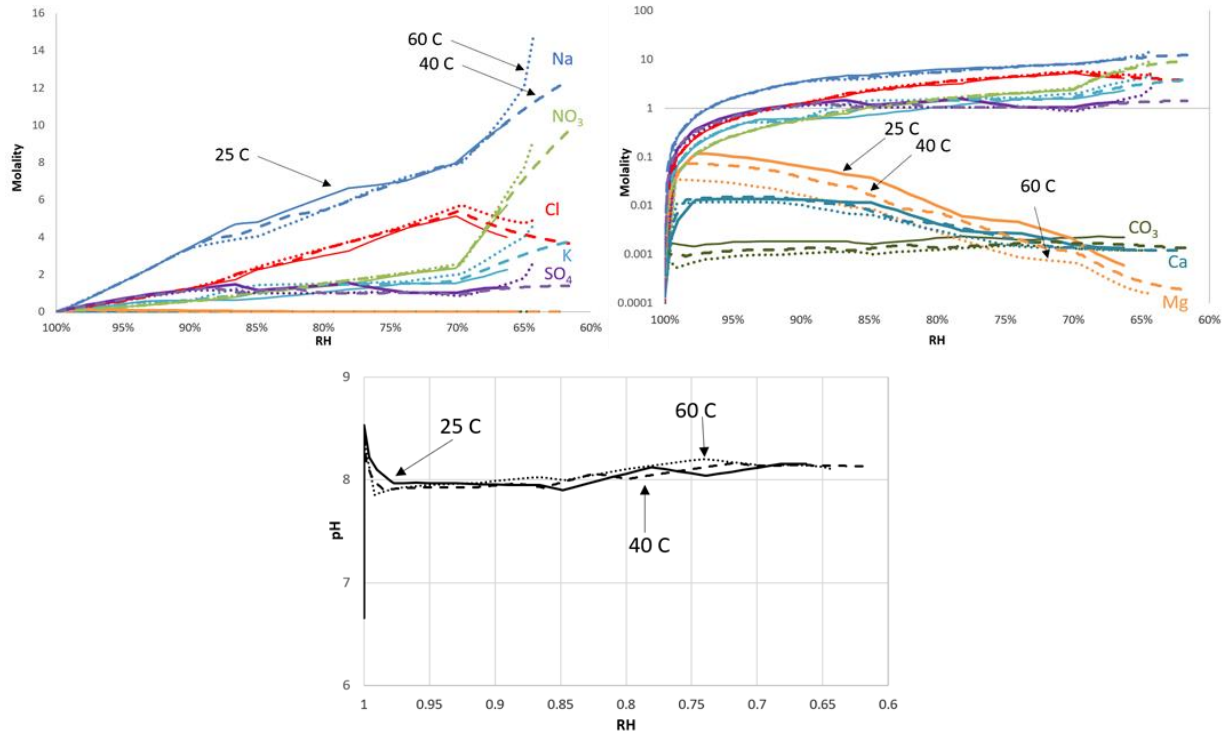

Figure 49. Predicted evaporative evolution of Hope Creek salts at 25 °C, 40 °C, and 60 °C a) Brine compositions on a linear scale; b) brine composition on a log scale; c) solution pH.

Compared to Maine Yankee, the Hope Creek soluble salts may be enriched in sea salts, as indicated by higher relative concentrations of Na^+ and Cl^-. However, overall brine evolution trends (Figure 50) do not

differ greatly between the two brines, with the exception of nitrate, which is significantly higher in the Maine Yankee samples. Due to the higher concentrations of Na^+ and Cl^-, halite precipitates at a higher RH during evaporation of the Hope Creek brine versus the Maine Yankee brine, and the brine dries out entirely at about ~66% RH compared to ~58% RH for the Maine Yankee brine. The pH of the two brines also evolves relatively similarly, maintaining a near-neutral value; this is likely due to the relatively high sulfate concentration or the brines. The Maine Yankee brine is slightly more acidic (pH 7.5-8) than the Hope Creek brine (pH ~8).

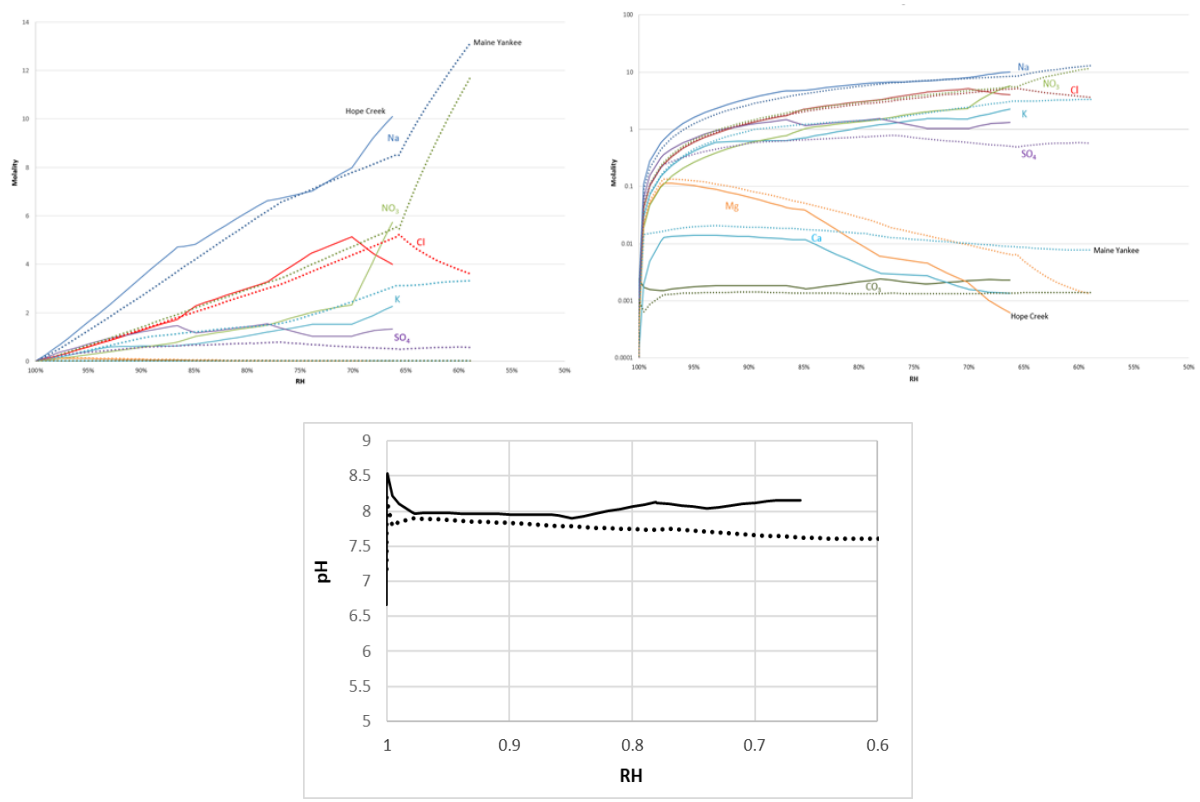

Figure 50. Predicted evaporative evolution of Hope Creek salts compared with Maine Yankee Salts. (Hope Creek- solid lines; Maine Yankee – dotted lines). a) brine compositions on a linear scale; b) brine composition on a log scale; c) pH.

2.2.3.3 Summary

The impact of the compositional differences between the Maine Yankee and Hope Creek salts may be explored experimentally. However, at least initially, the Maine Yankee data will be used. The Maine Yankee data set is considered the better of the two data sets, because of the very low concentrations of the Hope Creek soluble salt samples and the correspondingly high analytical uncertainties.

If nitrate is inhibitive, there is sufficient nitrate present at Maine Yankee, which is a relatively near-marine site, to be beneficial. However, nitrate-chloride mixtures will deliquesce at significantly lower RH values (and hence, higher temperatures) than just chloride mixtures. Lower deliquescent RH values means that a brine can exist at higher temperatures than for the chloride-only systems. Also, brine volumes will be larger at any given RH, for instance, sea-salt brines show a drastic decrease in volume below 74% RH, when halite is predicted to precipitate. However, for the Maine Yankee and Hope Creek

brines, the first nitrate or chloride salt does not precipitate until the RH drops to 66% RH at Maine Yankee (Figure 38); and 70% at Hope Creek (Figure 46); between 74 and 70% or 66% RH, a much larger volume of brine would be present in the case with nitrate. Hence, if nitrate does not prove to be inhibitive, then its presence may be detrimental, as brines could form at higher temperatures, and under most circumstances, a thicker brine layer would be present.

2.2.4 Characterization of Inert Dust particles on Dry Storage Canister Surface Deposits

Information on the composition and range of inert dust particle sizes generally present on the surface of SNF dry storage canisters is available from the various sampling campaigns that have been undertaken over the past several years. These have demonstrated that deliquescent salts are present on dry storage canister surfaces, but also that they are only a small fraction of the dusts present. The large majority of the dust particles are detrital mineral grains, mostly quartz and aluminosilicate minerals such as feldspars and clays. These are likely to be relatively inert in brines formed by deliquescent salts. However, they may still serve to influence corrosion processes, by physical effects (Figure 51). Small grains may spread the brine via capillary processes, creating a continuous brine film that promotes corrosion by allowing development of separate anodic and cathodic regions. Or, it may increase localized corrosion (pitting) rates by creating a larger cathode. One assumption of the current SNL probabilistic storage canister SCC model is that deliquesced brines form a uniform layer on the canister surface, allowing the application of a maximum pit size model based on cathode currents; the presence of inert dust particles may increase the validity of that assumption. Large dust grains may have an additional effect; they may create occluded regions that result in crevice corrosion. The potential effects of inert dust particles on canister corrosion have never been explored. The analysis here provides dust particle size distributions that are being used to plan corrosion experiments with mixed salt and inert dust particles.

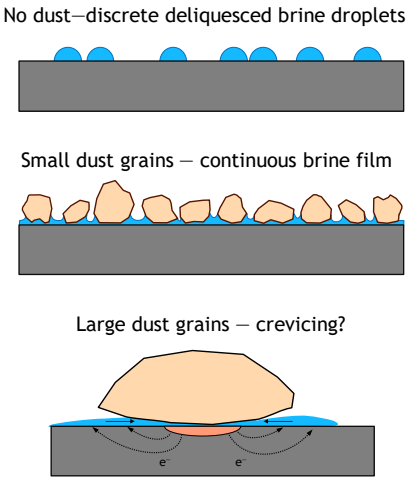

Figure 51. Possible effects of inert mineral grains on corrosion processes. Small grain may act to spread the brine into a continuous layer, while larger grains may act as crevice formers.

Information on the size and distribution of salts and inert mineral grains is based on those previous sampling campaigns. However, there are several limitations with respect to the data. Sampling methods varied, and they varied in terms of their efficiency at collecting a representative sample of the dust on the surface. Second, access to different locations on the canister surfaces was limited and varied with overpack design.

Two types of locations are of importance with respect to canister penetration due to SCC. The first is on the vertical sides of upright canisters, such as those sold by HOLTEC and NAC; the second is on the horizontal sides of canisters stored on their sides, such as Orano (formerly Transnuclear). Some direct sampling from the sides of vertical canisters has been accomplished, using coarse abrasive pads. While it is possible that coarser dust falls off these pads, these samples are the most representative available for the vertical canister sides. For horizontal canisters, only a single ISFSI site has been sampled, and that is Calvert Cliffs. It was sampled twice; however, only few samples were available from the first sampling and those analyzed by Sandia were stored in a desk for 6 months prior to being shipped to Sandia; coarser particles may have fallen off during storage. Moreover, the most heavily coated parts of the canister (the top) were inaccessible and were not sampled. The second sampling at Calvert took place on a rainy day, and the samples got wet—by the time they had been delivered to Sandia, they were covered with mold and were unusable.

In all sampling campaigns, it has been observed that horizontal surfaces of canisters collect heavier dust loads than the vertical surfaces. This is true for both vertical and horizontal storage systems. This makes sense, as particles can accumulate via gravitational settling on horizontal surfaces. Can the tops of vertical canisters act as analogs for the tops of horizontal canisters? Probably not. The tops of vertical canisters are relatively heavily coated with dust and that dust can be relatively coarse, as discussed below. However, it is likely that it blows in through the outlet vents, rather than entering at the inlets and rising up the annulus. The Orano horizontal storage systems have a heat shield plate in place between the top of the canister and the overpack to protect the concrete; this prevents material from blowing in the outlet vent and settling directly onto the canister surface. Hence, it is likely that the particles that settle onto the surface of horizontal canisters may be smaller than those observed on the tops of vertical canisters.

Particle Size Analysis

The goal of this work is to gain an understanding of the particle size distribution of dust on the surface of the SNF canisters that occurs at ISFSI sites. This will not only help better characterize what is being deposited on the surface of SNF canister but also provide the framework for corrosion studies in which inert dust is co-deposited with salt.

Methodology

SEM images were obtained from previous reports of field sampling activities at four ISFSI sites; Calvert Cliffs, Hope Creek, Diablo Canyon, and Maine Yankee. The sampling methods varied slightly from site to site and many biases, but the goal of this analysis is to gain a representative understanding of the distribution of dust sizes that adhere to the SNF canisters, so all available data were used.

The particle sizes were evaluated using ImageJ software. For each image, the scale bar was traced with the line tool to convert pixels to μm using the "Set Scale" function. Then the line tool was used to estimate the length of each particle and the measurement was recorded using the "Measurement" function. Attempts were made to analyze as many particles as possible for each image. While these analyses are likely a sufficient representation of the particle distribution, there are inherent biases and uncertainties in this process. There is a both a systematic bias to this process to favor larger particles (i.e. most or all of the large particles were counted, but not all of the smaller particles were counted) and a sampling bias; only 8-12 SEM images were analyzed from each ISFSI site. Finally, there is added uncertainty in the measurements due to estimating the size of the particles visually.

2.2.4.1 Calvert Cliffs

Dust on a Calvert Cliffs canister was sampled in 2013. The canister was a Transnuclear (now ORANO) horizontal canister, stored in a concrete crypt. To collect the sample, the door was taken off the overpack, and a water-filled polyethylene plug was inserted. Around the annulus of the plug, a hollow rod was inserted, with a sampling head. The sampling head held a coarse Scotch-brite™ abrasive pad, backed with a paper filter. The sampling head was scrubbed over the canister surface, and a vacuum, transmitted

through the rod, pulled dislodged dust through the abrasive pad and onto the filter. Examples of these are shown in Figure 52. Both the Scotch-brite™ pad and filter were analyzed. Two samples were analyzed, one very lightly coated with dust from below the canister midline, and one from the canister upper surface (about 10 o'clock position) with a much higher dust load (the heavier one is shown in Figure 52).

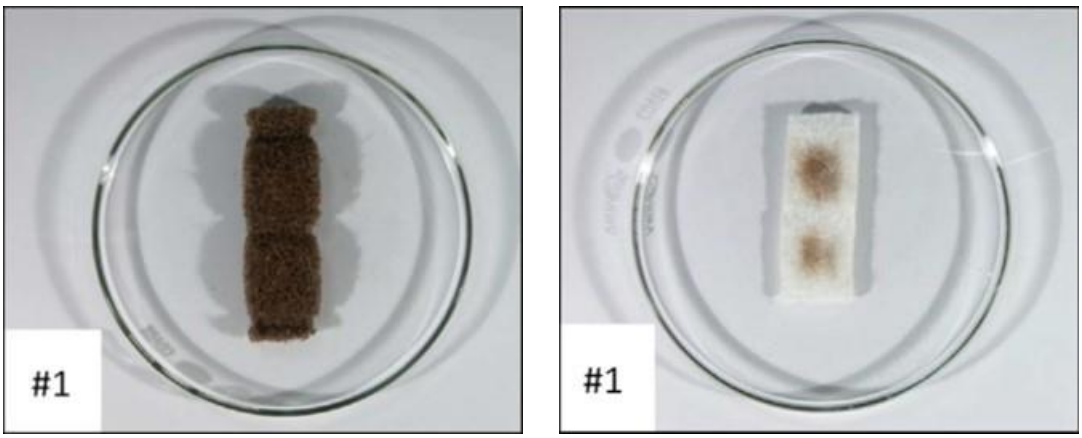

Figure 52. Scotch-brite™ pad (left) and polyester fiber filter (right) used in sampling canister dust at Calvert Cliffs (note that the Scotch-brite™ pad is brown in color).

The dust load was observed to vary on the canister surface, with a light load on the bottom and sides of the canister and a heavy load on the top (Figure 53). Because there is a head shield to protect the concrete over the top of the canister, it is inferred that this dust did not blow into the outlet vents and settle onto the top of the canister, but rather was carried up from the inlet vents. Samples were taken from a few different locations on the canister surface; however, the most dorsal location sampled was about the 10 o'clock position, because the annulus between the heat shield and the canister was too narrow to sample the exact top of the canister.

Calvert Cliffs dust characteristics

SEM photos from the abrasive pads and filters show the general morphology and size range of the dust that was collected from the Calvert Cliffs canister. Images from the Scotch-brite™ pads were used to quantify the dust particle size distributions.

Figure 53. Dust on the top of the canister at Calvert Cliffs.

Abrasive Pads

Dust adhering to the fibers of the abrasive pads (Figure 54 and Figure 55) was primarily detrital minerals. The mineral particles were dominantly 2-5 µm in size, but particles in the 10-20 µm range were not uncommon. Larger particles, like the pollen and possible coarser mineral grains, had not adhered to the abrasive pad; they may have passed through or have been dislodged during handling. These images were used for particle size analysis.

Filters

The brown discoloration on the filters (Figure 52) was mainly due to pollen and other plant particles, which apparently comprise the majority of the dust. The pollen ranged in size from roughly 20 µm to 80 µm; stellate trichomes were also present and were more than 100 µm across. Other than pollen, only a few small particles of mineral dust adhered to the filters. A few larger mineral particles, in the range of 20 µm in diameter, were present. Most of the mineral dust was apparently retained by the abrasive pads or may have been fine enough to pass through the filters. SEM images of the filters are shown in Figure 56. Note that despite the brown stain on the filters, particles were rare as imaged by the SEM—the particles readily dislodged from the filters, and most particles were probably lost during sample preparation, either falling off or working their way deeper into the fibrous filter. Because of the paucity of particles, the filter SEM images were not used in the particle size analysis; however, they do indicate that the abrasive pad data are probably biased towards smaller particle sizes relative to what was on the canister.

Dust Particle Size Distributions

The dust particle size distribution was determined using SEM photos of dust from the Calvert Cliffs canister and is shown in Figure 57. The mineral particles were dominantly <5 µm in size, but particles in the 10-20 µm range were not uncommon. Larger particles, like the pollen and possible coarser mineral grains, had not adhered to the abrasive pad. The range of particle diameters detected was from 0.27 µm to 32.8 µm, with a median particle diameter of 3.9 µm and the average particle diameter of 4.8 µm (N= 250).

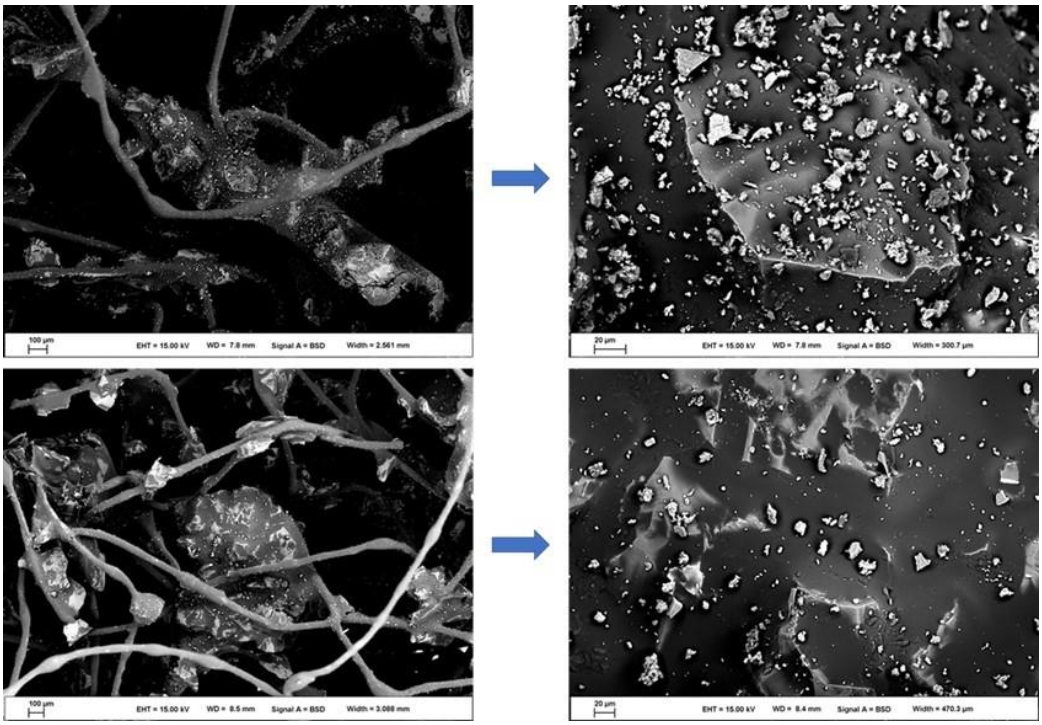

Figure 54. SEM images of Calvert Cliffs dust adhering to the fibers of a Scotch-brite™ abrasive pad. Left—low magnification; right—high magnification.

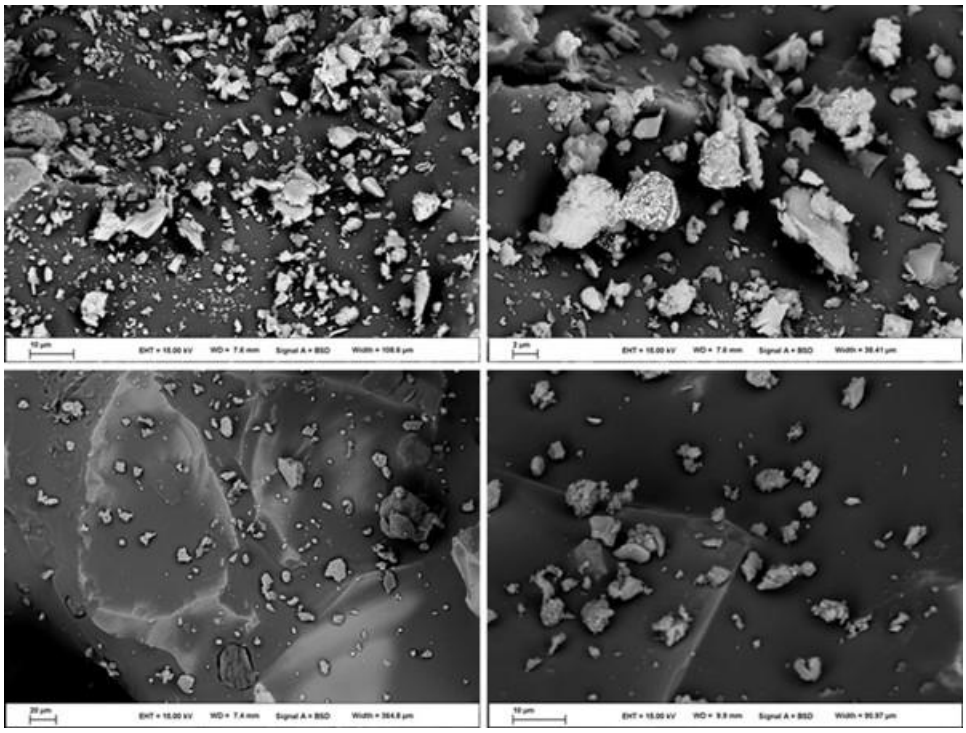

Figure 55. High magnification SEM images of dust adhered to Scotch-brite™ abrasive pad at Calvert Cliffs.

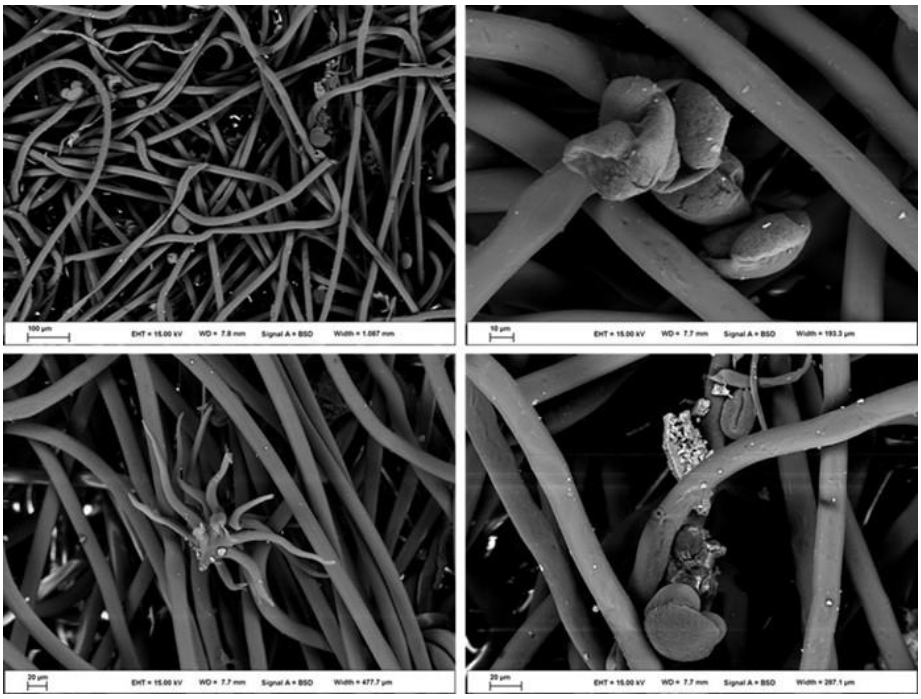

Figure 56. SEM image of dust adhered to filters at Calvert Cliffs

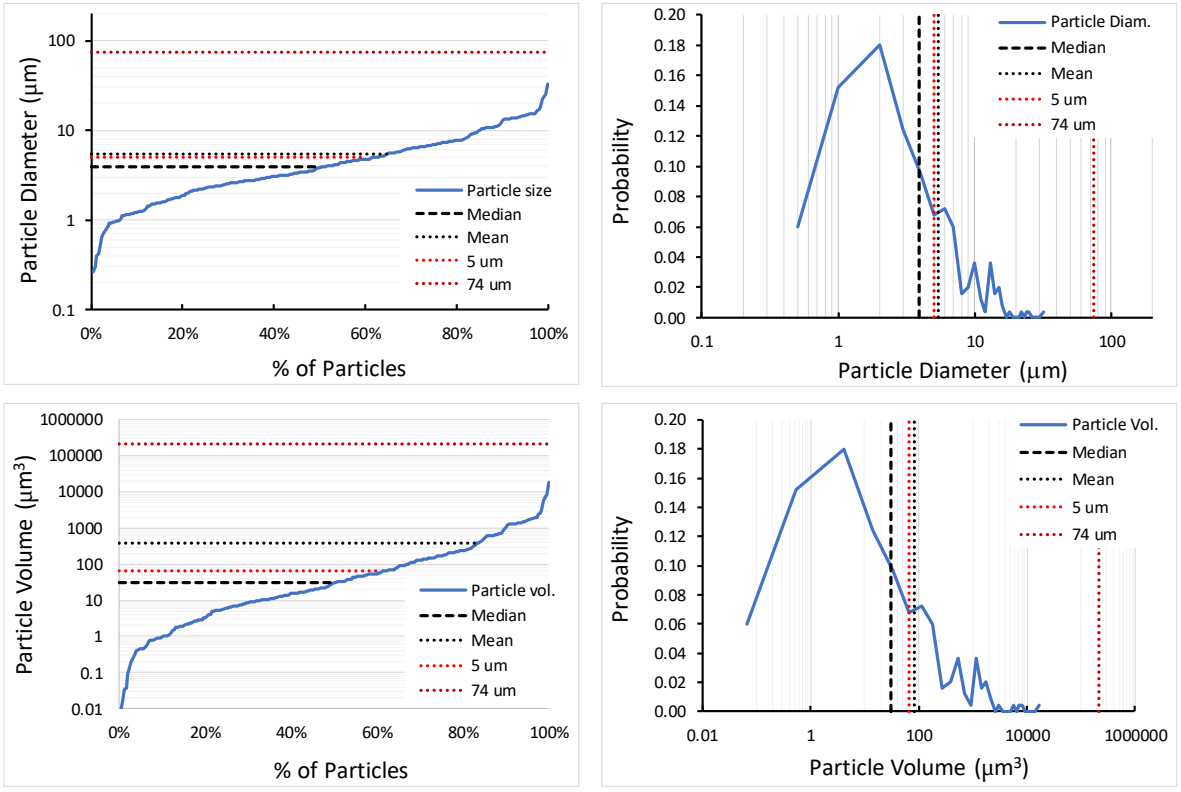

Figure 57. Particle size distributions determined for Calvert Cliffs dust samples. Both particle diameter distributions (upper) and particle volume distributions (lower) are provided.

2.2.4.2 Hope Creek

At the Hope Creek ISFSI, two canisters were sampled. The canisters were vertical canisters, that had been in storage for approximately 10 years. Sampling was done with Scotch-brite™ pads (white this time) and SaltSmart™ pads to measure soluble salts. Dust loads on the sides of the canisters were extremely light—few particles were found on the Scotch-brite™ pads; however, there was sufficient dust to discolor the Scotch-brite™ pads very slightly in most cases. The SaltSmart™ pads showed little or no discoloration. The dust load on the top of the canister was much heavier; both SaltSmart™ and Scotch-brite™ pads from the top of the canister were heavily discolored; see Figure 58 and Figure 59).

Figure 58. SaltSmart™ pads from Hope Creek canisters 144 and 145. Discolored samples are from the canister tops.

Figure 59. Scotch-brite™ pads from canisters 144 and 145. Samples 144-011, 144-012, and 145-012 are from the canister tops. Note that these Scotch-brite™ pads are white and contain no alumina.

Dust on Scotch-brite™ pads from the sides of Hope Creek canisters

Note these Scotch-brite™ pads did not contain abrasive grains, but did contain talc (Magnesium silicate), which shed small particles when abraded. SEM images of dust on the Scotch-brite™ pads are shown in Figure 60.

Dust on Scotch-brite™ pads from the tops of Hope Creek canisters

As noted previously, the dust on the tops of the canisters may have blown in through outlet vents. Since there are no through-thickness welds on the tops of vertical canisters, this area is of little interest with respect to corrosion. Nevertheless, the data from the tops of Hope Creek canisters are presented here, because they represent the majority of the data from Hope Creek. Overall, the particles from the canister tops cover a wider range than on the sides of the canisters, extending towards larger particles. Particles less than 5 µm are still abundant, but many particles are in the 5-20 µm range, with a few extending up to 30-40 µm (Figure 61 and Figure 62).

Hope Creek Dust Particle Size Distributions

The particle size distribution was determined using SEM photos of dust from the Hope Creek canisters and is shown in Figure 57. The mineral particles were dominantly <5 µm in size (~50 %), but about 25% of the particles were in the 10-20 µm range. The range of particle diameters detected was from 0.12 µm to 45.3 µm, with a median particle diameter of 5.8 µm and an average particle diameter of 8.4 µm (N= 328).

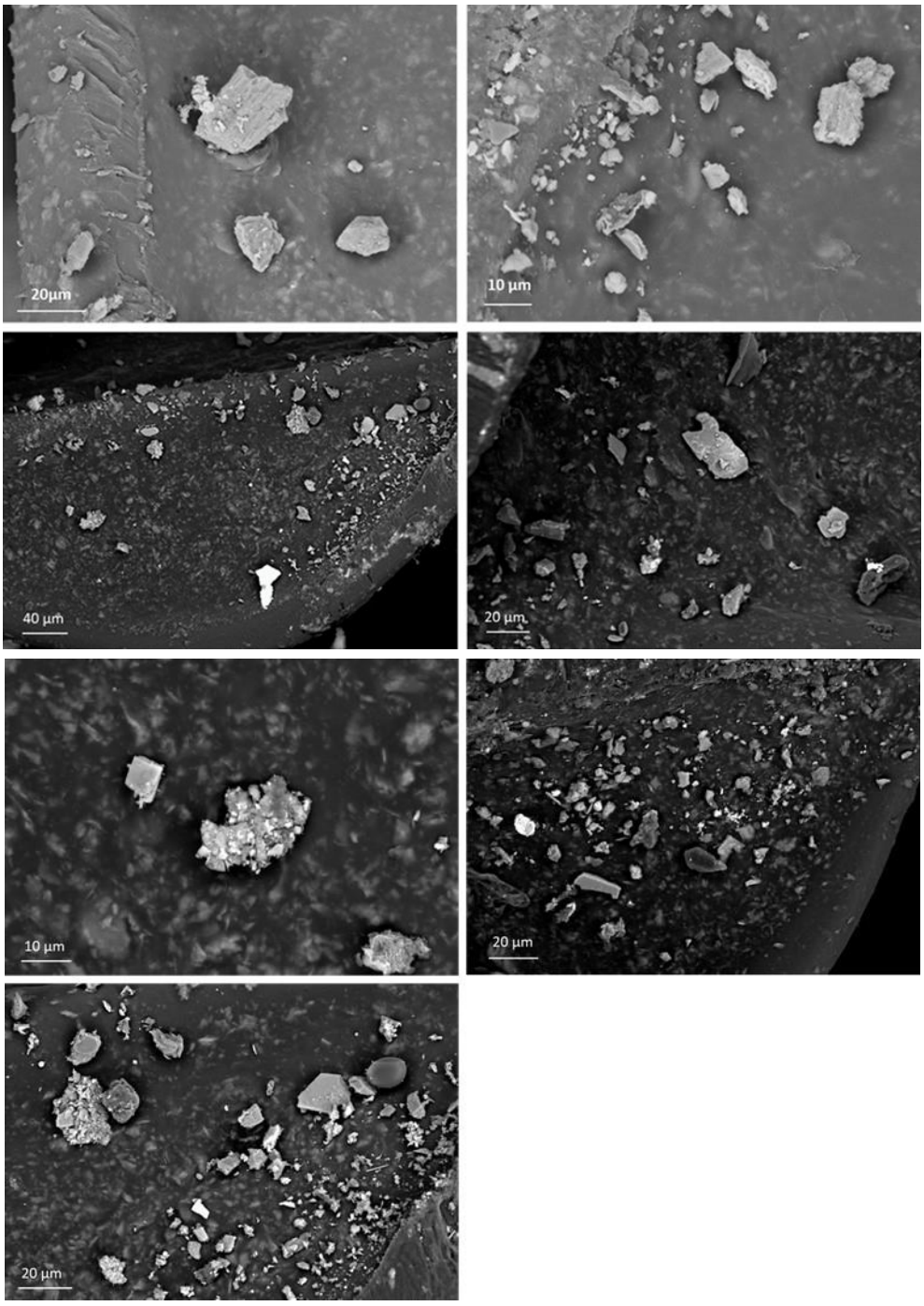

Figure 60. SEM images of Scotch-brite™ dust samples from the sides of the Hope Creek canisters.

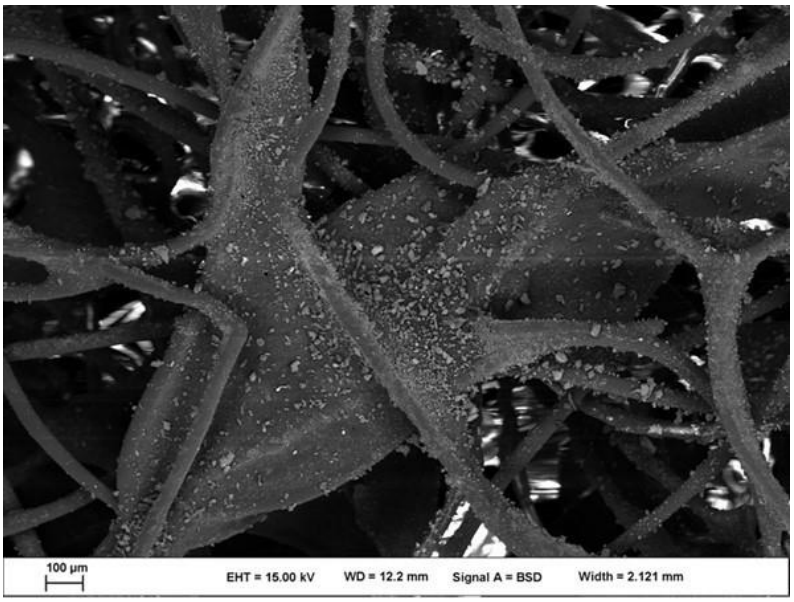

Figure 61. Low magnification images of the dust on the Scotch-brite™ samples from the top of the Hope Creek canisters.

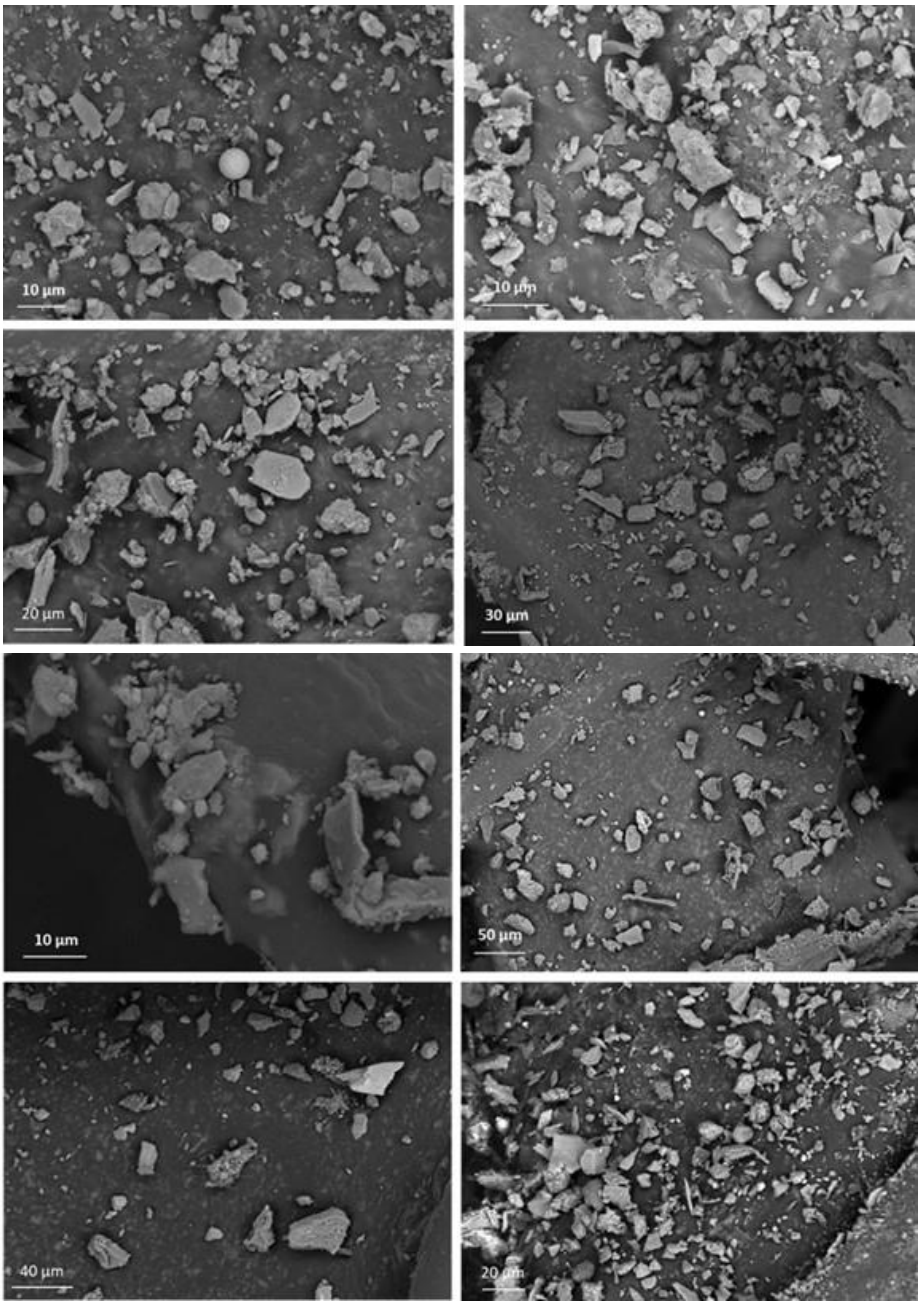

Figure 62. Close-up images of dust particles from the top of the Hope Creek canister.

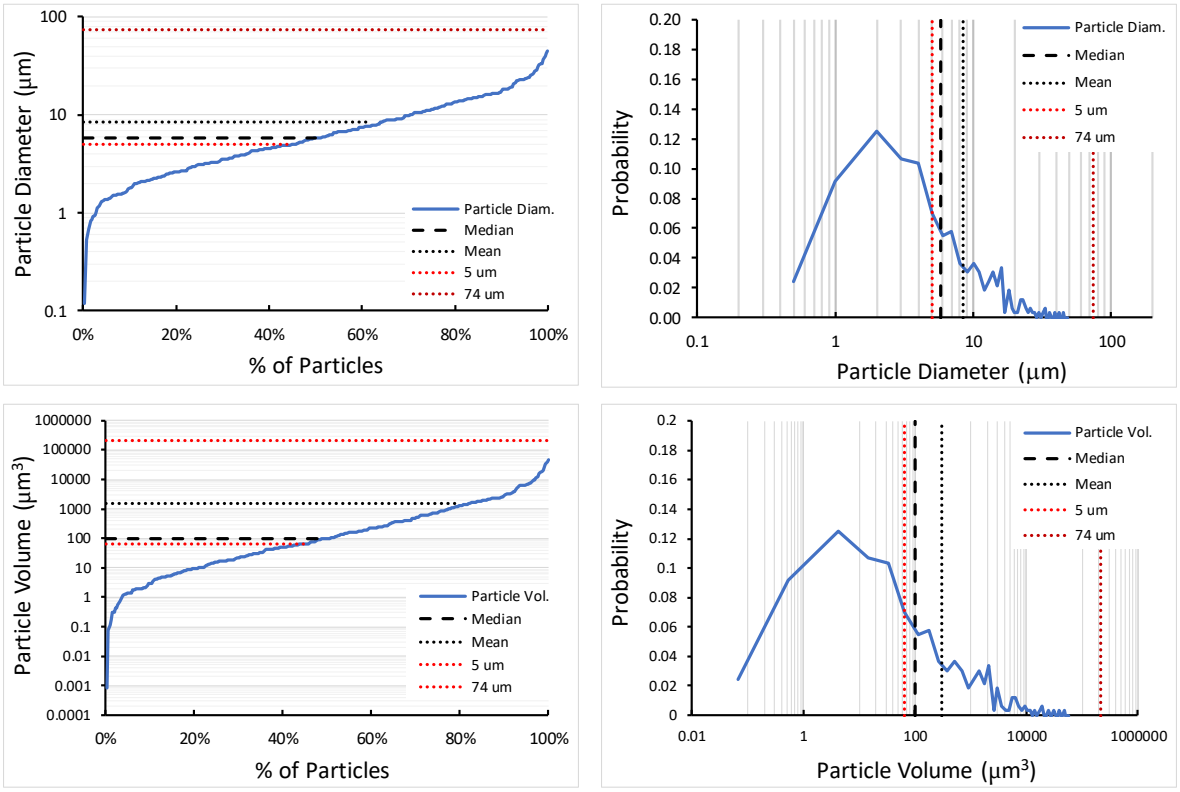

Figure 63. Particle size distributions determined from SEM images of dust from in-service Hope Creek canisters. Both particle diameter distributions (upper) and particle volume distributions (lower) are provided.

2.2.4.3 Diablo Canyon

At the Diablo Canyon ISFSI, two canisters were sampled. The canisters were vertical canisters, that had been in storage for approximately 2 and 4 years. Sampling was done with Scotch-brite™ pads (white this time) and SaltSmart™ pads to measure soluble salts. Scotch-brite™ samples were collected everywhere, but, the surface temperatures on these young canisters were so hot that some areas could not be sampled using the SaltSmart™ devices—they melted at temperatures of over 70 °C - 80 °C. The dust load on the top of the canister was much heavier than the sides (Figure 64), and possible water stains were present. Dust loads on the sides of the canisters were extremely light, and the SaltSmart™ pads showed little or no discoloration (Figure 65), but there was sufficient dust to discolor the Scotch-brite™ pads slightly in most cases (Figure 66).

Figure 64. Photographs of the tops of the two canisters sampled at Diablo Canyon. These canisters were 2-4 years in storage at the time of sampling.

Figure 65. SaltSmart™ pads from Diablo Canyon canisters 123 and 170. No samples were collected from the canister tops.

Figure 66. Scotch-brite™ pads from Diablo Canyon canisters 123 and 170. Note that 123-001 and 170-001 are from the gamma shields at the outlet vents, and samples 123-011, 123-012, and 170-003 are from the tops of the canisters.

Dust on Scotch-brite™ pads from the sides of Diablo Canyon canisters

Note the Scotch-brite™ pads used in this sampling episode did not contain abrasive grains, but did contain talc (Magnesium silicate), which shed small particles during abrasion. Dust loads on the sides of the Diablo Canyon canisters were very light, and pads reflect that (Figure 67). The other SEM images of the dust focused on areas where particles were concentrated and are not representative of what was present over the Scotch-brite™ pad as a whole (Figure 68).

Dust on Scotch-brite™ pads from the tops of Diablo Canyon canisters

Given the visible dust on the canister tops, it is not surprising that there is much more dust on the Scotch-brite™ samples from this area; this is illustrated by the low magnification SEM image in Figure 69. High magnification SEM images used to evaluate the particle size distribution are shown in Figure 70. The mineral grains are dominantly inorganic mineral grains or clusters of fine-grained mineral grains.

Diablo Canyon Dust Particle Size Distributions

The particle size distribution determined from the SEM photos is shown in Figure 71. The mineral particles were dominantly <5 µm in size (~50 %), but about 20% of the particles were in the 10-100 µm range. The range of particle diameters detected was from 0.30 µm to 73.3 µm, with a median particle diameter of 4.1 µm and an average particle diameter of 6.3 µm (N= 311).

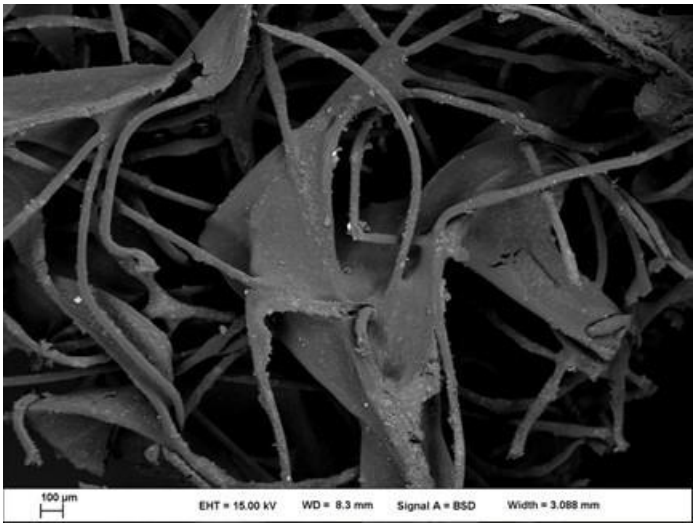

Figure 67. Low magnification view of a Scotch-brite™ pad used to sample the side of a Diablo Canyon canister. Note the abrasion damage to the high points.

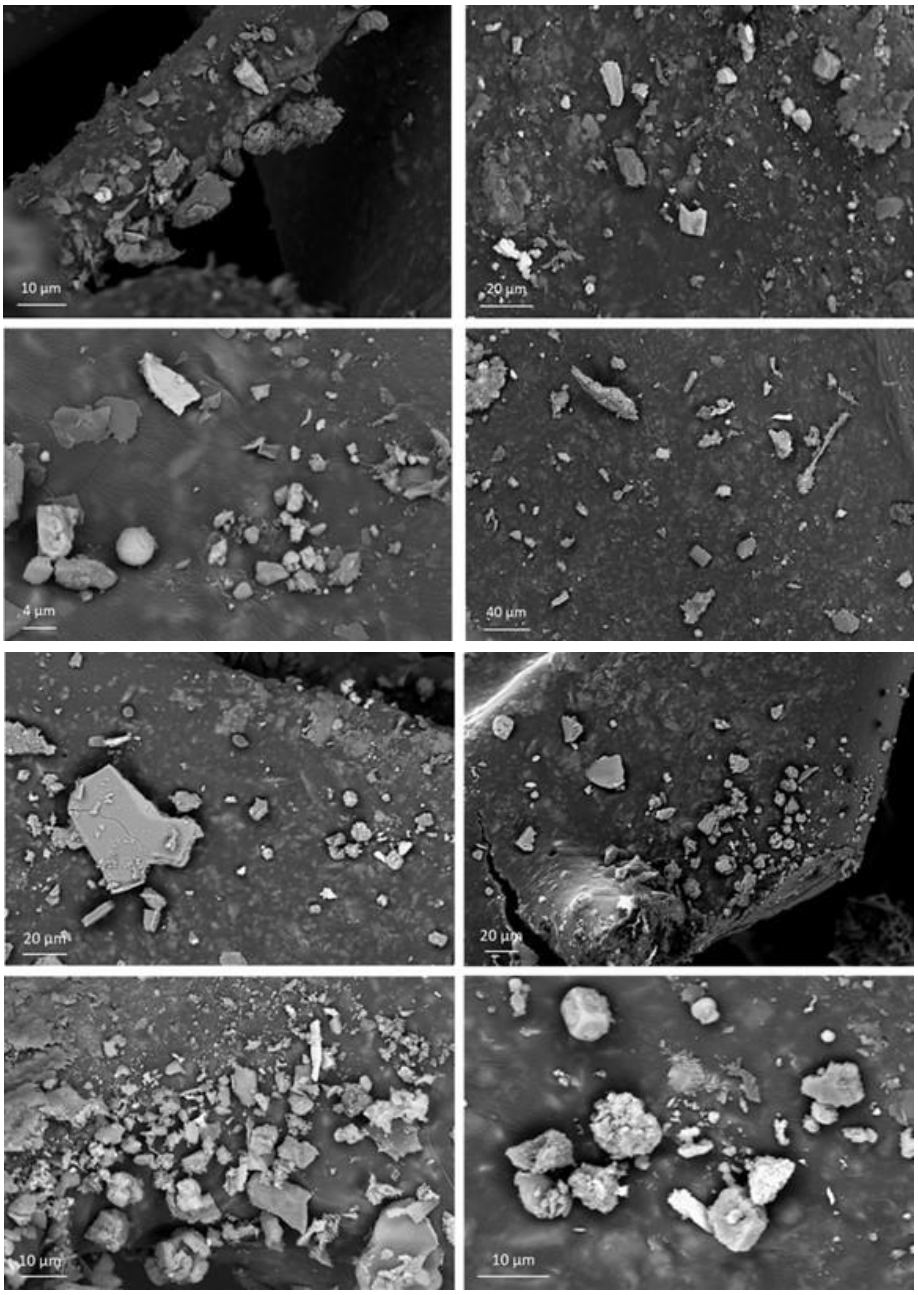

Figure 68. Close-up images of dust on the Surfaces of Scotch-brite™ pads used to sample the sides of Diablo Canyon canisters. Note that most of the finest particles (on abraded edges) are talc, abraded from the pad itself.

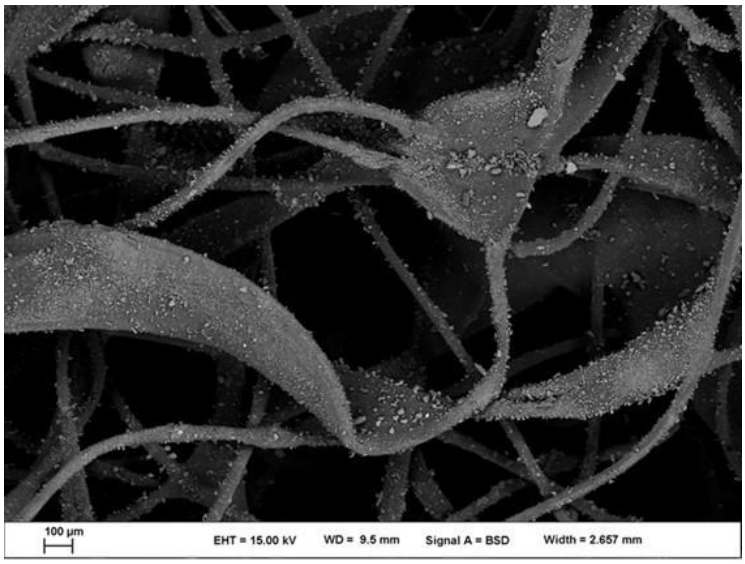

Figure 69. Low magnification image of dust on Scotch-brite™ pads used to sample the tops of Diablo Canyon Canisters

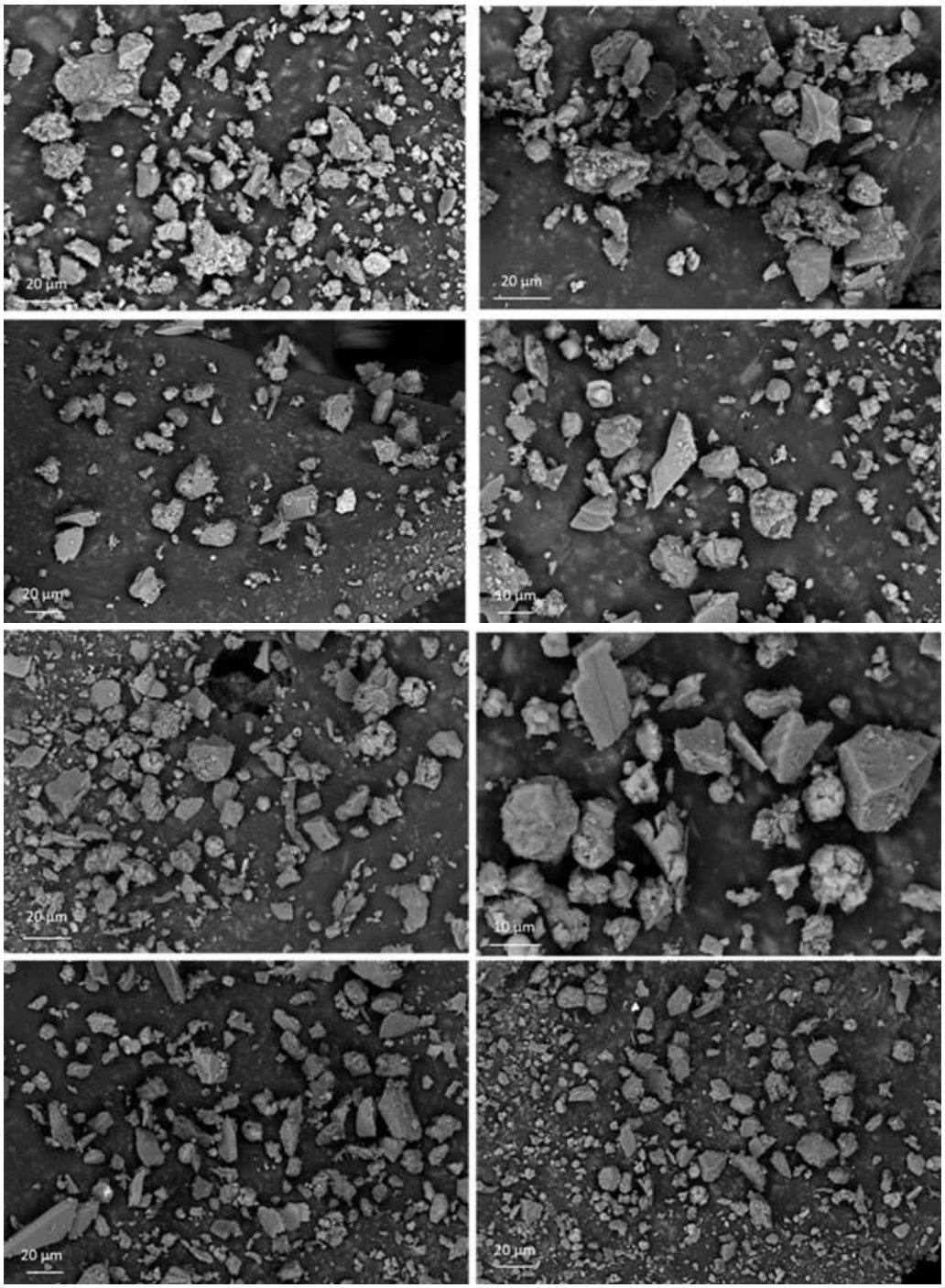

Figure 70. High magnification images of dust on Scotch-brite™ pads used to sample the tops of Diablo Canyon Canisters.

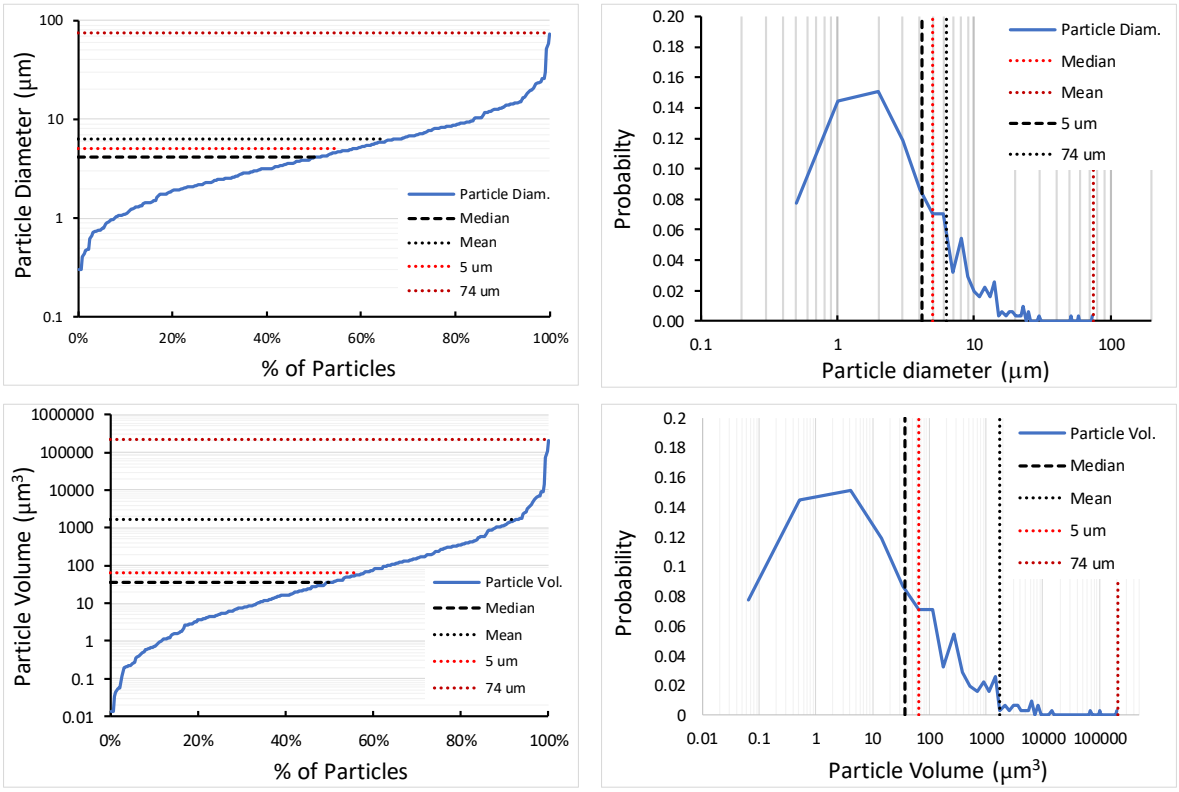

Figure 71. Particle size distributions for the Diablo Canyon dust samples. Both particle diameter distributions (upper) and particle volume distributions (lower) are provided.

2.2.4.4 Maine Yankee

Three samplings have been done at Maine Yankee. In 2016, a robot was used to sample dust within an overpack containing a canister with Greater than Class C (non-heat generating) waste. Samples were collected from the shield plug over the canister, and from shelves within the overpack, but not from the canister itself. In 2018, the lid of an overpack was removed, and samples were collected by hand from the top of a SNF canister; both dry (Scotch-brite™) and wet sponge samples were collected. Samples from the vertical canister walls were not collected in either the 2016 or 2018 sampling episodes. Finally, in 2019, dust collection coupons were retrieved from the inlet and outlet vents of four different canisters.

This discussion will focus on the data from 2018, as these were collected from the canister surface. As noted previously, the tops of vertical canisters are not of concern in terms of SCC and may not be relevant to NUHOMS-type horizontal canisters as the horizontal canisters have a heat shield that prevents direct deposition of coarse materials that might have blown in the outlet vents. Nevertheless, the data from the top of the Maine Yankee canisters does at least provide some information on what can enter an overpack. Moreover, because the samples were collected by hand and immediately packaged, coarser dust that fell off the Scotch-brite™ pads was retained. As described below, this dust is quite coarse, and suggests that in inspections at other sites—where the Scotch-brite™ was robotically applied—a significant fraction of coarser material may have been lost and is not represented by what was observed on the pads.

While The sponge samples had adhering coarse dust, that is not described here. Instead, the loose dust that fell from the Scotch-brite™ pads, and the finer material that adhered to the pads, is examined. These Maine Yankee samples are from the top of a storage canister. Pictured below are photos of coarse dust that fell off the Scotch-brite™ during transport. Following that are photos of the dust that remained adhering to the Scotch-brite™.

Dust from Scotch-brite™ pads used to sample the top of Maine Yankee Canister

Loose dust that fell off the Scotch-brite™ pads during transport

This dust consists primarily of organic matter—stellate trichomes and pollen (Figure 72). The stellate trichomes and other plant fibers can be up to several hundred microns in longest dimension; the pollen grains vary in size with species, but the larger ones are in the 50-80 μm range. Coarse mineral grains (quartz, feldspar, and micas) are also present; the largest of these are generally in the 50-100 μm range, but some mica particles are up to a few hundred microns in size. This is because mica occurs as thin, flat sheets with a large area relative to their aerodynamic diameter—they are readily wafted to into the air relative to other blockier minerals. Because they are flat, they may tend to form crevices more readily than other minerals. In addition to those detrital minerals, large (several hundred micron) plates of calcite/calcium silicate efflorescence from the concrete were also present. It is assumed these are not relevant, especially to horizontal canisters, where the heat shield prevents direct deposition onto the canister of particles generated from the overpack.

Particles on the Scotch-brite™ themselves:

SEM images of the dust on the Scotch-brite™ pads themselves are shown in Figure 73. This dust is much finer than the articles that fell from the Scotch-brite™ pads, illustrating that the coarse fraction is frequently lost from this medium. The mineral grains are dominantly inorganic mineral grains or clusters of fine-grained mineral grains.

Maine Yankee Dust Particle Size Distributions

The particle size distribution determined from the SEM photos is shown in Figure 74. The dust particles were larger than the other ISFSI sites; only about 30% of the dust grains were <5 μm in size. About 40% of the particles were > 10 μm. The range of particle diameters detected was from 1.07 μm to 180.3 μm, with a median particle diameter of 7.4 μm and an average particle diameter of 16.2 μm (N= 391).

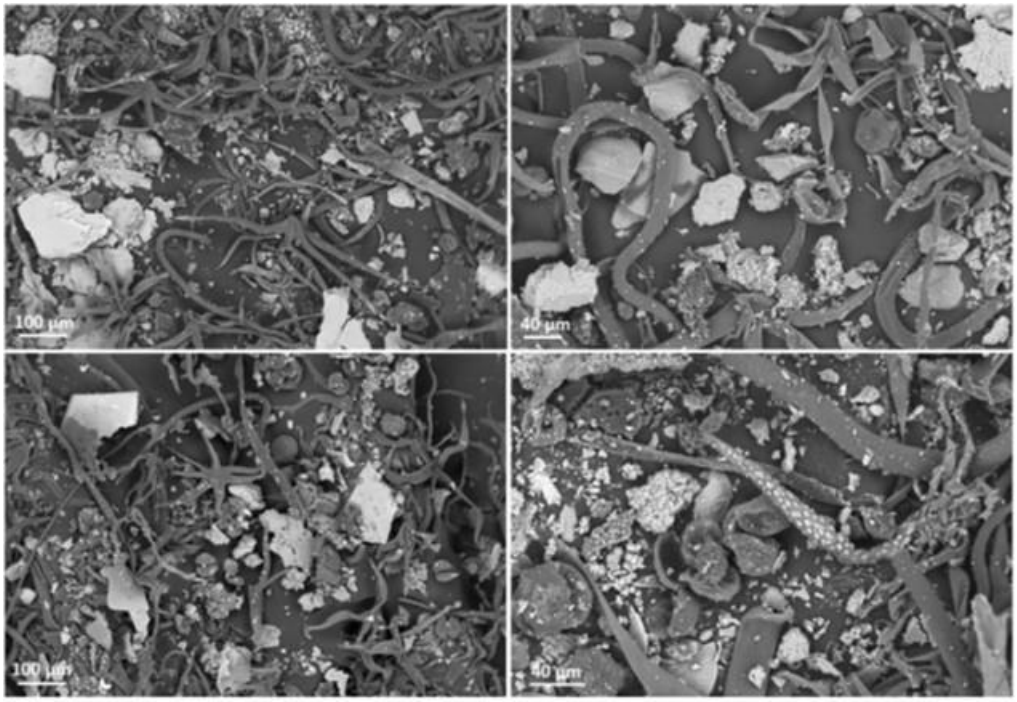

Figure 72. Images of dust that fell off of Scotch-brite™ pads used to sample the tops of Maine Yankee Canisters.

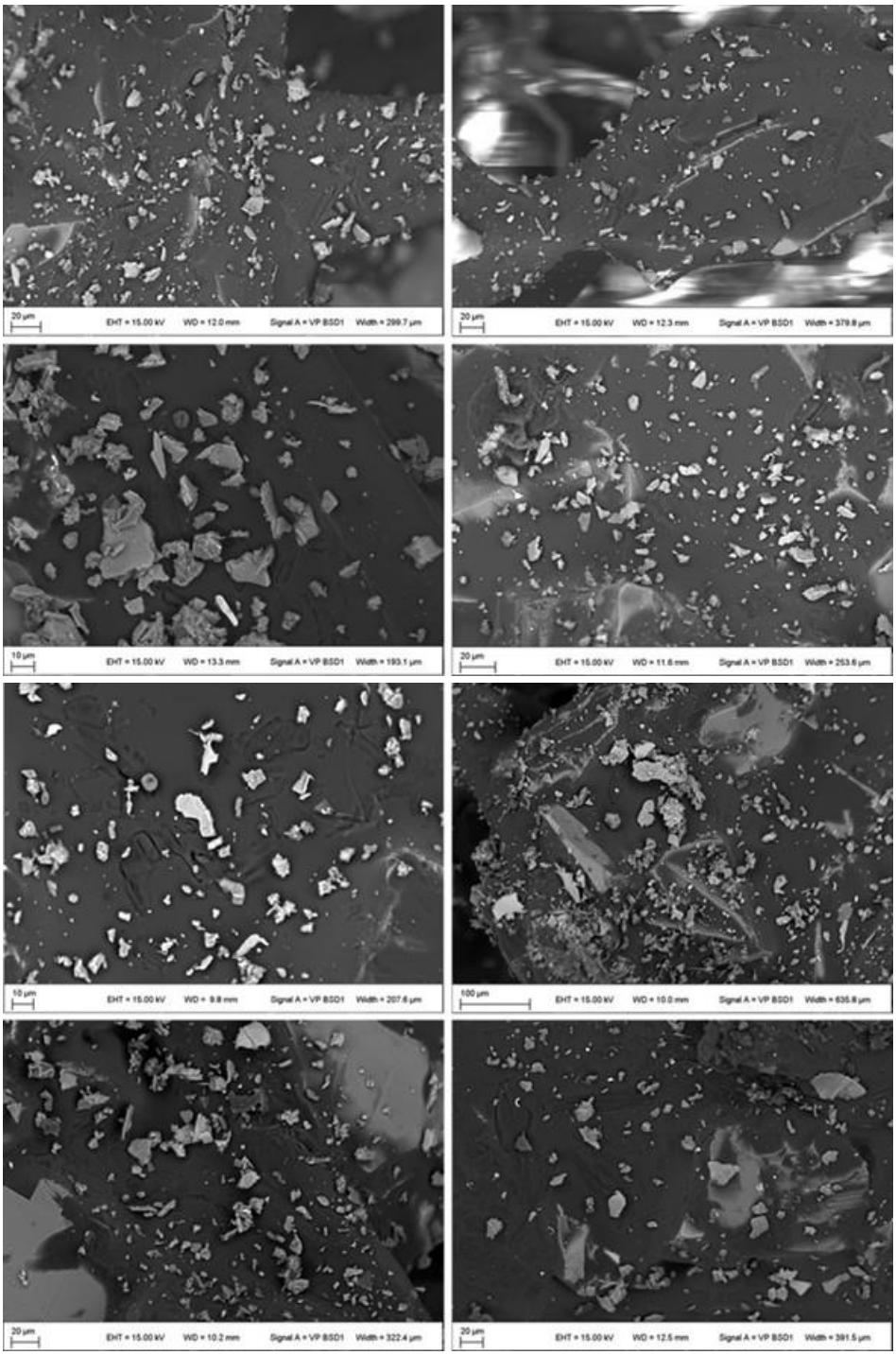

Figure 73. Images of dust on Scotch-brite™ pads used to sample the tops of Maine Yankee Canisters.

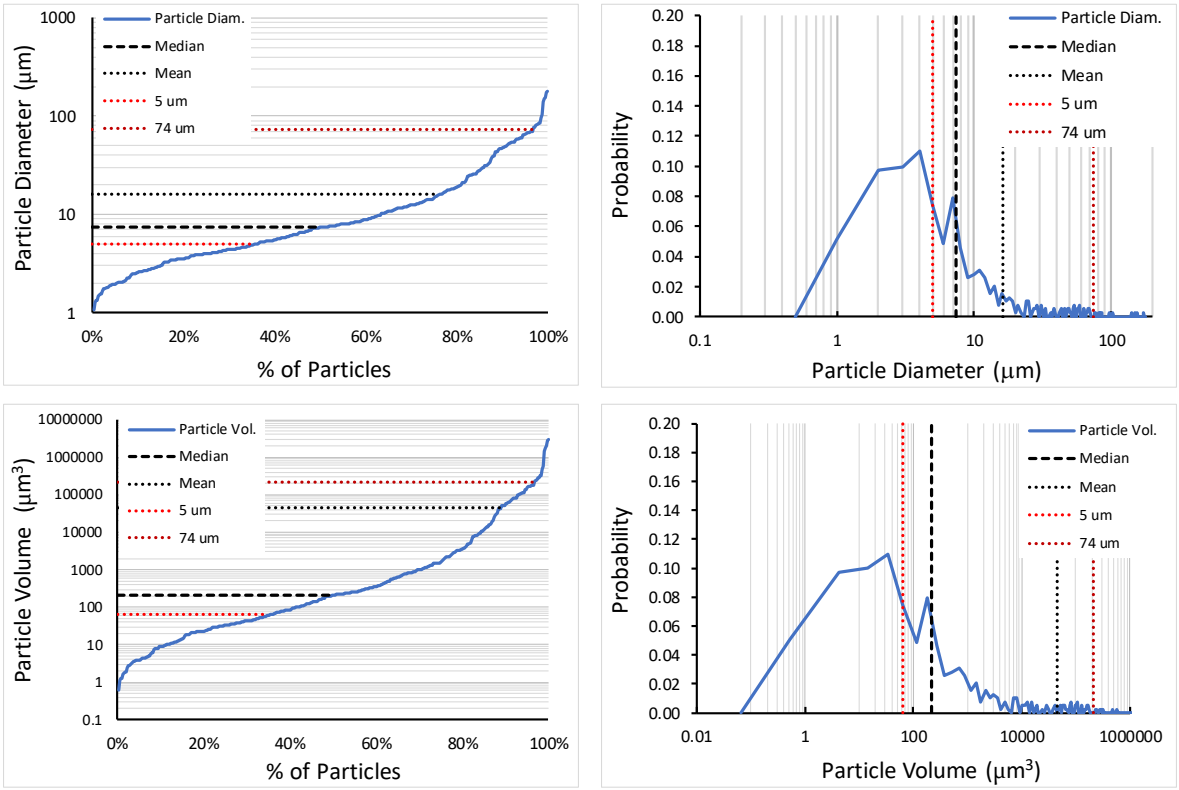

Figure 74. Particle size distributions for the Maine Yankee dust samples. Both particle diameter distributions (upper) and particle volume distributions (lower) are provided.

2.2.4.5 Summary and Conclusions of Inert Dust Sizes

The following are general observations from the SEM images of the dust collected from the four ISFSIs. It should be remembered that the measured dust distributions are biased towards finer grains; larger grains were preferentially lost during the sampling process.

Calvert Cliffs

- 10 o'clock position on a horizontal canister
  - Pollen in the 20-80 micron range is very abundant.
  - Mineral particles on Scotch-brite™ pads were mostly in the 1-5 µm range, but a few particles were as large as 20 µm.

Hope Creek

- Side of vertical canister
  - Dust and salt loads were very light
  - Mineral particles were sparse, mostly in the 5-10 µm range, but some finer and in some the 20-30 µm range
- Top of vertical canister
  - Dust and salt loads much heavier than the canister sides
  - Mineral particles in the 2-10 µm range common, frequently up to 20-30 µm.

Diablo Canyon

- Side of vertical canister
  - Dust and salt loads very light
  - Mineral particles observed: Some smaller particles, but many (most?) in the 10-40 µm range
- Top of vertical canister
  - Dust and salt loads were much heavier than on the canister sides
  - Mineral particles sizes varied: grains in the 10-30 µm range abundant, but in some samples, mostly 2-10 µm grains.

Maine Yankee

- Top of vertical canister
  - Large grains fell off the Scotch-brite™ during transport, but were retained and analyzed (suggesting that Scotch-brite™ samples from other sites may have also lost large grains)
  - Large loose grains:
    - Dominated by organic matter (plant fibers, stellate trichomes) up to several hundred µm in the long dimension
    - Mineral grains in the range of 50-100 um, with mica flakes up to 150-200 microns
  - Material retained on Scotch-brite™ pads: Mostly in the 2-10 µm range. Some coarser particles to 20 µm.

Measured particle size distributions are summarized in Figure 75. Given the caveat that the distributions are largely based on Scotch-brite™ samples and are likely biased towards smaller dust particles, the distributions for the four sites do not differ greatly. In all cases, the measured particles are mostly in the 1-10 µm range, with a tail extending to larger particle sizes. Maximum mineral particle sizes were in the 100-200 um range, although it is clear that at Maine Yankee, much larger particles of organic matter—plant fibers up to several hundred microns in length—were common on the top of the canister.

Using these distributions, it is evident that small dust particles, <5 µm in size, dominate in terms of the particle numbers on canister surfaces. For experimental evaluation of the effects of small mineral grains, SNL has chosen to use 5 µm Min-U-Sil®, a well-sorted, high-purity crushed quartz, as an analog for the small size fraction of detrital grains on canister surfaces. For testing to evaluate potential dust crevicing, 200 mesh (74 µm) Sil-Co-Sil® quartz will be used. The effects of each size fraction will be evaluated

individually, and a mix of both sizes with be used to examine coupled effects. The planned test matrix is given in Table 22. Exposures will be carried out at 75% RH and 50 for up to 2 years.

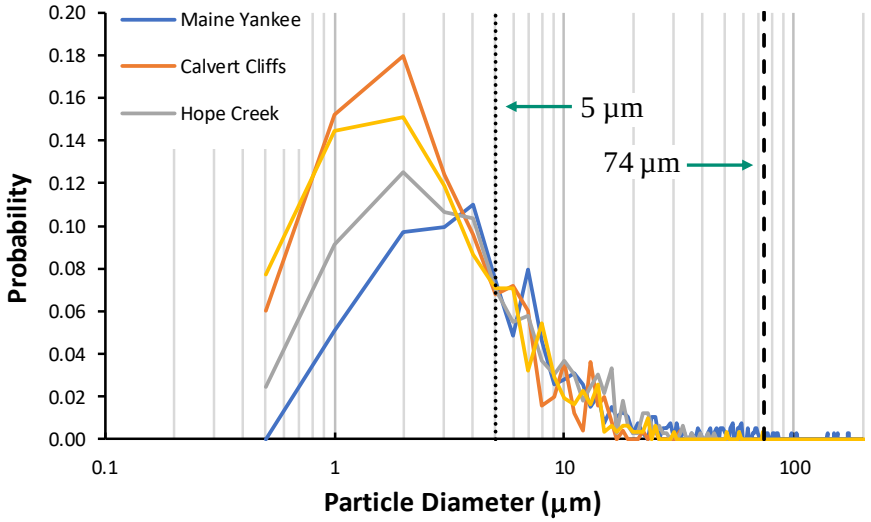

Figure 75. Summary of the particle sizes of the dust on the SNF canisters at Maine Yankee, Calvert Cliffs, Hope Creek and Diablo Canyon.

Table 22. Testing matrix for inert dust exposure experiments

Coupon Size, in.	Total	5 µm	74 µm	5-74 Mix	No Dust	1 mo.	6 mo.	12 mo.	24 mo.	Notes
8x8	6	2	2	1	1	0	0	1	1	* Pull *no dust* and *mix* at 24 months
4x4	18	5	5	5	3	0	2	2	2	*Pull *no dust* at final three sampling intervals
2x2	67	21	21	21	4	5	5	6	6	*Pull one *no dust* per time interval
2x1	38	11	11	11	5	3	3	3	3	*Pull one *no dust* per time interval and two at 24 months
2x1 (304L)	31	9	9	9	4	2	2	3	3	*Pull one *no dust* per time interval
Total	**160**	**48**	**48**	**47**	**17**	**10**	**11**	**12**	**15**	

2.3 $MgCl_2$ Brine Stability

The stability of $MgCl_2$ brines plays a significant role in the risk of CISCC to occur on SNF canisters. This is true for several reasons, 1) $MgCl_2$ salts are among the first salts to deliquesce on the surface of SNF canisters as the temperature of the canister decreases and the RH increases, 2) the presence of $MgCl_2$ brines on SS has been demonstrated to have anomalous effects on the electrochemistry and corrosion (See Section 3), and 3) $MgCl_2$ brines have been shown to be unstable at elevated temperatures leading to the formation of less deliquescent phases and subsequent brine dry out. These three factors are important to develop a predictive understanding when a corrosive brine exists on an SNF canister surface as a function of temperature and relative humidity, and the resulting impact on corrosion, pitting, and cracking.

In FY20, work continued to evaluate the stability of $MgCl_2$ brines as a function of environment. This was performed through a series of experimental and modeling approaches. First, investigation of the stability of $MgCl_2$ droplets on an inert substrate aged in an environmental chamber with continuous airflow to monitor the conversion to Mg-carbonate and Mg-hydroxychloride phases was carried out (see Section 2.3.1). Efforts were also continued to improve thermodynamic geochemical modeling of the Mg-OH-Cl-H_2O system as a function of temperature (see Section 2.3.2). Lastly, synthesis and in-depth characterization was performed on various phases predicted from the geochemical modeling, including the 3-1-8 magnesium hydroxychloride phase, in order to inform potential effects on corrosion and risk of CISCC (see Section 2.3.3).

2.3.1 $MgCl_2$ degassing experiments (40°C, 48% RH, 9.0 L airflow)

Similar to investigations performed in FY17 - FY19, SNL continued evaluating the stability of magnesium chloride brines in FY20. As demonstrated previously, it is essential to understand the stability of $MgCl_2$ brines in order to predict when a corrosive environment can exist on the SNF canister surface (with respect to time as it cools) and its impact on corrosion, pitting, and cracking. Bischofite ($MgCl_2 \bullet 6H_2O$) is the first sea-salt aerosol to deliquesce as the canister surface temperature decreases (and a subsequent increase in RH is observed). In these experiments, $MgCl_2$ was inkjet printed (Schindelholz and Kelly, 2010b) onto an inert substrate (25 mm diameter silicon wafer) (Figure 76), and placed in an environmentally controlled chamber (T and RH) with continuous airflow, generated with a Zero Air Generating system that removes all contaminants (acid gases, organics) from the air stream, and periodically sampled. Importantly, CO_2 is not removed from the air by the Zero Air Generating system. Previous analyses of $MgCl_2$ degassing experiments were performed at two conditions, first at 48 °C, 40 % RH (Bryan and Schindelholz, 2018b; Schaller et al., 2019; Schindelholz et al., 2017b), representing conditions close to the highest temperatures where bischofite could deliquesce in a real canister environment, and second, at 80 °C, 35 % RH, representing accelerated conditions at which significant Cl^- degassing is likely to occur (Schaller et al., 2019). Each of these experiments were performed with 2 L/min continuous airflow. In the canister relevant conditions (48 °C, 40 % RH), minimal conversion was observed over the 10-week experimental duration, where the calculated chloride loss was ~4% in roughly 4 weeks and ~6% in 10 weeks. SEM/EDS analyses demonstrated the formation of Mg-CO_3 bearing species, which was preferential to smaller droplets (where the surface area to volume ratio is largest) – however X-ray diffraction (XRD) analyses only showed the presence of bischofite (XRD is not sensitive to minor phase contributions). In efforts to observe a greater degree of conversion, the testing conditions in FY18 were accelerated (80 °C, 35 %, 2 L/min). Under these conditions, significantly more Cl^- was lost over the 8-week experiment. Where 10-20% Cl^- was lost within 4 weeks and upwards of 40% was lost during the entire 8 weeks. XRD experiments demonstrated the formation of a high temperature magnesium hydroxychloride phase (2-1-4 phase) under these conditions, confirming predictive stabilities in the geochemical modeling and agreeing with other environmental studies in which this 2-1-4 phase was observed under similar conditions (Bryan and Schindelholz, 2018b; Schaller et al., 2019).

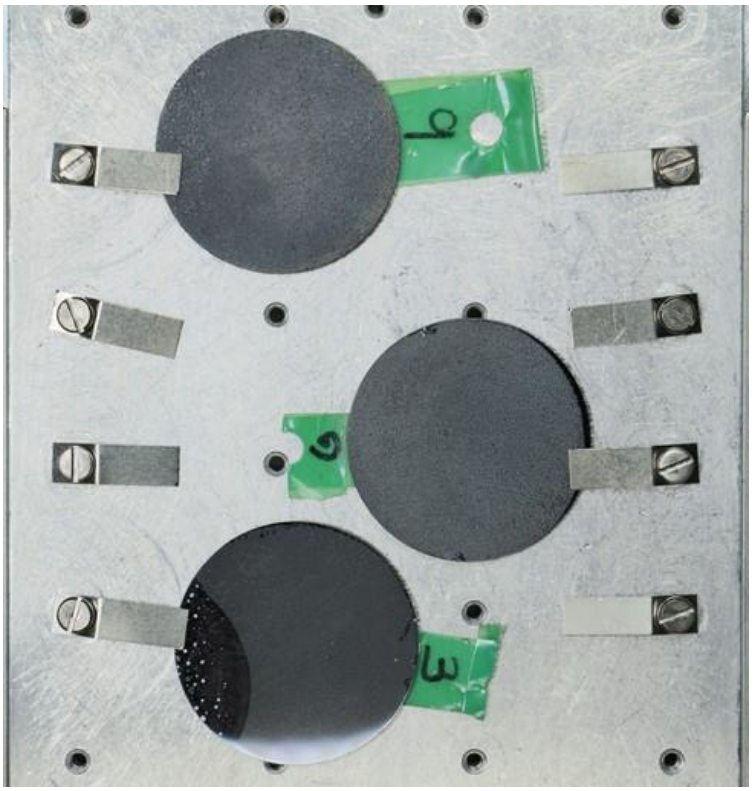

Figure 76. Image of silicon wafer with $MgCl_2$ deposition after 4 weeks of exposure (sample 3), 8 weeks (samples 6), and 16 weeks (sample 9).

2.3.1.1 Bulk chemistry and evolution

In FY20, a follow-on experiment for degassing analysis was performed in which the stability of $MgCl_2$ brines at canister relevant $MgCl_2$ deliquescent conditions (48 °C, 40 % RH) were investigated. However, in these exposures, the air flow rate was increased from 2 L/min to 9 L/min and exposed for a longer time period (16 weeks). In order to increase the airflow, the sample chamber was modified, as shown in Figure 77. Under these conditions a greater degree of conversion is anticipated as compared to that observed in the FY17/18 studies (Bryan and Schindelholz, 2018b; Schindelholz et al., 2017b). In the FY20 exposures a greater consistency with maintaining canister relevant exposures was also employed, in contrast to the accelerated conditions in the FY18/19 analysis (Bryan and Schindelholz, 2018b; Schaller et al., 2019). In addition, the instrumental capability to measure dissolved inorganic carbon (DIC) directly was recently added at SNL and therefore the amount of carbonate adsorbed by the sample was quantifiable in the FY20 exposures.

Figure 77. Photos of the modified environmental chamber in order to increase the airflow rate to 9 L/min.

The measured bulk compositions of each sample following environmental exposure are shown in Figure 78. As seen previously, there appears to be variation in the deposition of $MgCl_2$ via ink jet printing, as $MgCl_2$ notoriously clogs the printer heads (Bryan and Schindelholz, 2018b; Schindelholz et al., 2017b). For this analysis, the variation in the amount of $MgCl_2$ deposited does not affect the study, as we are investigating (i) the change in the Cl:Mg ratio, (ii) changes in the mineral assemblages, and (iii) the degree of carbonation. Under these conditions, according to geochemical modeling and previous experimental evidence (Altmaier et al., 2003; Bryan and Schindelholz, 2018b; Pannach et al., 2017; Schaller et al., 2019; Schindelholz et al., 2017b), the expected magnesium hydroxychloride phase would be the 3-1-8 phase ($2Mg_2(OH)_3Cl•4H_2O$), as defined by the following reaction in which HCl degasses from a deliquesced $MgCl_2$ brine:

$$4Mg^{2+}_{(aq)} + 8Cl^{-}_{(aq)} + 6H_2O \rightarrow 2Mg_2(OH)_3Cl : 4H_2O_{(s)} + 6HCl_{(g)}$$

While a greater degree of conversion was expected as compared to the analyses in FY17, due to the higher air exchange rate and an increased duration of exposure (16 weeks), the amount of Cl^- degassed appeared roughly the same (Figure 79). Potential reasoning for why this occurred will be discussed in Section 2.3.1.3. Under these conditions, the maximum $\%Cl^-$ loss increased over time, suggesting continuous degassing of HCl over the course of the experiment. After 16 weeks, about 12% of the Cl^- was lost. While Cl^- was lost, the Cl:Mg ratio did not suggest that conversion to the 3-1-8 phase was as wide spread as shown in Figure 80, where the Cl:Mg ratios of the samples are compared with expected ratios in bischofite and the 3-1-8 phase, the trend indicates that Cl:Mg ratio steadily decreased.

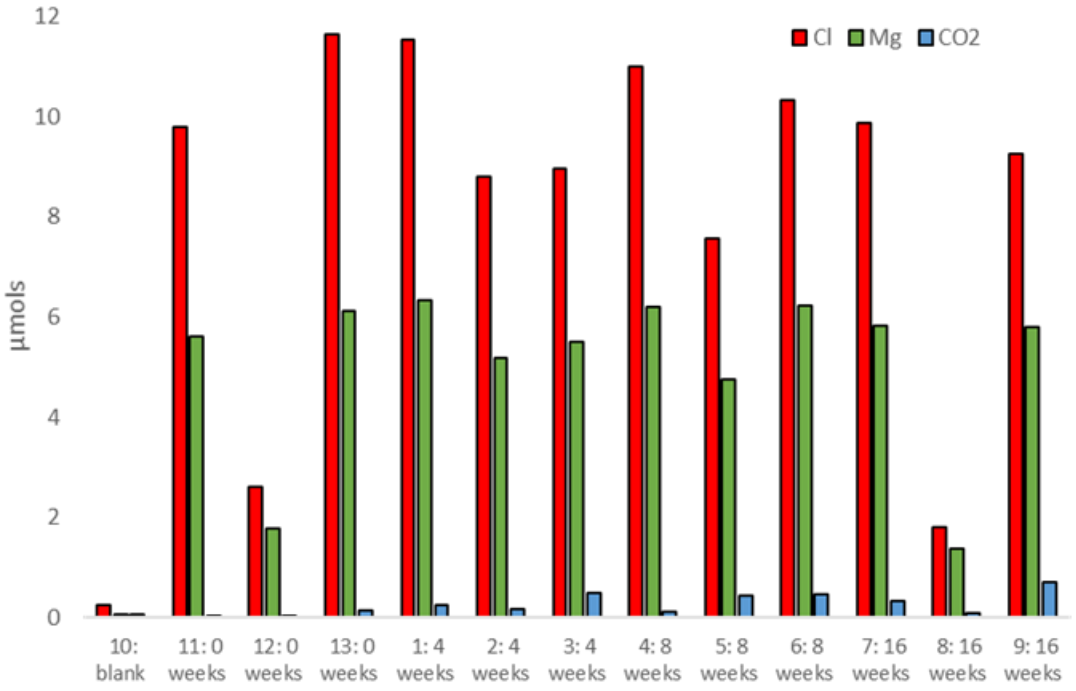

Figure 78. Composition of the salt after environmental exposure.

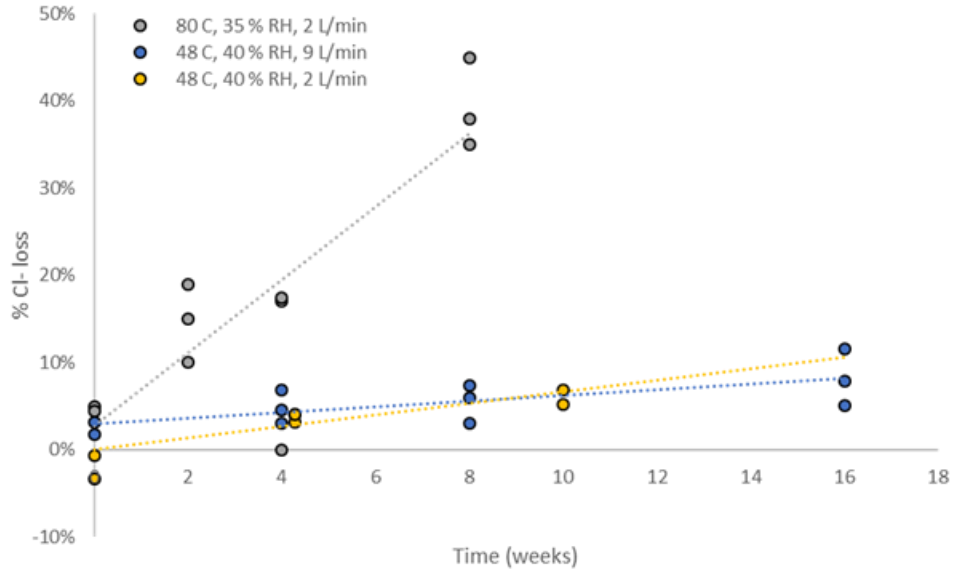

Figure 79. Estimated percent chloride lost under various conditions. Where blue represent work in this report, high airflow rate and canister relevant conditions (48 ºC, 40 % RH, 9 L/min), gray represents the high temperature environment (80 ºC, 35 % RH, 2 L/min), and yellow data points are low airflow rate and canister relevant conditions (48 ºC, 40 % RH, 2 L/min)

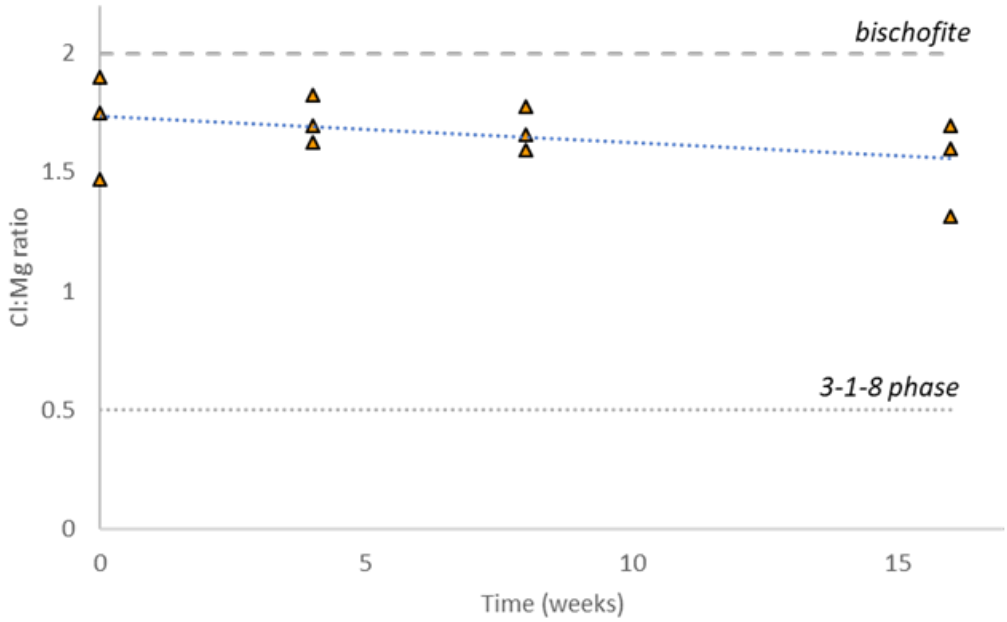

Figure 80. Cl:Mg ratio as a function of time shown with the expected ratios of bischofite along with the 3-1-8 magnesium hydroxychloride phase

As mentioned previously, in FY20 SNL added the capability to directly measure DIC from solution. This allows quantification of the amount of carbonation that occurs over time in the $MgCl_2$ droplets. Shown in Figure 81, a steady increase in the amount of carbonate over time was observed and is shown normalized to the amount of Mg present. While variation was observed, generally, the carbonation increased with more environmental exposure, where the 16-week samples resulted in ~0.1 μmol carbonate/μmol Mg. Large variation in the degree of conversion to carbonate has been observed in every experiment, not just chemically, but also by SEM/EDS and other methods (see Section 2.3.1.2). Possibly, conversion depends on where in the exposure chamber the sample is located, or the sample orientation, both of which may affect the amount of airflow past the sample. Although evidence supported the change in the bulk chemistry of the droplet over time to more carbonate-rich, the change was not observed by XRD (Figure 82); the carbonate any/or hydroxychloride phase that formed may be poorly crystalline. The XRD patterns as a function of time only show bischofite presence. Due to the differences in the deliquescence RH between bischofite and the predicted deliquescence RH for the 3-1-8 phase or for a carbonate phase, allowing the sample to deliquesce allowed for suppression of the signal from crystalline bischofite in the XRD pattern, however when this was performed the XRD pattern displayed no distinct features – suggesting no crystalline phases could be identified. This is consistent with findings from (2017b), where the chemical analysis suggested Cl^- degassing; however, only in one sample was the evolved 3-1-8 phase identified.

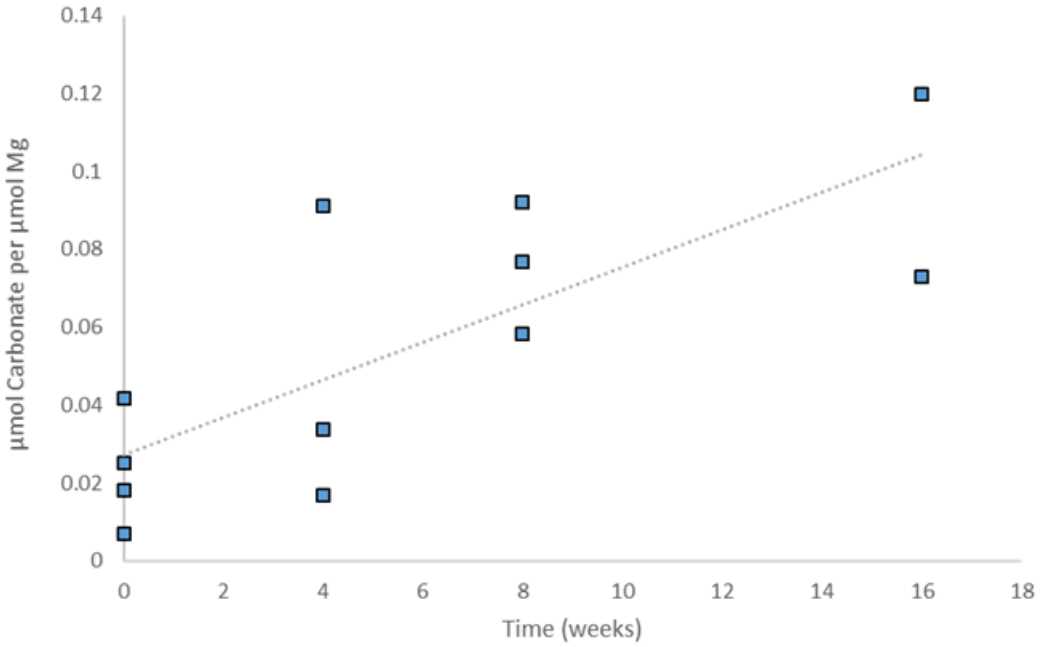

Figure 81. Carbonate gained over time normalized to the amount of Mg deposited.

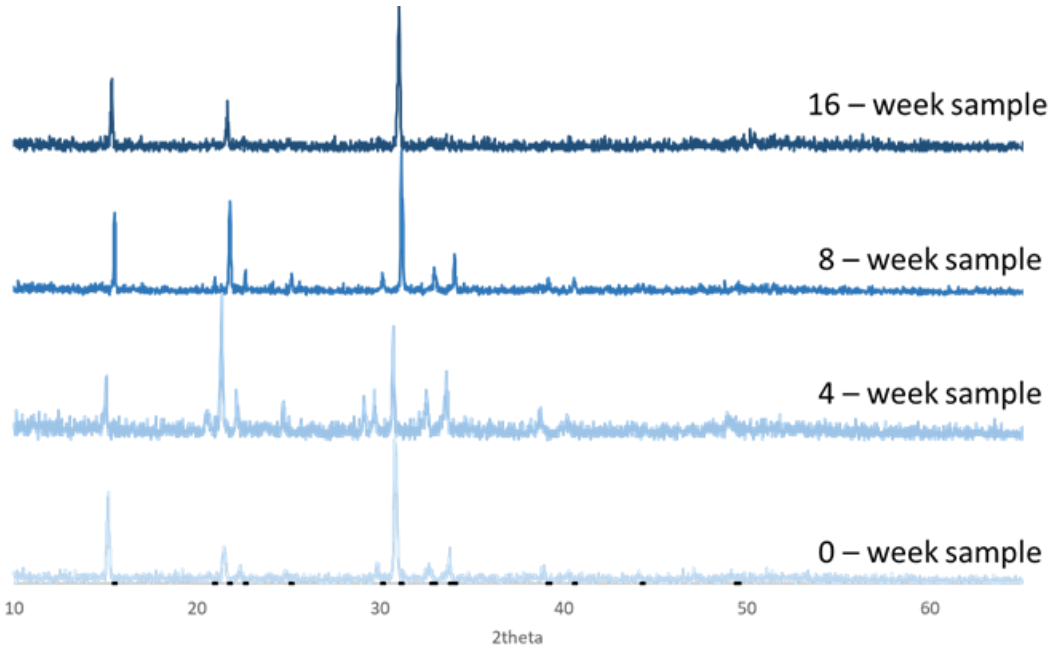

Figure 82. XRD analysis of dry 0-week, 4-week, 8-week, and 16-week samples compared with the primary peaks of bischofite.

2.3.1.2 Observed Droplet Evolution

While IC and XRD can provide bulk information quantifying the degree of Cl^- loss and carbonate adsorbed, samples were also analyzed with SEM, EDS, Raman, Fourier transfer infrared spectroscopy (FTIR), and time of flight secondary ionization mass spectrometry (ToF-SIMS) to evaluate the relationship between the particle morphology and size to the resulting degree of conversion.

SEM images and EDS elemental mapping of the wafers demonstrate both carbonation and Cl^- degassing. Figure 83 shows the intensity of elemental contributions of Mg, C, O, and Cl on samples that were aged for 4, 8 and 16 weeks. As evidence, most notably in the 8-weeks sample, smaller droplets displayed a higher signal for C and were associated with a decreased Cl signal. Additionally, smaller droplets, or the outer rings of droplets, appear to have a stronger O-contribution and a weaker Cl-contribution, this likely corresponds to the transition from $MgCl_2{:}6H_2O$ to carbonate, and possibly $Mg_2(OH)_3Cl{:}4H_2O$. These images illustrate how inconsistent the degree of conversion was—the 8-week sample showed a much greater degree of conversion than the 16-week sample.

To explore the relationship between drop size and degree of conversion, X-ray spot analyses was performed to qualitatively assess the Mg:Cl ratio as a function of droplet size, as previously done in (Bryan and Schindelholz, 2018b; Schaller et al., 2019). Consistent with previous observations, smaller droplets appeared to undergo more Cl-degassing and increased conversion to carbonate or hydroxychloride phases. Shown in Figure 84, are the Mg:Cl ratio as a function of droplet size and time compared to measurements made on bischofite and 3-1-8 phase. Though this is only a qualitative measurement, this plot demonstrates that the Mg:Cl ratio increases as droplet size decreases, and that the 16 weeks samples showed the greatest degree of Cl^- degassing in the smallest particles. Overall, the largest particles measured showed relatively no change in the Mg:Cl ratio. Note that the change in Mg/Cl ratio was much greater in the previous experiment—probably because the brine droplets were much smaller, allowing for greater conversion.

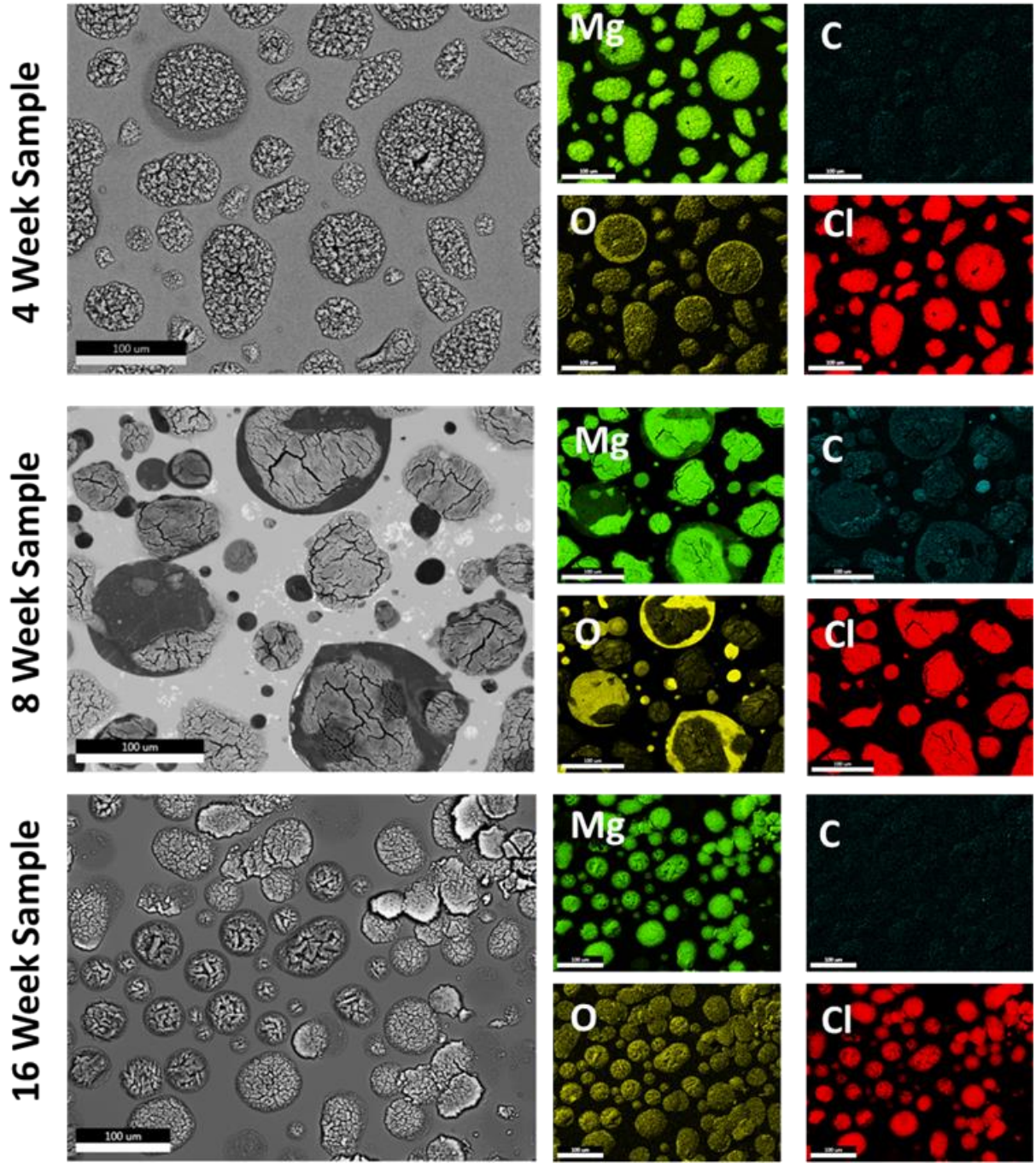

Figure 83. SEM and EDS maps of the $MgCl_2$ as a function of time (4, 8, and 16 weeks), showing the intensities of Mg, C, O, and Cl.

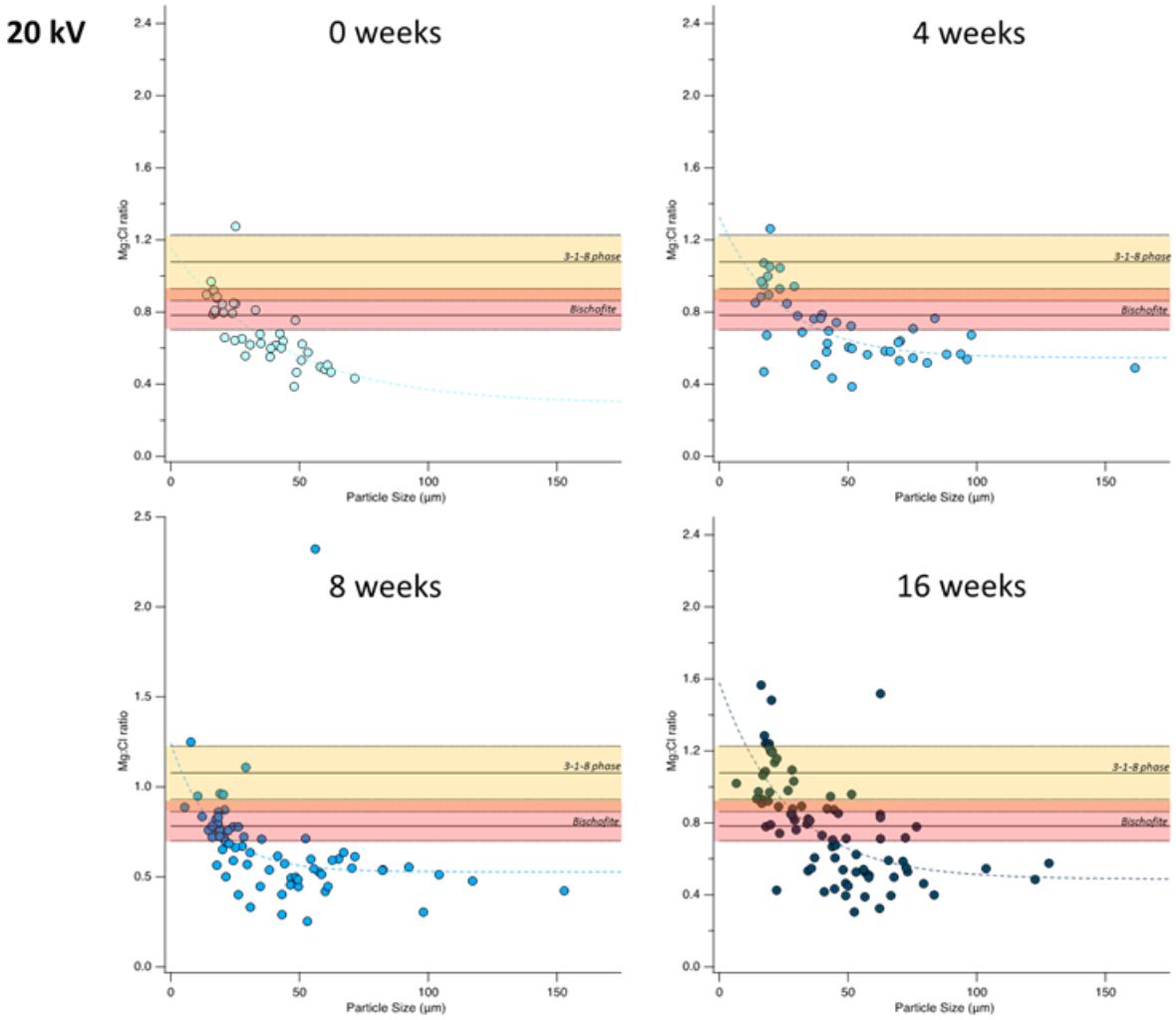

Figure 84. Qualitative assessment of the Mg:Cl ratio versus droplet size as a function of time (0 weeks, 4 weeks, 8 weeks, and 16 weeks) at 20 kV X-ray energy. These ratios were compared with measurements of bischofite ($MgCl_2 \cdot 6H_2O$) and the 3-1-8 magnesium hydroxychloride phase.

To further verify the conversion to Mg-hydroxychloride or Mg-carbonate phases, ToF-SIMS was performed. For ToF-SIMS analysis, as described previously (Schaller et al., 2019), the samples are bombarded with bismuth ions, which cause polyatomic fragments to spall off the surface for mass spectroscopic analysis (mass/charge). Like EDS mapping, quantitative information is very challenging to obtain using ToF-SIMS, however, qualitative differences in the intensities of specific polyatomic fragments can elucidate the presence of specific phases of interest. The relationships between i) $MgOH^+$ (red), and $MgCl^+$ (green), ii) $MgOH^+$ (red), $MgCl^+$ (green), $MgHCO_3$ (blue), and iii) $MgOH^+$ signal normalized to $MgCl^+$ signal as a function of time (4 weeks, 8 weeks, and 16 weeks) are provided in Figure 85. ToF-SIMS supports the understanding that smaller particles and particle edges convert more readily from $MgCl_2$ to Mg-hydroxychloride and Mg-carbonate species. This occurred more readily in samples that have been aged longer in the environmental chamber.

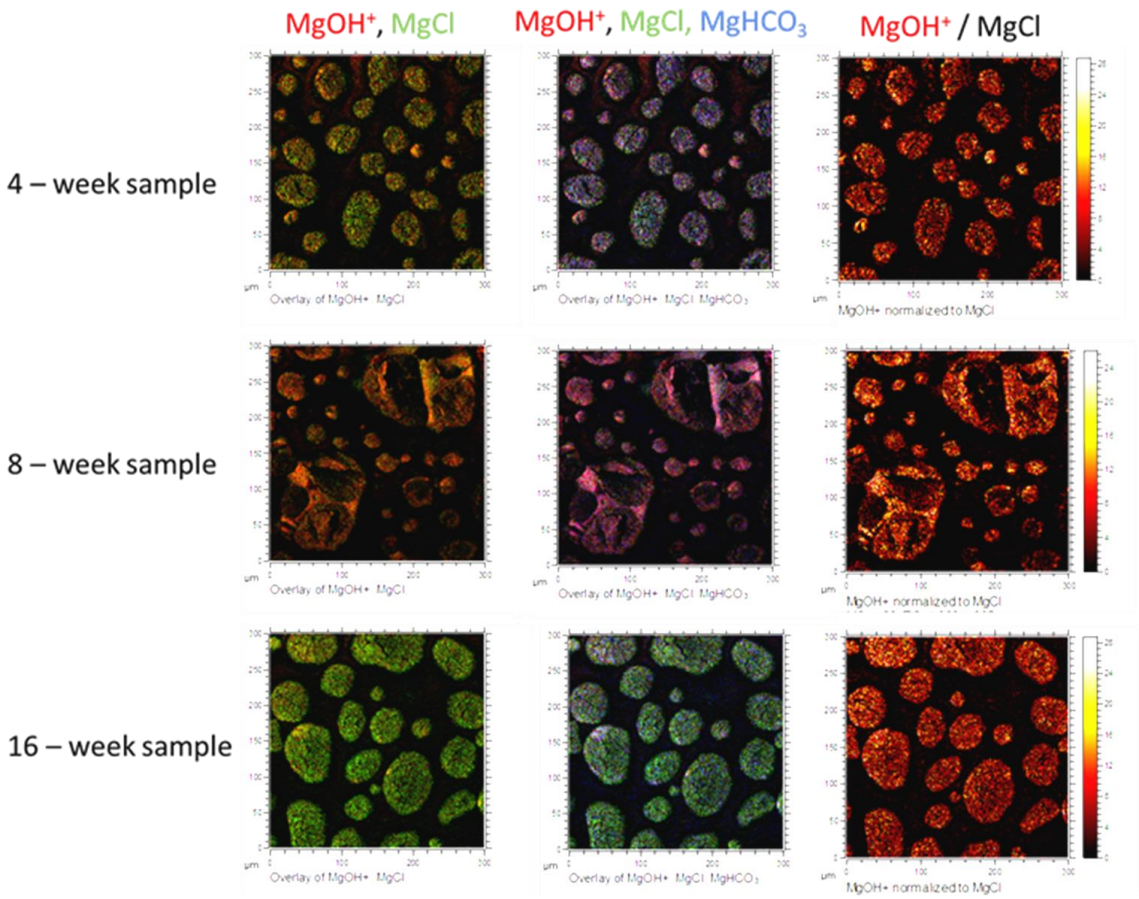

Figure 85. Time of flight secondary ionization mass spectroscopic analysis (TOF-SIMS) of 4 week, 8 week, and 16 week samples. The first column shows a color overlay of the signal achieved from the mass that corresponds to $MgOH^+$ (red) fragments and $MgCl^+$ (green) fragments. The second column is a color overlay of the signal achieved from the mass that corresponds to $MgOH^+$ (red) fragments, $MgCl^+$ (green) fragments, and $MgHCO_3^+$ (blue) fragments. The final column is the signal associated with $MgOH^+$ fragments normalized to the $MgCl^+$ intensity, where brighter pixels are associated with a greater $MgOH^+$ intensity.

FTIR and Raman analyses were also applied to identify evidence of conversion. The silicon wafer was moved to a special cell, designed and manufactured by SNL (Schaller et al., 2019), allowing the infrared beam to pass through a KBr window to the sample, sealed within a desiccated chamber. Movement of the sample from the plastic sample container to the IR cell was performed in a dry N_2 glove box. FTIR data were collected in reflectance mode, using silicon or stainless steel reflectance as the background. Experimental settings are described in Table 23.

Table 23. Summary of FTIR and Raman sampling details

Parameter	***FTIR***	***Raman***
Sampling	Reflection, reduced aperture, referenced to Si.	Laser: 532 nm @ 10 mW, 50x objective lens
Resolution	Resolution: 6 cm^{-1}	Integration Time: 2 sec
Co-added Scans	Co-added Scans: 16	Co-added Scans: 32

Data collected from the Si surfaces indicates primary features that suggest various states of hydration of $MgCl_2$. Other bands within the IR data do suggest the presence of Mg-O-Cl salts, in addition to carbonate species that are possibly identified as well. Specifically, literature suggests $MgCl_2$ with varying degrees of hydration have an $O\text{-}H_{MgCl2:XH2O}$ stretch that is red shifted compared to $O\text{-}H_{H2O}$ (3600 – 3000 cm^{-1}), and that shift increases with increased hydration number, in contrast the O-H bending mode remains unshifted (1630 cm^{-1}) (Shi et al., 2019). FTIR of magnesium oxide, Mg-O bands were noted to be at 945 cm^{-1} and 845 cm^{-1} (considered to be overtones), with the main band at 473 cm^{-1} (Hanna, 1965), while $MgOH_2$ (brucite) analysis showed bands at 1419 cm^{-1} and 1481 cm^{-1}, which were assigned to Mg-OH (Hofmeister and Bowey, 2006). In a study of magnesium hydroxide chloride hydrate, bands at 1157 cm^{-1} and 1439 cm^{-1} were tentatively assigned to the association of water with chloride ion (Chen et al., 2011).

The FTIR reflectance data is shown in Figure 86, for samples from 0 weeks to 16 weeks. Similarities and differences are evident, where consistent bands are 3650 cm^{-1} and 3000 cm^{-1} (consistent with hydrated salts), the feature between 2500-2000 cm^{-1}, and a band near 1630 cm^{-1} (which suggest a 4 or 6 hydrated Mg-salt (Shi et al., 2019). The observed peak around 1606 cm^{-1} in wafer 8 (16-weeks) could be associated with a carbonate species.

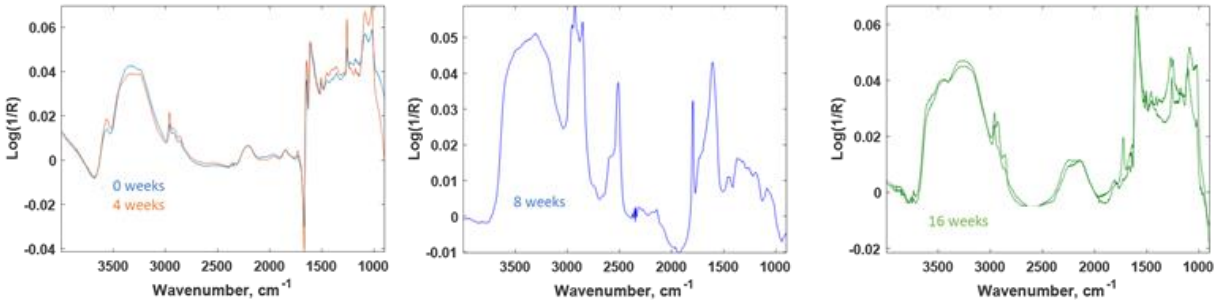

Figure 86. FTIR reflectance of $MgCl_2$ droplets on silicon from 0 to 16 weeks.

Raman analyses of $MgCl_2$ hydrates identifies doublet peaks for the six and eight H_2O hydrates between ~3500 cm^{-1} and 3200cm^{-1}, with stronger singlet peaks with smaller shoulder for the single, two, four and twelve H_2O hydrates (Shi et al., 2019). Raman O-H bending modes are variable in location, with bands between 1588 cm^{-1} and 1632 cm^{-1}. Raman analyses of brucite ($MgOH_2$) indicated four primary bands: 3652 cm^{-1} (O-H symmetric vibration), 728 cm^{-1}, 279 cm^{-1}, and 443 cm^{-1} (Duffy et al., 1995; Katona et al., 2020b). Raman spectroscopic studies of magnesium hydroxychloride phases identified bands in both $Mg_2(OH)_3Cl{\bullet}4H_2O$ (3-1-8 phase) and $Mg_3(OH)_5Cl{\bullet}\ 4H_2O$ (5-1-8 phase) forms (Dorrepaal and Gowen, 2018b). Bands at 3639 cm^{-1} and 3657 cm^{-1} were due to the symmetric O-H stretch, with a broader doublet water band was observed between 3511 cm^{-1} and 3324 cm^{-1}, for the 3-1-8 phase, while 3608 cm^{-1} and 3691 cm^{-1} were assigned to 5-1-8 phase (Kanesaka and Aoyama, 2001). Water bands associated with 5-1-8 phase were noted to be more of a single peak between 3500 $cm^{-1}$and 3300 cm^{-1}. Distinct bands for 3-1-8 phase are also noted at 593 cm^{-1} (assignment not known), 451 cm^{-1} (Mg-O) and 150 cm^{-1} (Mg-O).

Raman data collected from the $MgCl_2$ salts on Si wafers are shown in Figure 87. The large narrow band at 532 cm^{-1} is due to the Si-Si stretch of the Silicon wafer background. The spectra for 0-weeks and 4-weeks are qualitatively the same, suggesting minimal conversion had occurred in the first 4 weeks. Two spectra were collected from the 8-week and 16-week samples. In both the 8-week and 16-week samples, the O-H stretch peak (~ 3500 cm^{-1}) has a distinct shoulder around 3600 cm^{-1}. This could be indicative of the presence of a magnesium hydroxychloride phase or of brucite. However, in this context it would be unlikely for $MgCl_2$ to degas Cl^- entirely to form brucite, therefore the presence of this is likely either the phase 3 or phase 5 magnesium hydroxychloride. A few new bands were noted as well, at ~970cm^{-1} and ~310cm^{-1}. While the band at ~970 cm^{-1} is consistent with the fundamental perchlorate stretch (Crocella et al., 2017), this is highly unlikely. Additionally, the band at 310 cm^{-1} could not be correlated with any species. Therefore, the bands at 970 cm^{-1} and 310 cm^{-1} could not be assigned.

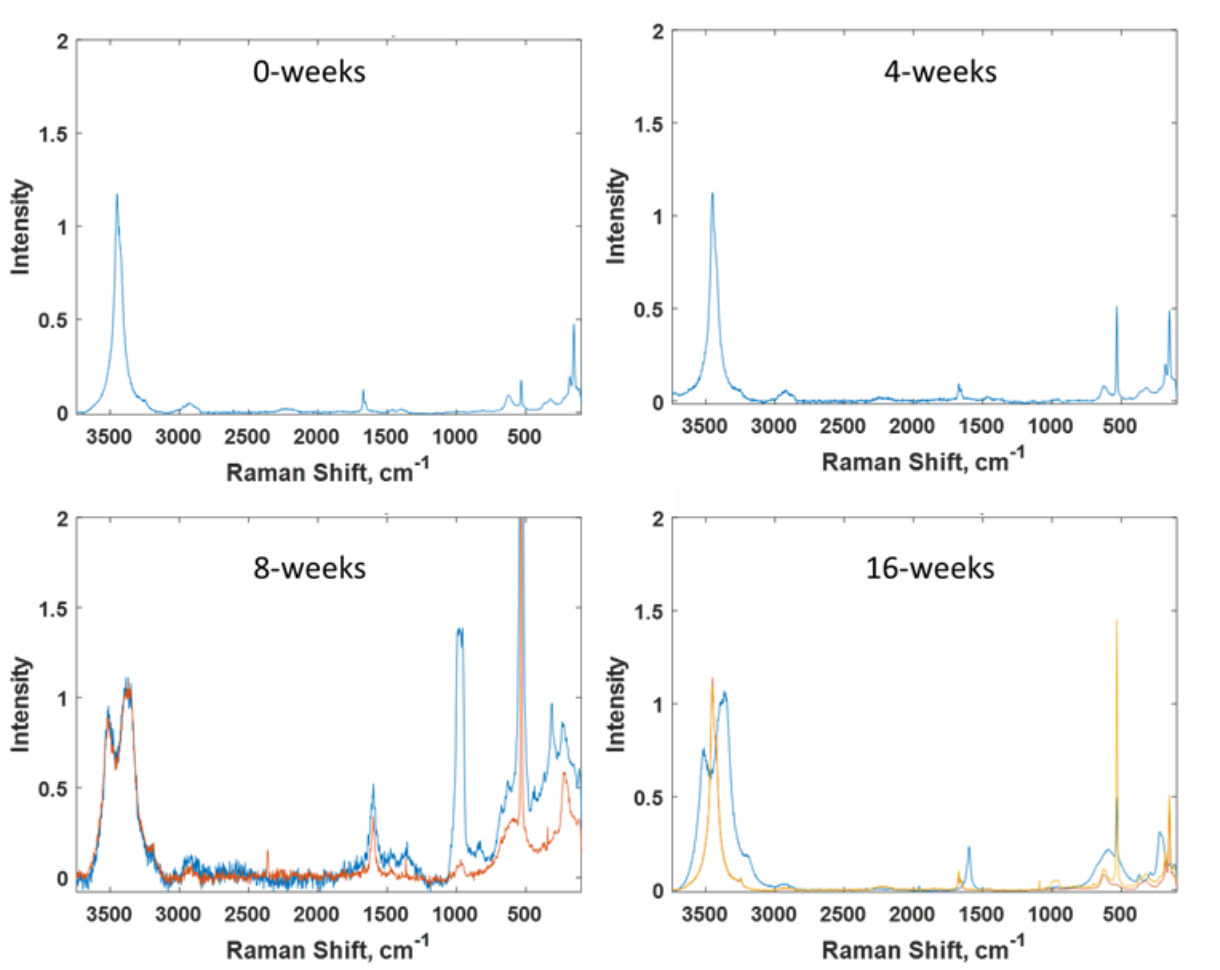

Figure 87. Raman spectra of $MgCl_2$ droplets on silicon from 0 to 16 weeks.

2.3.1.3 Conclusions and FY21 work

The bulk chemical data along droplet analyses demonstrate that some conversion had occurred over the course of the 16-week experiment. More conversion than previous studies had been expected due to the increased airflow, the salt loading and average particles sizes may have played a significant role in slowing down the Cl^- degassing and phase conversion. In addition, the equilibrium vapor pressure of $HCl_{(g)}$ above a chloride solution varies directly with pH, so if it is high above an acidic brine (like $MgCl_2$; pH ≈ 4.1), it is higher than it would be in the surrounding air. To add, the vapor pressure of $HCl_{(g)}$ increases with increasing temperature, due to the fact that $HCl_{(aq)}$ formation, via

$$H^+_{(aq)} + Cl^-_{(aq)} \xrightarrow{yields} HCl_{(aq)}$$

becomes more favorable as temperature increases—and $HCl_{(aq)}$ is the species that degasses. However, when $HCl_{(g)}$ degasses, the solution pH increases, causing the partial pressure of $HCl_{(g)}$ generated by the brine to decrease, and slowing degassing. Hence, it is self-limiting—unless a buffering reaction occurs to limit the rise in pH from $HCl_{(g)}$ degassing. The precipitation of carbonate or hydroxychloride is one such

reaction, and could act as a buffer to limit the change in the solution pH as demonstrated in Figure 88 (Katona et al., 2020a).

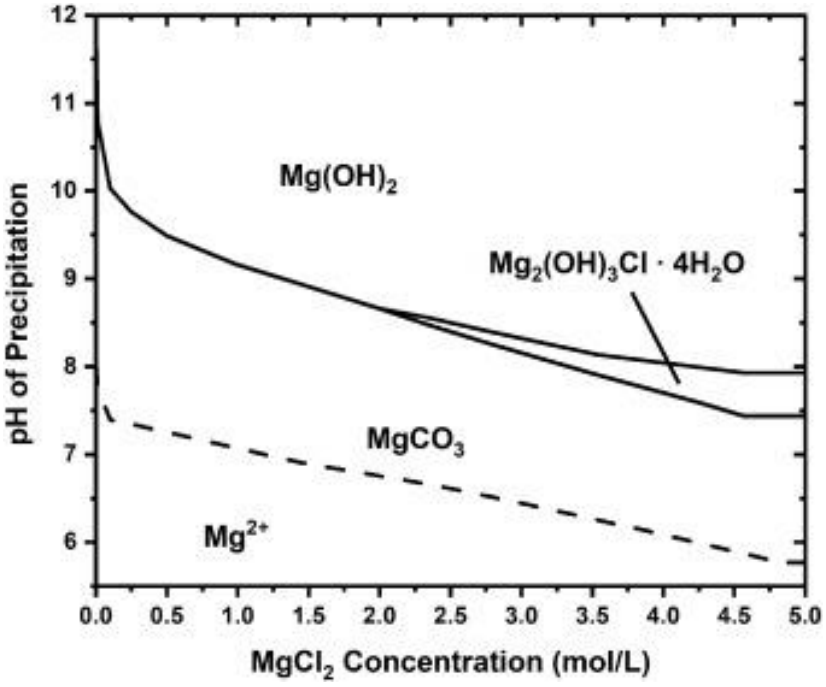

Figure 88. Stability diagram for dissolved H_2O-O_2−CO_2-$MgCl_2$ at 25 °C from Katona et. al 2020a

When comparing our results from FY20 to the previous experiments in FY17/18 and FY18/19, this phenomenon is consistent across these. In FY17/18, when $MgCl_2$ was coated on an inert substrate (silicon) and aged at 48 °C, 40% RH, 2 L/min airflow over 10 weeks resulted in partial conversion to carbonate and hydroxychloride. At that temperature, the degassing rate, assuming pH buffering by carbonate precipitation, would be less than 3 µg/m^3 of air passing through the chamber. With the low airflow in this experiment, it would take a very long time for complete conversion to carbonate phases via degassing of HCl. In the FY18/19 experiment, 80 °C and 35% RH, 2 L/min airflow over 8 weeks, degassing occurred rapidly and was fast enough to overshoot the carbonate equilibrium, which resulted in a raise in pH that was sufficiently high to precipitate hydroxychloride phase. In the experiment in FY20, we adjusted our FY17/18 conditions, in effort to observe more conversion; the temperature and RH remained the same (48 °C, 40% RH), but the airflow was increased 9 L/min airflow over 16 weeks. However, an increase in the percent of conversion was not observed—the overall amount of chloride lost was larger, however because the salt load in the FY 20 experiment was much higher (~200 ug/cm^2 $MgCl_2$:$6H_2O$ in the FY20 experiment, vs ~13 ug/cm^2 $MgCl_2$:$6H_2O$ in the FY17 experiment) this potentially impeded conversion. Also, the drop sizes were larger (~25 µm or larger) compared to the FY17 experiment (~10 µm), and smaller droplets, with a higher surface area to volume ratio, appear to convert more readily than larger droplets.

Tying these results back to the improving understanding of the risks of CISCC on SNF canisters, these experiments represent degassing at near-neutral conditions, where the brine present is buffered by the formation of carbonate or hydroxychloride precipitates which occur at the cathode. Therefore, this result suggests that the degree of $HCl_{(g)}$ is controlled, in part, by temperature as well as the precipitation of Mg-carbonate or Mg-hydroxychloride species.

In FY21, the experimental matrix for the $MgCl_2$ aged on inert substrate experiments will be expanded. The conversion of $MgCl_2$ droplets aged at 48 °C, 40% RH, 9 L/min airflow will be evaluated again, however, this time a lighter salt loading will be used, and the ink jet printing process adjusted to deposit smaller droplets. In this experiment, the hypothesis that the salt loading and droplet size play a role in the degassing of $HCl_{(g)}$ will be tested. In addition to carbonation and hydroxychloride precipitation via adsorption of CO_2 and degassing of $HCl_{(g)}$, other possible reactions can occur in field conditions. These include reactions with acid gases (i.e. H_2S and NO_x), which can also lead to the degassing of $HCl_{(g)}$ and conversion to additional Mg-phases. We will begin exploring the effects of these reactions via thermodynamic modeling as well as experimentally.

2.3.2 Geochemical modeling of the Mg-OH-Cl-H_2O system as a function of temperature

In order to better understand the stability of $MgCl_2$ brines on heated surfaces, continued modeling efforts from FY19 were further explored in FY20 to develop a detailed thermodynamic database for the Mg-OH-Cl-H_2O system from 25 °C to 150 °C (Schaller et al., 2019). In FY19, known literature values to estimate heat capacities (Mostafa et al., 1996) and thermodynamic values (ΔG_f^o S^o, and ΔH_f^o)(Chermak and Rimstidt, 1989) to derive LogK grids [0 °C – 25 °C – 60 °C – 100 °C – 150 °C] (Dick, 2019) for several Mg-chloride, Mg-hydroxide, and Mg-hydroxychloride phases for which little or no data is currently available were compiled. Using these derived values, thermodynamic modelling of the Mg-OH-Cl-H_2O system was carried out and calculated LogK values using experimental data from recent literature were refined (Pannach et al., 2017).

In order to improve the thermodynamic model to fit experimental data, in FY20 the Geochemist's Workbench (Bethke, 2008) and a thermodynamic database modified from the Yucca Mountain Project (YMP) were applied to:

- Adjust $LogK_{brucite}$ and $LogK_{bischofite}$ as a function of temperature using modeled and experimental literature values
- Adjust Pitzer interaction parameters to amend the shapes of the modeled solubility diagram
- Adjust temperature dependent Pitzer interaction parameters to account for any temperature dependent interactions.

2.3.2.1 Refinement of brucite and bischofite LogK values as a function of temperature

While there is limited data available on the Mg-hydroxychloride phases, there exists experimental data characterizing the solubility and equilibrium values of brucite and bischofite (Christov, 2009; Krumgalz, 2017; Lambert and Clever, 1992; Li et al., 2019; Linke, 1965; Travers and Nouvel, 1929). Therefore, the first step in FY20 was to further refine values for bischofite and brucite, to develop and further build the thermodynamic model for the Mg-hydroxychloride phases. A recent manuscript, within the last year, has been published on modeling of the thermodynamics of the $Mg(OH)_2$-$MgSO_4$-H_2O system using a similar approach to that applied at SNL in FY19 (Li et al., 2019; Schaller et al., 2019). In addition to modeling the Mg-sulfate system and its various phases, Li et al. also refined the LogK values of brucite using compiled literature data. From this data, and their model, the calculated $LogK_{brucite}$ values were refined to accurately fit experimental data from Lambert and Clever (1992), shown in Figure 89. For bischofite, Christov (2009) modeled the $MgCl_2$-H_2O system as a function of temperature and demonstrated an improved fit of experimental data from Linke (1965), Pannach et al. (2017), and Krumgalz (2017).

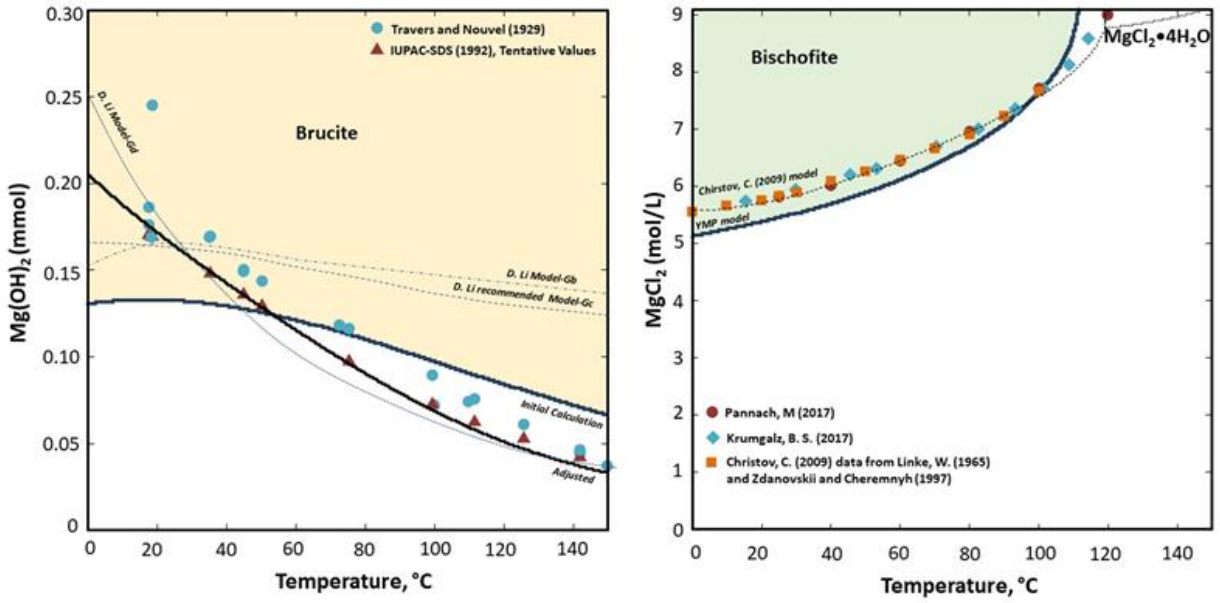

Figure 89. Brucite and bischofite solubility diagrams as a function of temperature shown with available experimental data (Christov, 2009; Krumgalz, 2017; Lambert and Clever, 1992; Li et al., 2019; Linke, 1965; Pannach et al., 2017; Travers and Nouvel, 1929).

The adjustments made to the $LogK_{brucite}$ and $LogK_{bischofite}$ are summarized in Figure 90 and Table 24. Overall the adjustments to brucite were minor (especially over the temperature range of interest), and converged at 60 °C. Likewise, for bischofite, the adjustment resulted in a small change to the LogK grid, however, one advantage of the adjusted LogK values is the improved phase prediction of the phase boundary between bischofite and $MgCl_2$:$4H_2O$ (Figure 89).

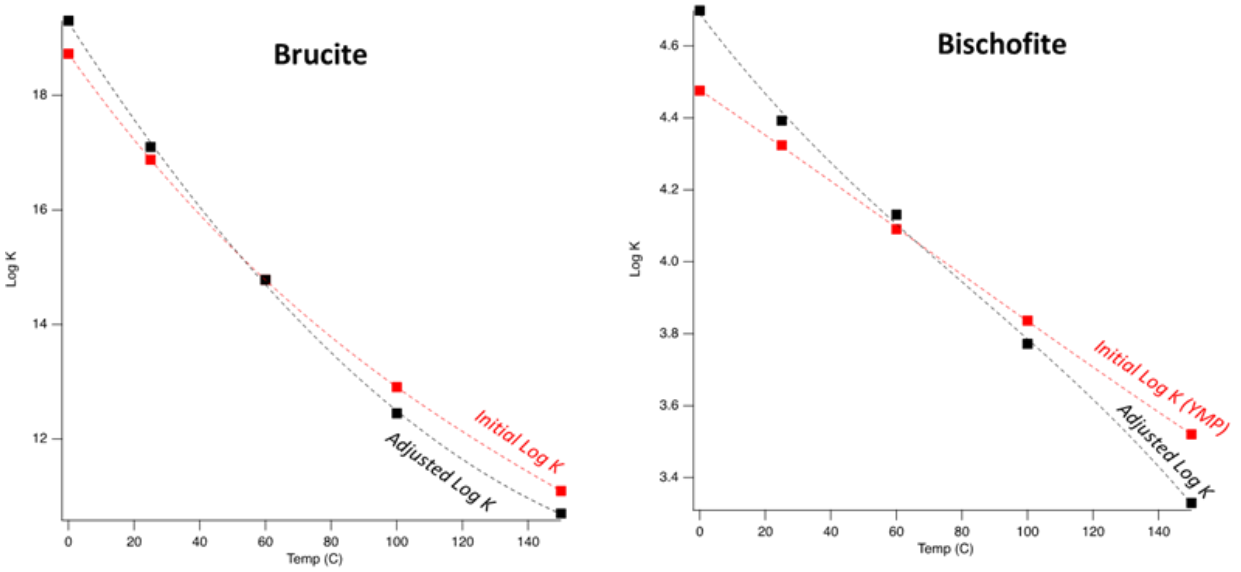

Figure 90. Initial calculated and adjusted LogK values for brucite and bischofite as a function of temperature.

Table 24. Adjusted $LogK_{brucite}$ and $LogK_{bischofite}$ as a function of temperature [0, 25, 40 , 60, 100 ºC].

Phase	0 °C	25 °C	40 °C	60 °C	100 °C
Brucite	19.30	17.10	14.78	12.45	10.30
Bischofite	4.70	4.39	4.13	3.77	3.33

2.3.2.2 Modification of Pitzer interaction parameters at 25 °C

From thermodynamic modeling of the Mg-Cl-OH-H_2O system in FY19, it was concluded that the modeling fit the experimental data relatively well at low temperatures. However, at higher temperatures the fit to the data was unattainable without significant changes to the calculated LogK values (Schaller et al., 2019). While it is expected to need adjustments of calculated LogK values at higher T, making significant modifications would result in significant changes to the calculated thermodynamic values (i.e. ΔG_f^o S^o, and ΔH_f^o) – which had fit closely to values found in the literature. Another adjustment that can be made to improve the fit is to modify the Pitzer interaction parameters. These Pitzer parameters are a semi-empirical model where linear combinations of a virial expansion of the excess Gibbs free energy are used to characterize interactions among ions and solvent, which become increasingly important in high ionic strength environments (Pitzer, 1973; Simoes et al., 2016). These parameters are typically used to describe doublet interactions (cation-anion, cation-cation, ion-neutral species), and triplet interactions (Bethke, 2008; Simoes et al., 2016). Briefly, these parameters can be summarized as:

- A^{φ} : Debye-Huckel coefficient for the osmotic coefficient.
- B^{φ}: Second virial coefficient for the osmotic coefficient
- $\beta^{(o)}$, $\beta^{(1)}$, $\beta^{(2)}$ and c^{φ}: Second virial coefficients representing short range binary interactions
- c^{ψ} : Third virial coefficient representing short range tertiary interaction

As the FY19 model was unable to fit the shape of the experimental solubility plot in the Mg-OH-Cl-H_2O system as a function of temperature, it is believed that the $MgOH^+$ — Cl^- cation-anion Pitzer interaction parameters needed adjustment. It is anticipated that the strength of the $MgOH^+$ — Cl^- interaction, will impact the overall solubility of the system as the [Cl^-] and pH increase.

The impact of $MgOH^+$ -- Cl^- ($\beta^{(2)}$) parameter

While the $\beta^{(o)}$ and $\beta^{(1)}$ Pitzer interaction parameters for the $MgOH^+$ — Cl^- are well-vetted values (SNL, 2007), the $\beta^{(2)}$ has remained unchanged, and therefore small adjustments to this value may improve the ability to model the Mg-OH-Cl-H_2O system. Figure 91 shows the impact of adjustment made to the $\beta^{(2)}$ parameter at 25 °C.

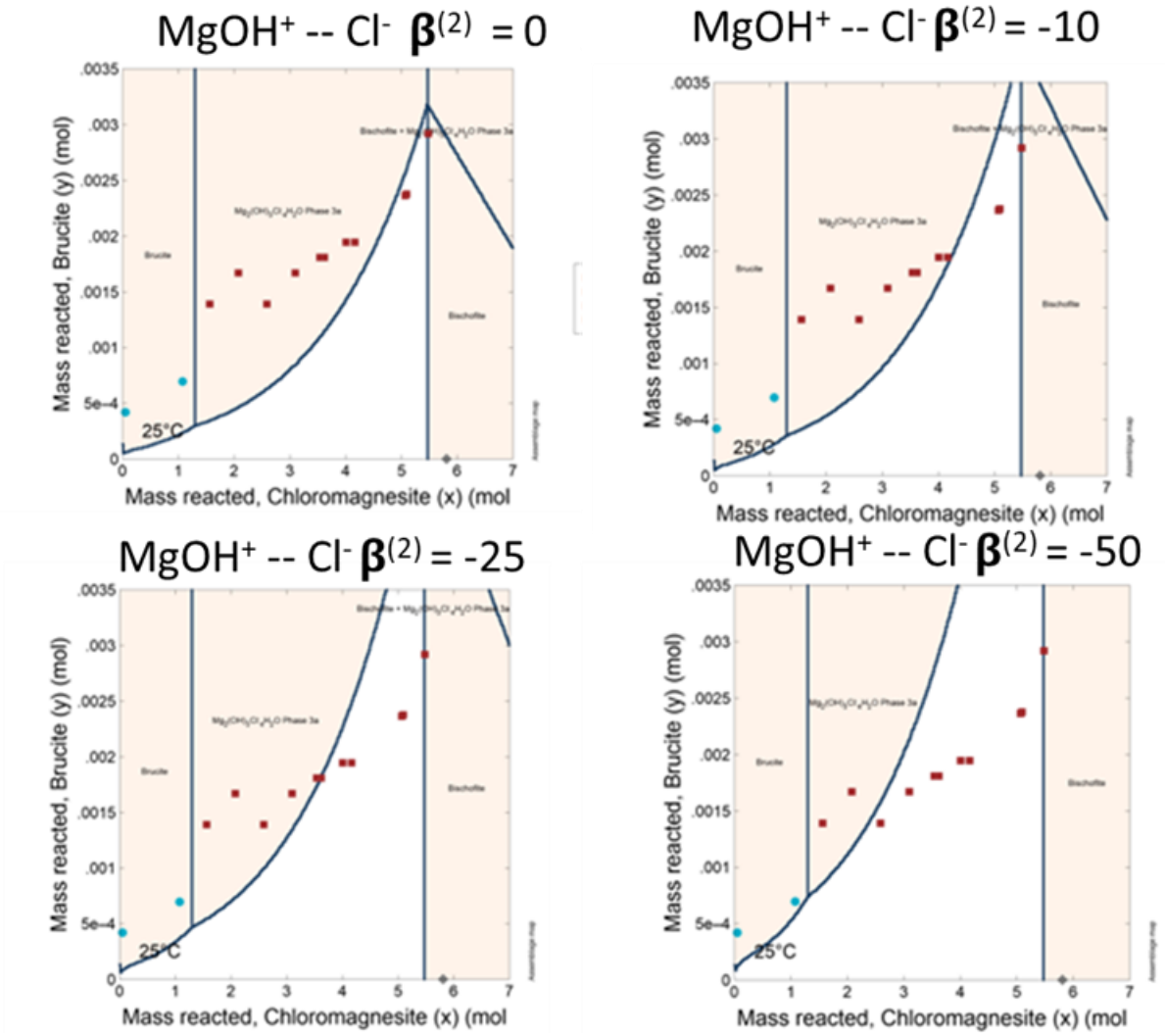

Figure 91. The impact of adjustments made to the $\beta^{(2)}$ Pitzer interaction parameter for $MgOH^+$ — Cl^- at 25 °C.

The impact of the $MgOH^+$ — Cl^- $\beta^{(2)}$ parameter at 25 °C is inversely proportional to the total solubility of the system, where the steepness of the assemblage/aqueous interface becomes increasingly steep with a more negative value of the $\beta^{(2)}$. The solubility of the system increases over the entirety of the $MgCl_2$ domain; however, the impact is increasingly sensitive as the [$MgCl_2$] or ionic strength increases. While the solubility of the system is very sensitive to the $\beta^{(2)}$, the phase boundaries remain unchanged. This suggests that the phase boundaries are largely defined by the LogK values.

The impact of $MgOH^+$ - Cl^- (c^{φ}) parameter

In addition to the $MgOH^+$ — Cl^- $\beta^{(2)}$, the c^{φ} can also be adjusted to modified the solubility of the Mg-OH-Cl-H_2O system. The impact of c^{φ} is shown in Figure 92. The c^{φ} parameter is inversely proportional to the overall solubility of the system and has a larger effect as the [$MgCl_2$] increases – or increase in ionic strength. In addition, c^{φ} differs from $\beta^{(2)}$ because c^{φ} has a smaller impact at low ionic strength, and increases with increasing ionic strength. Due to these slight differences, a combined effect of small

changes to both c^{φ} and $\beta^{(2)}$ will allow for a better match to the shape of the solubility curve seen in the data from Pannach et al. (2017).

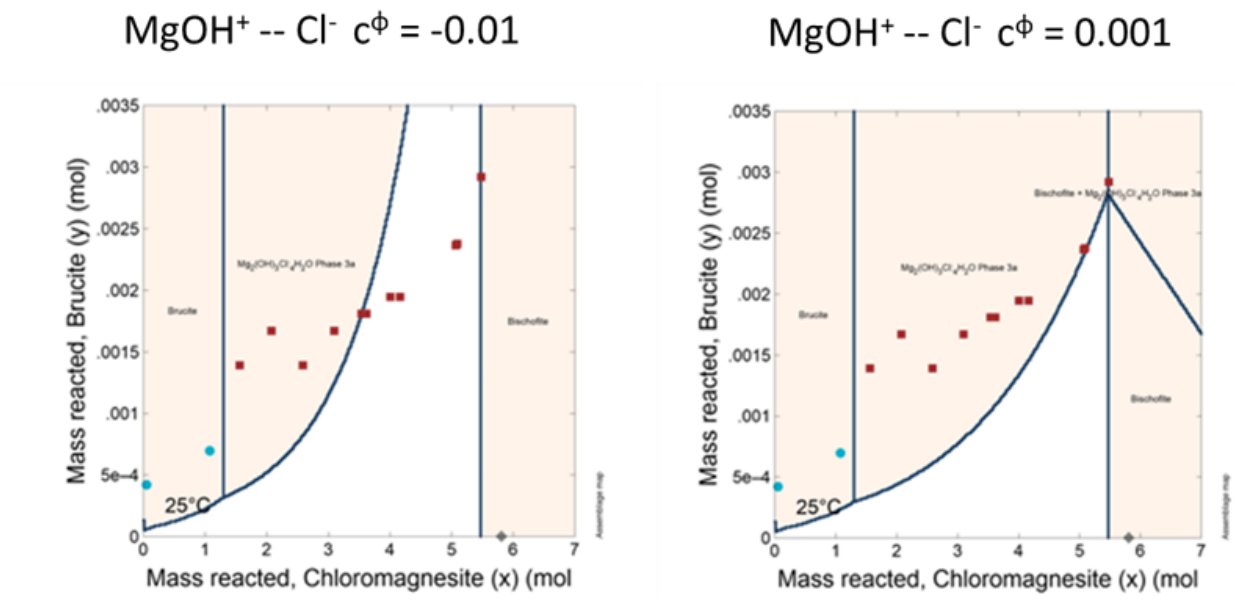

Figure 92. The impact of the $MgOH^+$- Cl^- c^{φ} interaction parameter at 25 °C

The impact of combined effect of $MgOH^+$ — Cl^- (β_2) and $MgOH^+$ — Cl^- (c^{φ}) adjustments

Due to the slight differences in the way that $\beta^{(2)}$ and c^{φ} affect the solubility of the precipitating phases as a function of [$MgCl_2$] or ionic strength, the combined effects of adjusting these parameters will allow for an improved fit to the experimental data. Since there are many combinations of $\beta^{(2)}$ and c^{φ} that could improve the fit, the goal was to minimize the magnitude of the changes to these parameters to minimize any potential impact that changes may have on the brucite and bischofite solubility (which was verified with each adjustment).

To do so, a matrix was constructed, shown in Figure 93, where the $\beta^{(2)}$ changes in the x-direction and c^{φ} changes in the y-direction. At this point, there is not a way to statistically defend the choice of an individual combination of $\beta^{(2)}$ and c^{φ} to match the data, however some combinations are clearly better representations than others. For example, when $\beta^{(2)}$ = -35 and c^{φ} = 0.008, as the [$MgCl_2$] or ionic strength increases, the model begins to overestimate the solubility of the system (where the green data points are experimental data points achieved from oversaturated solutions). In contrast, when $\beta^{(2)}$ = -35 and c^{φ} = 0.010, the model appears to slightly suppress the solubility as [$MgCl_2$] or ionic strength increases. This combination appears to fit the experimental data at 25 °C reasonably well – especially when considering the spread in the experimental data. Therefore, the values of [$\beta^{(2)}$ = -35; c^{φ} = 0.010] will be applied to update the SNL thermodynamic database (Table 25).

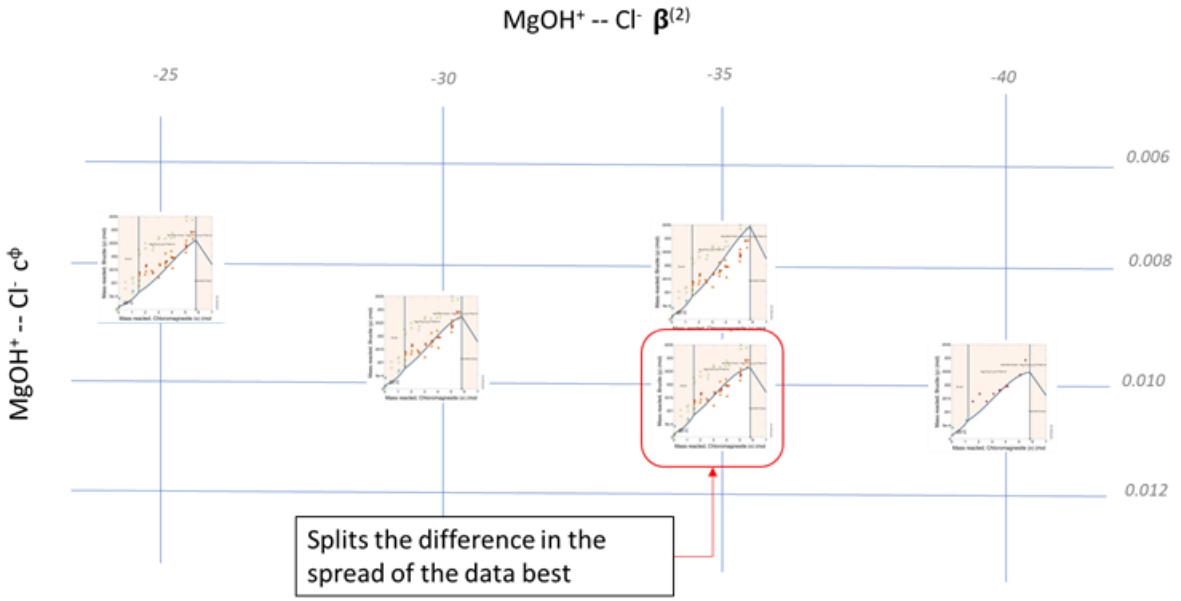

Figure 93. Matrix showing the combined impact of adjustments made to the $MgOH^+$ — Cl^- $\beta^{(2)}$ and c^φ Pitzer interaction parameters at 25 °C.

2.3.2.3 Modification of temperature Dependent Pitzer interaction parameters

Now that the temperature dependent LogK values have been determined for brucite and bischofite and the Pitzer interaction parameters for the $MgOH^+$ — Cl^- interaction at 25 °C were selected to improve the fit of the available experimental data, the temperature dependent Pitzer parameters must be considered. These temperature dependent Pitzer parameters are related to the room temperature Pitzer parameters through the following polynomial equation from Bethke (2008):

$$\beta_T = \beta_{25} + c_1(T_K - T_R) + c_2\left(\frac{1}{T_K} - \frac{1}{T_R}\right) + c_3 \ln\left(\frac{T_K}{T_R}\right) + c_4 (T_K^2 - T_R^2) + c_5 \left(\frac{1}{T_K^2} - \frac{1}{T_R^2}\right)$$

Where β_T is the β parameter at temperature = T (in K), β_{25} is the β parameter at 25 °C (298.15 K), T_K is the absolute temperature, T_R is the reference temperature (298.15 K), and $c_1 - c_5$ are polynomial coefficients that describe the relationship between the β parameter and T. For simplicity sake, focus was placed on one parameter at a time, and again, attempted to minimize adjustments made to limit any unintended consequences from these changes. To start, the c_1 parameter was adjusted for both the $\beta^{(2)}$ and c^φ Pitzer interaction parameters for the $MgOH^+$ — Cl^-. Similar to the approach of examining the combined effects of $\beta^{(2)}$ and c^φ at 25 °C (Section 2.3.2.2), a matrix was created to explore the combined effects of modifications made to the c_1 coefficient of both the $\beta^{(2)}$ and c^φ Pitzer interaction parameters for the $MgOH^+$ — Cl^-. The resulting solubility diagrams at 40 °C, 60 °C, and 100 °C, where $MgOH^+$ — Cl^- $\beta^{(2)}$ c_1 parameter changes from -1.65 to -1.75 in the x-direction and the $MgOH^+$ — Cl^- c^φ c_1 from 0 to -0.00004 in the y-direction, are shown in Figure 94. Unlike the adjustments made at 25 °C, where it could be independently evaluated, the solubility diagrams at 40 °C, 60 °C, and 100 °C are all dependent upon the changes in the polynomial coefficients c_1-c_5 and cannot be individually evaluated. Therefore, Figure 94 presents the solubility diagrams of the Mg-OH-Cl-H_2O at 40 °C, 60 °C, and 100 °C together with each c_1 adjustment.

Again, without a statistical metric for evaluating the goodness of fit and the need to evaluate all three temperatures together, it is relatively qualitative – however there is a small window where the fit is

obviously improved. Overall, the impact of the adjustments to c_1 are most notable at 100 °C. For example, when $\beta^{(2)}c_1 = -1.65$ and $c^{\varphi}c_1 = 0$, then the solubility of the system underestimates the solubility of phases at high ionic strength – this is most obvious for the 9-1-4 phase (orange diamonds) and 2-1-4 phase (blue triangles) at 100 °C – but overestimates the solubility to brucite (light blue squares) at low ionic strength. Using just the c_1 parameter, the best fit of the experimental data is when $\beta^{(2)}c_1 = -1.75$ and $c^{\varphi}c_1 = 0.00002$, while this model slightly overestimates the solubility of brucite at 100 °C and slightly under estimates the solubility of the 9-1-4 phase, it fits the 2-1-4 reasonably well (considering uncertainty in the experimental data) and predicts the invariant point of brucite and the 9-1-4 phase accurately.

The thermodynamic database was updated with respect to the $MgOH^+$ — Cl^- Pitzer interaction parameters that improve the thermodynamic model to accurately fit the data. The changes to the thermodynamic database are summarized in Table 25, where the italicized numbers were updated from 0.

Table 25. Updated Pitzer parameters for the $MgOH^+$ — Cl^- interaction, where the numbers in italics were updated and adjusted from the initial values of 0.

Parameter	$\beta^{(0)}$ [$MgOH^+$ — Cl^-]	$\beta^{(0)}$ [$MgOH^+$ — Cl^-]	$\beta^{(0)}$ [$MgOH^+$ — Cl^-]	c^{φ} [$MgOH^+$ — Cl^-]
25 °C	-0.1	1.658	*-35*	*0.01*
c_1	0	0	*-1.75*	*-0.00002*
c_2	0	0	0	0
c_3	0	0	0	0
c_4	0	0	0	0
c_5	0	0	0	0

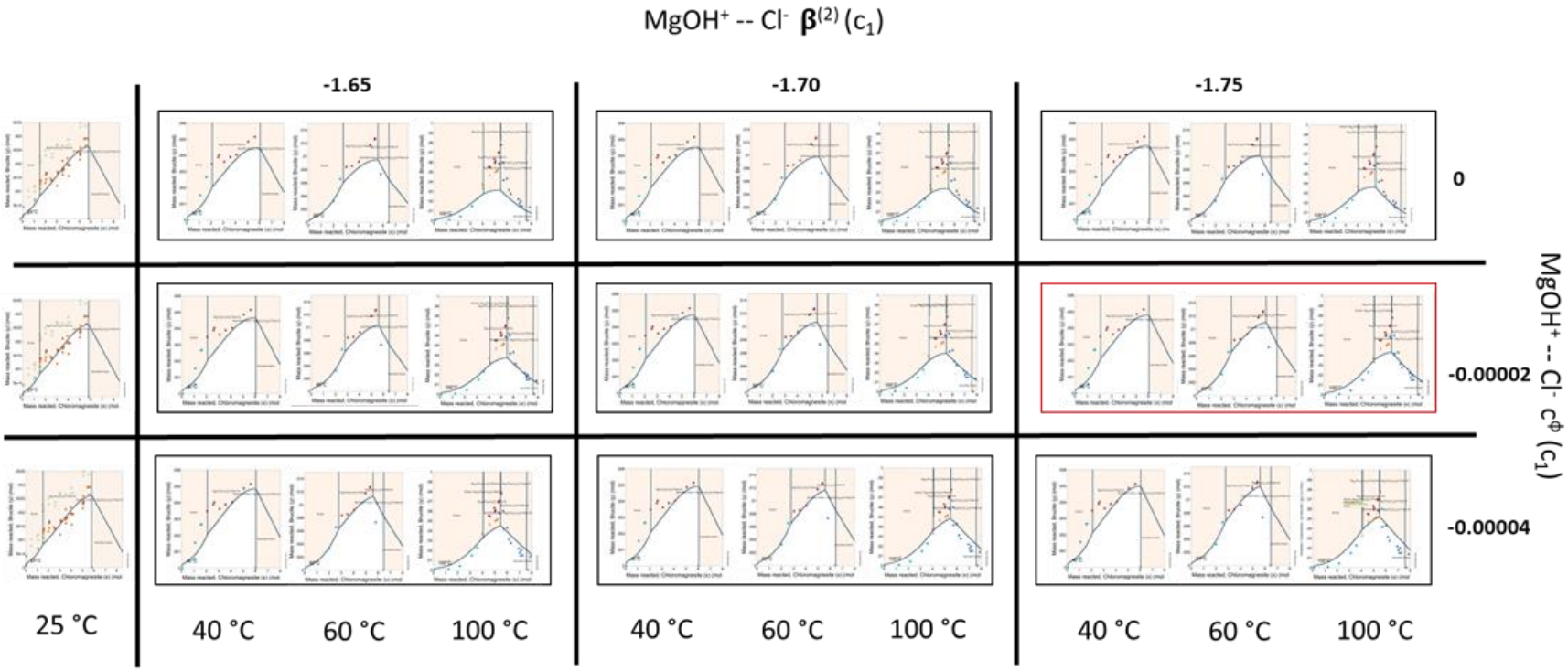

Figure 94. Matrix showing the impact of adjustments made to the first temperature dependent Pitzer interaction parameter, c1, for the $MgOH^+$ — Cl^- $\beta^{(2)}$ and c^{φ} interactions.

2.3.2.4 Final LogK adjustments to Mg-hydroxychloride phases

With the updated LogK values for bischofite and brucite along with updated $\beta^{(2)}$ and c^{φ} Pitzer interaction parameters for the $MgOH^{+}$ — Cl^{-} as a function of temperature, the initial LogK was adjusted and applied to calculate values that better match the phase boundaries in the experimental data (Pannach et al., 2017). The initial calculated LogK (red) plotted with the adjusted LogK (black) as a function of temperature are shown in Figure 95. From this figure, it is clear that only minor changes were made to the 3-1-8 phase. This is reasonable as some thermodynamic data in the literature exists to help bound these calculations. For the 2-1-4 phase, which begins to form when T >40 °C, the adjustments made to LogK increase with temperature and were consistently less than originally calculated. This could be related to the need to further refine the temperature dependent Pitzer parameters (i.e. c_2-c_5). With respect to the 9-1-4 phase, which forms when T > 80 °C, there are only two data points that can be modified to match the experimental data. One of the adjustments led to a smaller $LogK_{9\text{-}1\text{-}8}$, the other to a larger $LogK_{9\text{-}1\text{-}8}$. This could either be due to the temperature dependent Pitzer parameters or the minimal number of data points to evaluate and determine a potential trend. Lastly, no changes were made to $LogK_{2\text{-}1\text{-}2}$, as it only forms when T > 100°C, and only one data point is available. In addition, the model at 120 °C poorly represents the experimental data, and therefore more work is needed to refine the thermodynamic model when T > 100 °C.

2.3.2.5 Conclusions and future work on magnesium hydroxychlorides

The solubility diagrams for the Mg-OH-Cl-H_2O system at [25, 40, 60, 80, 100, and 120 °C] compared to the experimental data from Pannach et al. (2017) are shown in Figure 96. Overall, the thermodynamic modeling fits the experimental data more accurately than in FY19; however, there are still several discrepancies. These are primarily seen at 80 °C and 120 °C, where limitations in the Geochemists Workbench do not allow for direct adjustments to the LogK values to temperatures apart form 0, 25, 40, 60, 100, and 150 °C. Another systematic discrepancy is accurately fitting the invariant point between the 2-1-4 phase and the 3-1-8 phase (at 60 °C and 80 °C) or with the 9-1-8 phase (at 100 °C and 120 °C).

Creating an accurate thermodynamic database is very important in order to predict $MgCl_2$ brine stability on the SNF canisters as function of temperature and RH. As was demonstrated previously, the deliquescence RH for a magnesium chloride brine is highly dependent upon which phase is stable on the SNF canister surface (Bryan and Schindelholz, 2018b; Katona et al., 2020a; Katona et al., 2020b; Schaller et al., 2019). If bischofite ($MgCl_2$:$6H_2O$) from deposited sea-salt aerosol deliquesces and degasses Cl^{-} to form a magnesium hydroxychloride phase (phase is dependent upon the temperature), then, for a brine to persist on the SNF canister surface, the RH will need to be much higher—hence a much lower temperature on the canister surface—before deliquescence will occur. This would delay the timing of corrosion and SCC initiation. Moving forward in FY21, continued refinement of the thermodynamic parameters will help improve the accuracy of the modeled system. To do so, this may also require additional experimental data such as synthesis and characterization of magnesium hydroxychloride phases to further evaluate their properties and conditions of stability. Some of this work was initiated in FY20 (see Section 2.3.3). The primary goal is to develop and experimentally verify a set of LogK values for use in predicting magnesium-containing brine stabilities on heated SNF storage canisters as a function of temperature and other environmental factors, such as atmospheric acid gas reaction and the presence of CO_2.

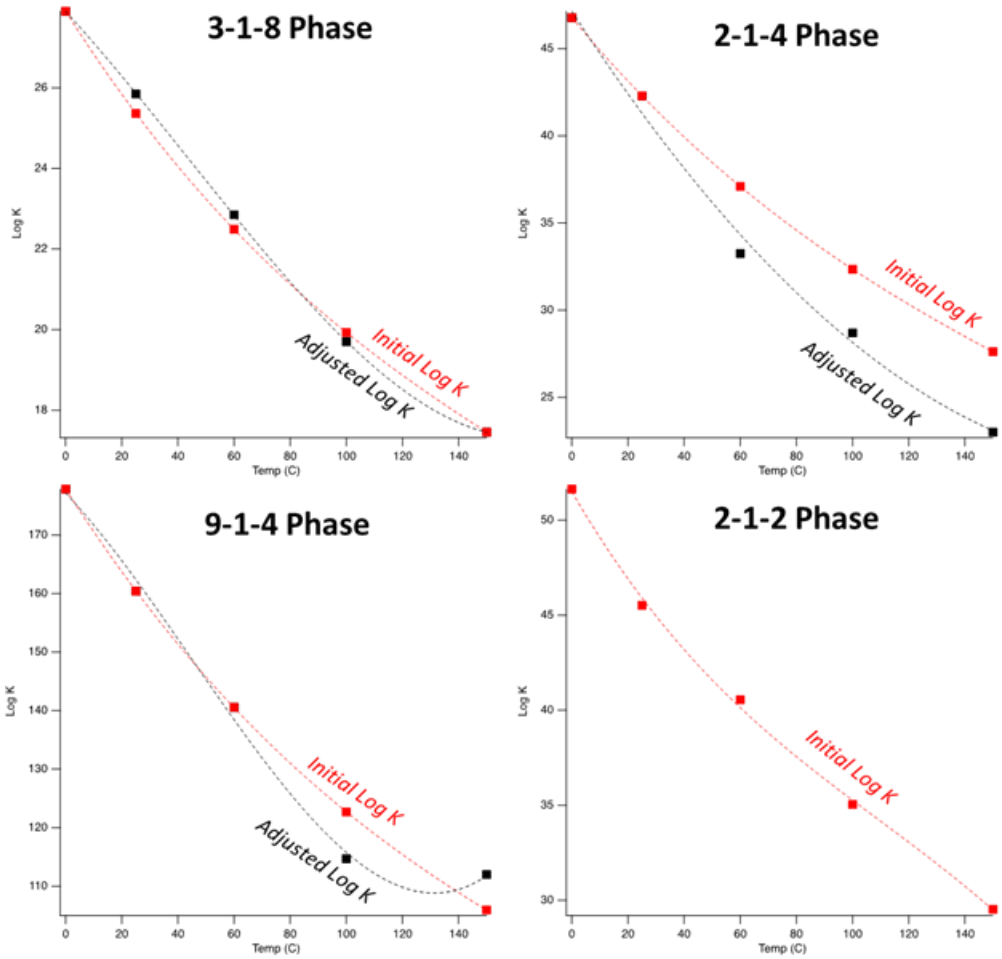

Figure 95. Initial LogK (red) and Adjusted LogK values (black) as a function of temperature for Mg-hydroxychloride phases, including the 3-1-8 phase, 2-1-4 phase, 9-1-8 phase, and the 2-1-2 phase.

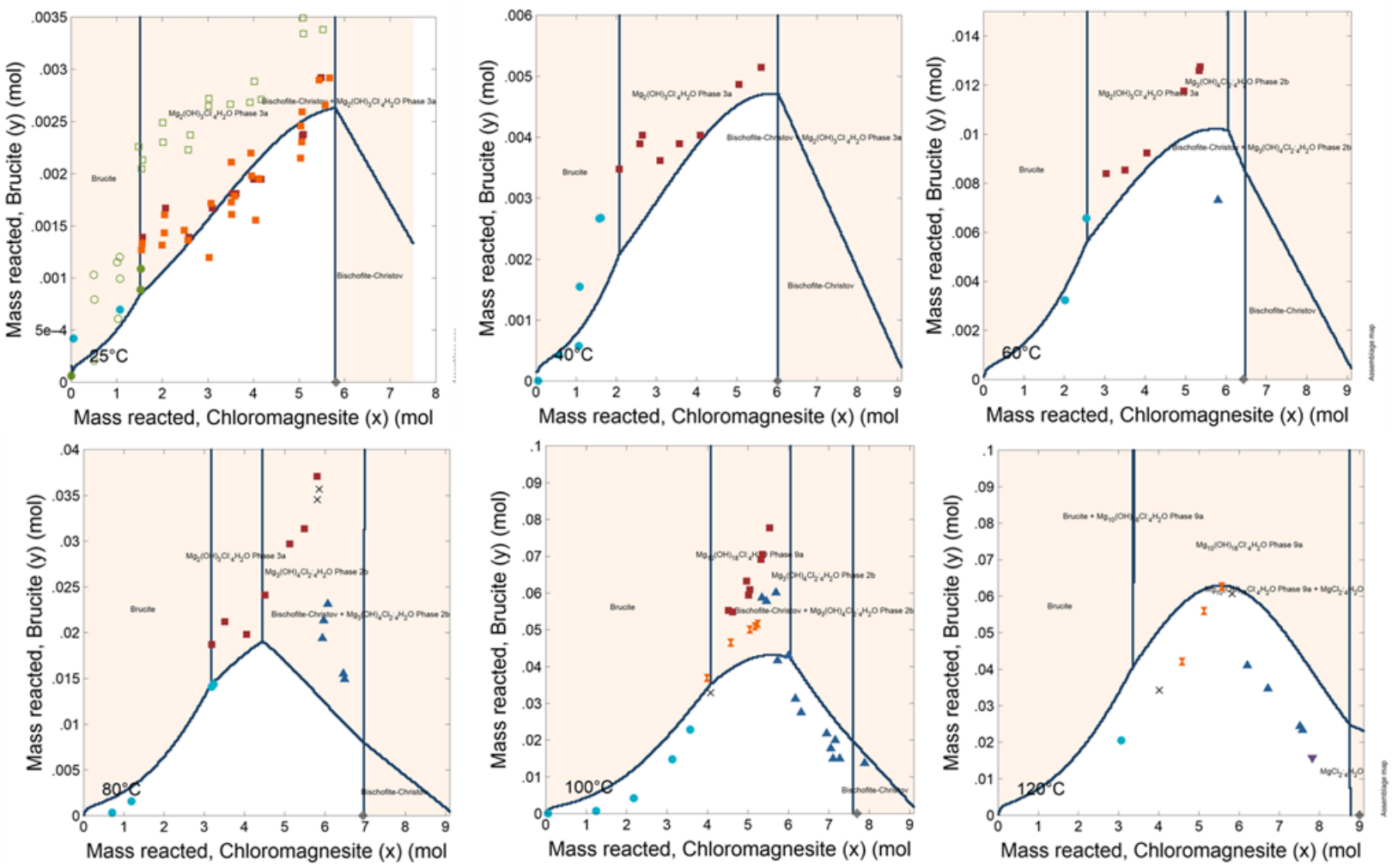

Figure 96. The solubility diagrams for the Mg-OH-Cl-H_2O system at [25, 40, 60, 80, 100, and 120 °C] compared to the experimental data from Pannach et al. (2017).

2.3.3 Precipitation and characterization of Mg-bearing phases

In FY20, initial synthesis and characterization of Mg-bearing mineral phases was carried out to both improve thermodynamic modeling (see Section 2.3.2) and better understand the influence of brine behavior on electrochemistry and corrosion (See Section 3). The work performed in FY20 was motivated by the challenges associated with analyzing Mg-bearing films that form during rotating disc electrode (RDE) polarization experiments (Schaller et al., 2019). Instead, the electrochemistry was mimicked by rapidly raising the solution pH of a $MgCl_2$ brine with the addition of 3 M NaOH. This is meant to simulate the increase in pH of the cathode as a result of OH^- formation—which is believed to be a significant driving factor for the formation of Mg-bearing films that form during RDE experiments.

2.3.3.1 Mg-hydroxychloride synthesis

XRD and SEM characterization was applied to the Mg-film that forms due to the rapid increase in pH of $MgCl_2$ solution. Four solutions of $MgCl_2$ were analyzed (0.18, 1.25, 3.3 M, and saturated). For each solution roughly 15 mL was added to a scintillation vial, the pH was increased using 3 M NaOH (~200 µL). A gel formed immediately and was analyzed by SEM and XRD through a few different preparation and isolation techniques. First, the gel was immediately removed and transferred to a large Whatman filter to dry out and wick away the brine. Once dry, the samples were mounted and analyzed via XRD and SEM. XRD analysis showed the presence of halite in all the analyzed gels at each initial $MgCl_2$ concentration (Figure 97). As the concentration of the $MgCl_2$ solution decreased, brucite peaks began to emerge and became the dominant phase in the lowest concentration solution examined, 0.18 M $MgCl_2$.

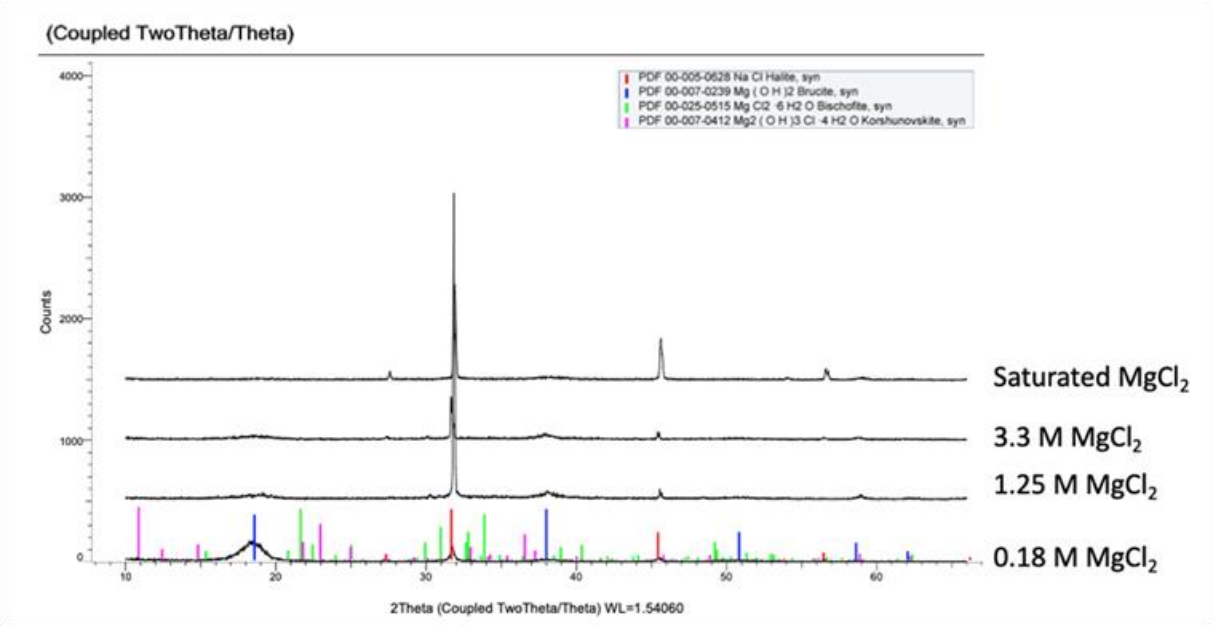

Figure 97. XRD of the gels that formed from exposure in 0.18 M to saturated $MgCl_2$ solutions

The SEM images of the gel formed from saturated $MgCl_2$ and 1.25 M $MgCl_2$ show the presence of halite crystals, as evidenced by the large peak at ~31 2-theta. In saturated $MgCl_2$ the gel appears to be primarily composed of halite; as the solution contained nearly 12 moles of Cl^- when the gel formed and encases the NaOH droplet, the local Na concentration is very high, and halite readily precipitates. This also occurred in the 1.25 M $MgCl_2$ solution, but to a lesser degree as the concentration of Cl^- is much lower.

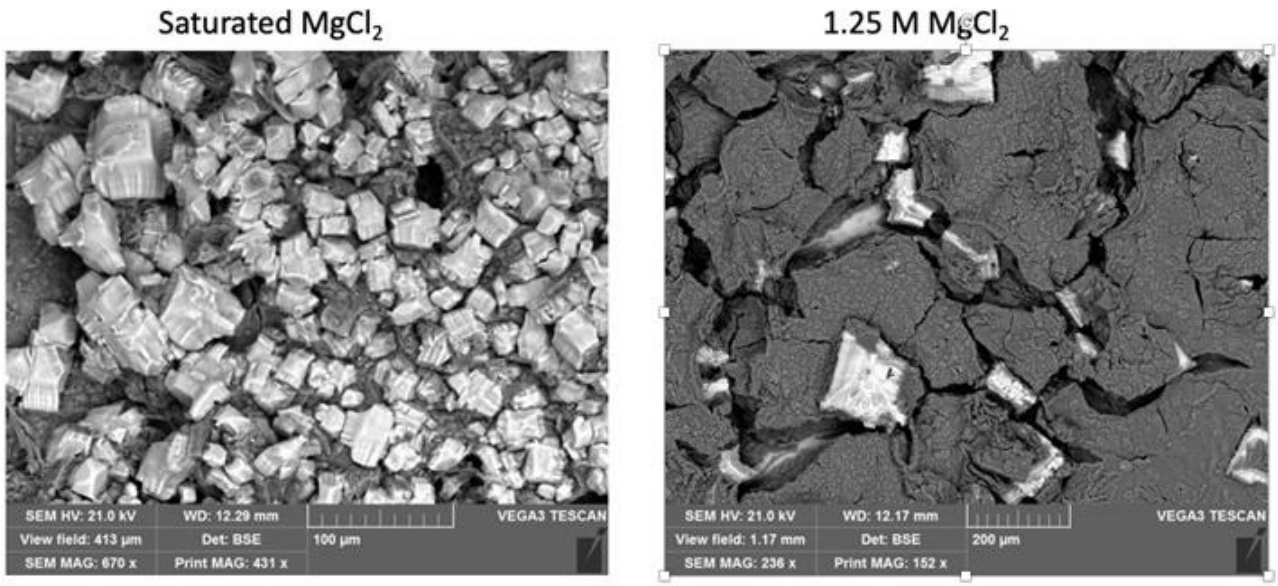

Figure 98. SEM images of $MgCl_2$ gels when analyzed immediately after exposure showing the presence of large halite crystals.

As halite is not expected to be the primary phase to form in RDE experiments, subsequent gels were thoroughly mixed and allowed to age for 1 hour, 24 hours, and 72 hours. In this case, a new method was applied to separate the phases. Instead of using a Whatman filter to wick away the brine, the gels were vacuum filtered to dryness and carefully rinsed to remove any NaCl that formed. XRD analysis of the gel formed from saturated $MgCl_2$ aged at different times shows the evolution of the precipitate that formed (Figure 99). When analyzed immediately and again, after 1 hour of aging, halite is the most dominant peak. Although there is likely to be a significant amount of Mg in the precipitate however, it is probably present as an amorphous phase. After 24 and 72 hours of aging, the XRD pattern strongly matches the 3-1-8 magnesium hydroxychloride phase predicted to form from thermodynamic modeling (See Section 2.3.2).

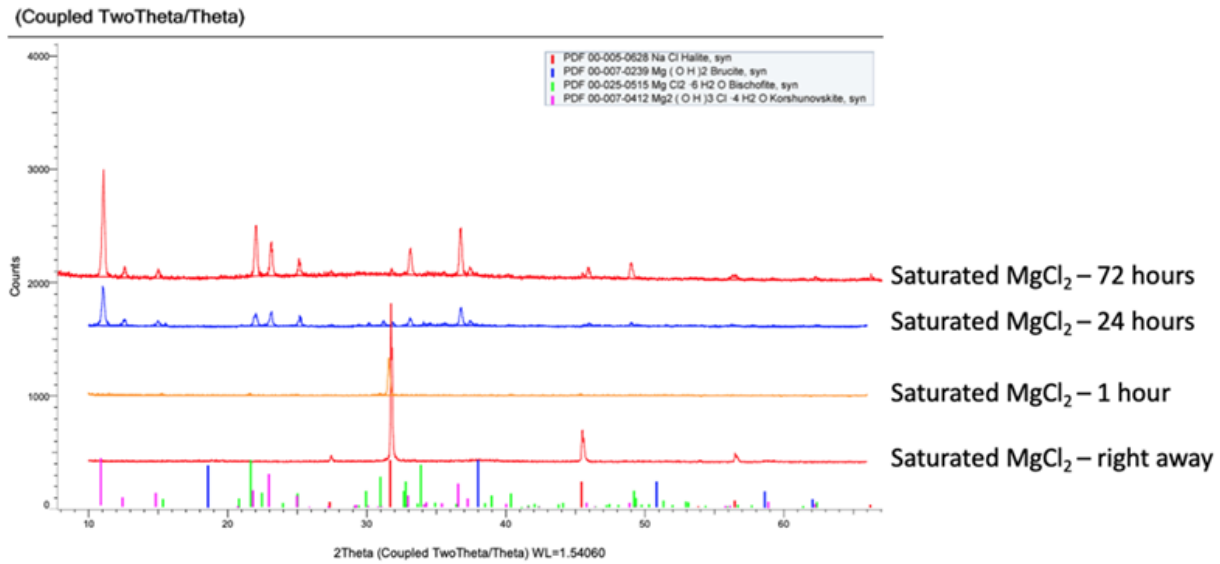

Figure 99. XRD analysis showing the evolution of the $MgCl_2$ gel showing that as the $MgCl_2$ solution ages, the NaCl peak disappears and the 3-1-8 magnesium hydroxychloride phase becomes the dominant phase.

SEM analysis of the gels that formed from saturated $MgCl_2$ aged for 24 hours and 72 hours displays long needle-like crystals, consistent with previously reported SEM images of the 3-1-8 phase (Figure 100). The crystals formed are significantly larger after 72 hours of aging as compared to the 24 h aged sample.

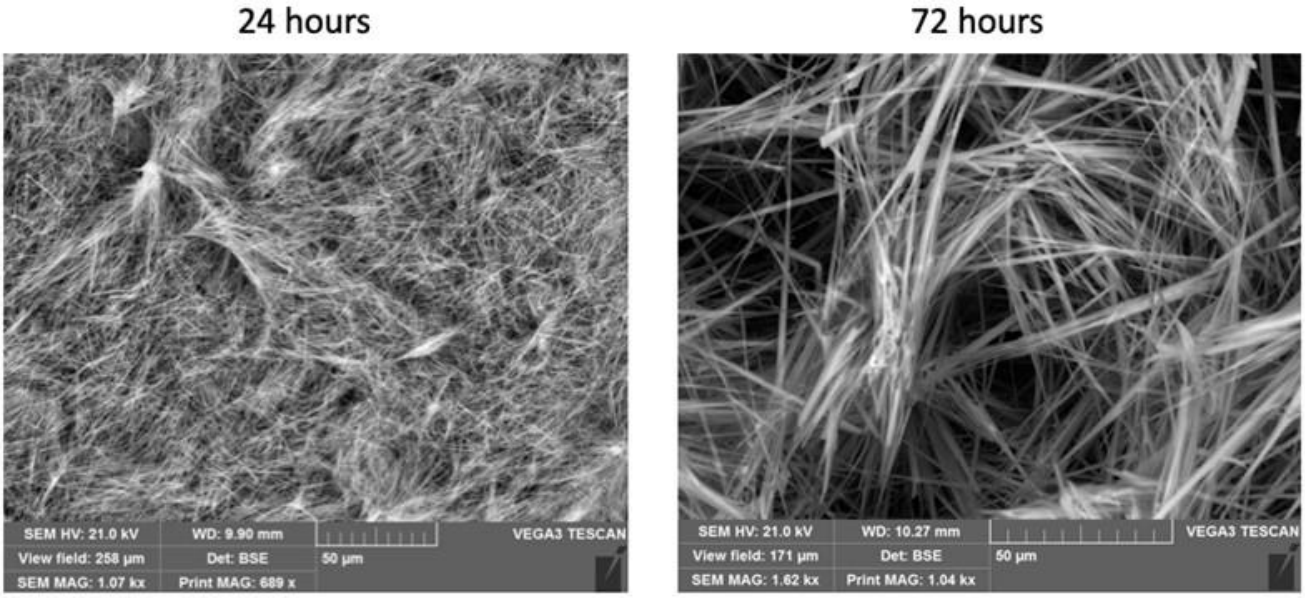

Figure 100. SEM images of the gel that forms in saturated $MgCl_2$ after 24 and 72 hours.

The 3-1-8 phase was dominant in a gel formed from a 3.3 M $MgCl_2$ solution aged for 72 hours (shown at two different magnifications), again consistent with the phase that is predicted by thermodynamic modeling (Figure 101).

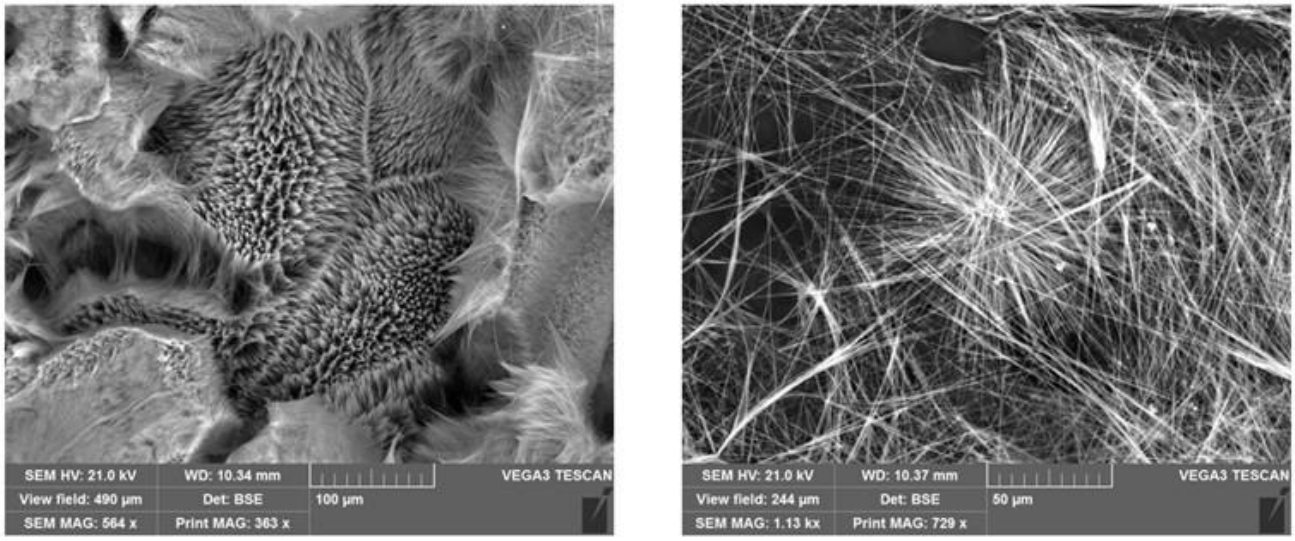

Figure 101. SEM image of the gel that forms from 3.3 M $MgCl_2$ exposure after 72 hours aging.

The XRD analysis of each of the solutions [0.18, 1.25, 3.3 M, and saturated $MgCl_2$] aged for 72 hours shows the evolution of the gel as a function of the initial $MgCl_2$ concentration (Figure 102). In dilute systems, 0.18 M and 1.25 M $MgCl_2$, brucite is the primary Mg bearing phase that forms (with some halite). When the concentration of $MgCl_2$ is higher, 3.3 M and saturated, the 3-1-8 magnesium

hydroxychloride phase forms. A Raman spectrum was collected for the 3-1-8 phase synthesized from a solution of saturated $MgCl_2$ aged for 72 hours. The primary identifying feature in the Raman spectrum is the O-H stretch at ~3650 cm^{-1}, which is a doublet peak and is consistent with literature reported spectra (Dorrepaal and Gowen, 2018a).

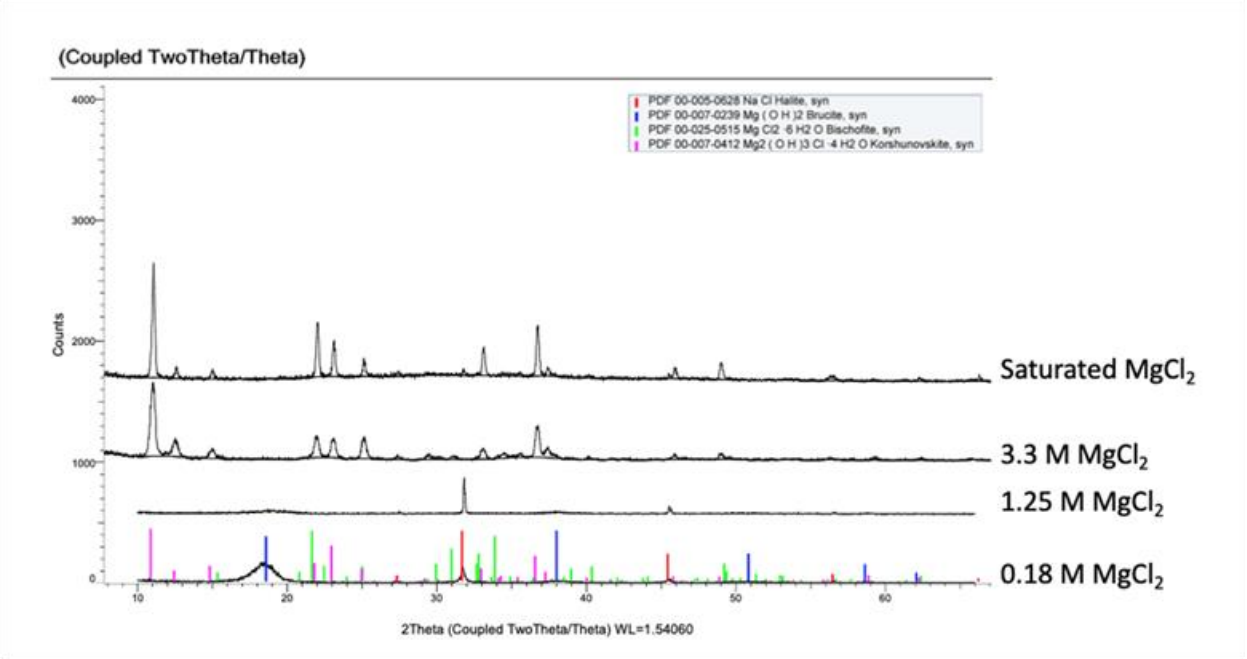

Figure 102. XRD analysis of the gel that forms as a function of the concentration of $MgCl_2$ after 72 hours aging.

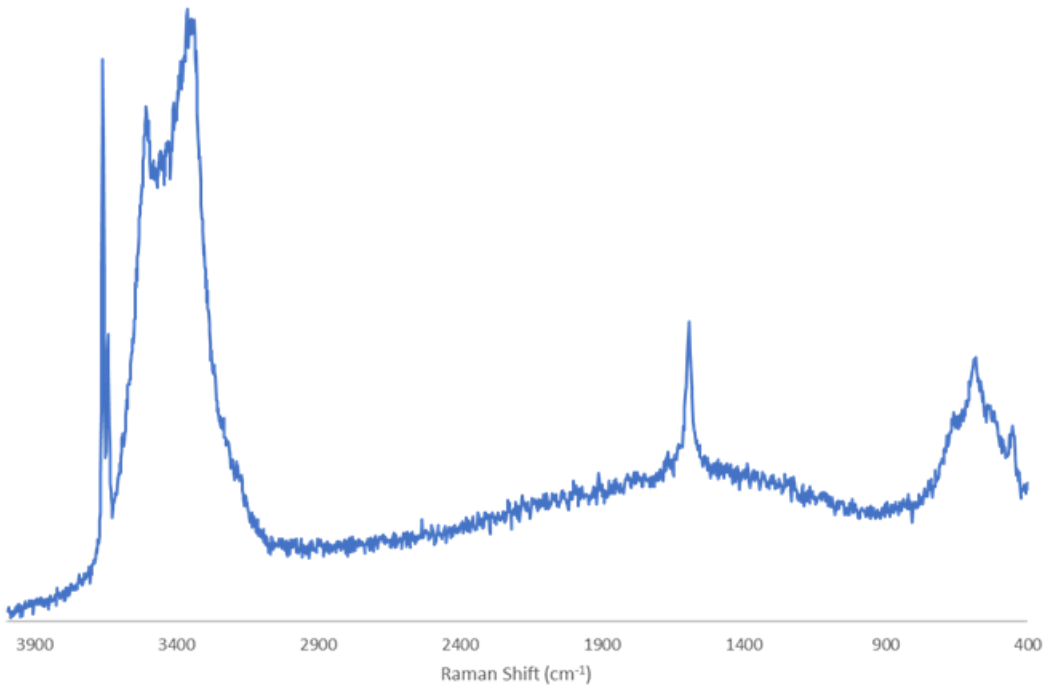

Figure 103. Raman spectrum of the 3-1-8 magnesium hydroxychloride

These identified phases, when plotted along with a calculated phase diagram, correspond with the expected phase formation as shown in Figure 104. The phase diagram was calculated using the Geochemist's Workbench (Phase2 module) (Bethke, 2008) and the Yucca Mountain Project thermodynamic Pitzer database (SNL, 2007).

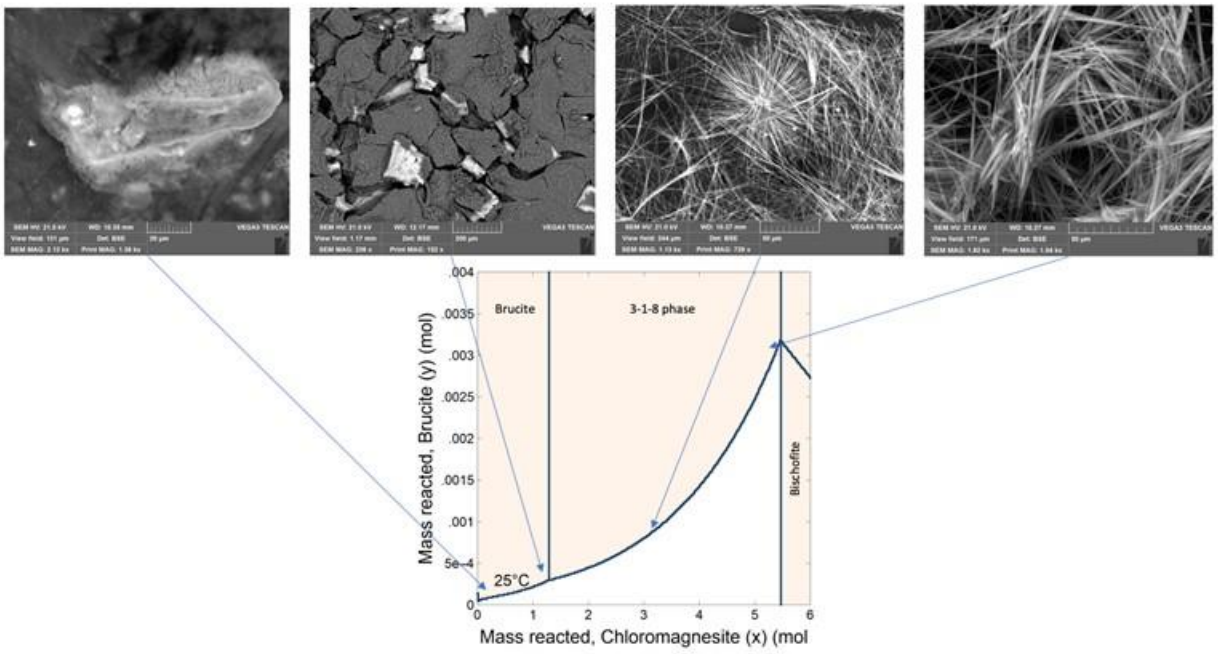

Figure 104. Experimental conditions of Mg-phase precipitation on the phase diagram at 25°C. The SEM images highlight the phases present, where at low [Mg] < 1.5 M, brucite forms irregular block crystals, while when 5.48 M < [Mg] > 1.5 M, the 3-1-8 forms long needle-like crystals. The phase diagram was created using the Geochemist's Workbench (Bethke, 2008).

2.3.3.2 Deliquescence RH and conclusions

Once the 3-1-8 phase was identified, isolated, and characterized, a test was developed to measure the deliquescence RH via thermogravimetric water adsorption measurements. These measurements were performed using a QuantaChrome AutoSorb-iQ2 water sorption analyzer, where the sample was equilibrated at low RH for 24 hours at 60°C. The RH was controlled by mixing water saturated and dry air, and was increased by introducing more saturated air into the sample chamber (while maintaining a constant temperature) and measuring the weight gain of the sample from adsorbed water. The rate of RH increase was 1% RH/min. The resulting thermogravimetric analyses (solid lines) and differential scanning calorimetry (dotted lines) as a function of water adsorbed by the sample are shown in Figure 105, where the green line is bischofite and the blue line is the 3-1-8 phase. The shaded regions show the initiation of a large gain in mass associated with an exothermic response. These regions likely indicate initiation of deliquescence as the experimental value (~28% RH) compares well to the calculated deliquescence of bischofite (~30 % RH at 60 °C). The resulting deliquescence RH of the 3-1-8 phase is ~78 %RH. There also appears to be some bischofite present in the sample, as demonstrated by the weight gain at about ~30 %RH.

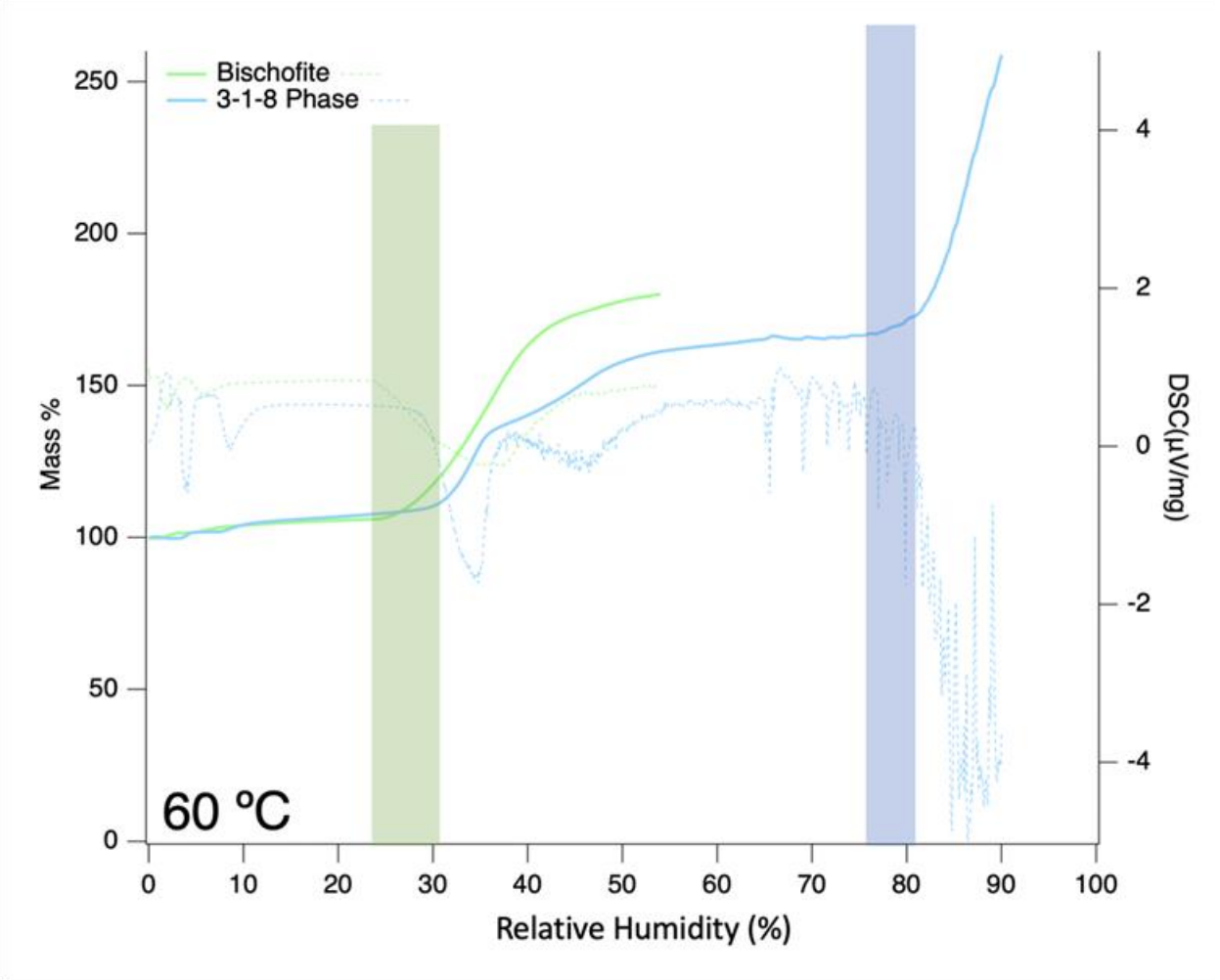

Figure 105. Water adsorption thermogravimetric experiment of bischofite (green lines) and the 3-1-8 phase (blue lines) demonstrating through mass gain and calorimetric response the approximate deliquesce RH.

The significance of this result is that the 3-1-8 magnesium hydroxychloride phase has a much higher deliquescence RH than bischofite – and even higher than halite. This means that the conversion of $MgCl_2$ rich brines to magnesium hydroxychloride phases will increase the RH at which a brine will persist on the surface of the SNF canisters. This result also helps illuminate the observation of brine dryout (observed on the big plate studies and 4-point bend tests discussed in Section 3.5 that were seen previously (at 80 °C 35% RH). For a reactant limited case, or singular deposition of $MgCl_2$ on the surface prior to exposure, as the $MgCl_2$ degasses Cl^- and converts to Mg-hydroxychlorides, Mg-carbonates, or reacts with corrosion products, the experimental conditions are no longer below the deliquescence RH of the mineral phases, and the assemblages precipitate out.

Work in FY21 will analyze additional Mg-hydroxychloride phases, including 2-1-4, which has been observed in many prior experiments, to determine their deliquescence RHs. This information will be useful to validate the ongoing work to determine thermodynamic parameters for the Mg-OH-Cl-H_2O system, as discussed in detail in Section 2.3.2 and the FY19 report (Schaller et al., 2019).

This page is intentionally left blank.

3. Canister Corrosion Experimental Studies

3.1 Effect of Brine Composition on pitting/cracking

In FY 18-19, Weirich *et al*. (2019) explored 304 SS pitting under seawater droplets for one year in controlled atmospheric exposures, and found that pit morphology was highly dependent on exposure RH. Pits grown at 40% RH displayed an irregular, cross-hatched morphology with fissures resembling microcracks. However, pits that formed at 76% RH displayed crystallographically faceted ellipsoids with no associated microcrack-like fissures or irregular morphology. These results suggested that RH, and therefore brine composition, played an influential role in determining susceptibility to pitting, microcracking, and possible eventual SCC. In FY20, a manuscript was submitted on continuation of this work, and explored further the effects of RH and brine composition, on pit morphology at longer exposure times. Additionally, further research into the driving force for variations in pit morphology was conducted, including exposures of SS304 coupons in full-immersion brines to isolate certain variables. As exposure RH changes, not only does the brine composition change, but the surface water layer thickness, brine morphology, formation of solid precipitates, conductivity, and brine concentration are all altered. The current research has elucidated some of the contributing factors, such as brine composition and will be discussed herein, but further determination of the specific variables influencing pit morphology will be carried out in FY21.

3.1.1 Differences in pitting morphology as a function of brine composition

In FY20, observations of pit morphologies of SS coupons exposed in the same RH environments (40% and 76% RH at 35ºC) as the Weirich study were consistent for exposures carried out to 2 years (Figure 106) (Srinivasan et al., 2020). Exposure at 40% RH, corresponding to a $MgCl_2$-dominated brine, resulted in pits with again, an irregular, cross-hatched morphology, while crystallographically faceted, ellipsoidal pits developed at 76% RH in the NaCl-dominated brine. The cross-hatched morphology of the pits that formed at the lower RH implied that attack followed selective dissolution of a fixed active area due to growth at critical chemistry conditions (Hebert and Alkire, 1988). Pit growth at 76% RH likely occurred at conditions between stability and saturation (Sato, 1982), resulting in preferential dissolution along specific crystallographic planes, which caused faceting. Micro-cracks were observed to be present after 40% RH exposure, even at times as short as 1 week, and without the presence of any externally applied load. The development of pit morphology is schematically described in Figure 106-c. For the low RH exposure, growth of the pit occurs close to repassivation, thus limiting the area for dissolution and a fixed active area is established. As limited current supply is available, selective dissolution occurs, resulting in the cross-hatched morphology. However, in the case of the high RH exposure, growth of the pit occurs between the critical chemistry for pit stability and $FeCl_2$ saturation, and growth occurs with an increasing active area over time.

In addition to pit morphology observations, post-exposure measurements of the aspect ratio of the pit populations on the coupons were collected. A quantitative measurement for comparing pit morphologies is the aspect ratio (*AR*) calculated from the ratio of the pit diameter to pit depth. However, the ability to discern pit shape, hemispherical versus non-hemispherical, is limited as several pit shapes may have the same *AR* value. Additionally, analysis of the appropriate depth and diameter measurements, whether it be maximum, average, Feret, etc., can affect the resultant ratio. Nonetheless, as complimentary analysis, *AR* provides a useful quantitative tool to evaluate pit shape development. Optical profilometry (OP) measurements were collected for pit populations across the exposed coupons and compared to X-ray computed tomography (XCT) measurements collected for a select set of pits to gain a better understanding of not only pit morphology, but also of potential changes to pit aspect ratio due to the differing RH/brine environment exposure. As indicated by the *AR* data in Figure 107, the majority of pits detected were wider than they were deep, *i.e.* $AR > 1$. It was noted *AR* decreased slightly with exposure time for long-term exposures. This decrease may be due to limited available cathodic current from a finite cathode and the lower likelihood of meeting the anodic demand as growth progresses (Chen et al.,

2008; Chen and Kelly, 2010). One possible manner in which pit growth could respond to this limiting cathode current would be to grow in a more restricted geometry which requires a lower critical anodic stability parameter (Woldemedhin et al., 2014). This would result in pits that are more likely to grow in depth rather than width as the exposure duration increased.

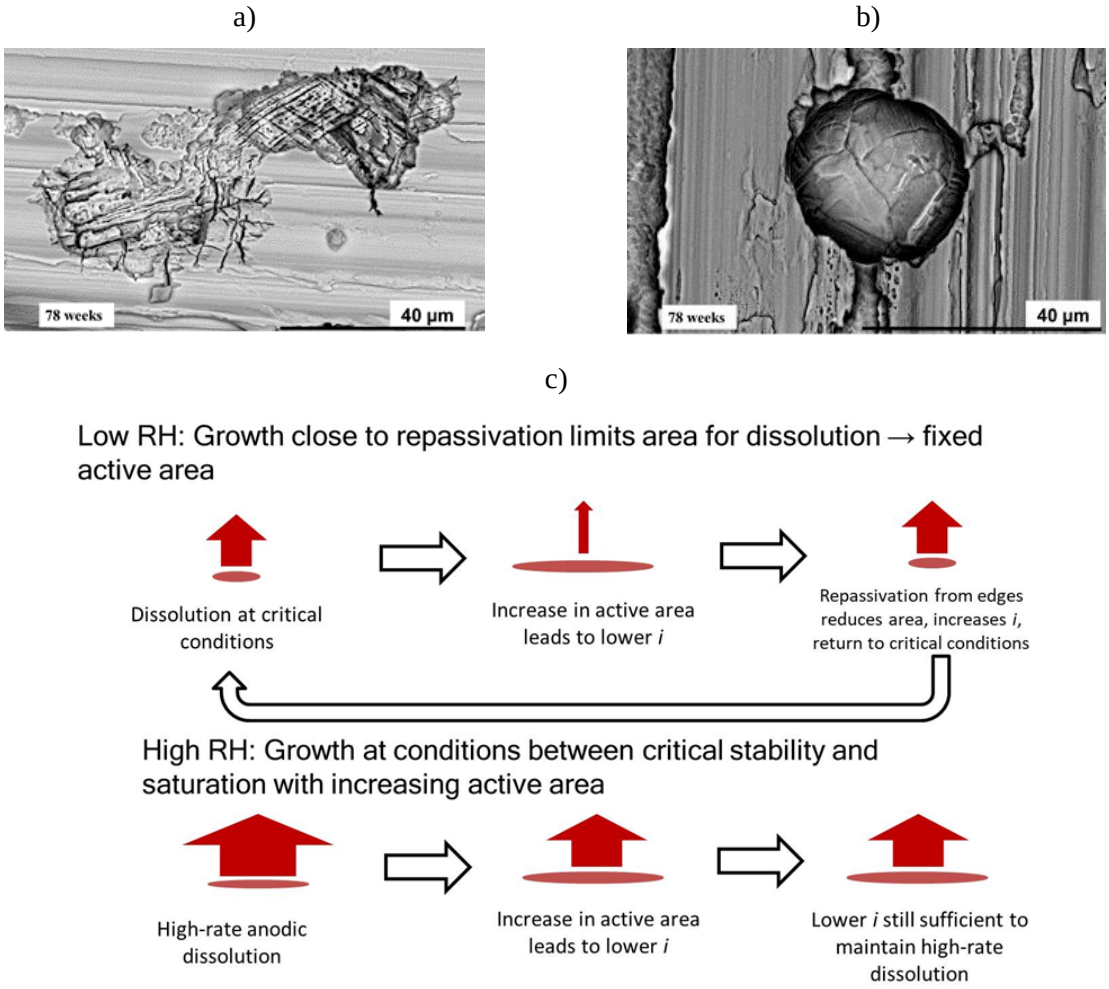

Figure 106. Secondary electron images from SEM indicating pit morphology differences following exposure for 78 weeks at (a) 40% RH and (b) 76% RH. Note the faceting observed in the pits. (c) Schematic outline of the electrochemical rationale for observed difference in pit morphology between RH conditions.(Srinivasan et al., 2020)

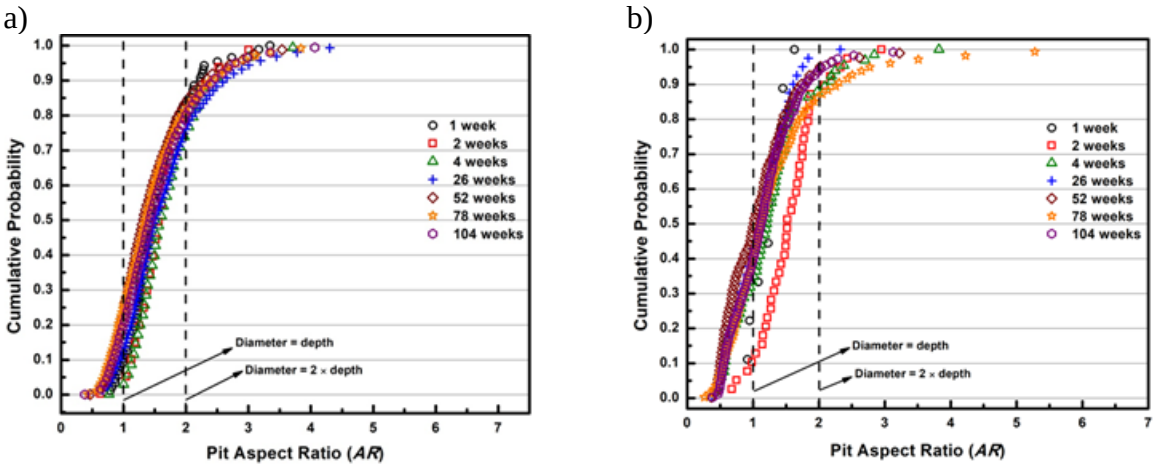

Figure 107. Time-evolution of pit geometry plotted in terms of pit aspect ratio (*AR*) distribution at each timepoint for the (a) 40% RH and (b) 76% RH exposures. *AR* was calculated by dividing the measured pit diameter by the measured pit depth (Srinivasan et al., 2020).

In Figure 108, measurements obtained from OP and XCT are compared, and the OP data were, on average, greater than the corresponding XCT measurements. The trends did not clearly support the idea that XCT provides deeper and more accurate depth measurements due to the potential to resolve features more clearly than pure line-of-sight techniques such as OP (Figure 108-b). However, as these plots are only a summary of a single sample studied and the low number of pits identified (8 for XCT, 14 for OP), these data are not sufficient to conclusively rule out this supposed advantage either. It was found that XCT does have the advantage of providing subsurface pit morphology, such as undercuts and fissures (Figure 108-a). It is therefore advantageous to use both techniques, as OP can provide better lateral resolution while XCT can identify and spatially locate critical subsurface features. Continued efforts in FY21 will explore further these techniques and others for high resolution observation of pit morphology with 3-dimensional detail, including ion mill sectioning combined with SEM imaging. This will not only help elucidate potential differences in pit morphology across exposure environments, but also to identify points of higher stress concentration and/or crack initiation sites not specifically observable or identifiable through OP or SEM imagining alone.

Pitting morphology in atmospheric exposures continues to be dependent on RH/brine composition even at longer exposure times. SEM imaging, OP, and XCT provide useful methods for analysis and comparison of pits across exposures; however, further development of analysis techniques to better measure the true pit morphology may aid in an understanding of pit growth over time in different environments. An enhanced understanding of pit development over time will help the identification of the controlling factors for pit growth and morphology and will better aid in prediction of susceptibility to SCC. The following section explores further the relationship between exposure environment and resultant pit morphology, specifically focusing on brine composition.

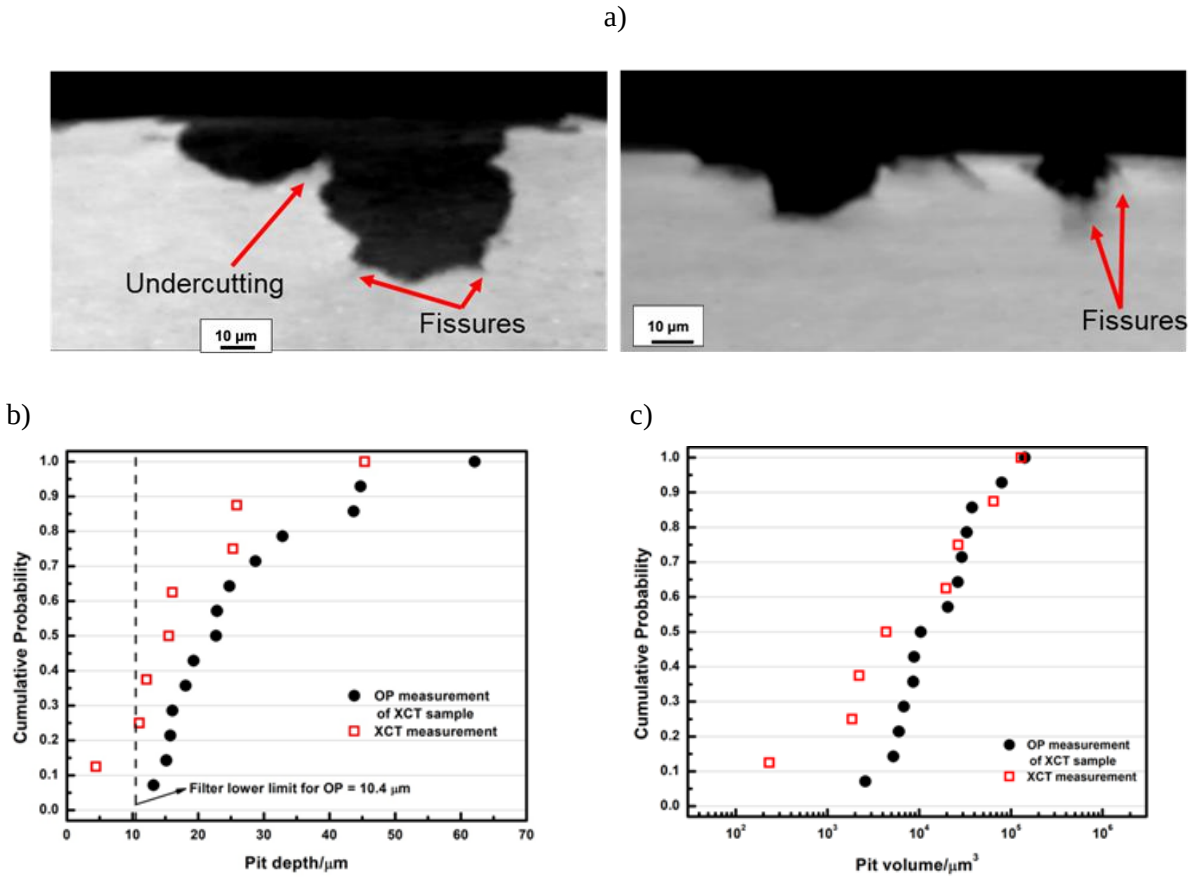

Figure 108. (a) Cross-sectional slices of XCT scans. Possible fissures/microcracks emanating from the pit base and undercutting are indicated in the images. Comparison of geometric data collected by OP and XCT in terms of distributions of (b) pit depth and (c) pit volume.(Srinivasan et al., 2020)

3.1.2 Evaluation of brine composition effects through pitting in full immersion

From work carried out in FY19 & 20, it was hypothesized that specimens exposed at a lower relative humidity exhibit more irregular pits, crosshatching, and increased microcracking due to the presence of Mg^{2+} ions. In FY20, full immersion experiments were explored to isolate the effects of brine composition, by essentially removing the cathodic limitations observed in atmospheric exposures (potential cathode limitations in bulk solution are due to changes of the brine composition/conductivity rather than water layer thickness or droplet size, distribution, etc.). Isolating some of the exposure variables by implementation of full immersion exposures helped to better understand the controlling factors for pit morphology development, especially in the $MgCl_2$ rich brines of interest. SS304L coupons were exposed for 2-7 weeks at 35°C in surrogate brines of NaCl and $MgCl_2$ as well as equivalent seawater brines (Table 26, same compositions as the atmospheric exposures discussed in 3.1.1) to further explore the potential roles of the cations.

Table 26. Summary of exposure brines and pitting observations for SS340L exposed in full immersion environments.

Salt Type	Salt Conc.	Equiv. RH	Equiv Salt	Time	Pitting?
Seawater	-	76%	-	2 Weeks	Yes
Seawater	-	40%	-	1 Week	Yes
Seawater	-	40%	-	2 Weeks	Yes
Seawater	-	40%	-	4 Weeks	Yes
NaCl	5.22 M	76%	NaCl	1 Week	Yes
NaCl	5.22 M	76%	NaCl	2 Weeks	Yes
NaCl	5.22 M	76%	NaCl	7 Weeks	Yes
$MgCl_2$	0.566 M	76%	$MgCl_2$	1 Week	No
$MgCl_2$	0.566 M	76%	$MgCl_2$	2 Weeks	No
$MgCl_2$	0.566 M	76%	$MgCl_2$	4 Weeks	No
$MgCl_2$	0.566 M	76%	$MgCl_2$	7 Weeks	Yes
$MgCl_2$	2.61 M	76%	NaCl	1 Week	No
$MgCl_2$	2.61 M	76%	NaCl	2 Weeks	Yes
$MgCl_2$	2.61 M	76%	NaCl	7 Weeks	Yes
$MgCl_2$	4.47 M	40%	$MgCl_2$	2 Weeks	Yes

Full immersion exposures indicated that brine chemistry was the primary factor governing differences in pit morphology. Immersion tests of SS304L coupons exposed under similar conditions and with similar brine chemistries, i.e. NaCl-dominant or $MgCl_2$-dominant, again exhibited similar pit morphologies to the atmospheric experiments. Hemispherical pits, with faceted, crystallographic attack were observed in NaCl or NaCl-dominated brines, whereas irregular-shaped pits with cross-hatching or microstructural etching were seen in the $MgCl_2$ and $MgCl_2$-dominated brines. Images from the two-week exposure samples are shown in Figure 109 as an example. In short-term exposures, $MgCl_2$ brine, in equal concentration to that in seawater brine at 40% RH, influenced the pit morphology, with irregular shapes and cross-hatching (Figure 109-d); however, it did not result in the microcracking as seen in 40% RH simulated seawater solutions (Figure 109-b).

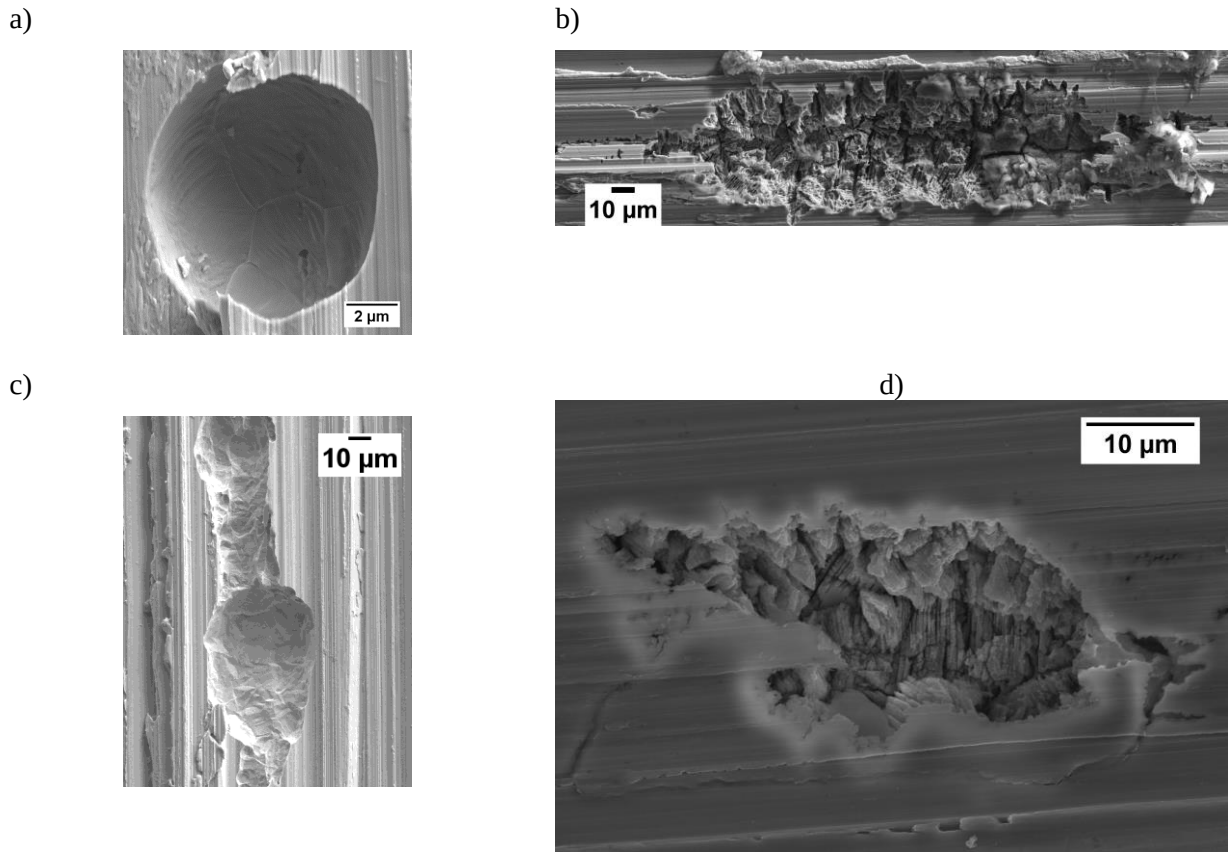

Figure 109. Typical pit morphologies observed for SS304L exposed for two weeks at 35ºC in full immersion in brines of (a) 76% RH simulated seawater, (b) 40% RH simulated seawater, (c) 5.22 M NaCl, and (d) 4.47 M $MgCl_2$.

Through the study of these full immersion exposures, the pit morphology and microcracking observed in the 40% RH atmospheric exposures has been related to the chemical species or chemical concentrations present in 40% RH artificial seawater. Additionally, potential influences due to pH differences between 40% RH seawater and 76% RH seawater could also play a role. FY21 will focus on efforts to further understand the impacts of brine composition on pit morphology, including determination of why and when the microcracking occurs at the irregular shaped pits in some $MgCl_2$-dominated brines. Plans for exposure of annealed samples, to alleviate near-surface stresses imparted by polishing, will help to answer

what microstructural features are governing the localized cross-hatching or selective dissolution in $MgCl_2$ dominated brines.

Overall, $MgCl_2$ brines, as previously discussed in Section 2, are of greater interest as they are expected to dominate the potential brines present on the canister surface for greater than 300 years. Understanding the pit morphology development versus both time and brine composition will help inform predictions for susceptibility to SCC. Moreover, $MgCl_2$-rich brines are of great interest because the irregular-shaped pits with associated microcracking are only observed to develop in these brines; these geometries lend themselves to points of greater stress concentration and thus may be more likely to initiate SCC. In addition to gaining an improved ability to predict pit growth, efforts in FY21 will focus on finite element modeling of real pit geometries formed in these $MgCl_2$ rich brines (obtained from XCT) to determine true stress concentrations and potential features for enhanced SCC initiation.

3.2 Importance of Cathodic Kinetics and Dependence on Brine Composition

In addition to determination of potential pit morphology influences on SCC initiation, the pit size also plays a governing role. The current model for understanding SCC under ISFSI relevant conditions relies heavily on the accurate prediction of the maximum pit size possible for a given environment. Pit size governs where and how stress is concentrated around a pit and the potential for crack initiation.(Turnbull et al., 2006) As such, parameterization and understanding of the potential limitations of current deterministic models for predicting pit sizes (Chen and Kelly, 2010; Macdonald and Urquidi-Macdonald, 1991; Newman, 2002) is necessary. In several SCC and pitting models, it is assumed that the surface external to the crack (or pit) acts as the cathode, supplying the electrochemical driving force for growth (Figure 110). Thus, under the atmospheric conditions pertinent to canisters, the surface environment, which is a function of the relative humidity, temperature, and deposited aerosol load, would be expected to control cathode properties and hence, corrosion damage rates. However, there is a lack of understanding of exactly how the local canister environment affects the cathode properties, and in turn, the corrosion damage rates. This research will address this by quantitatively linking expected canister surface conditions to the electrochemical processes driving pitting (cathodic kinetics), using existing models as an initial basis for understanding.

In FY18 and 19, electrochemical experiments were performed to measure the oxygen reduction reaction (ORR) and the anodic kinetics on 304L and 316L in analog brines representative of chemistries and conditions expected on canisters. This enabled the determination of the pit stability product, $(i \cdot x)_{sf}$, and the repassivation potential (E_{rp}), for input into the maximum pit size model (Chen and Kelly, 2010) and prediction of maximum pit depths for the SNL probabilistic SCC model. Additionally, kinetic parameters were explored in surrogate alkaline brines, devoid of chlorides, to determine the effect of surface chemistry on subsequent cathodic kinetics.

As determination of the brine development on the canister surface has been enhanced over the past few years with increased canister thermal modeling and brine thermodynamic modeling, as well as ISFSI site sampling, interest in $MgCl_2$-dominated brines has increased. These brines have the potential to form within the first 10-20 years as the canister surface cools and are expected to persist for greater than 300 years, before RH conditions are such that NaCl-dominant brines can form. In FY19 and 20, potentiodynamic measurements were expanded to include sea-salt and simulated brines expected to form in these canister relevant conditions ($MgCl_2$ and artificial seawater) as well as alkaline solutions (representative of cathodic regions). The focus was to both generate data as input for SNL's SCC model, specifically with respect to the maximum pit size, and determine potential limitations of the model. The emphasis on $MgCl_2$ brines follows the developments made both in the understanding of persistence of $MgCl_2$-dominated environments for longer time frames and the irregular corrosion morphologies observed in $MgCl_2$ brines, which may lead to stress concentrators and potentially enhance SCC initiation (discussed further in 3.1.1). The $MgCl_2$ brine research performed in FY20 resulted in the development of

three manuscripts, two which have been published (Appendices A and B) and a third that is currently under review. These will be briefly summarized here.

Prior to summarizing the published works, a brief review of the Chen and Kelly (Chen and Kelly, 2010) maximum pit size model is presented here for context. This model relates the maximum predicted pit size to the available cathodic current under a specific water layer thickness and brine composition (schematic in Figure 110).

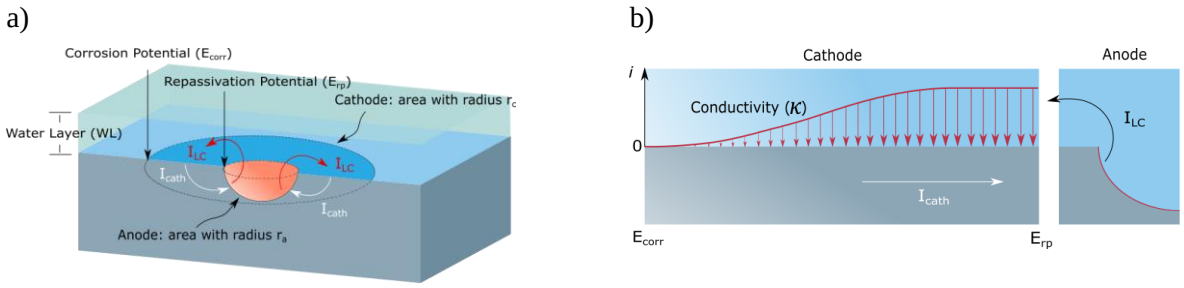

Figure 110. Conceptual schematic of electrochemical SCC model proposed by Chen and Kelly, a) view of pit, and b) current across the anode and cathode.(Katona et al., 2019)

The maximum cathode current, $I_{C,max}$, can be determined by:

$$lnI_{C,max} = \frac{4\pi\kappa(WL)\Delta E_{max}}{I_{C,max}} + ln\left[\frac{\pi e r_a^2 \int_{E_{corr}}^{E_{rp}} (i_c - i_p) dE}{\Delta E_{max}}\right]$$

Where κ is brine conductivity, WL is the brine thickness, and ΔE_{max} is the difference between the E_{rp}, repassivation potential, and the E_{corr}, corrosion potential, e, is the number of electrons transferred, ra, is the radius of the anode, and i_c (cathodic current density) and i_p (passive current density of the cathode), represent the cathodic kinetics.

The maximum pit size, r_{max}, can be determined from the intersection of the anodic current demand with the maximum cathode current:

$$I_{LC} = \left(\frac{i_{pit}}{r_{pit}}\right)_{crit} r_a$$

where i_{pit}/r_{pit} is the pit stability (related to i·x by geometry) and I_{LC} is the current required to produce a pit of radius r_a, with the maximum cathode capacity (calculated from the acquired cathodic polarizations). Results of calculations for saturated $MgCl_2$ are shown below as an example in Figure 111, where the intersection of the I_{cath} (solid line) and the corresponding I/r (dotted line) represents the maximum pit size (373.5 µm) predicted under the brine (4.98 M $MgCl_2$) and exposure conditions used in testing. Using the maximum pit size framework, it was found in previous work, that an increase in pit size and cathode radius occurred with increasing chloride concentration and temperature (Katona et al., 2019).

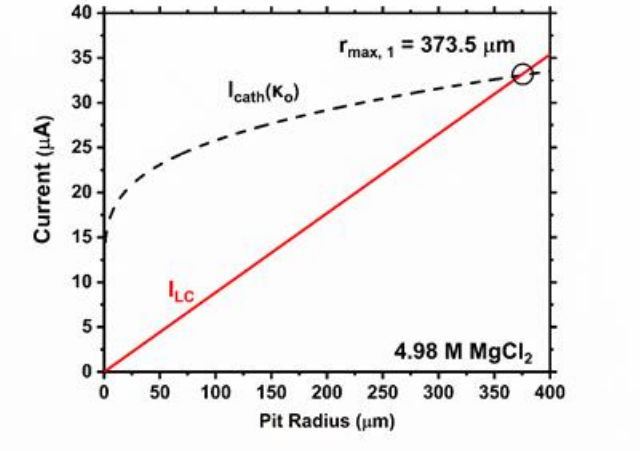

Figure 111. Cathode current and anode current for saturated $MgCl_2$ (4.98 M, RH = 38 %) at 25ºC. ILC is that needed to maintain concentration of 50% of saturation.(Katona et al., 2020a)

The current maximum pit size predictions are produced using a model that makes several overarching assumptions including treating the pits as hemispherical in shape, the brine layer as a uniform thin film with static properties, and exposure in a homogeneous material and mechanical environment (e.g., stress/strain). Work in FY 20 focused on addressing and adjusting assumptions made, primarily with regards to the static brine conditions in $MgCl_2$ brines and is summarized below.

3.2.1 Use of in situ Raman spectroelectrochemical technique to explore atmospheric corrosion in marine-relevant environments

The first manuscript (Appendix A) addresses the assumption that the brine layer is static and unchanging over time. During cathodic polarization in $MgCl_2$ brines, formation of a thin film, or coating on the surface, was observed for SS materials, however, was uncharacterized during experimentation in FY19. In FY20, through development of in situ Raman techniques, a method for chemical identification measurement in flow cell environments was developed and validated. It was then applied to the relevant SNF exposure conditions. As seen in Figure 112, a magnesium hydroxide film was identified to form during in situ cathodic polarization of the SS304L in $MgCl_2$ brine. This not only provided the first characterization of this film formation *in situ*, but also confirmed details of brine development over time, including pH evolution. This work helps inform model inputs for the enhanced prediction of maximum pit sizes. The detailed description of the development of this Raman technique, including experimental methods, equipment testing and calibration procedures, and identification of film formation is described in the published manuscript in Appendix A. Additionally, the identification of this film helped further establish the scientific understanding of the cathodic kinetics in $MgCl_2$ brines that govern pit growth, as discussed in sections 3.2.2 and 3.2.3.

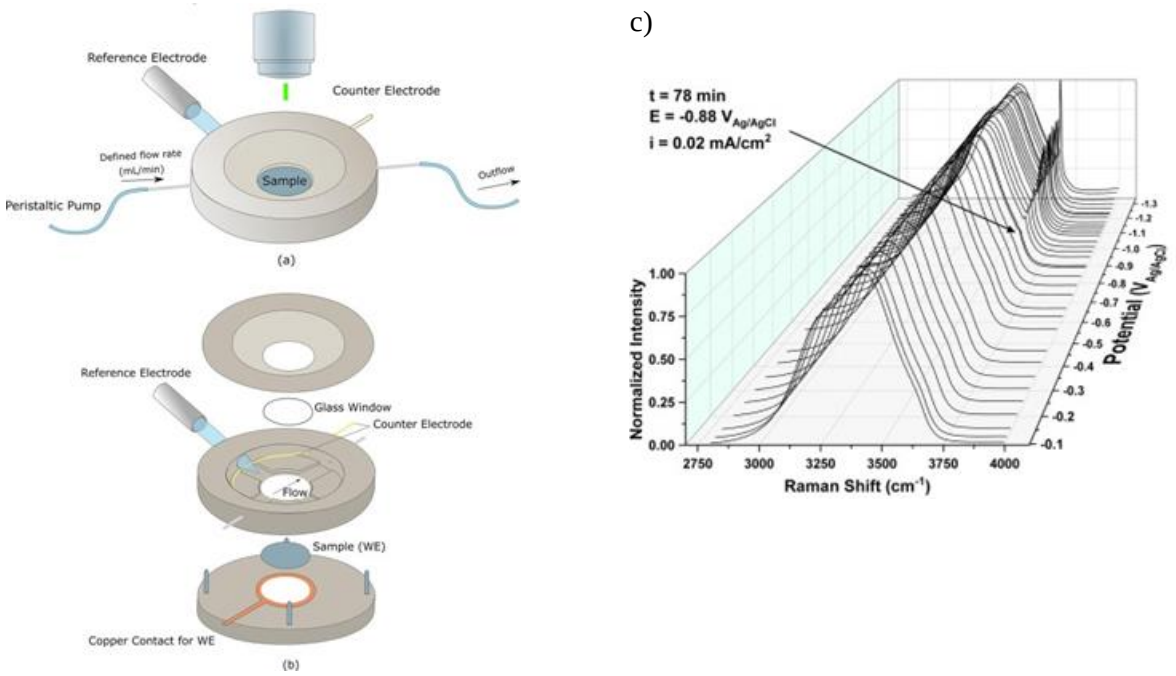

Figure 112. Experimental setup for *in situ* Raman analysis: (a) overall set-up and (b) inside configuration of flow cell. (c) Polarization scan of SS304L in 0.189 M $MgCl_2$ with i*n situ* Raman characterization as a function of potential indicative of $Mg(OH)_2$ formation (Katona et al., 2020b).

3.2.2 Importance of the hydrogen evolution reaction in $MgCl_2$ solutions on stainless steel

Experiments performed in FY19 in $MgCl_2$ solutions highlighted possible limitations of assumptions applied in the current maximum pit size model. This was further explored and evaluated in a manuscript developed and published in FY20 in Appendix B (Katona et al., 2020a) in which the controlling cathodic kinetics were evaluated. Experimental methods, equipment testing and calibration procedures, and data collection is described in the published manuscript in Appendix B. While Pt electrodes continue to display a 2-electron transfer for ORR in $MgCl_2$ solutions (Figure 113-a), the SS304L electrodes displayed non-Levich behavior for ORR (Figure 113-b). This was determined not to be governed by precipitation of Mg-carbonates through CO_2-scrubbed cathodic polarizations in Figure 113 (further validated by the Raman measurements described previously). Rather, this was indicative of ORR suppression and buffering of near surface pH by Mg-hydroxide or hydroxychloride species precipitation. The primary cathodic reaction is shifted to the hydrogen evolution reaction (HER) in saturated $MgCl_2$. Implications of the dominance of HER in the cathodic kinetics are discussed throughout the manuscript with regards to atmospheric corrosion and stress corrosion cracking. In summary, as ORR is suppressed as the dominant cathodic reaction, the available cathodic current density is also suppressed, thus reducing potential pitting damage across the surface. Additionally, as precipitates form, brine volume decreases; this can lead to brine dry-out on the surface (Schindelholz and Bryan, 2018). Third, the cathodic sites can become physically blocked by precipitates, thus reducing available cathodic area and again reducing the cathodic current density. And finally, insoluble precipitates can alter the conductivity of the brine layer. While the dominance of HER as the cathodic reaction may lead to a reduced cathodic current availability, it has also been suggested that the influence of the HER may lead to the near surface micro-cracking observed in long term pitting exposures in $MgCl_2$-dominant brines (section 3.1.1). Therefor further study into pitting

and SCC initiation in $MgCl_2$-dominant brines is necessary to fully understand the SCC susceptibility under canister relevant conditions. The influence of the non-static brine conditions on the maximum pit size is further explored in the third manuscript produced on this topic in FY20, and is summarized below in Section 3.2.3.

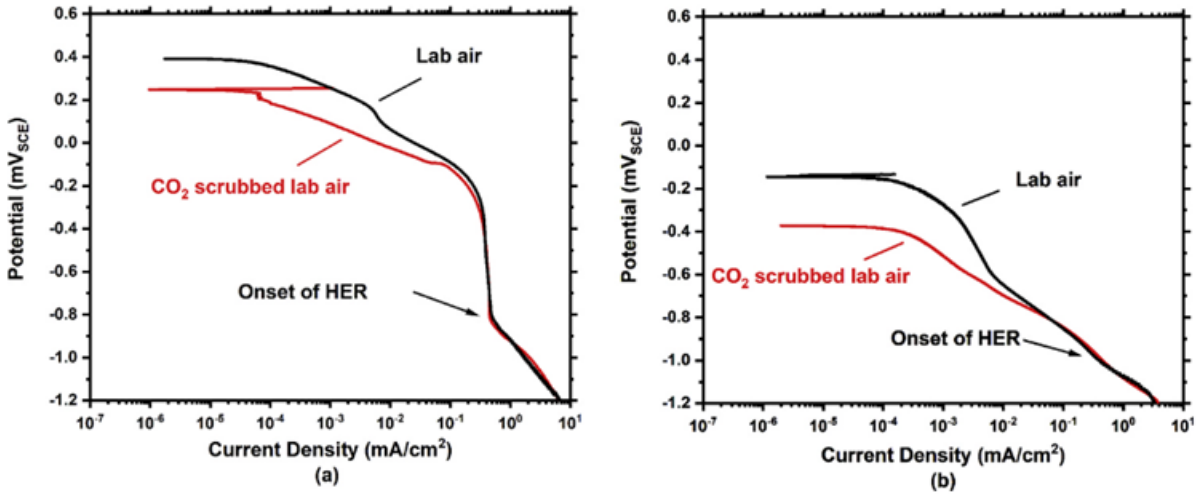

Figure 113. Polarization scans on (a) Pt and (b) SS304L in the presence of atmospheric CO_2 and with the sparged CO_2 concentration <1 ppm in 0.189 M $MgCl_2$ at a rotation rate of 500 rpm (Katona et al., 2020b).

3.2.3 Quantitative assessment of environmental phenomena on maximum pit size predictions in marine environments

The current Chen and Kelly model (Figure 114-a) does not account for the significant effects of brine evolution and corrosion on the environmental conditions, as it applies the assumption of a static brine without changing composition, conductivity, or morphology over time. Solution conductivity is one of the important factors in the current pitting model. When there are solid products, such as insoluble hydroxides or carbonates, the conductivity decreases in solution (Figure 114-b). In addition, as mentioned, cathodic sites can be physically blocked by solid precipitates (Figure 114-c). A decrease in conductivity will decrease the overall cathodic current available for dissolution; thus, the maximum achievable pit size will decrease, all else being held constant. Another phenomenon that can occur in these $MgCl_2$ solutions is dry-out of the cathode. As pointed out by Bryan and Schindelholz (2018a), highly deliquescent $MgCl_2$ can be replaced with a non-deliquescent solid and the brine will dry out as reactions on the surface (corrosion) progress to completion. This means one of two things can happen: (1) the equivalent cathode size can decrease or (2) the water layer will decrease (Figure 114-d). In both cases, the current the cathode can supply will decrease, and decrease the maximum attainable pit on the surface.

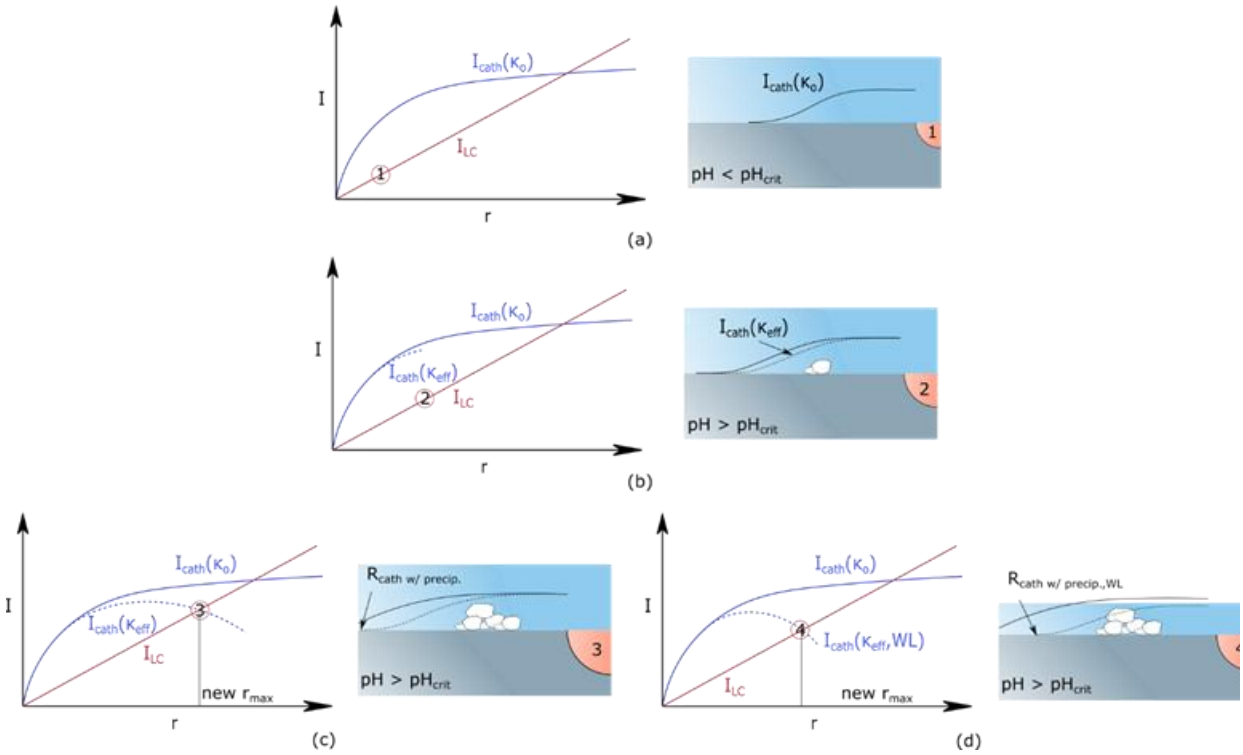

Figure 114. Qualitative representation of governing reactions for atmospheric corrosion and relative severity for solutions containing precipitates. (a) A small pit that has not reached the bounding cathodic current nor the critical pH for precipitation. (b) A medium sized pit that has not reached the bounding cathodic current however has reached a pH in which precipitation is thermodynamically possible. (c) Maximum pit size when only precipitation is considered in the cathode. (d) Maximum pit size when precipitation and dehydration are considered in the cathode.(Katona et al., 2020c)

Again, in the current maximum pit model, dynamic brine conditions, such as changing conductivity, precipitation, and dry-out, are unaccounted for. The maximum pit size model studies in FY20 addressed these concerns, accounting for each in the maximum pit model in high and low concentration NaCl and $MgCl_2$ brines as well as seawater. Figure 115 displays the influence of each of these phenomena on the calculated maximum pit size; (a) shows the influence of the change in conductivity in 4.98 M $MgCl_2$, with a reduction in pit radius by almost 75 µm. Figure 115(b) displays the influence of dehydration of the brine due to precipitation, where the radius for the maximum pit size dropped roughly 150 µm. Finally, Figure 115 (c) displays the influence of a precipitate film present on the surface in 0.189 M $MgCl_2$, which results in a drop of the predicted maximum pit size radius by almost half.

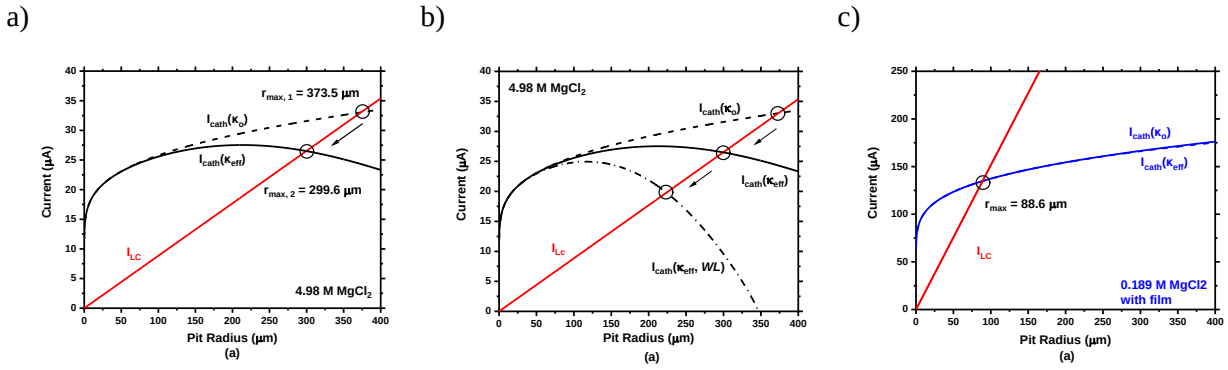

Figure 115. Maximum pit predictions shown (a) both with and without the consideration of precipitation in the cathode for 4.98 M $MgCl_2$. LD = 3 g/m^2 and I_{LC} is for 50% of salt film saturation on the surface of the pit. (b) Effect of dehydration reactions on maximum pit sizes predictions for 4.98 M $MgCl_2$. A pit saturation level of 50% was used with LD = 3 g/m^2. (c) Influence of $Mg(OH)_2$ film on the surface of SS304L on maximum pit size predictions for 0.189 M $MgCl_2$.(Katona et al., 2020c)

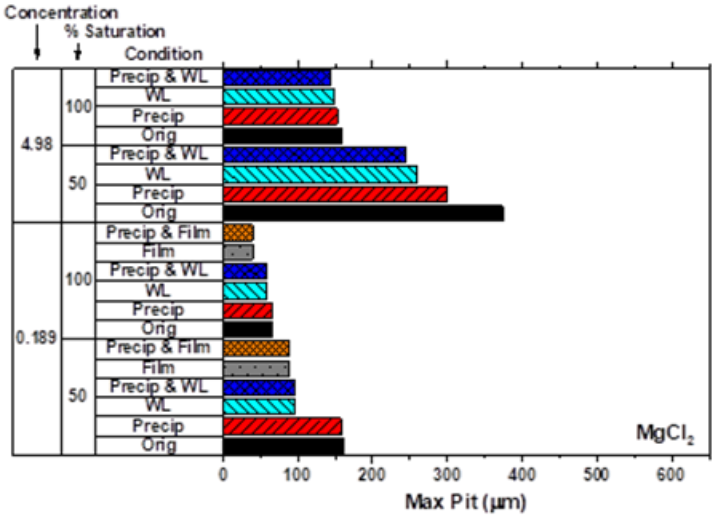

Figure 116. Influence of all cathode evolution scenarios explored for $MgCl_2$ electrolytes on pit size. LD = 3g/m^2 in all scenarios. The labels correspond to the following scenarios: Orig – Original maximum pit formulation; Precip – Considering precipitation reactions and the influence on conductivity; WL – considering only dehydration reactions; Precip & WL – considering Precip. and WL together; Film – Original formulism with new cathodic polarization; Precip & Film – New cathodic polarization scan and precipitation reactions.(Katona et al., 2020c)

These effects were not only evaluated as singular influences, but their combined consequences were considered across 0.6 and 5 M NaCl, 0.189 and 4.98 M $MgCl_2$, and the equivalent seawater brines at 40 and 76% RH. Example results of the implications on the predicted maximum pit size for the $MgCl_2$ brines are shown in Figure 116. In all cases, inclusion of the influences of a non-static brine in the maximum pit size model reduces the maximum pit size predicted. This is of particular significance to

potential predictions for risk of SCC, because SCC initiation is dependent on pit size. Thus, a reduction in pit size in $MgCl_2$-dominated brines could lead to a potential reduction in severity for SCC.

3.3 Significance of $MgCl_2$ Brines for Corrosion and SCC Initiation

Continued modeling efforts in FY20 combined with increased ISFSI site sampling has aided the further determination of canister-relevant environments. Specifically, analysis of brines at the Maine Yankee ISFSI has helped elucidate composition of the potential brine formation in near-marine sites. Applying the information gained about these brines to develop enhanced corrosion testing in FY21; including both potential corrosion accelerants (cycling and dust) and inhibitors (nitrates) will help further parameterize the maximum pit model for canister-relevant conditions and determine significant factors for corrosion and SCC initiation. Additionally, as results have shown that $MgCl_2$-dominant brines will be present for long time periods (>300 years) on the canister surface, emphasis on testing in FY20 has focused on these environments. FY21 will continue to explore these $MgCl_2$ rich brines because two significant factors for pitting and potentially, SCC initiation have been established: 1) $MgCl_2$ brines influence the pit morphology towards the formation of more irregular shapes with near surface microcracks and 2) $MgCl_2$ brines influence the controlling cathodic kinetics through dominance of the HER cathodic reaction and formation of precipitates that lower the predicted maximum pit size. Understanding how these potentially competing effects enhance or reduce the potential for SCC initiation will be one focus of studies in FY21. Efforts focused on FEA modeling of stress concentrations around real geometries of irregular-shaped pits formed in $MgCl_2$ brines will provide insight into their significance for SCC initiation. Additionally, tensile testing in $MgCl_2$ brines and atmospheric environments will help determine SCC initiation rates under such conditions.

3.4 Weld Characterization

SNF canisters consist of 304 SS with multi-pass welds, predominantly utilizing the submerged arc welding process with a double-V edge preparation (Figure 117-a). During the gas tungsten arc welding (GTAW) process, the weld material experiences high temperatures, ranging from 400 – 800 °C, and varied cooling rates both of which can greatly modify the microstructure of the weld and near weld regions. The high temperatures and cooling rates are governed by the welding parameters such as heat input ([current × potential]/travel speed), inter-pass temperature, material thickness, and thermal properties of the material (Paulraj and Garg, 2016). When high heat inputs occur, there are significantly higher temperatures and slower cooling rates observed within the SS material. The resultant microstructure and residual stresses developed in the weld and heat affected zone (HAZ) are determined by these input parameters (Murugan et al., 2001). With the presence of high tensile residual stresses and subsequent installation of the canister at an ISFSI site, where aerosol deposition and cooling of the canister surface over time can lead to brine formation; chloride-induced stress corrosion cracking (CISCC) may cause early or unexpected failure of the canister leading to potential risk of exposure (Enos and Bryan, 2016b). In FY20, a better understanding of specific microstructural development and weld characterization was carried out in order to support determination of canister-relevant material susceptibility to CISCC. Investigations focused on development of the microstructure in and around the weld, including the HAZ, and the factors that contribute to the changes in residual stress and local microstructure. These factors include potential sensitization due to elemental microsegregation in the weld and HAZ and/or new microstructural formation (grain size, delta ferrite, etc.) (de Lima-Neto et al., 2008), the degree of work hardening due to weld shrinkage (hardness $\propto$ work hardening) (Milad et al., 2008), and residual stresses (Murugan et al., 2001). The focus on these factors is due to their likely detrimental impact with respect to corrosion and CISCC resistance of the material (Angeliu et al., 2000; de Lima-Neto et al., 2008; Enos and Bryan, 2016b; Milad et al., 2008; Mirshekari et al., 2014; Murugan et al., 2001; Nikitin and Besel, 2008; Phillips, 2016; Prevey et al., 1996; Singh and Shahi, 2018; Unnikrishnan et al., 2014).

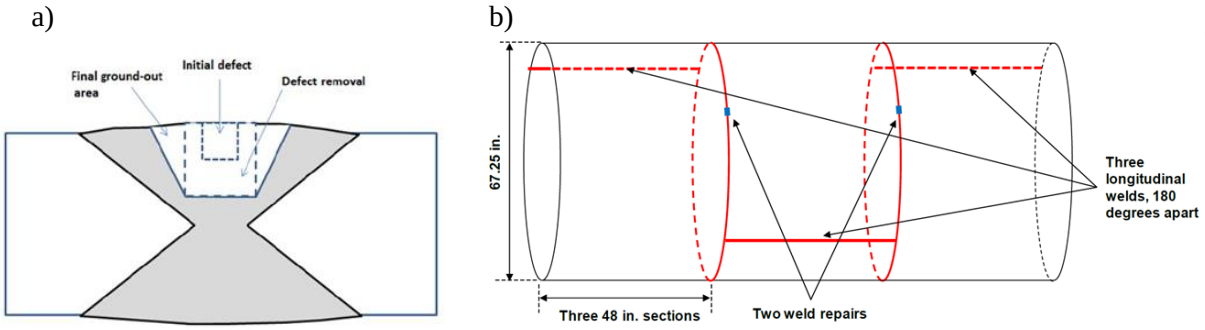

Figure 117. (a) Cross-sectional weld schematic representing a re-welded defect region using the gas tungsten arc welding technique. (b) The full-scale mock storage container manufactured at Ranor.(Enos and Bryan, 2016b)

3.4.1 Factors Influencing the Weld Microstructure

Sensitization of SS occurs during heating of material through a specific temperature range, typically 400-800 °C (de Lima-Neto et al., 2008). Within this temperature range, the diffusion of chromium initiates and allows for the precipitation of chromium carbides, $M_{23}C_6$ (where M is Cr), to take place at the grain boundaries (gb) (Willis, 1990). Precipitation of these carbides along the gbs depletes the nearby surrounding matrix of Cr, thus lowering the corrosion resistance of the passive layer in the near-gb regions (Mirshekari et al., 2014). This high temperature range is commonly achieved in welding processes such as arc welding, applied on the SS canisters. The SS material is susceptible to sensitization in the weld and heat affected zone (HAZ) and the degree of this sensitization depends on the specific input parameters. However, lower C content materials, such as SS304L, of which the canisters are made, can alleviate concerns of carbide precipitation, thus reducing susceptibility to sensitization. In addition to sensitization, Mishekari et. al (2014), showed that different cooling rates dictated the formation of ferrite and austenite (γ) in the weld and HAZ. During the cooling process, it was observed that the primary δ-ferrite solidifies first in the fusion zone, followed by the $\delta \rightarrow \gamma$ transformation. With the $\delta \rightarrow \gamma$ transformation being a diffusion-controlled process, there is insufficient time to complete the phase transition under the fast-cooling rates of the GTAW process (Mirshekari et al., 2014). It has been observed that a skeletal δ-ferrite morphology is formed during slow cooling rates, where austenite consumes ferrite until ferrite is sufficiently enriched in ferrite-promoting elements (Cr) and depleted in austenite-promoting elements (Ni) that are stable at lower temperatures where diffusion is limited. However, when the cooling rates were sufficiently high, a lathy δ-ferrite morphology was formed. This lathy morphology phase forms due to restricted diffusion during the ferrite–austenite transformation. It was shown that the enhanced chloride sensitivity of the HAZ in stainless steel specimens after repeated welding is due to the transformation of the original ferrite phases in the austenite matrix into a fine distribution of short ferrite precipitates (Garcia et al., 2008; Kokawa et al., 2000; Lin et al., 1995; Martins et al., 2004; Palumbo and Aust, 1990; Srinivasana and Kumar, 2009; Stoenescu et al., 2007). Since these short ferrite precipitates are susceptible to corrosion, Cl^- ions will preferentially attack these small ferrite phases and lower the overall corrosion resistance of the material (Lin et al., 2012).

During the welding process, the base and weld material undergo work hardening due to weld shrinkage. When the SS material begins to cool, weld shrinkage occurs during the solidification of the metal in the weld fusion zone (FZ) (Enos and Bryan, 2016b). In order to ensure that there is minimal deformation that occurs, the SS material is cold worked prior to welding. When cold working, plastic deformation occurs which in turn can increase the stress resistance of the SS material (Milad et al., 2008). However, this property can also exacerbate the effects of sensitization when exposed at higher temperatures. Shah et al. (1990), found that the degree of cold work prior to annealing impacted the SS material. Samples that

were cold worked at 5% and annealed at 400 ºC demonstrated no sensitization. However, for 304 SS samples cold worked at 10%, 20%, and 30%, sensitization occurred as low as 400 ºC. This implies that the degree of cold work greatly impacts the sensitization temperature. Shah found that cold work can induce low temperature sensitization susceptibility even if carbide nuclei are absent. With cold working, it is kinetically feasible for precipitation and growth of chromium carbides at the grain boundaries to occur without the introduction of high temperatures due to an increase in dislocation density which, in turn, causes an increase in diffusion rates for Cr. This may play a significant role for multi-pass welds (relevant to canister construction), because even though the high temperatures necessary for Cr diffusion may not be achieved, the cold work due to work hardening from weld shrinkage could lead to lower temperature sensitization.

During the welding process, as mentioned, the SS material undergoes thermal expansion, followed by rapid cooling, which can lead not only to work hardening, but to residual stresses within the weld and HAZ. Residual stresses not only affect the fatigue life of the material but can also decrease the overall corrosion resistance (Unnikrishnan et al., 2014). As described above, the weld process and parameters greatly impact the properties of the SS material. Murugan et al (Murugan et al., 2001) showed that the first weld pass on SS material resulted in residual stresses, with the peak tensile stress on the root side (base) of the weld. However, the peak tensile stress on the root side will be reduced with increasing the number of passes in stainless steel. With the additional weld passes, the temperatures seen by the top surface increased, leading to progressively higher residual stresses at the top surface and redistribution of residual stresses in the weld pad (Murugan et al., 2001). Another example from Unnikrishnan et al. (Unnikrishnan et al., 2014) discussed the impact of residual stresses after welding 304L SS at different heat inputs. It was shown that residual stresses were tensile near the weld region that saw the highest heat input (0.85 kJ/mm) and were compressive in regions of the lowest heat input (0.58 kJ/mm). Overall, it was observed if tensile residual stresses remain in the SS material, the material displayed increased susceptibility to CISCC (Murugan et al., 2001).

Sensitization, the degree of work hardening due to weld shrinkage, and residual stresses are the main factors that contribute to the potential lowering of corrosion and SCC resistance in welded SS material. Understanding the specific microstructural behavior of a weld can lead to developing strategies and solutions to counter these detrimental impacts to the weld microstructure, which will in turn, lead to improvement of DCSS's lifetime and decrease the risk of exposure due to SCC.

3.4.2 Canister Mockup Welds

The welds investigated herein are from the SNL Canister mockup detailed in "*Final Report: Characterization of Canister Mockup Weld Residual Stresses*"; a summary of the welding procedures is provided in that document (Enos and Bryan, 2016b). The design schematic of the canister mockup can be seen in Figure 117-b. Three plates are cold formed into a cylinder and then is welded using a single longitudinal weld to form a closed cylinder. The dimensions of an individual cylindrical shell are 48 inches in length, 67.2 inches in diameter, and 5/8 inches thick. All three cylinders were then welded together using two circumferential welds to form a single large cylinder, 12 feet in length. Each cylindrical shell is made of dual-certified 304/304L SS. The weld filler metal used was 308L SS. The compositions of the 304/304L SS plates and the 308L SS filler material are given in Table 27.

Table 28 shows the parameters for the multi-pass submerged-arc welding (SAW) process. Before each weld, a 30-degree bevel with a quarter inch land was used. The inner diameter was welded first, followed by the outer diameter. Each inner-diameter weld consisted of three passes, and each outer-diameter weld was made with four, with one exception (the exception had 5 passes on the outer diameter).

Table 27. Composition of 304L Plate and 308L Filler Metal Used to Construct Mockup.

	C	Co	Cr	Cu	Mn	Mo	N	Ni	P	S	Si
Plate Material (304/304L)	0.0223	0.1865	18.1	0.4225	1.7125	0.318	0.0787	8.027	0.0305	0.0023	0.255
Weld Filler (308L) (lot)	0.014	--	19.66	0.16	1.7	0.11	0.058	9.56	0.025	0.01	0.39
Weld Filler (308L) (lot 2)	0.012	--	19.71	0.192	1.73	0.071	0.053	9.75	0.024	0.012	0.368

Table 28. Example of Weld Parameters for One Longitudinal and Horizontal Weld.

	Interpass temperature	Amperage	Voltage	Travel Speed (IPM)	Heat Input (J/in)
Longitudinal Weld Joint 1 (WJ-1)					
ID - Pass 1	74	400	30	15.4	46753
ID - Pass 2	199	400	30	15.42	46755
ID - Pass 3	214	400	30	15.4	46753
OD - Pass 1	69	400	30	15.16	474493
OD - Pass 2	104	400	30	15.16	474493
OD - Pass 3	110	400	30	15.16	474493
OD - Pass 4	177	400	30	15.16	474493
Horizontal Weld Joint 4 (WJ-4)					
ID - Pass 1	70	400	30	16.4	43902
ID - Pass 2	199	400	30	16.4	43902
ID - Pass 3	214	400	30	16.4	43902
OD - Pass 1	74	400	30	15.8	45454
OD - Pass 2	85	400	30	15.8	45454
OD - Pass 3	110	400	30	15.8	45454
OD - Pass 4	88	400	30	15.8	45454
OD - Pass 5	97	400	30	15.8	45454

It has been indicated that repairs are necessary at regions along the welds where the nondestructive testing indicated that the weld did not conform to the criteria of the ASME code which addresses the rules for construction of nuclear facility components and supports (*ASME B&PVC Section III, Division 1, Subsection NB*). Repair regions have been identified by numerous researchers as having dramatically elevated residual stresses when compared to unrepaired portions of a weld (Bouchard et al., 2005; Dong et al., 2005; Dong et al., 2002; Elcoate et al., 2005; George and Smith, 2005; Hossain et al., 2011; Hossain et al., 2006). During fabrication of the mockup, all the welds were subjected to a full radiographic inspection, and no indications requiring repair were found. As the primary purpose of the mockup was to measure weld residual stresses, weld repair regions were of great interest. For that reason, two simulated weld repairs were added.

The base material used for all experimental procedures was dual certified 304/304L SS cut from weld sections of the mockup canister. Samples with dimensions of 76.2 x 12.7 x 15.9 mm, were waterjet cut from the circumferential and longitudinal weld plates (Figure 118). The chemical composition of the SS material is shown in Table 27.

a) **b)**

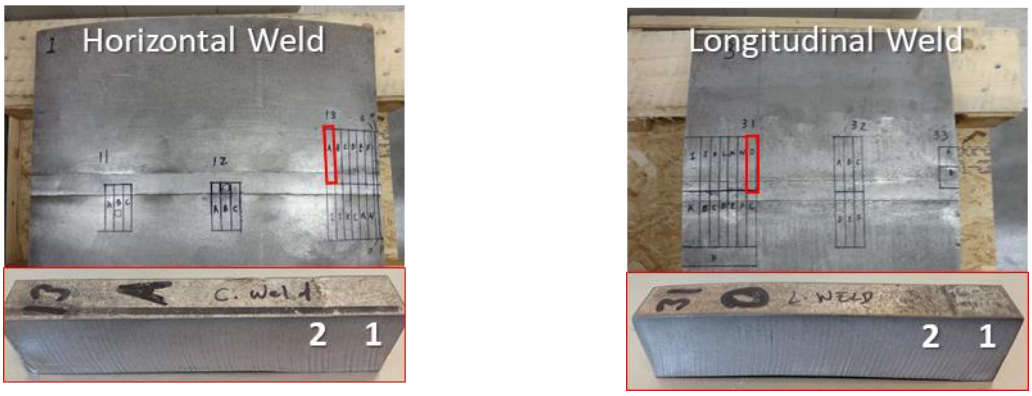

Figure 118. (a) Weld section 13-A from the horizontal weld. (b) Weld section 31-O from the longitudinal weld. Both sample insets are labeled 1 and 2; where region 1 is the measured region from the weld and 2 is the measured region from the HAZ for DLEPR testing.

3.4.3 Mockup Weld Characterization

In order to understand the weld metal properties, the weld and HAZ regions were evaluated for possible sensitization, increased hardness, and changes in microstructure, which can all affect corrosion properties. The applied methods include the double loop electrochemical potentiodynamic reactivation (DLEPR) tests (ASTM International, 2015c), microstructural etching, SEM combined with electron backscatter diffraction (EBSD), microhardness mapping, and surface stress measurements (center hole drilling).

3.4.3.1 Sensitization - Double Loop Electrochemical Potentiodynamic Reactivation Tests

The DLEPR technique, for evaluation of possible sensitization in and near the weld, was performed in accordance to ASTM G108-94.(ASTM International, 2015c). All samples were ground to a 1200 grit SiC finish then cleaned in ethanol and soapy water respectively, followed by a DI water rinse. The samples were epoxy-mounted with the region of interest exposed in a standard three electrode horizontal flat cell, with a Pt mesh counter electrode and an Ag/AgCl electrode as the reference. The testing solution used was reagent grade sulfuric acid (H_2SO_4) and potassium thiocyanate (KSCN) in reagent-grade water as follows: 1 L of 0.5 M H_2SO_4 + 0.01 M KSCN. The potentiostat was set to a 0.1667 mV/s scan rate with an initial applied voltage of -200 mV versus the open circuit potential (OCP), then scanned up to 0.3 $V_{Ag/AgCl}$, and reversed down to -0.5$V_{Ag/AgCl}$.

To determine sensitization, the following ratio was examined (International Standard ISO, 2006). The peak current for the reactivation scan (I_r) and for the activation scan (I_a) were measured (as noted on Figure 119-a for the weld polarization) and the ratio taken as:

$$Degree\ of\ Sensitization = \frac{I_r}{I_a}$$

After obtaining values for the degree of sensitization, $\frac{I_r}{I_a}$, the following table was used to determine the level of sensitization (Table 29). The threshold for sensitization to occur is a ratio above 0.01, indicating that the measured region exhibits microstructure that has been sensitized.

Table 29. Correlation of I_r/Ia with the degree of sensitization

$\frac{I_r}{I_a}$ value	General Interpretation of the degree of sensitization
< 0.010	Unsensitized
0.01 to 0.05	Slightly sensitized (might pass Streicher, Strauss and Huey tests)
> 0.05	Sensitized (could pass Streicher, Strauss and Huey tests)

In FY20, two regions from the horizontal and longitudinal welds were examined; one in the weld and one in the HAZ. In example polarization scans from the longitudinal weld (Figure 119-a) and images below, the region in the HAZ (Figure 119-b), demonstrated an extremely low Ir/I_a ratio of 6.6 x 10^{-5}, which indicated the region was unsensitized. This may be in part due to the low C content (0.0223 wt%) of the dual-certified SS304/SS304L. The region in the weld (Figure 119-c) demonstrated a value that is above the threshold for sensitization ratio (0.102). However, it was determined that the measured value was enhanced by the dissolution of delta ferrite; based on the morphology of the attack in the weld region following polarization (and subsequent comparison to microstructural characterization in the following sections), where the preferential dissolution appears to occur along regions where δ-ferrite had precipitated. In FY21, continued DLEPR testing will be conducted on all regions of the samples in order to further evaluate the potential sensitization of both the horizontal and longitudinal welds.

a) b) c)

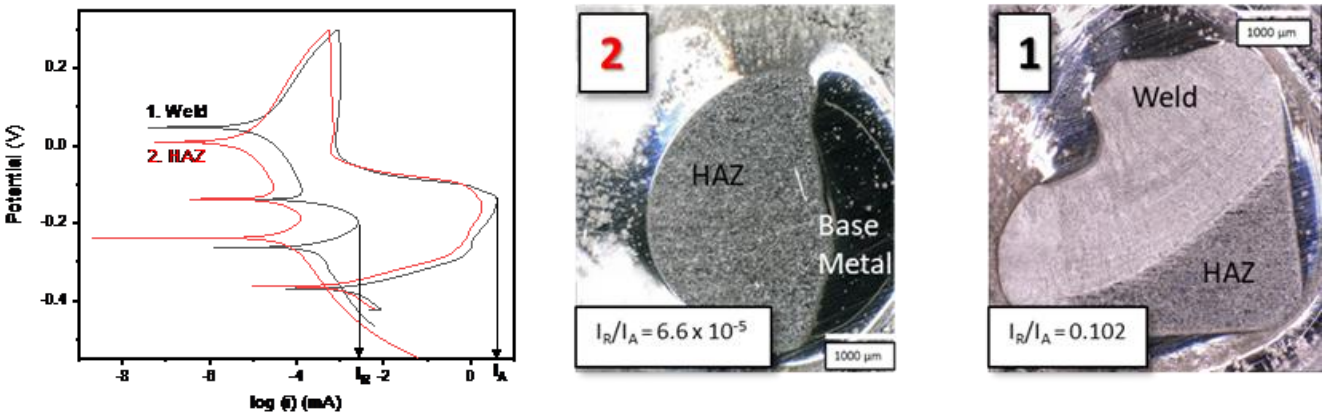

Figure 119. (a) DLEPR Potentiodynamic polarization for the longitudinal weld and HAZ regions. (b) optical micrograph of region 2, primarily the HAZ and (c) region 1, primarily weld.

3.4.3.2 Microstructural Characterization - Optical

Microstructural evaluation of the horizontal and longitudinal welds via optical microscopy was performed on etched samples to observe the weld and HAZ regions (Figure 120). Samples were etched in a 60/40

ratio of HNO_3/H_2O solution at an applied voltage of 2 V for 10 seconds to expose the underlying microstructure. There exists a notable difference between the weld (Figure 120-b, c) and the near-weld edge (Figure 120-d) which begins to display microstructure more similar to that further into the base material (Figure 120-e). Within the weld, there is an oriented structure, with elongated dendritic grains. Further into the material, in the HAZ and far from the weld, an equiaxed grain structure is observed.

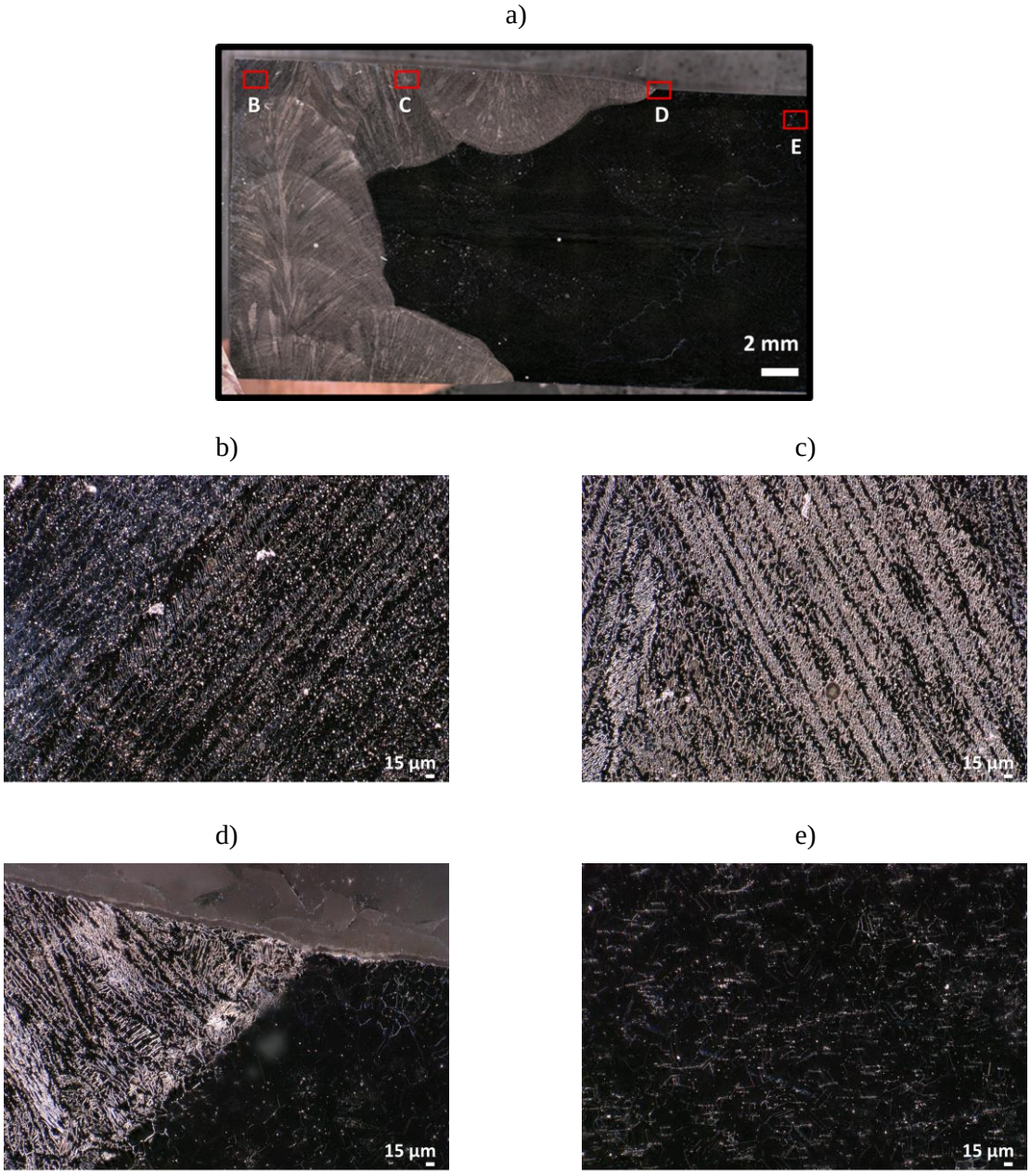

Figure 120. Optical micrographs of horizontal weld section 13-A (post-etch) with (a) large overview and (b)-(e) insets of indicated regions.

3.4.3.3 Microstructural Characterization - Scanning Electron Microscopy Combined with Electron Backscatter Diffraction

Further characterization of the weld and near weld microstructure was performed through SEM and EBSD. These micrographs were collected using a Zeiss Supra 55-VP field emission SEM equipped with a Symmetry EBSD detector with an accelerating voltage was 15 kV. The step size used for EBSD was 50 nm unless stated otherwise.

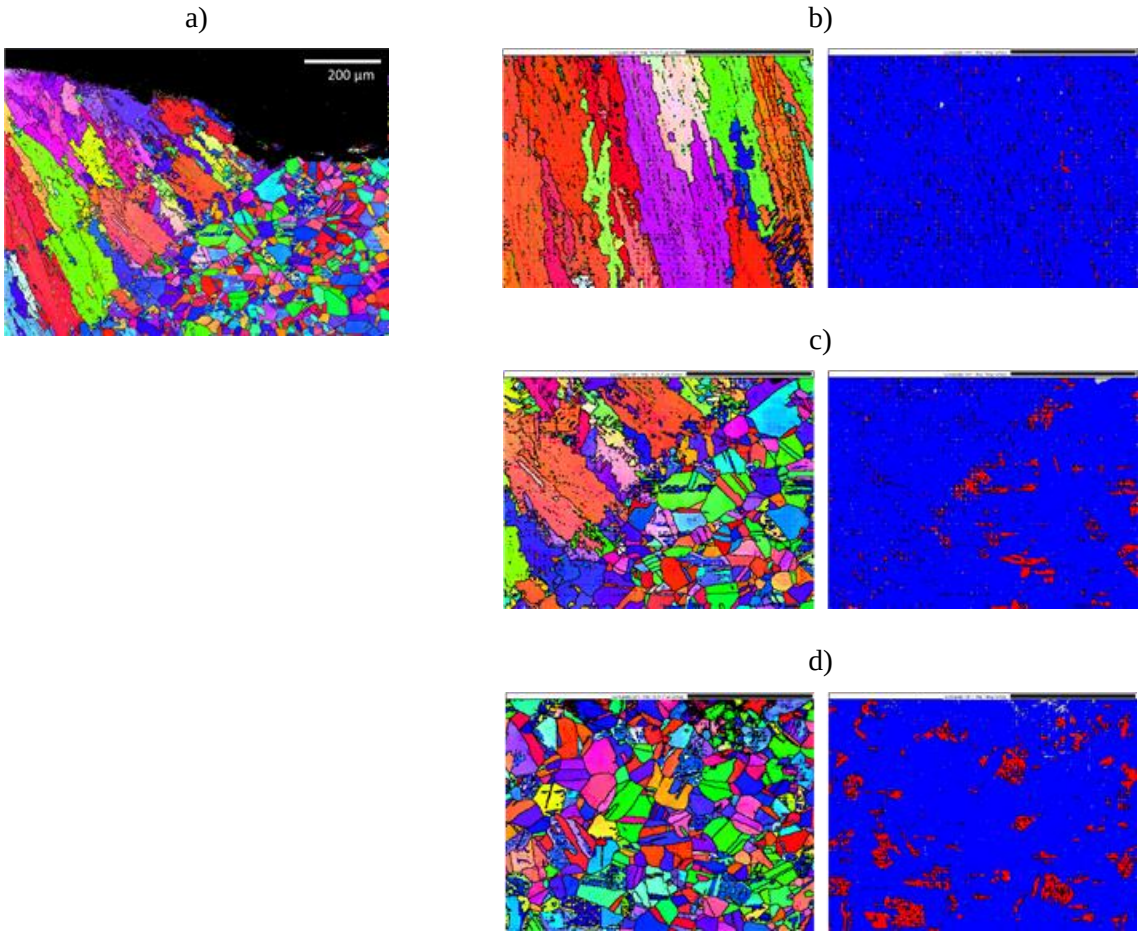

Figure 121. a) EBSD of horizontal weld section 13-A with insets of EBSD and corresponding phase contrast map in which blue represented FCC phases and red, BCC phases, of regions b) within the weld, c) at the weld edge, and d) the HAZ.

EBSD revealed similar morphology to the optical micrographs; within the weld interface there were larger, elongated grains while outside of the weld were smaller equiaxed grains. In Figure 121-b, a higher-resolution grain orientation map and phase contrast map, display the BCC phases within the weld, likely δ-ferrite, precipitated along the gbs. However, at the weld interface and outside of the weld in the HAZ (Figure 121-c, d), BCC phases that were present that were more likely martensitic regions. It is believed these were formed due to polishing procedures and were not fully removed by the electrochemical etch. However, re-evaluation of the phase contrast maps, including more controlled electropolishing, will occur in FY21to determine the true BCC phase distribution in the near weld region. While EBSD indicated the presence of delta ferrite within the weld, further microstructural analysis combined with DLEPR testing in FY21 will determine potential sensitization affects not apparent in EBSD.

3.4.3.4 Cold Work and Residual Stress Evaluation – Vickers Hardness and Center Hole Drilling

In addition to microstructural evaluation, the microhardness of the weld samples was measured to obtain a better understanding of the level of cold work that occurred within the weld and HAZ. Vickers microhardness measurements were taken using a 0.2 kg load and a 40X objective. Maps were acquired with the topmost row spaced at 3d, then 60 indents spaced at 10d, where d is the diameter of the indent (Figure 122-a).

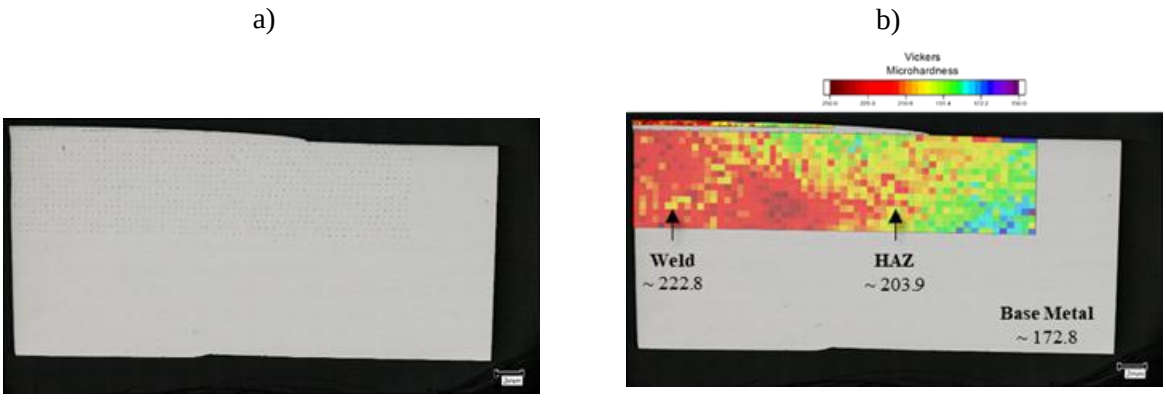

Figure 122. (a) Map of microhardness indentations used for mapping Vickers hardness across horizontal weld section and (b) overlay of Vickers hardness measurements with average values for the weld, HAZ, and base metal.

The Vickers microhardness measurements of the horizontal weld sample displayed an increased hardness within the weld that dropped with distance away from the centerline into the base metal (Figure 122-b). A second set of measurements was taken on the base metal far from the weld and average values reported herein. The average microhardness was the highest in the weld region at 222.81 HV, decreasing to 203.98 HV in the HAZ, and to 172.8 HV in the base metal. Microhardness can be an indication of the average tensile stress of the material.(Milad et al., 2008; Nikitin and Besel, 2008) A correlative trend between the average tensile strength in MPa to the average hardness in HV was established for SS304L by Milad et. al (Milad et al., 2008). If one were to apply a similar trend here, the average tensile strength values could be estimated across the weld. From comparison to Milad's correlation; the average tensile strength in the weld region was the highest at roughly 668 MPa, decreased in the HAZ to roughly 612 MPa, and was lowest in the base metal region at about 518 MPa. While these high tensile strength values likely do not indicate the true tensile strength of the 304L material measured here, as this relationship was not derived for this specific lot of material, they do present a method to evaluate potential changes of cold work across the material. From comparison of the average yield strength values to Milad's study, the weld region examined here exhibits roughly 10% higher cold work than the surrounding base material. This change in cold work could greatly affect subsequent resistance of the material to corrosion and SCC, as previously described, and can be applied as a parameter for investigation in crack growth rate studies.

Finally, with respect to weld characterization of the mockup canister welds, center hole drilling measurements were taken to determine the residual stresses in the near surface region and with depth into the plate around the weld. However, to take accurate measurements of residual stresses due to welding, rather than small weld sections, a large weld plate (roughly 2′ by 2′) was measured to avoid relaxation of the stresses. As the plate retained curvature from the canister formation, this somewhat complicated the traditional mounting procedures, and the plate was instead mounted to an optical table as shown in Figure

123 to assure sufficient rigidity for center hole drilling. Additionally, this allowed for indexing of the plate by shifting it either in the vertical or horizontal direction around the weld, as shown in the inset in Figure 123-b. The material parameters applied to calculate the residual stress for the SS304L were a Young's Modulus of 198 GPa and a Poisson ratio of 0.3. A hole diameter of 1.575 mm was drilled at multiple depths, with steps of 0.043 mm to a depth of 0.6 mm (14 steps). This theoretically allows the stress to be calculated at different depths but may result in large errors. Variation in measurements from different depths are provided to observe general trends and minimize interpretation of potential errors.

a) b)

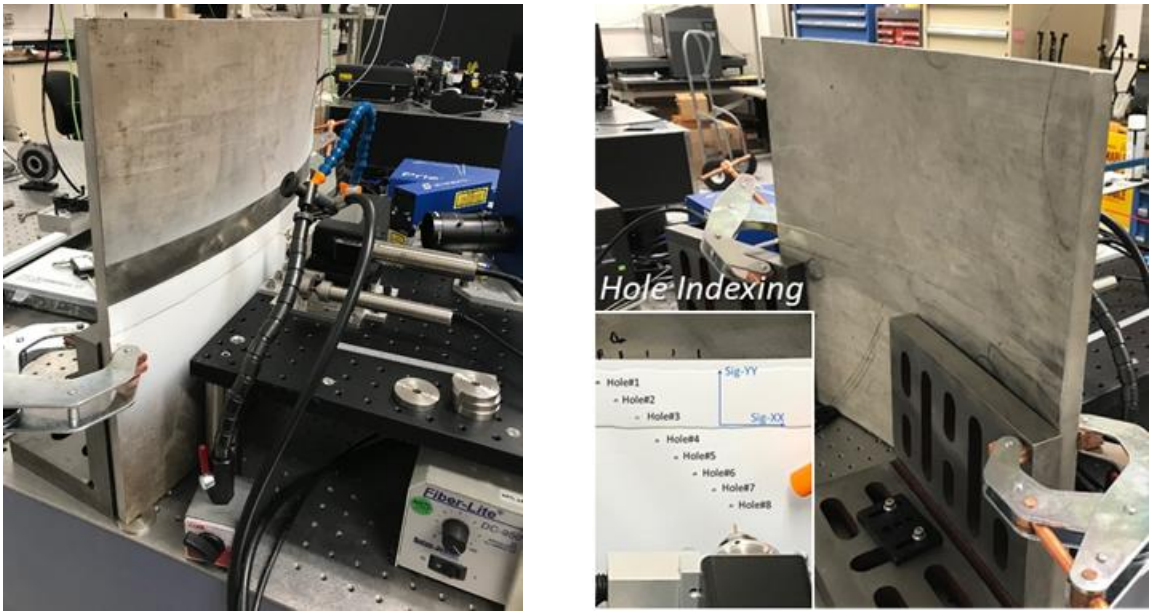

Figure 123. Center hole drilling mounting configuration for horizontal weld plate at SNL (a) front view and (b) back view with indexing inset.

Figure 124-a provides the average stress measurement for two drill depths; the blue curve is the average stress to a depth of 0.6 mm, while the red curve is at the surface down to a depth of 0.042 mm. As can be seen, the stress at the surface is generally negative (indicative of compressive stresses), while the average stress down to a depth of 0.6 mm is typically positive (tensile) in value. These values generally agree with the results of the stress profile over the entire drill depth in Figure 124-b. In Figure 124-b results are arranged by "near weld", "HAZ", and "far from weld" regions. Again, for all holes in the near surface area, stresses appear to be compressive, but with depth, tend to be more tensile. Continued study, with potentially enhanced resolution for center hole drilling will be pursued in FY21 to better establish the near surface residual stresses. Determination of near-surface residual stresses is significant as these can either minimize, in the case of compressive stresses, or exacerbate, as in the case of tensile stresses, the corrosion damage and pit growth on the canister. Additionally, the type and magnitude of residual stresses could also influence the pit to crack transition by governing the depth a pit need to achieve to initiate SCC. Therefore, continued efforts in FY21 will focus on further evaluation of these stresses including application of potentially higher resolution systems.

a) b)

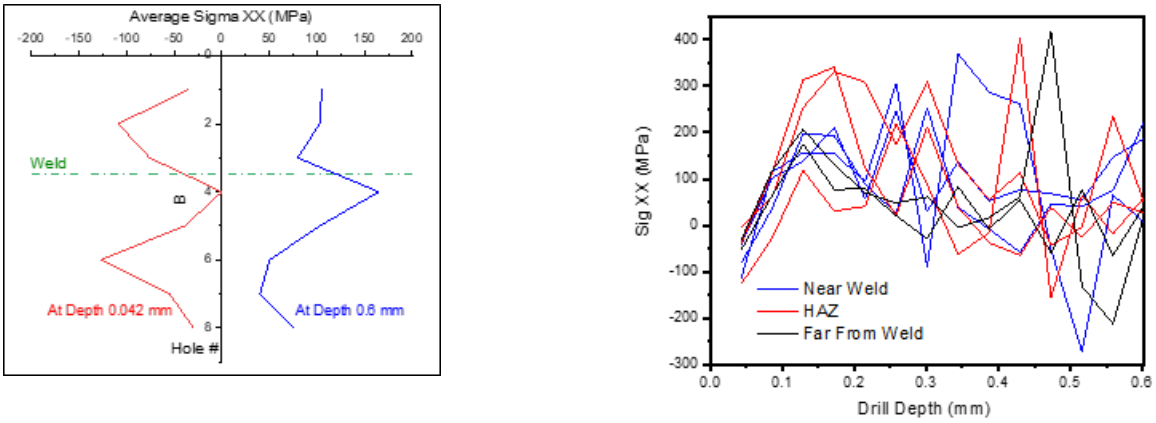

Figure 124. (a) Center hole drilling # vs. residual stress, Sig XX (MPa), measured at two drill depths 0.042mm and 0.6m and (b) Residual Stress, Sig XX (MPa) vs drill depth (mm) for drilled holes grouped by "near weld", "HAZ" and "far from weld".

3.5 Big Plate and 4-Point Bend Exposure Tests

In FY20, post-exposure analyses of SCC from the exposure tests involving the large mock-up canister plates and a large 4-point bent witness specimen were completed. In FY18, and summarized in detail in FY19, the effects of material characteristics and mechanical environment (microstructure, composition, residual stress) on the distribution of pitting damage and rates, the conditions for pit-to-crack transition, and crack growth rates under canister-relevant conditions were evaluated (Bryan and Schindelholz, 2018b; Schaller et al., 2019). The goal of these large-scale exposure tests was to:

- Determine the importance of canister stress levels as a parameter in pitting susceptibility.
- Determine crack initiation and growth rate behavior in canister relevant materials and stress conditions.

To achieve these, exposures of large canister mock-up plates (containing welded regions) and a large 4-point bend specimen in an aggressive corrosion environment were carried out. These provided post-mortem information regarding pitting and potential SCC in canister relevant exposures as well as information regarding the location and orientation of SCC cracks with respect to welded regions. The determination of SCC susceptibility spatially with respect to different canister regions will aid in performing canister surface inspection during ISFSI site aging management programs. The conditions of the exposure test in FY19 were a 12-month exposure at 80 °C and 35 % RH of canister mock-up plates and large 4-point bends coated with ~10 g/m^2 of $MgCl_2$ (initially ~2g/m^2 then an additional ~8 g/m^2 were added). The salt was deposited uniformly across the sample surfaces using a custom salt fog chamber. Samples exposed under these conditions included, i) a weld intersection, ii) a circumferential weld, iii) a longitudinal weld, and iv) a 4-point bend witness specimen (subject to the same stress levels as the weld regions of the mock-up plates). There was also one additional circumferential weld mock-up plate sample that was exposed to a potassium tetrathionate solution for 6 months (3 months at room temperature and 3 months at 40 °C). Potassium tetrathionate is an extremely aggressive environment and therefore this experiment sought to force the plate to crack in order to determine the location and orientation of SCC that may form in the canister weld regions. Additional details of the experimental methods are described in the FY19 report (Schaller et al., 2019).

3.5.1 Summary of Results from FY19

The longitudinal weld was evaluated in FY 19 after 8-months of exposure. It is significant to note that post exposure, the surface was heavily corroded, but the brine had completely dried. This brine dryout of $MgCl_2$, was likely due to degassing and brine conversion to Mg-carbonate or hydroxychloride phases and/or to reactions with corrosion products. Loose corrosion products were brushed off after 8 months and analyzed by SEM/EDS and XRD. The remaining samples were removed from the environmental exposure chamber at 12-months. All samples were heavily corroded and entirely dry. Again, the corrosion products were brushed off the surface and collected for analysis by SEM/EDS and XRD.

SEM/EDS and XRD analyses of corrosion products from the surface showed the presence of iron-rich loose whisker-like products as well as salt crystals. There were distinct regions of Mg-rich particles as well as Fe-rich corrosion products. Spot analyses and EDS maps of the Mg-rich regions demonstrated the presence of magnesium hydroxychloride phases—which were identified by regions rich in Mg and O, but depleted in Cl. The Mg-hydroxychloride phase could not be confirmed through XRD, however its presence is likely the 2-1-4 phase based upon the environmental conditions (See Section 2.3.2) and previous experimental observations (Bryan and Schindelholz, 2018b; Schaller et al., 2019). This is one possible explanation for brine dryout as the precipitated magnesium hydroxychloride phases have a higher deliquescence RH than bischofite and higher than the exposure conditions (35 %RH). Another potential explanation for brine dryout comes from analysis of the Fe-rich regions. In these Fe-rich regions the primary phases were Fe-oxides, which XRD analysis showed included akageneite ($Fe^{3+}_{7.6}Ni_{0.4}O_{6.4}(OH)_{9.7}Cl_{1.3}$). Akageneite can contain up to 6% chloride and lead to potential gettering of Cl^- from the brine, leading to brine dryout.

Following the corrosion product analysis, samples were cleaned using the ASTM G1 standard method (0.66 M diammonium citrate bath), along with additional cleaning in concentrated nitric acid to remove strongly adhering corrosion products on the surfaces to prepare for non-destructive evaluation (NDE). NDE tests, including dye penetrate, eddy current, and phased array tests were performed to identify the location and orientation of any SCC cracks that formed during exposure.

3.5.2 Post-Exposure Analysis for SCC

NDE tests were performed on each of the samples to evaluate the presence, location, and orientation of SCC cracks that formed during a 12 month exposure at 80 °C and 35% RH (circumferential weld, longitudinal weld, 4 point bend specimen) and potassium tetrathionate exposure (circumferential weld).

3.5.2.1 Fluorescent Dye Penetrant Testing

For fluorescent dye penetrant testing, "Method C" was performed. In this method, a Level III fluorescent penetrant was strategically applied over the entire weld face and heat-affected zone and allowed to dwell on the parts for 30 minutes. The excess penetrant was wiped away using dry wipes, then a nonaqueous developer was applied and allowed to dwell for 15 minutes. The parts were inspected in a darkened room using a black-light to visually inspect for surface breaking defects. While no indications were found on the mock-up plate samples, the 4-point bend test specimen showed multiple crack indications, all located along the edges of the specimen (Figure 125) Post inspection, the parts were cleaned once again with the nonaqueous solvent to prepare for subsequent NDE testing. A summary of the analysis is presented in Table 30.

One limitation of dye penetrant testing is that it is possible that cracks are present in the mockup weld samples but remain filled with corrosion products (even post cleaning), and hence did not absorb the dye during dye penetrant testing. To assess this, the plates were analyzed further by eddy current/ultrasound testing.

Table 30. Dye penetrant inspected specimen and the noted indications.

Part Inspected	Exposure	Crack indications	Notes
Circumferential weld	3 % potassium tetrathionate, pH= 1	No	
Circumferential weld	80 °C, 35 % RH	No	
Longitudinal Weld	80 °C, 35 % RH	No	High background due to corroded surface
4-point Bend Specimen	80 °C, 35 % RH	Yes	

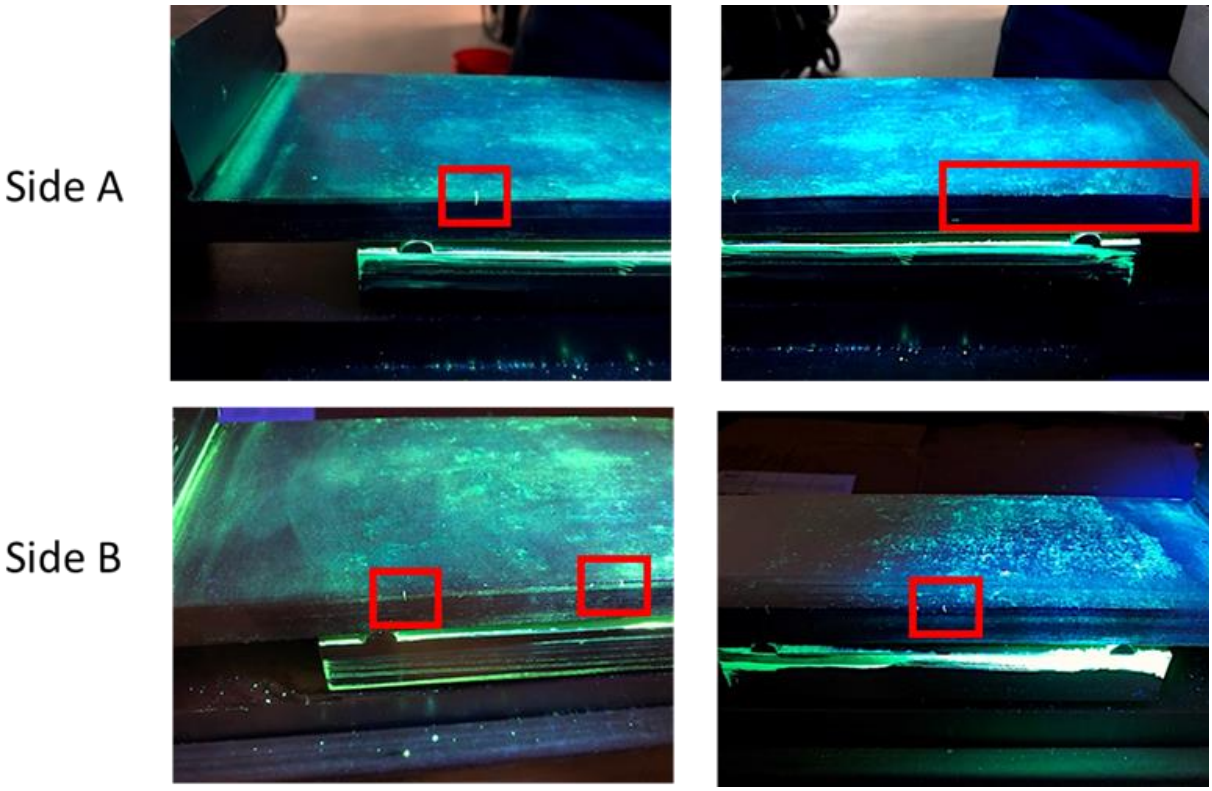

Figure 125. Photographs of the 4-point bend specimen under an ultraviolet light. Side A images show a series of cracks on one edge of the 4-point bend specimen, displaying one large crack and several smaller cracks. Side B shows the presence of small cracks.

3.5.2.2 Eddy Current and Ultrasonic Phased Array Testing

Ultrasonic phase array (UT) and eddy current array testing were performed to identify SCC cracks on the surface of the mock-up plates. This was performed in addition to dye penetrant testing as these

techniques have a greater degree of sensitivity and can detect a crack even in the presence of corrosion product – unlike the previously described dye penetrant testing.

UT consists of many small ultrasonic transducers that can be pulsed independently. Through the variability in the timing of the pulse, a pattern of constructive interference is achieved that results in radiating a quasi-plane ultra-sonic beam at a set angle. By this process, UT can probe the surface and identify SCC cracks and other surface defects. UT was performed using an Olympus Omniscan MX2 equipped with a 5L 16A10 probe with a SA10-N4SS wedge and an Olympus encoder (Figure 126). The resolution was 12 steps per mm. UT data was recorded using the Omniscan's MXU software and evaluated with OmniIPC. All inspections were performed from left to right on the top and bottom sides of the plates using four different probe offsets each (Figure 127). The inspection frequency was 5 MHz with a sectoral beam from 40° to 70° (Figure 128).

Figure 126. Photos of the ultrasonic phase array setup.

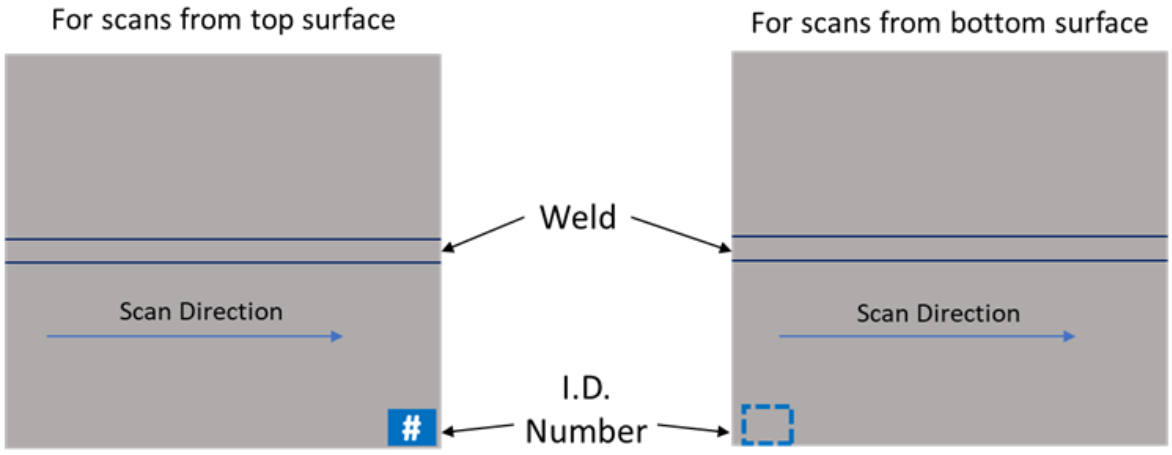

Figure 127. Schematic showing the analysis direction.

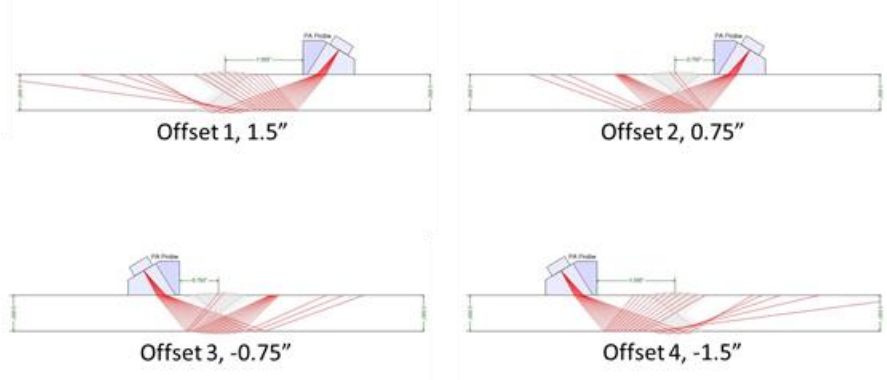

Figure 128. Schematic of each of the scanning offset positions from the center line of the weld for UT inspections. This process was repeated on the tops and bottom sides of the plate to ensure adequate coverage of the weld.

Eddy current array testing drives an array of coils, which are arranged in a specific pattern, to generate a surface profile to target SCC cracks and other surface defects. Eddy current array was performed with an Olympus Omniscan MX instrument, an Olympus R/D tech SBB-051-150-032 probe with an Olympus Gilder encoder (Figure 129). Data was collected with the Omniscan MXE software, and scans were performed from left to right on both the top and bottom side of the plate using four probes at each position (Figure 127). The inspection frequency was set to 150 kHz.

Figure 129. Photos of the Eddy Current Array Setup.

The results of UT and eddy current array are shown in Figure 130 and Figure 131. Overall, the UT results showed few surface indications. The indications that were observed with UT are shown in Figure 130; in the circumferential weld, exposed to 80 °C, 35 % RH for 12 months, an indication wa present that potentially resembled a crack. However, upon visual inspection, that indication is a result from the difference in the surface finish of the metal (Figure 130); no additional evidence suggested that a crack had formed. The second indication found by UT was on the circumferential weld mockup plate that underwent the potassium tetrathionate exposure. Again, upon visual inspection, the indication was clearly not a crack, but a weld mark from manufacturing (Figure 130).

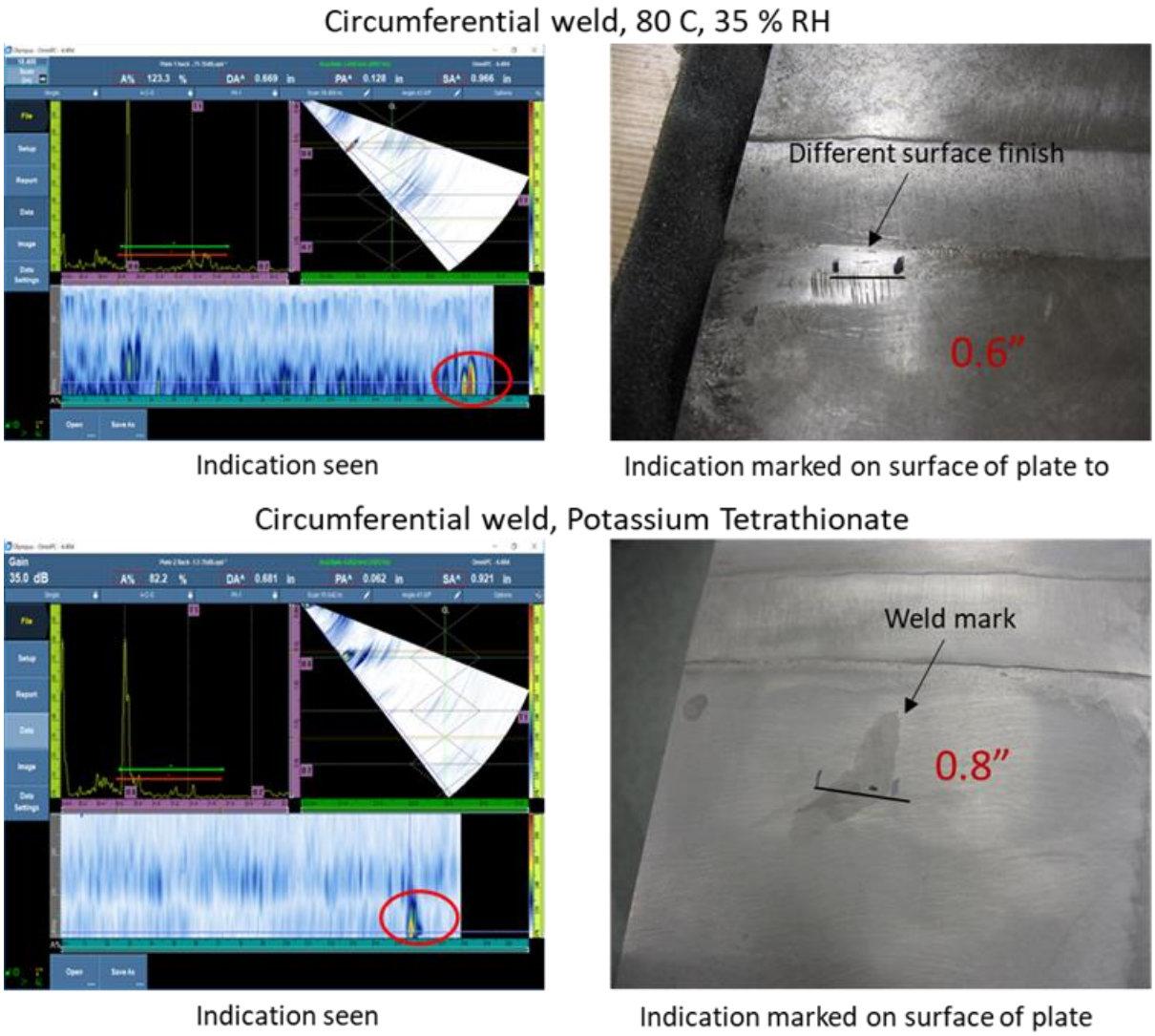

Figure 130. Phased array analysis of a mock-up plate samples. Showing the circumferential welds exposed to 80 C, 35 % RH and potassium tetrathionate. Images at right correspond to indications from UT; suggest indications are results from manufacturing processes.

Similar to UT results, the eddy current array results showed the presence a few flaw indications. In both circumferential weld samples, no indications were seen near the weld nor on the weld (Figure 131). One flaw indication was observed in the longitudinal weld mock-up plate near the heat-affected zone of the weld, however upon visual inspection this was most likely caused from a manufacturing process and not by the formation of an SCC crack (Figure 131).

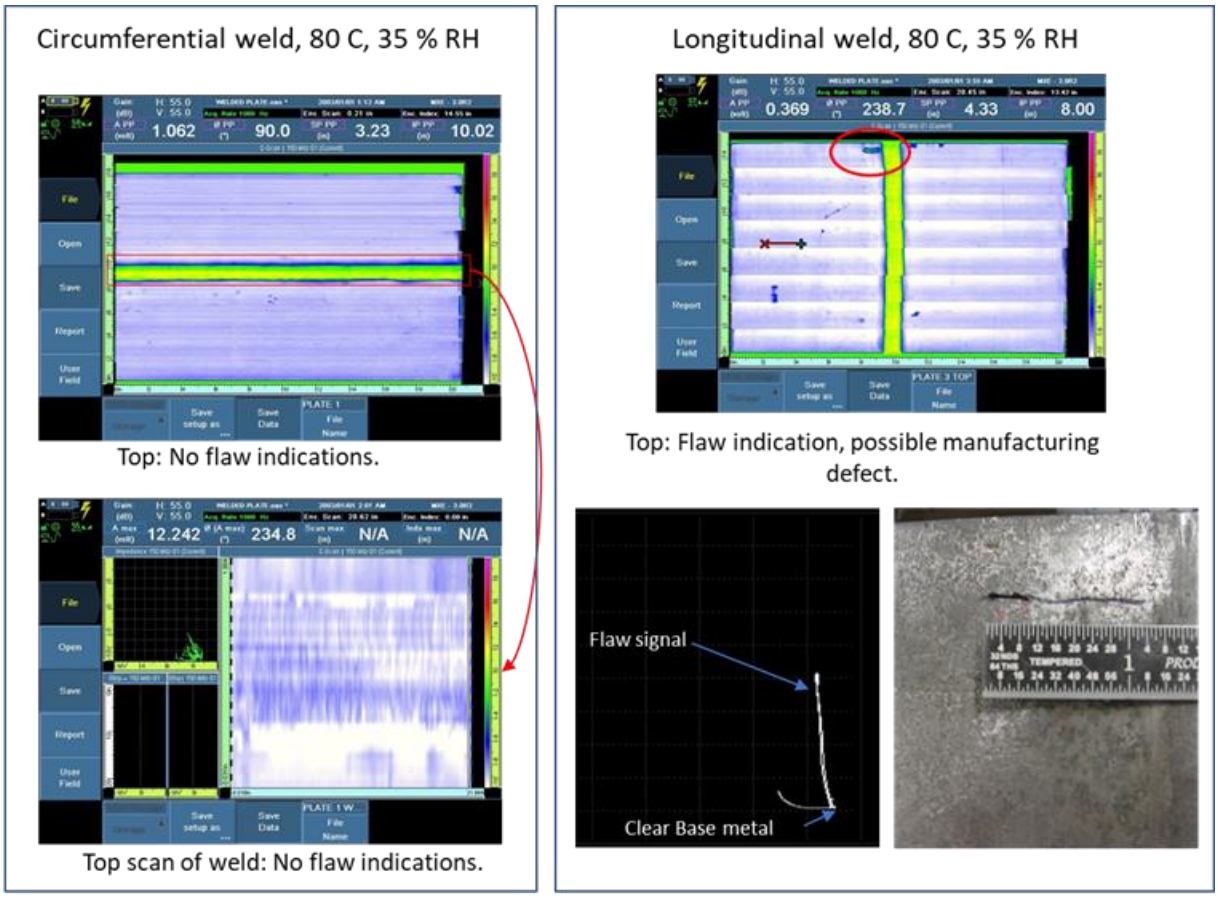

Figure 131. Eddy current array analysis of the circumferential and longitudinal weld mock-up plates after exposure to 80 °C, 35 %RH for 12 months showing no flaw indications in the circumferential weld and possible indications, likely from manufacturing defects, in the longitudinal weld.

3.5.3 Conclusions and Follow-on Analyses

The primary goal of the large plate tests was to provide a better understanding of the location and orientation of SCC cracks that form as a result of exposure to an aggressive environment (either 80 °C and 35 % RH, or potassium tetrathionate at 40 °C). While an improved understanding of the factors that lead to brine dry-out – including the formation of Mg-hydroxychloride phases (specifically the 2-1-4 phase) and reactions with corrosion products (to form akageneite) – was gained, no observation of SCC from NDE analyses was obtained. There are a few hypotheses as to why cracks may not have been evident; i) the brine dry out may have stifled pit-to-crack transitions from occurring; ii) the stresses in the material may have been altered (reduced) when the plates were cut from the mock-up canister. Alternatively, SCC may have been inhibited because the shallow compressive stresses imparted to the metal by the grinding of the weld, as indicated by the center hole stress measurements discussed in Section 3.4.3.4. As a follow-on, samples were sectioned into smaller specimens for a detailed analysis by EBSD to evaluate the microstructure of the base and weld metal regions (results were provided in Section 3.4 of this report).

4. SCC Crack Growth

One of the primary goals of this research is to determine how SCC susceptibility is affected by the atmospheric exposure environment. Specifically, how are the crack growth rate $\left(\frac{da}{dt}\right)$ and threshold stress intensity for SCC (K_{ISCC}) effected by ISFSI-relevant atmospheric conditions? As there is currently very limited data in the literature on crack growth rates (CGR) for SS304L, let alone atmospheric cracking data pertinent to ISFSI sites, so there remains much work to pursue in this area. One of the main goals of the Sandia-led effort in FY 20 and continued in FY21, is to determine the relationship between the environmental conditions, the cathodic kinetics, and the subsequent control of the crack initiation and crack growth. Knowledge of this will enable better prediction of the occurrence and rate of SCC cracking and identification of deleterious factors, potentially leading to new mitigation strategies.

4.1 Introduction

The primary goal of this research effort is to determine crack growth rate (CGR) is influenced by atmospheric conditions at ISFSIs for SNF interim storage containers. SNF canisters are fabricated from a very common stainless-steel alloy (304L or UNS S30403), yet an understanding of its performance in long-term storage conditions is lacking. CISCC is possible in many alloys and occurs when the required conditions are present, including tensile stresses (such as residual stresses found after welding), a corrosive environment, and a susceptible material. Several other factors such as cold work or surface finish can magnify or intensify CISCC. Efforts to characterize residual stresses and corrosion behavior of areas localized around the welded regions in SNF canisters have yielded a better understanding of the conditions that may give rise to CISCC in interim storage environments (Bryan and Enos, 2016; Enos and Bryan, 2016a). The surface conditions in salt-enabled deliquesced environments have also been studied(Enos and Bryan). While these efforts provide insight into SCC initiation through the dependence of pitting on environment and material, thus informing pit-to-crack transition, a better understanding of the dependence of CGR on environmental factors is necessary for more accurate lifetime predictions. Very little data on high fidelity CGR characterization of SS304L is available in literature (Bryan and Enos, 2016), especially high fidelity CGR determination in atmospheric conditions such as those to which SNF canisters are exposed. With this in mind, the focus during FY20 has been developing the capability to measure crack growth rates in relevant conditions for SS304L at SNL. A detailed description of the SNL CGR testing setup is provided in the subsequent sections along with a summary of initial testing completed during FY20.

4.1.1 Testing Capabilities

CISCC research at Sandia has been primarily focused on establishing an adaptable, parallelized testing facility. Four electromechanical CISCC testing frames and cells were procured from Det Norske Veritas Group (DNV-GL) in FY20. Three of the cells were setup in a specially outfitted half-size intermodal transportation container while the fourth was installed in the basement of an SNL building (Q2 FY20). Currently, efforts are underway to consolidate all CISCC test capabilities near the fourth test cell in the basement of an SNL building (by Q1 FY21). The cells feature a maximum load of 15,000 lbs and large volume (2-3 liter), temperature-controlled gas/liquid sealed immersion cells (Figure 132). Three of the frames are positioned in the vertical direction (force is applied normal to the floor) and one frame is in the horizontal direction (force is applied parallel to the floor)shown in Figure 133. The fourth frame orientation in the horizontal direction will allow for investigation free of potential gravitational effects, which may be beneficial to testing in various atmospheric scenarios; including salt printing and exposure to a humid environment, where control of a thin water layer is crucial. High fidelity crack size measurements are made in-situ via a direct current potential drop (DCPD) system comprising of a precision nanovolt meter and a precision alternating current source as is common in the literature.

Environmental control is achieved using an inline exposure chamber shown in Figure 132. The DCPD connections, reference electrode (saturated calomel electrode) and thermocouple, are inserted through

holes in the top flange while gas connections and fill/drain connections for fluid solutions are plumbed to the bottom flange. The loading shafts are sealed using ¾" plastic compression fittings. The solution is heated above room temperature using a flexible adhesive-backed heating plate attached to the outside of the cylindrical exposure chamber. The multiple ports available also allow for solution to flow from an external reservoir. Components of the frame that are in contact with the test environment (loading clevis', cell walls, electrodes, fittings, etc.) are all made from corrosion resistant materials such as Hastelloy C-276 or perfluoroalkoxy (PFA) alkane plastic. The sample is electrically isolated from the rest of the frame and the loading clevis' by ceramic-coated steel loading pins.

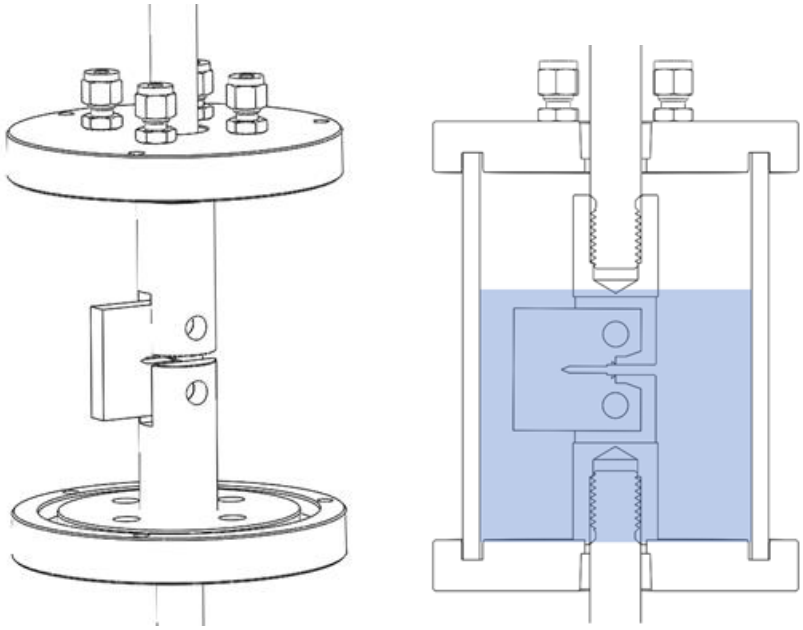

Figure 132. Cross-Sectional view of DNV-GL designed environmental exposure chamber with example of fully-immersed CT specimen.

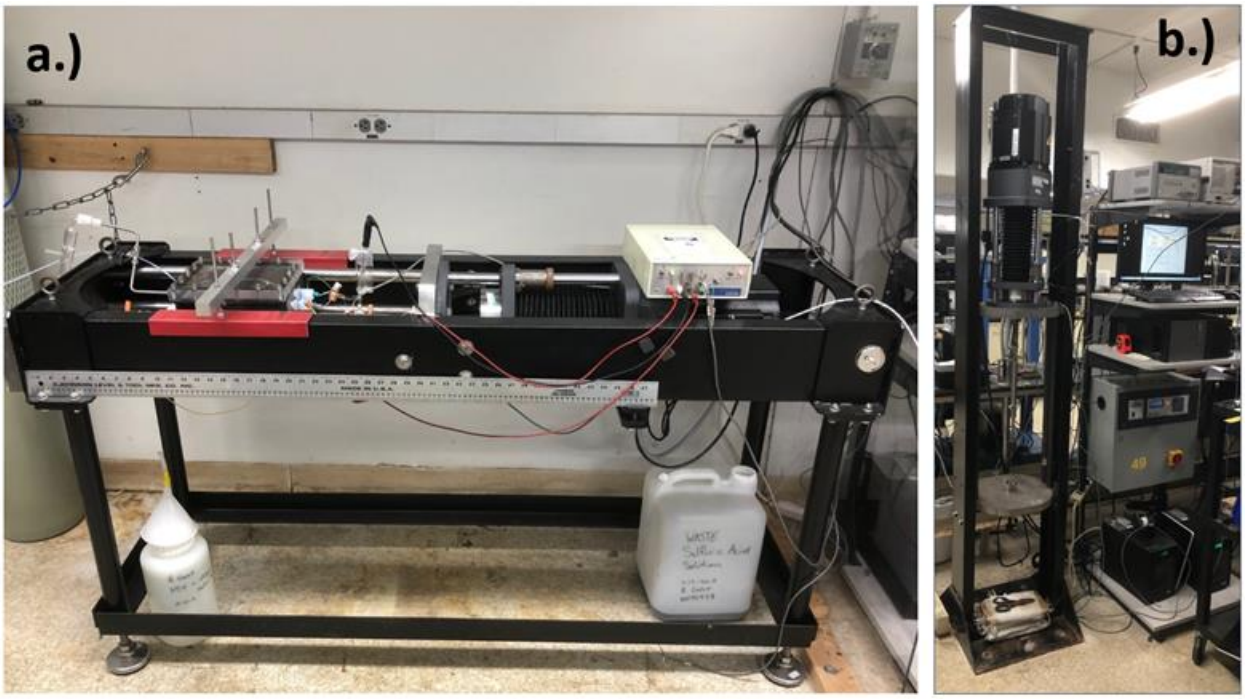

Figure 133. Load Frames in a.) Horizontal and b.) Vertical Orientation

4.2 DCPD Measurement

A schematic of the DCPD set-up is shown in Figure 134. In general, a current is passed through the specimen and the voltage across the crack mouth is measured. This voltage is further converted to crack length. The locations of the current and voltage probes are seen in Figure 134. In addition to these probes, reference voltage probes are used to compensate for any variations in material resistivity that may not be due to crack growth (*i.e.* fluctuations in temperature) and are placed on the posterior side of the specimen. Finally, one additional wire is welded to the sample in order to measure the open circuit corrosion potential (OCP) during the experiment with respect to a reference electrode (typically silver/silver chloride, VAg/AgCl). Reference probes will be placed approximately in the same location, it will be ensured that the potential value is stable before testing (Tong, 2001). The attachment points and the wires must be isolated from the testing environment to prevent them from providing stray currents or corroding, potentially contributing ions and influencing the result of the test. This is achieved by using polytetrafluoroethylene (PTFE) or PFA polymer-insulated wire and covering any exposed wire at or near the attachment points with high-strength, yet flexible 2-part epoxy. Efforts to improve the test setup hinge on the ability to weld the electrodes mentioned previously ex-situ. Currently, low-gauge solid platinum wires are being used but investigations into the use of stranded and solid copper wires are also in progress and are nearly complete (Q4 FY20 to Q1 FY21).

As mentioned previously, the DCPD system is comprised of a precision alternating-current power supply (in current-control mode) and a nanovolt/microohm meter. When wired as shown in Figure 134, the nanovolt meter allows resolution of tiny changes in crack length (0.01 to 0.1 micrometers). The amount of current passed through the sample during the test must be large enough to give sufficient voltage drop (SNL uses 4 amps) across the sample to be resolved using the volt meter (such that the desired minimum change in crack length is resolved by the voltage measurement), but not so large that sample heating or electrolysis occur.

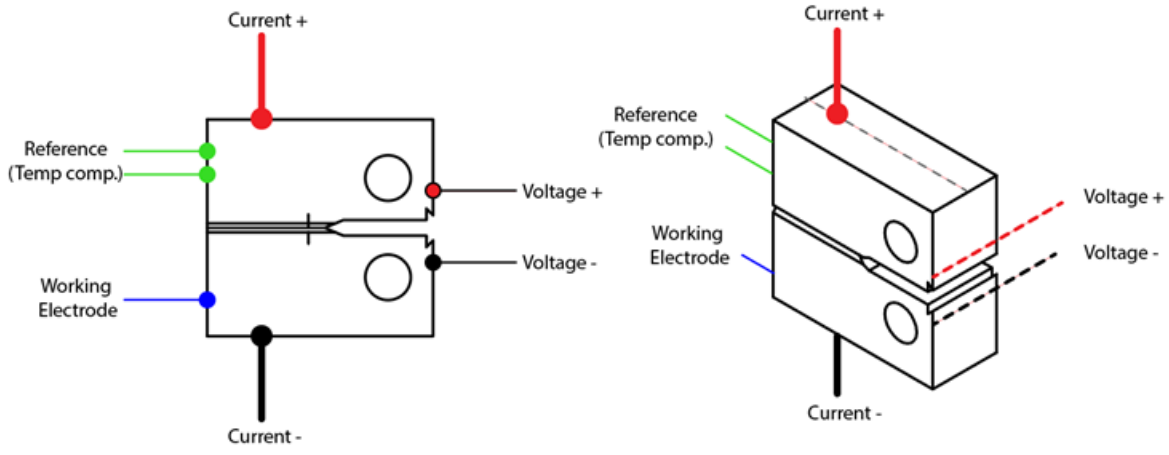

Figure 134. Wiring diagram for compact tension specimens showing location of welded probes.

The Johnson equation (Chen et al.; Johnson, 1965) is used to calculate the crack length in a specimen based on the real-time voltage drop across the crack mouth during a DCPD measurement. When the initial crack length a_o is known (initially assumed as the notch length), a baseline voltage U_o can be measured and used as reference condition for calculating the crack length based on the potential drop

measurement, U. A simple analysis using the Johnson equation shows the importance of having a high resolution on any voltage measurements. In the Johnson equation, a, the crack length, is given by:

$$a = \frac{2W}{\pi} cos^{-1}\left[\frac{\cosh\left(\frac{\pi y}{2W}\right)}{\cosh\left[\left(\frac{U}{U_0}\right) cosh^{-1}\left[\frac{\cosh\left(\frac{\pi y}{2W}\right)}{\cos\left(\frac{\pi a_0}{2W}\right)}\right]\right]}\right]$$

where U is the potential drop measurement, y is half of the potential gauge span (4.445mm for CT specimens) W is the specimen width, a_0 is the initial crack length and U_0 is the initial potential drop measurement.(Johnson, 1965) The ability to measure with a resolution of 10 nanovolts enables the measurement of a crack length change of 0.16 micrometers. A resolution of 1 nanovolt enables the measurement of a crack length change of 0.016 micrometers. The equipment procured by SNL from DNV-GL has a resolution of 10 ± 0.5 nanovolts (resulting in 0.160 ± 0.008 micrometer resolution), but is also capable of a resolution of 1 nanovolt ± 0.05 nanovolts (0.016 ± 0.0008 micrometer resolution) with increased averaging times. The manufacturer specifies a combined measurement accuracy within 0.005% (0.002% of reading + 0.003% of the range) of the reading in the 1mV instrument range over a 90-day period (translates to 30 nanoVolts or 0.477 µm for a typical DCPD reading near 800 uV) regardless of the resolution. This means while it is possible to resolve a 1 nanovolt change in potential drop across the sample (or a 0.016 µm change in crack length) the reading is only accurate to within 0.477 µm. Thus, under constant-K scenarios, the crack length needs to extend past 0.477 µm (4.78×10^{-4} mm). Measurements during constant-K will be taken at 10 times this value (4.78×10^{-3} mm) to reduce influence from noise. This analysis does not account for averaging, noise or other sources of uncertainty in the measurement system but demonstrates the importance of having high-resolution/high-accuracy voltage measurements in DCPD systems. During constant-K testing, the current growth rate is acquired roughly every 30 s, if a value is outside of 10% of the average (taken as a rolling average), the value is ignored.

4.3 Test Plan

4.3.1 Materials & Properties

Basic material properties such as the Young's modulus, Ultimate Tensile Strength (UTS), and the strain-hardening coefficient will better characterize each material lot. The UTS, combined with the YS, will enable calculation of more accurate local crack tip stresses. Pursuant to methods described later, these properties were measured for each lot of material that is planned to be used for CGR experiments to maximize the accuracy with which CGR measurements are taken. Using literature values for any of the parameters would not be advisable as slight compositional changes can greatly affect material properties. Material like plate #206972 in Table 31 was selected due to extremely low concentrations of sulfur while plate #208866 was selected to represent a "dirty" SS304L alloy with elevated sulfur content. While the alloys meet the composition requirements for SS304L according to ASTM A666-15 (ASTM International, 2015a), the mechanical properties measured by the manufacturer are different than typical SS304L. For example, on average the yield strength (YS in Table 31) for SNL procured materials is as much as 55% higher than typical minimum literature values while the UTS is 38% higher.

Table 31. Material lots for use in CGR studies and their respective mill certified mechanical properties for SS304L.

Lot #	Plate #	Heat #	Thickness	UTS (KSI)	YS 0.2% (KSI)	Elong. (%)	HRB
n/a	ASTM A666-15[8]	n/a	n/a	70 Min	25 Min	40 Min	<92
1	*213104*	04E28V AA	1.499”	90.4	42.3	62.9	80.5
2	*213156*	SD41059	1.5”	86	35.1	61.3	77.7
3	*206972*	SD23822	1”	93.8	38.8	57.6	82.2
4	*208866*	863831	1”	81.48	36.36	51.7	75

4.3.2 Composition

Plate chemical compositions (Table 32) of each of the lots of material were measured by the manufacturer and provided on the specification sheet with tensile properties as shown previously. These composition values will be confirmed in FY21 through further quantitative analysis.

Table 32. Plate chemical composition (wt%) as measured by manufacturer.

		Chemical Composition (%) from Mill Spec, Fe Balance											
Lot#	Plate #	C	Si	Mn	P	S	Cr	Ni	Mo	N	Co	Cu	Ti
	ASTM A666-15 [8]	0.03	0.8	2	0.045	0.03	18-20	0.05	-	0.1	-	-	-
1	213104	0.017	0.236	1.78	0.037	0.001	18.06	8.03	0.41	0.08	0.23	0.41	-
2	213156	0.020	0.38	1.64	0.031	0.007	18.18	8.06	0.1	0.071	0.21	0.33	0.003
3	206972	0.02	0.4	1.7	0.031	0.004	18.14	8.04	0.08	0.07	0.2	0.25	0.001
4	208866	0.01	0.4	1.4	0.025	0.023	18.28	8.16	0.27	0.07	0.14	0.34	0.003

4.3.3 Microstructure

EBSD was performed on samples from two lots from Table 31. Samples were collected in three planes denoted in Figure 135 as longitudinal transverse (LT), short transverse (ST) and rolling direction (RD).

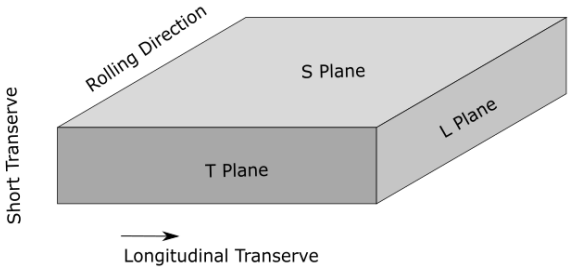

Figure 135. Plate directions with respect to rolling direction (RD), short transverse (ST), and longitudinal transverse (LT) directions.

4.3.4 General Mechanical Properties

Conventional tensile tests pursuant to ASTM E8 (ASTM international, 2016) (see Figure 136) will be performed on tensile specimens cut from 1”-1.25” thick plates of four lots of SS304L (see Table 31) and one lot of SS316. Five specimens were cut from each plate and will be tested to failure on an MTS servo-hydraulic load frame while measuring strain using a standard Digital Image Correlation (DIC) technique and DCPD using similar methods to those discussed earlier. The purpose of these tests is twofold: to procure precise tensile properties of each material lot, as well as characterizing the effective use of DCPD to measure the elastic/plastic transition during tension. Previous studies have shown that DCPD can be used to see the precise elastic/plastic transition more easily than strain measurement techniques like DIC or extensometry alone (Lambourg et al., 2020). Lot specific material properties would allow for more precise calculation of K-values during CGR tests through the direct measurement of strain hardening.

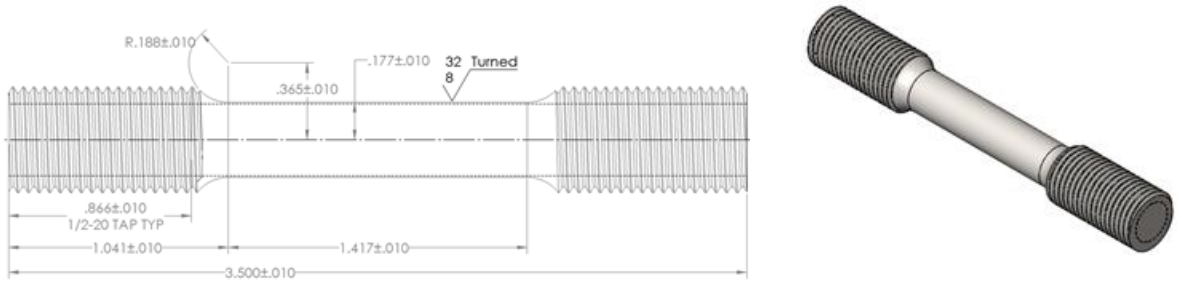

Figure 136. Conventional tensile test specimen conforming to ASTM E8 standard (ASTM international, 2016).

4.4 Specimen Geometry

4.4.1 Compact Tension (CT)

Compact tension (CT) specimens were selected as the test geometry for CISCC tests at Sandia as they are one of the more common geometries studied in literature for CGR measurements. CT specimens are rectangular in cross-section and feature a series of notches designed to focus stress and ensure that planar crack propagation occurs through the ligament of the sample(ASTM International, 2008; 2015b; 2017). A wire-electrical discharge machining (EDM) tool is used to create a large medial notch with a sharp tip through the cross-section of the sample. Small, lateral notches are machined on either side of the ligament to ensure cracking is planar through the middle of the ligament. This design is seen schematically in Figure 137. Calculations were performed to validate the geometry was favorable to plane strain and elastic fracture mechanics.

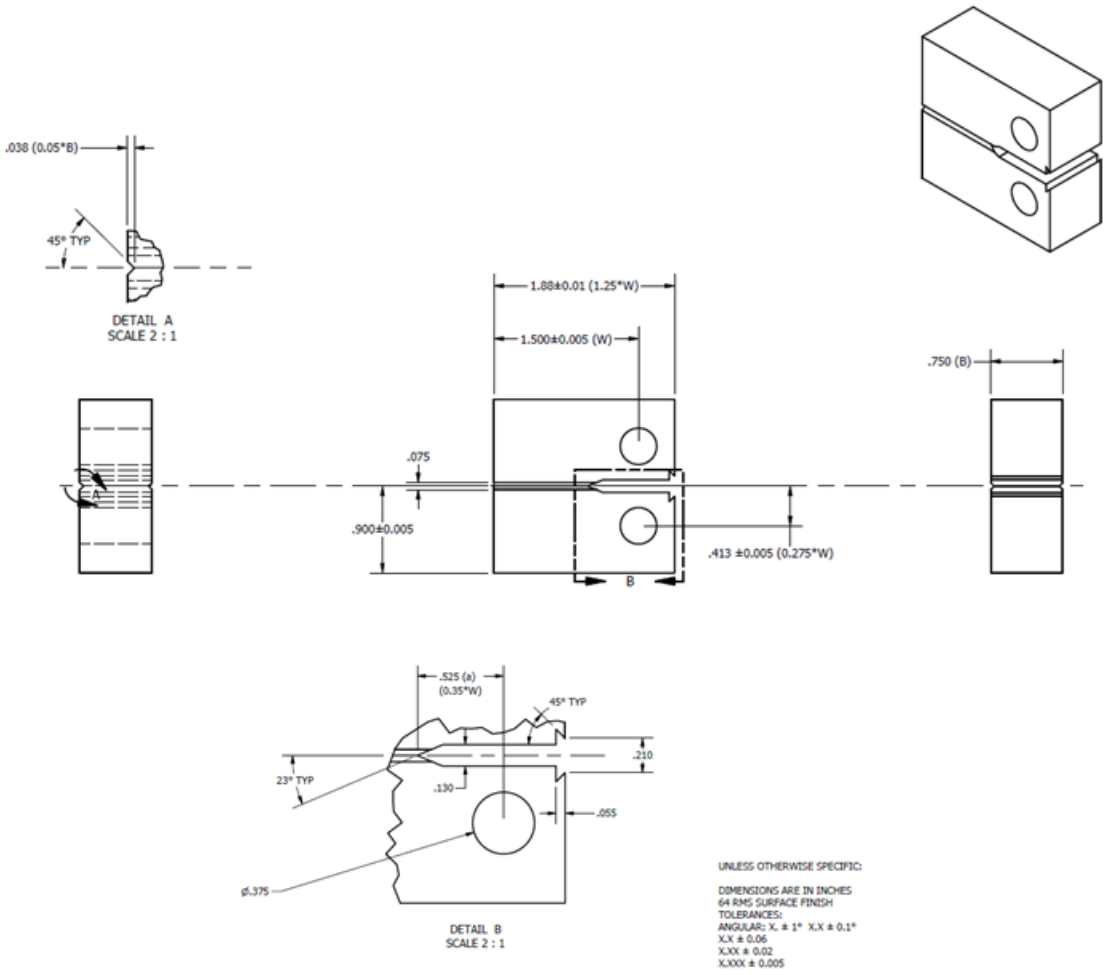

Figure 137. CT Specimen according to ASTM E1681-03(ASTM International, 2008) and ASTM E647(ASTM International, 2015b).

The stress intensity factor at the crack tip for CT specimens can be calculated using the equation below (Andersen, 2005; Chen et al.) .

$$K_{i,CT} = \frac{P_i S}{(BB_N)^{1/2} W^{3/2}} \times \frac{\left(2+\frac{a_i}{W}\right)\left[0.886 + 4.64\left(\frac{a_i}{W}\right) - 13.32\left(\frac{a_i}{W}\right)^2 + 14.72\left(\frac{a_i}{W}\right)^3 - 5.6\left(\frac{a_i}{W}\right)^4\right.}{\left(1-\frac{a_i}{W}\right)^{3/2}}$$

Where P_i is the load at the i^{th} data point, S is the specimen span dimension, B is the specimen thickness, B_n is the specimen net thickness, a_i is the crack length at the i^{th} data point, and W is the specimen width (effective from the holes for pins).

4.4.2 SENT (Single Edge Notched Tension)

In addition to CT specimens, single edge notched tension specimens (SENT, Figure 138) will be utilized to help simulate cracking in atmospheric environments. SENT specimens appear very similar to standard tensile specimens (ASTM international, 2016) with the exception of a notch that is machined into one edge of the sample. The notch serves as a stress concentrator and ensures that a crack forms at its tip(British Standards Institution, 2015). While CT specimens are widely used and their efficacy has been proven, the electrolyte conditions on the surface of the alloy and thus the cathodic current (which is

potentially generated on the surface) can be controlled in an easier manner. SENT specimens will allow control of electrolyte layers on the surface of the alloy (Steiner and Burns, 2018).

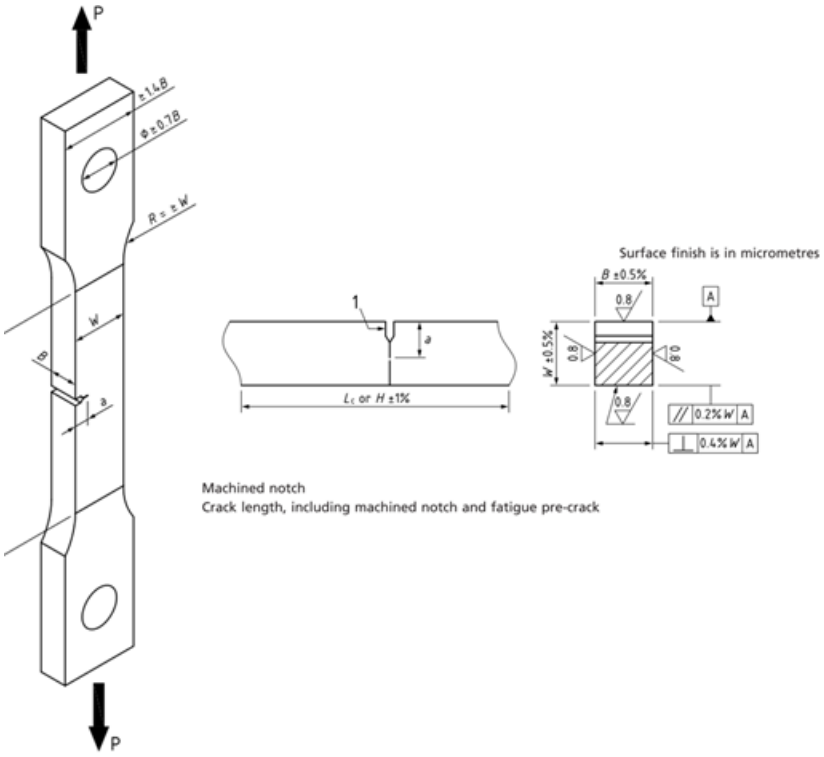

Figure 138. Pin loaded SENT specimen from BSI 8571-2014.

The stress intensity factor for SENT, $K_{i,SENT}$, specimens may be calculated using the following (Andersen, 2005; Chen et al.):

$$K_{i,SENT} = \frac{P_i S}{(BB_N)^{1/2} W^{3/2}} \times \frac{3\left(\frac{a_i}{W}\right)^{1/2}\left[1.99-\left(\frac{a_i}{W}\right)\left(1-\frac{a_i}{W}\right)\left(2.15-3.93\left(\frac{a_i}{W}\right)+2.7\left(\frac{a_i}{W}\right)^2\right)\right]}{2\left(1+2\frac{a_i}{W}\right)\left(1-\frac{a_i}{W}\right)^{3/2}}$$

Where P_i is the load at the i^{th} data point, S is the specimen span dimension, B is the specimen thickness, B_n is the specimen net thickness (if side grooves are machined), a_i is the crack length at the i^{th} data point, and W is the specimen width (effective from the holes for pins).

4.5 Environments

As mentioned in previous sections, the goal of these experiments is to determine the CGR in environments relevant to conditions that SNF interim storage canisters might experience during their lifetime. These environments are complex and are highly dependent on the geographic location of the ISFSI that is being studied. For example, SNF interim storage canisters stored near coastlines will see high concentrations of complex salt mixtures deposited on the surface, consisting of Cl-NO_3-SO_3 rich salts. The temperature, RH, loading density, and composition of the surface species dictate the concentration and thickness of a water layer on the surface. A typical SNF canister can see deliquescence of bischofite (magnesium chloride hexahydrate or $MgCl_2$:$6H_2O$) in less than 20 years. Furthermore, dusts and other non-corrosive airborne particulates may settle on the surface of the canister over its storage lifetime. These particulates can be potential microscopic crevice formers. Detailed descriptions of the methods used for determination of these environmental parameters and dust deposition are outlined in section 2, these will be applied to inform decisions for CGR measurement environments.

CGR tests at SNL will focus first on full immersion concentrated brine environments, as there is still data lacking for CGR in 304L. This will enable comparison of CGR in 304L to known materials in the literature. Additionally, sample design and geometry will be validated in full immersion environments in which stable CGRs are more easily attainable and eventually transitioned to tests in atmospheric environments. Wicking (Figure 139-a), sprayed/atomized (Figure 139-b), printed (Figure 139-c), or membrane-limited (Figure 139-d) environments will be investigated to simulate atmospheric exposure environments. These methods have been demonstrated in recent literature as more realistic and interesting to applications such as SNF storage canisters (Schindelholz and Kelly, 2010a; Steiner and Burns, 2019; Steiner and Burns, 2018). Depending on the results of corrosion investigations into the influence of dust on pit formation, further SCC studies may be designed using brine compositions containing inert airborne particulates and various particulate sizes as a variable.

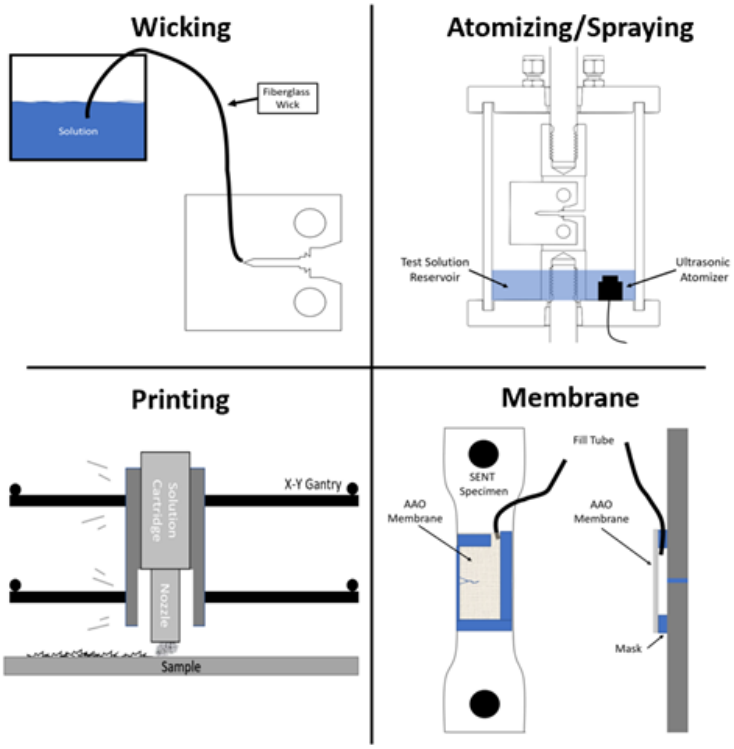

Figure 139 Diagrams of solution wicking, atomizing, printing and membrane-controlled methods in CGR CISCC tests.

4.6 Test Methodology

4.6.1 Pre-Cracking

Generally, before performing any CISCC test, an atomically sharp crack-tip must be created through the completion of a pre-cracking procedure. To perform a pre-crack, a sample is loaded into the test cell and cyclically fatigued for a long period of time (typically 30-60 hours) at low stress intensities until a crack of sufficient length has formed (until the plastic zone from the EDM has been surpassed). The pre-crack length is expressed as a ratio of a/W (crack length to sample width) with a desired value of 0.2 to 0.5. Loads on the sample can be controlled through the calculation of the stress intensity factor (K, expressed in $MPa\sqrt{m}$). Typically, an experimentalist can vary parameters such as stress application frequency and cyclic stress ratio ($\Delta K \; or \; R = \frac{K_{min,precrack}}{K_{max,precrack}}$) to achieve fatigue conditions which will produce a high quality, controlled-length pre-crack in a short amount of time. R can be chosen based on the Paris Law which describes the impact of R on the CGR during fatigue. At low R values, CGR is non-linear, and above a certain threshold (K_{ic}) CGR is extremely high and can lead to quick failure of the sample. Careful design of pre-crack conditions must be practiced to avoid applying cyclic stress ratios with maximum pre-crack K-values ($K_{max,precrack}$) that exceed the desired minimum test K-values ($K_{min,test}$). The size of the plastic zone and the amount of dislocations generated at the tip of the crack is highly dependent on K. The plastic zone size and the amount of dislocations at the crack tip also have a huge impact on CGR which means that if $K_{max,precrack}$ exceeds $K_{min,test}$, the CGR could be dramatically changed. ASTM E647-15 (ASTM International, 2015b) describes a load shedding process that allows rapid growth of a pre-crack at a high R followed by a transition to a lower R which has $K_{max,precrack}$ at below or equal to $K_{min,test}$.

The SNL team has been engaging with DNV-GL to establish a collaborative relationship to improve pre-cracking methods, as well as to improve safety features in the control software. SNL and DNV-GL have established a more direct process and are currently implementing these improvements on all four test cells. Implementation will be completed by Q4 FY20.

After pre-cracking, the sample is exposed to the testing environment. Typically, the testing environment can be a gaseous or liquid solution of inert or corrosive species and can be held at constant or variable temperature. After introduction of controlled environmental conditions, the sample is subjected to a defined load profile based on the type of test being conducted and the desired test conditions. K-values may be increased linearly (rising-K) or held constant (constant-K, also known as rising displacement){Andersen, 2005 #2} (Andersen, 2005; Dietzel et al., 2011){Andersen, 2005 #2}. The goal of the experiment is to determine CGR in different mechanical, thermal and environmental/chemical conditions (by varying chloride concentration for example). In FY21, investigation of potential differences between the CGR measurement methods will help determine which method results in the most consistent CGR measurement.

4.6.2 Constant-K

Constant-K tests are common in attempts to simulate the effect of CISCC on CGR. They enable a steady measurement of CGR that is unaffected by changes in K. These tests can take a long time to complete depending on stress levels, sample geometry and concentration of aggressive corrosion agents. Selection of applied stress intensities should be based on the expected application conditions.

The general procedure for conducting a constant-K test is to apply the constant-K-value at the peak of a trapezoidal-shaped waveform. The rise/fall conditions (frequency) of the trapezoidal waveform are varied in order to cause the crack to grow until a constant crack growth vs. time response (i.e. a linear line) is observed. While this cyclic stress profile would not be seen in SNF storage canisters, this method is recommended to encourage a transition from the transgranular nature of the pre-crack to intergranular for materials that are susceptible to intergranular SCC in the test environment. An example of this protocol is shown in Table 33 and in Figure 140.

Table 33. Example of applied load cyclic parameters for conducting constant-K CGR measurements.

Sequence Step #	Rise Time (s)	Fall Time (s)	Hold Time (s)	Equivalent Frequency (Hz)
1	9	1	0	0.1
2	90	10	0	0.01
3	900	100	0	0.001
4	900	100	9000	0.0001
5	900	100	86400	0.0000114

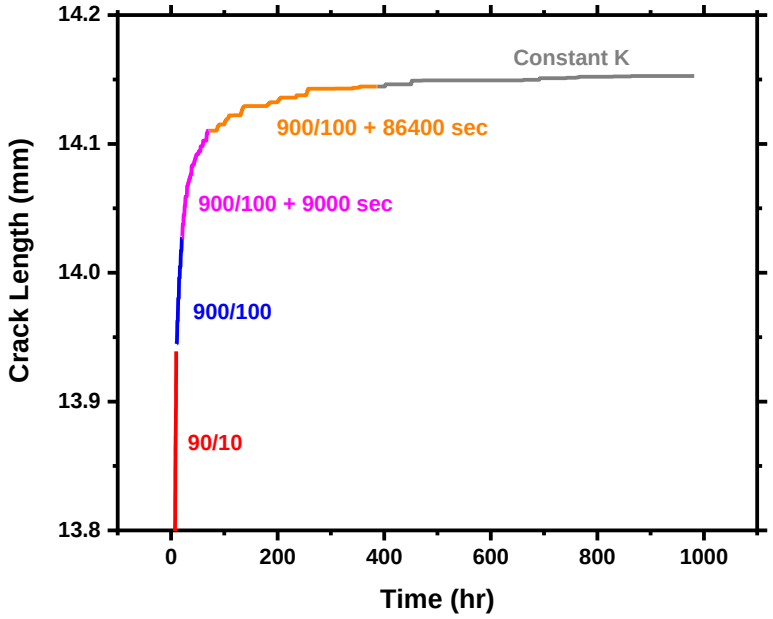

Figure 140. Tapered frequency approach to Constant-K CGR measurements.

4.6.3 Rising-K

Rising-K tests are used to understand the threshold stress intensity above which SCC initiates, known as K_{ISCC}, and the stress intensity/crack growth rate plateau that usually corresponds to transport and electrochemically-limited SCC ({, 2011 #34}Figure 141 (Dietzel et al., 2011)). These can be used to understand the ability of a material to resist SCC and the danger of failure under certain circumstances and are advantageous as they are typically much faster tests to perform. In a rising-K test, a specified K-rate (dK/dt) is applied to the sample (i.e. 1 $MPa\sqrt{m}/hr$). This is performed by actively measuring the crack length with DCPD and, based on the equation for K_i for a CT specimen (Section 4.4.1), with increasing crack growth, loads are reduced in order to maintain the K-rate desired. Such testing imposes a strain rate on the crack tip and can cause an increase in CGR kinetics with respect to constant-K testing depending on the testing conditions or material properties. Additionally, testing at a constant dK/dt imposes a resolution limit on DCPD measurements due to the fact that the plasticity around the crack tip is constantly increasing, changing the material resistivity, and causing a rise in voltage from the DCPD measurement. This resolution limit varies based on the K-rate used, alloy being used, and is a function of K (Crane and Gangloff, 2016; Crane et al., 2016; Gangloff et al., 2014). Although this may be the case, there are several advantages to testing in rising-K environments. First, the total test time is significantly reduced. In constant-K testing, CGR is measured at one K, one temperature, one solution composition, one concentration, and takes roughly one month to complete. In contrast, rising-K tests measure the CGR response as a function of K at one temperature, one solution composition, and one concentration and can take a significantly less amount of time. For example, CGR can be determined from a K range of 5-60 $MPa\sqrt{m}$ in just over a day if one is using a $dK/dt = 2\ MPa\sqrt{m}/hr$ and in just under a week if one is using a $dK/dt = 0.33\ MPa\sqrt{m}/hr$. Thus, CGR is determined at all K-values between 5-60 $MPa\sqrt{m}$ in a much short time period. Second, in constant dK/dt testing, one also obtains K_{ISCC} which is useful to determine the K at which SCC is possible. Having K_{ISCC} and CGR as a function of K is critical for a risk-based assessment for CGR as K is going to be constantly changing with localized corrosion feature size

and crack length. In some alloy systems and environments, enhanced CGR kinetics are experienced. While this may not be the case for every alloy in every environment, constant dK/dt tests will give the same or larger CGR response in comparison to constant-K testing and could help to accelerate the proposed work. It is noted that SNF storage canisters may not be exposed to a specific strain rate during exposure, but the method is important for determining threshold stress intensities and can produce conservative CGR measurements. This method needs to be evaluated for this alloy, in the conditions of interest in order to understand the efficacy of rising-K testing.

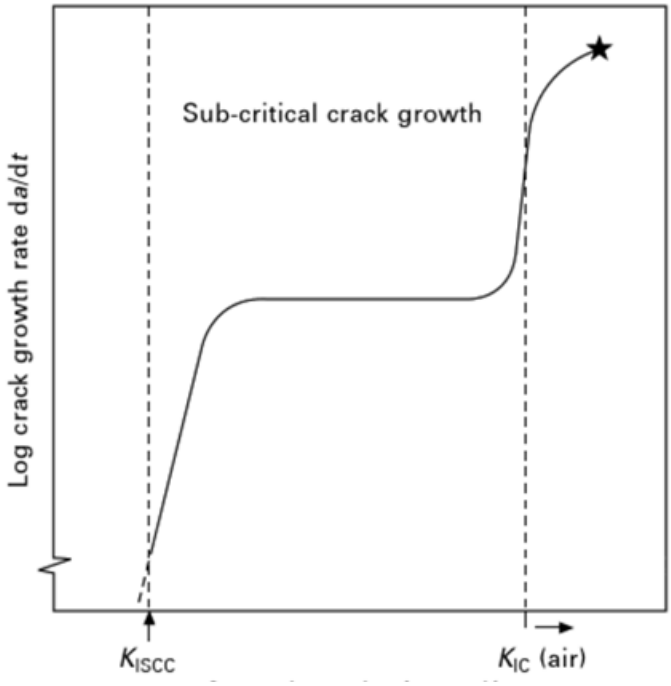

Figure 141. Log crack growth rate (da/dt) versus stress intensity factor (K)(Dietzel et al., 2011; Speidel, 1977).

4.7 CISCC CGR Test Plan

The CISCC CGR test plan includes two main goals: reproducing results obtained from DNV-GL to validate cross-laboratory measurements (see Table 34) and establishing CGR in 304 stainless steel in environments ranging from full immersion to gaseous/vapor atmospheric testing. Aside from the two testing methodologies (rising-K and constant-K), there are three main variables that are of interest to SNF interim storage canisters: salinity/pH of testing environment, temperature, and exposure method. In FY21, initial testing will also investigate potential differences between the rising-K and constant-K method for determining K_{iscc} and improving overall testing efficiencies. Additionally, the influence of decreasing the frequency of the trapezoidal waveform on CGR in constant-K tests will be evaluated.

These primary variables will all be investigated in full immersion tests due to the ability to maintain a "wet" environment at the crack tip. Once trends are established, atmospheric testing will be evaluated with various methods of "environmental application" such as wicking or misting, to determine the potential influences of electrolyte coverage (more similar to that of canister relevant environments) on CGR. Wicking is of particular interest because it has been shown in the literature to be an effective method to keeping the crack tip hydrated uniformly which allows for stable crack growth (Steiner and Burns, 2019) .

It is important to denote the bounds of the testing conditions present within the study. The temperature range of interest is 55 to 35 ˚C. A temperature of 55 ˚C represents a relatively conservative estimate to

the temperature in which a viable brine will first be present in the surface of the canister as it cools. At temperatures above 55 ˚C, it is impossible to form an aqueous brine in canister relevant conditions, therefore SCC cannot occur above this temperature. A temperature of 35 ˚C is chosen as this corresponds to a temperature where solutions are viable on the surface of a canister. This temperature also corresponds with 2-year pitting exposures that were conducted at SNL (Weirich et al., 2019). While some testing may occur at room temperature, the slightly elevated 35 ºC was also selected for acceleration of potential corrosion processes and thus SCC, as well as ease of temperature control (the slight elevation of T reduces the influences of diurnal fluctuations from the surrounding laboratory). Additionally, matching these temperature and solution compositions can help to give insights into SCC processes occurring on the exposure coupons.

4.7.1 Current Tests

Initial CGR testing was conducted at DNV-GL to investigate the influence of brine composition at various temperatures as seen in Table 34. The majority of tests were performed using CT specimens. However, as there is a desire to use SENT specimens for future atmospheric testing, certain tests were conducted with SENT specimens to compare potential differences/influences of geometry and are denoted accordingly. Tests were performed in CO_2 scrubbed air bubbled at less than 1 liter per minute in a large brine volume (4 L) which was temperature controlled above room temperature using a heating pad and thermocouple. The brine was not stirred or circulated during testing other than perturbations caused by bubbling gas. During cycling of the tests, K_{Max} was generally 44 $MPa\sqrt{m}$ with an R-ratio of 0.5. Frequencies were varied according to Table 33 and crack growth was measured under constant-K conditions.

Table 34. Summary of preliminary SS304L tests (performed at DNV-GL).

Temperature (˚C)	Frequency (Hz) K = 44 $MPa\sqrt{m}$ unless denoted	Environment Type	Sample
35	10^{-1}-1.14 x 10^{-5}, constant-K	5.3M NaCl	CT
45	10^{-1}-1.14 x 10^{-5}, constant-K	5.3M NaCl	CT
55	10^{-1}-1.14 x 10^{-5}, constant-K	5.3M NaCl	CT
35	10^{-1}-1.14 x 10^{-5}, constant-K = 49 $MPa\sqrt{m}$	4.98 M $MgCl_2$	CT
35	10^{-1}-1.14 x 10^{-5}, constant-K	4.98 M $MgCl_2$	SENT
55	10^{-1}-1.14 x 10^{-5}, constant-K	4.98 M $MgCl_2$	SENT
55	constant-K = 49 $MPa\sqrt{m}$	4.98 M $MgCl_2$	CT
77	constant-K = 49 $MPa\sqrt{m}$	4.98 M $MgCl_2$	CT
35	10^{-1}-1.14 x 10^{-5}, constant-K	40% RH Seawater	CT
35	10^{-1}-1.14 x 10^{-5}, constant-K	75% RH Seawater	CT

Table 35. Composition of Simulated Seawater Solutions (weights of the salts in g).

Solution	NaCl	KCl	$MgCl_2$:$6H_20$	$CaCl_2$	Na_2SO_4	$NaHCO_3$	KBr	H_3BO_3	H_2O
40% RH SW	10.42	4.62	1030.86	.35	7.85	9.58	25.68	5.59	413.58
76% RH SW	258.55	7.00	111.74	1.31	29.10	0.54	1.02	0.27	940.59

4.7.2 SNL Test Plan

4.7.2.1 Phase 1: Selection of Best Test Method

A series of tests will be conducted to determine the best testing methodology for measuring CGR in brines. To determine the best type, a series of identical tests will be run in fully immersed saturated (5M)

$MgCl_2$ at 55℃ on Lot 4 SS304L (Table 31). Samples will be pre-cracked using identical conditions in open air at a K_{max} of 20 $MPa\sqrt{m}$ and an R-ratio of 0.5. During the pre-crack, K_{max} will be shed from 20 $MPa\sqrt{m}$ to roughly 10 $MPa\sqrt{m}$. Constant-K and rising K tests will be performed in this study on CT specimens. These tests will be performed open to air, with solution flowing from a large reservoir (> 5L). The flow will not be directed at the crack tip to avoid influences from flow on CGR. Tests will be continuously temperature controlled (± 1 ˚C). Constant-K tests will be performed at 44 $MPa\sqrt{m}$ in accordance with results from SNL/DNV-GL and rising-K tests will be performed at a dK/dt of 0.33 $MPa\sqrt{m}/hr$ from 10 to 60 $MPa\sqrt{m}$.

For constant-K tests, the same sample will be utilized across the same solution composition. For example, the same CT specimen will be used to determine crack growth in saturated $MgCl_2$ at both 35 and 55 ˚C. Constant-K CGR will be compared with measurements performed at SNL/DNVGL as these tests will be performed at the same solution concentrations and temperatures and will confirm lab-to-lab consistency of CGR measurements. The previously tapered frequency procedure will be used to transition between different temperature exposures. By performing this procedure, clear demarcations between the controlled temperature CGR measurements will be observed. Additionally, measurements will be compared with collaborators from Pacific Northwest National Labs (PNNL, Mychailo Toloczko), although measurements at PNNL will be performed at 40 ˚C.

At the end of Phase 1, the best testing methodology will be determined by evaluating the CGR response in how conservative each approach is (variance etc.) and the efficiency with which the measurement can be conducted.

4.7.2.2 Phase 2: Investigate Key Variables for CISCC

The key variables which will be investigated in phase 2 are temperature, salt type, and the concentration of salt in the test solution. These tests will be performed using the best method as determined in Phase 1 and will be fully immersed in the brine performed on CT specimens. An example test matrix is shown in Table 36. Stress intensity ranges and pre-cracking conditions for the tests will be chosen based on the results of Phase 1.

These tests will be performed open to air, with solution flowing from a large reservoir (> 5L). The flow will not be directed at the crack tip to avoid influences from flow on CGR. Tests will be continuously temperature controlled (± 1 ˚C). This test will be performed on Lot 3. This will serve to evaluate multiple different phenomena including: (i) the effect of dissolved CO_2 on CGR, (ii) the effect of material properties on CGR, and (iii) and the effect of environment (composition and T) on CGR. Additionally, the result of these tests will allow for a cross laboratory comparison between CGR measurements from SNL, DNV-GL, and PNNL.

Table 36. Example test matrix for Phase 2 CGR Measurements.

Test Type	Temperature (℃)	Brine/Salt	Salt Concentration
Temperature	35	NaCl	Saturated
Temperature	35	$MgCl_2$	Saturated
Temperature	55	NaCl	Saturated
Temperature	35	$MgCl_2$	Saturated
Concentration	35	$MgCl_2$	½ saturation of NaCl
Concentration	55	$MgCl_2$	½ saturation of NaCl
Concentration	35	NaCl	½ saturation of NaCl
Concentration	55	NaCl	½ saturation of NaCl
Composition	35	40 % SW	N/A
Composition	35	76 % SW	N/A

**SW = Seawater*

4.7.2.3 Phase 3: Alternative Methods for Sample Exposure

All Phase 3 tests will be performed using the methods and best practices developed during the prior phases. During this phase, the effects of various atmospheric conditions will be evaluated. First, wicking experiments will be carried out in order to have solution only in the crack and in the notch. This will prevent the surface surrounding the crack mouth or the sides of the specimen from acting as a cathode. Further investigation is necessary to determine relevance to atmospheric environments. Second, misting/atomized tests will be performed and will be similar to accelerated corrosion testing. Next, specific WL will be targeted using an anodized aluminum oxide (AAO) membrane and will give rise to any water layer effects present in SCC of SS304L. Finally, tests will be carried out utilizing salt printing procedures(Schindelholz and Kelly, 2010a). These will be performed under the same conditions established in Phases 1 and 2 (Weirich et al., 2019).

These experiments will be performed at the two temperatures of interest (35 and 55 ˚C) and for the 2 solutions of interest ($MgCl_2$ and 40 % sea salt brine) on CT and SENT specimens. The experimental test matrix is presented in Table 37.

Table 37. Example test matrix for Phase 3 CGR Measurements.

Test Type	Temperature (˚C)	Brine/Salt	Actual Salt Concentration
Wicking	From Phase 1&2	$MgCl_2$	From Phase 2
Wicking	From Phase 1&2	40% SW	From Phase 2
Atomized	From Phase 1&2	$MgCl_2$	From Phase 2
Atomized	From Phase 1&2	40% SW	From Phase 2
Salt Printing	From Phase 1&2	$MgCl_2$	From Phase 2
Salt Printing	From Phase 1&2	40% SW	From Phase 2
Membrane	From Phase 1&2	$MgCl_2$	From Phase 2
Membrane	From Phase 1&2	40% SW	From Phase 2

4.7.2.4 Phase 4: Testing of Different Material Lots and Alloys

Phases 1-3 were focused on gaining a thorough understanding of the behavior of one lot of one SS304L alloy. SNL procured several lots of SS304L with varied alloying elements (such as reduced sulfur) and different resultant mechanical properties (though not widely different) as seen in Table 31 and Table 1. Results from Phase 4 will be directly compared to trends and findings by collaborators at PNNL. PNNL plans to use cold working to vary material properties and investigate SCC susceptibility(Toloczko et al., 2020). PNNL results will also be used to inform further tests that may yield interesting information about the concentration of alloying elements and important material properties and their impact on CISCC.

4.8 Results

It is important to note that all observations and trends present for CGR measurement are from initial results and thus far consist of only a single trial at each temperature and solution. Additionally, all experiments were conducted in a solution which was being constantly bubbled with CO_2 scrubbed air, therefore maintaining O_2 saturation. The effects of dissolved CO_2 as well as performing replicate experiments will be further explored in FY21.

4.8.1 Stress/Strain

Stress strain behavior for Lot 3, was performed by Westmoreland Mechanical Testing and Research Incorporated. The average 0.2 % yield strength (YS) is 243.62 MPa (35.3 ksi) and the average modulus of elasticity (E) is 207.54 GPa based in Figure 142. Tests were performed in compression and tension and yielded very similar behavior.

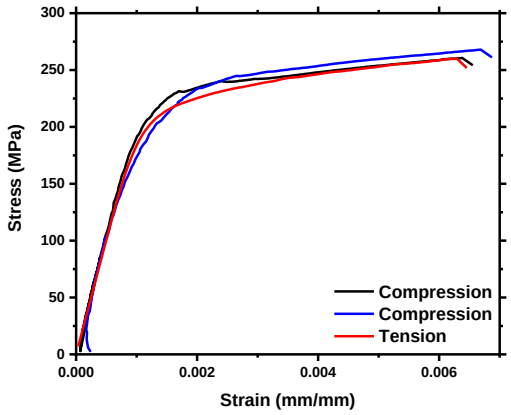

Figure 142. Stress strain curve for SS304L - Lot 3 Tests were performed at room temperature by Westmoreland Mechanical Testing and Research Inc.

4.8.2 Microstructure

Lot 3 and 4, were electrochemically polished for microstructural characterization. The samples were polished to using 50 vol% phosphoric acid, 20 vol% sulfuric acid, and 30 vol% DI water. A platinized Nb mesh cage was used as the counter electrode. The electro-polishing took place over 12 min at 5 A (4.9 V), which correlates to ~500 mA/cm^2. The polarity was reversed every 2 min, for 10 s, to reduce the oxide formed on the samples during polishing. Roughly 10 to 20 μm of material was removed after the 12 min electro-polishing process. After polishing, samples were analyzed in a SEM to determine the grain size, grain orientation, and phases present in the material. EBSD patterns of ST, LT, and RD (Figure 135) for 304L – Lot 3 can be seen in Figure 143(a, c, e) and 304L – Lot 4 can be seen in Figure 143 (b, d, f) respectively. The electron micrographs shown here are from the mid-thickness of the plate.

The microstructures present for both lots are typical of austenitic stainless steels taken from a plate. Grain banding is present, as signified by the alternating FCC (blue) and BCC (red) phases in the LT (Figure 143(c) and (d)) and RD (Figure 143(e) and (f)) planes. The grain shape is relatively equiaxed. It is noted that there is slight variation in the ST plane of Lot 3 (Figure 143(a)). Twinning occurs with moderate frequency throughout the microstructure.

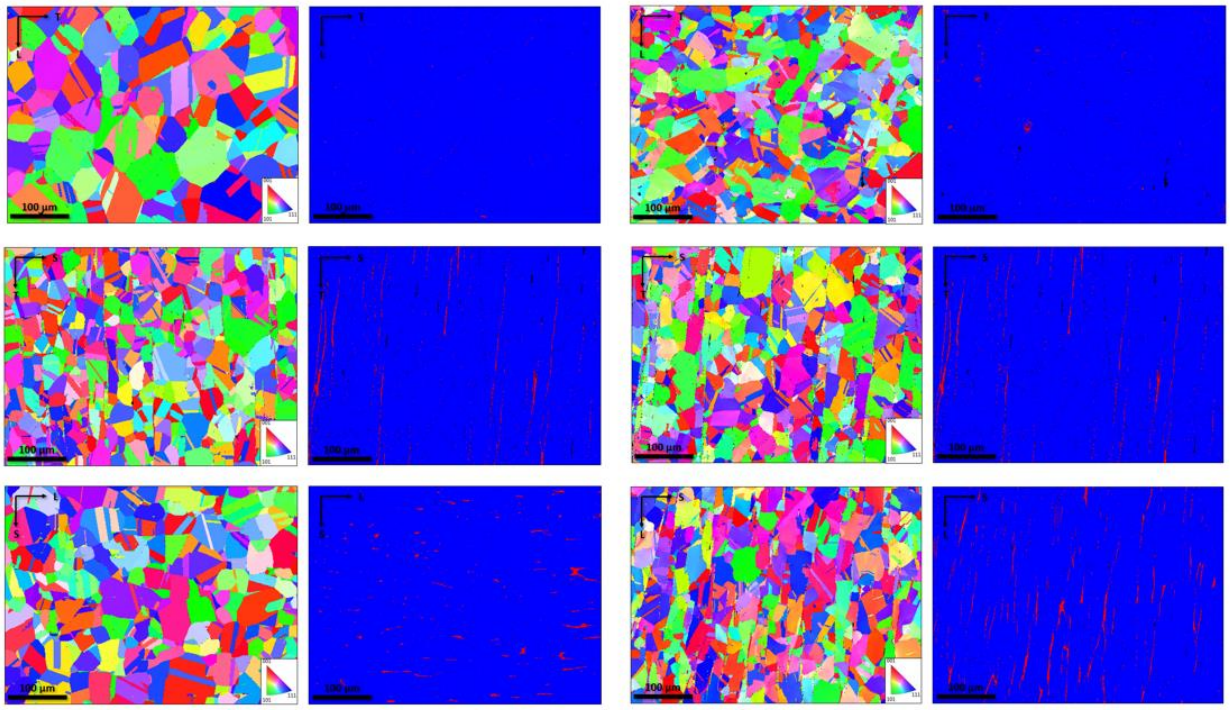

Figure 143. EBSD patterns of ST, LT, and RD for 304L – Lot 3 (a, c, e) and 304L – Lot 4 (b, d, f) respectively. It is noted that the blue represents FCC phases while the red represents BCC phases. Planes refer to Figure 135.

4.8.3 Pre-Cracking

As seen in Figure 144 the pre-cracking procedure described in section 4.6.1 was performed on two samples (SN022 and SN026). These samples were pre-cracked at SNL/ABQ. Despite being pre-cracked with the same parameters, sample SN022 took nearly 60 hours to reach the target crack length of 0.575" where SN026 reached that length in just 37 hours. Both samples were manufactured using SS304L from Lot 3.

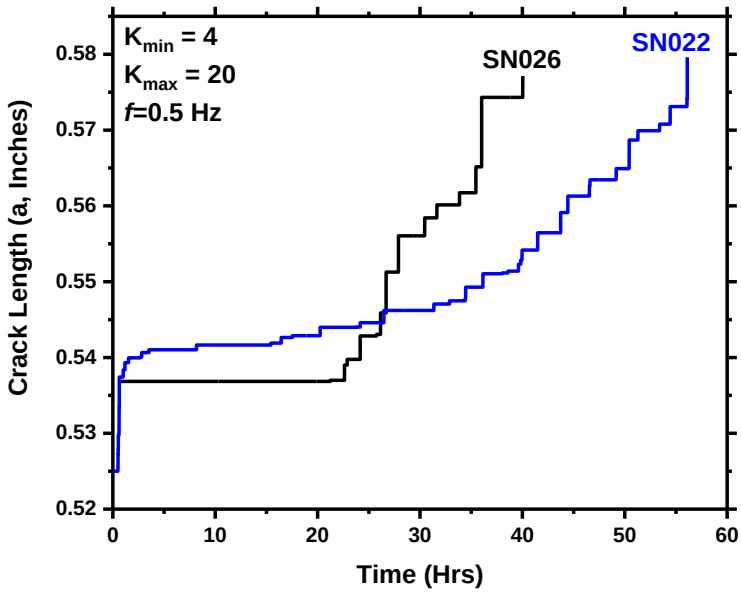

Figure 144. SNL pre-crack data from SN022 and SN026 specimens manufactured from Lot 3 material.

4.8.4 FY 20 Preliminary CGR Results

4.8.4.1 $MgCl_2$

The stress intensity examined herein was selected to be significantly above threshold stress intensities for CISCC growth based on previous research (Bryan and Enos, 2016) to ensure a CISCC response. Cracks were started from a fatigue pre-crack in air, grown from the machined notch in the specimen. The fatigue pre-cracks are typically transgranular in nature. If the particular material is susceptible to intergranular SCC (IGSCC) in the environment, then the transgranular pre-crack needs to be transitioned to an intergranular crack. This is accomplished through a series of decreasing frequency fatigue cycles shown in 140 and Figure 145(a) for a CT specimen in 4.98 M $MgCl_2$ at 35 ˚C. At each frequency, the crack length was actively monitored, allowing for control on K. Additionally, this allows for the calculation of both the crack growth rate ($CGR = \frac{\Delta a}{time}$) as shown in Figure 145(a) and (b). Finally, the corrosion fatigue crack growth rate response (CFCGR, mm/cycle) was evaluated at each frequency and is displayed in Figure 145(c).

In 4.98 M $MgCl_2$ at 35 ˚C, CGR decreases with decreasing frequency as seen in Figure 145(b) with CT (K_{max} = 49.5 $MPa\sqrt{m}$) and SENT (K_{max} = 44 $MPa\sqrt{m}$) specimen exhibiting nearly identical CGR behavior. It is interesting to note that the CFCGR, Figure 145(c), is relatively independent of frequency. Similarly, for CGR, CFCGR is also nearly identical for CT and SENT specimens across the range of frequencies studied. This is a good indication that both CT and SENT specimens can be utilized in this study.

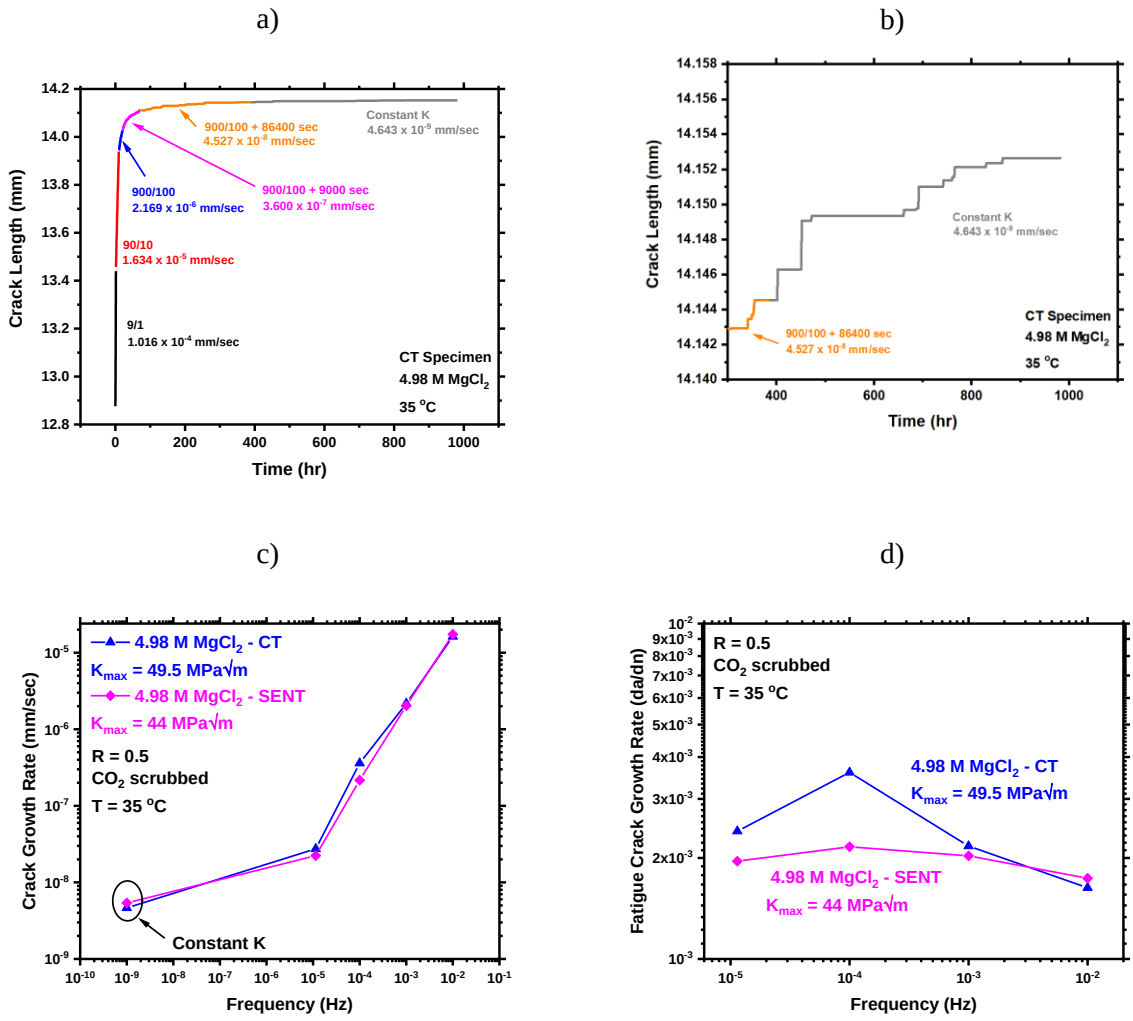

Figure 145. (a) Crack length and crack growth rate vs. time as a function of frequency for a CT specimen in 4.98 M $MgCl_2$ at 35 ˚C with (b) inset region. (c) Comparison of CGR for 4.98 M $MgCl_2$ for a CT (Figure 137) and SENT (Figure 138) specimen. (d) Comparison of corrosion fatigue crack growth rate vs. frequency as a function of sample geometry. It is noted that for all scenarios, the CT specimen had a K_{max} = 49.5 MPa(m)$^{1/2}$ and the SENT specimen had a K_{max} = 44 MPa(m)$^{1/2}$. Additionally, all tests were completed in CO_2 scrubbed environments.

The influence of temperature on CGR for an SENT in 4.98 M $MgCl_2$ is presented in Figure 146(a). CFCGR vs. temperature as a function of frequency is displayed in Figure 146(b). The CFCGR is relatively independent of frequency for both temperatures explored. It is noted that CGR measurements are still being conducted at 55 ˚C in order to determine the constant-K CGR response.

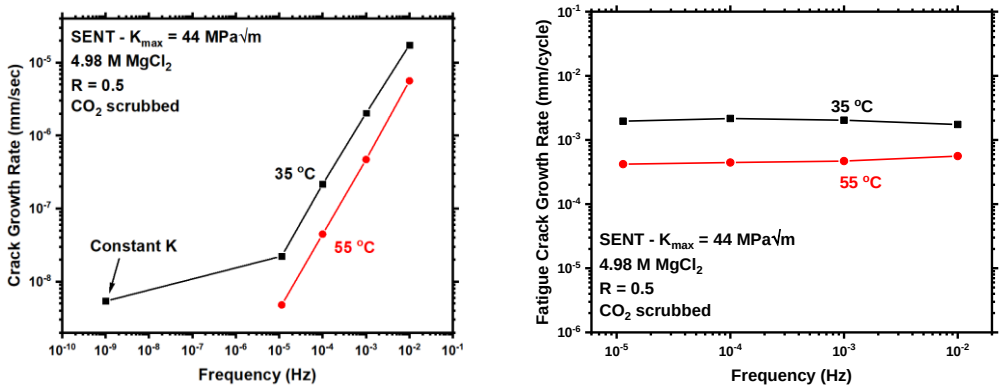

Figure 146. crack growth rate vs. frequency (Table 33) as a function of temperature for SENT specimen (Figure 138) in saturated $MgCl_2$ solutions. (b) Comparison of corrosion fatigue crack growth rate vs. frequency as a function of temperature in saturated $MgCl_2$ solutions.

4.8.4.2 NaCl

CGR for a CT specimen in 5.3 M NaCl as a function of both temperature and frequency is seen in Figure 147(a) and (b). The overall trends with respect to CGR present in saturated NaCl solutions are largely similar to the behavior of saturated $MgCl_2$ solutions. CFCGR for a CT specimen in 5.3 M NaCl as a function of both temperature and frequency is seen in Figure 147(c).

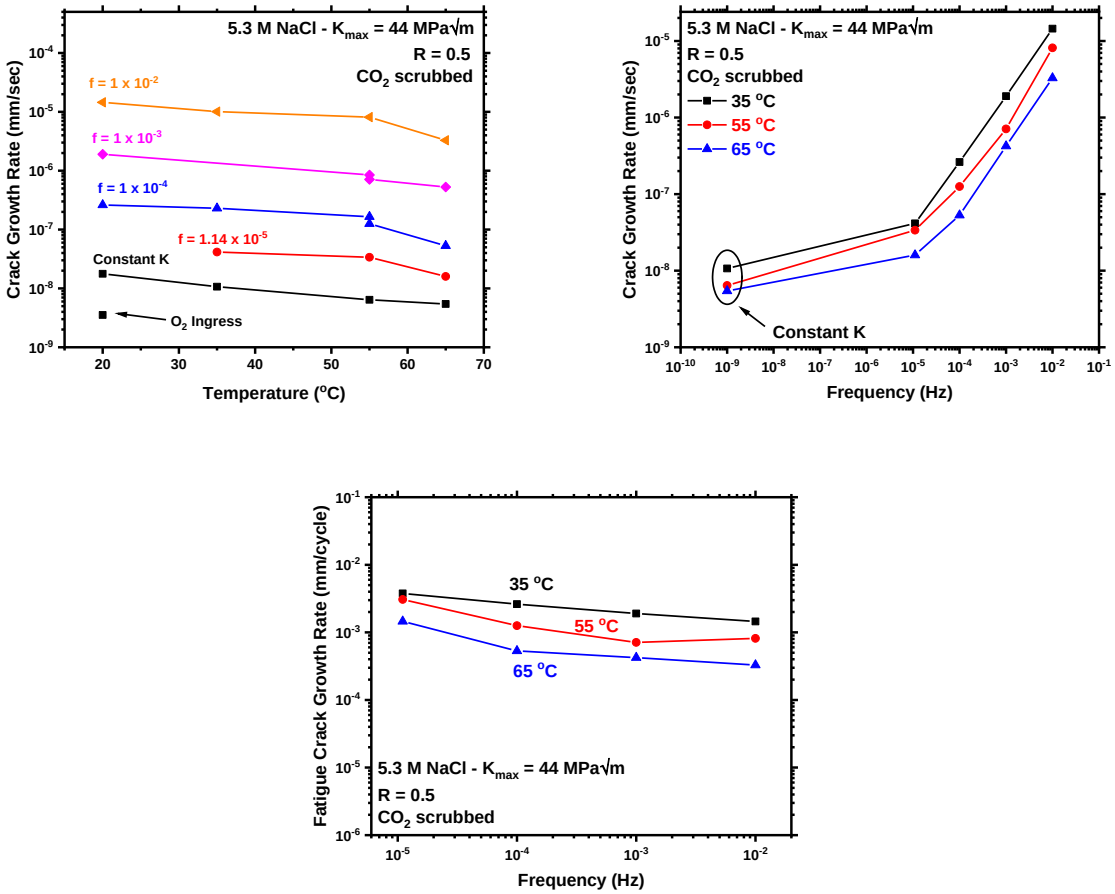

Figure 147. (a) Crack growth rate vs. temperature as a function of frequency for 5.3 M NaCl. (b) Crack growth rate vs. frequency for 5.3 M NaCl as a function of temperature. (c) Corrosion fatigue crack growth rate vs. frequency for 5.3 M NaCl as a function of temperature. It is noted that the measurements were taken with a CT specimen (Figure 137).

4.8.4.3 Seawater

CGR for a CT specimen in two seawater solutions (compositions given in Table 34) at 35 ˚C as a function of both temperature and frequency is seen in Figure 148(a). It is noted that the 76 % RH seawater is still being transitioned to a constant-K state. Generally, the two seawater brines (40 and 76 % RH) had very similar CGR over the frequencies tested. CFCGR is also presented for the two seawater brines in Figure 148(b) and again exhibits similar behavior across the entire range of frequencies explored.

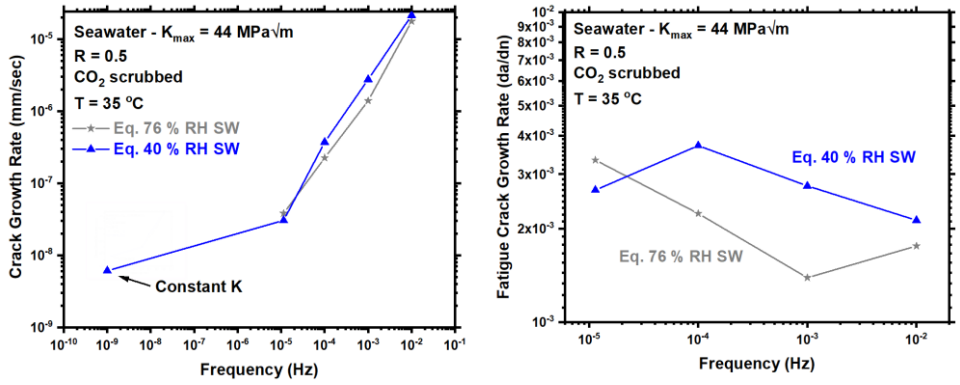

Figure 148. (a) Crack growth rate vs. frequency (Table 33) at 35 ˚C for CT specimen (Figure 137) in 76 and 40 % RH sea salt brines. (b) Comparison of corrosion fatigue crack growth rate vs. frequency as a function of temperature in 76 and 40 % RH seawater brines.

4.8.5 Overall

It is important to note that all observations and trends present are made comparing one trial of each temperature, and solution. Additionally, all experiments were conducted in a solution which was being constantly being bubble with CO_2 scrubbed air, therefore maintaining O_2 saturation. The effects of dissolved CO_2 as well as performing replicate experiments are currently being undertaken.

As seen in Figure 149(a) and (b), at 35 ˚C, 5.3 M NaCl and 76 % RH seawater brine (containing 4.4 M NaCl) behave similarly as a function of frequency. Additionally, at 35 ˚C, 4.98 M $MgCl_2$ and 40 % RH seawater brine (containing 5.1 M $MgCl_2$) behave similarly at a constant-K of 44 $MPa\sqrt{m}$ (Figure 149(c)) and as a function of frequency (Figure 149(d)).

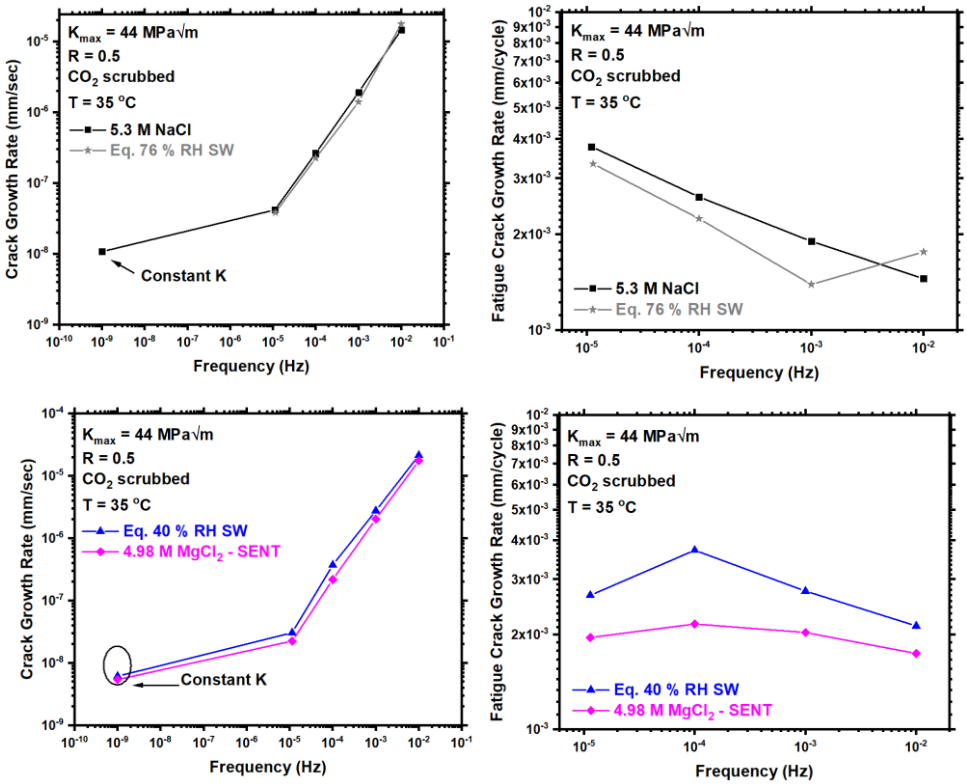

Figure 149. Comparison of (a) crack growth rate and (b) corrosion fatigue crack growth rate as a function of frequency in 5.3 M NaCl and 76 % sea salt brine at 35 ˚C. Comparison of (c) crack growth rate and (d) corrosion fatigue crack growth rate as a function of frequency in 4.98 M $MgCl_2$ and 40 % sea salt brine at 35 ˚C. It is noted that NaCl and 76 and 40 % RH sea salt brine were performed with CT specimens while $MgCl_2$ was performed with a SENT specimen.

Despite having almost double the chloride concentration, preliminary examination in saturated $MgCl_2$ solutions displays roughly the same, if not lower CGR kinetics in comparison to saturated NaCl solutions. Crack growth as a function of frequency and fatigue crack growth rate are presented in Figure 150(a) and (b) respectively comparing MgCl2 and NaCl solutions at 35 and 55 ˚C. Under a constant-K of 44 $MPa\sqrt{m}$ and a temperature of 35 ˚C, saturated $MgCl_2$ and NaCl have similar CGR with $MgCl_2$ being slightly under NaCl. When considering fatigue crack growth rate at 35 ˚C, $MgCl_2$ and NaCl have nearly identical CFCGR over the four orders of magnitude of frequency explored. At 55 ˚C, the saturated $MgCl_2$ is still being transitioned to a constant-K state, however, we can compare the CFCGR. As shown in Figure 150(b), the CFCGR is similar between saturated $MgCl_2$ and NaCl at 10^{-2} and 10^{-3} Hz however the behavior deviates slightly at 10^{-4} and 10^{-5}. At a frequency of 10^{-5}, saturated $MgCl_2$ has roughly an order of magnitude lower CFCGR in comparison to saturated NaCl.

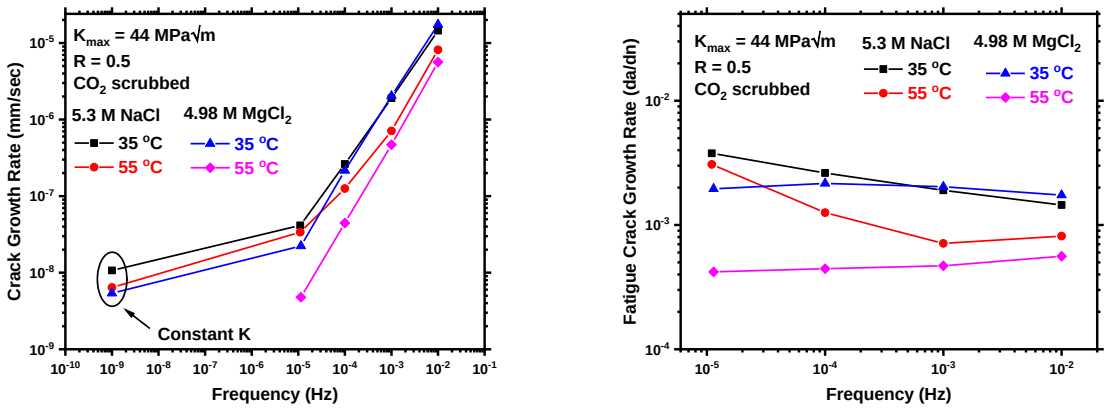

Figure 150. Comparison of (a) crack growth rate and (b) corrosion fatigue crack growth rate vs. frequency in saturated NaCl and $MgCl_2$ as a function of temperature. It is noted that a CT (Figure 137) was utilized in NaCl and SENT (Figure 138) specimen was utilized in $MgCl_2$.

Collaborations with PNNL for SCC testing are currently underway. During FY20, PNNL also began initial SCC testing (Toloczko et al., 2020). Both SCC testing programs began using non-programmatic material lots so it is difficult to draw comparisons between CGR obtained in each study. Constant-K CGR and CFCGR results from PNNL and SNL/DNV-GL are compared in Figure 151(a) and (b) respectively. SCC experiments performed at PNNL were at 40 ˚C while experiments at SNL/DNVGL were performed at 35, 55, and 65 ˚C all in saturated NaCl. As shown in Figure 151(a), constant-K CGR was roughly an order of magnitude higher for PNNL experiments in comparison to all experiments ran at SNL/DNV-GL. This is interesting considering PNNL used a lower K (26 and 20 $MPa\sqrt{m}$) in comparison to 44 $MPa\sqrt{m}$ that was used at SNL/DNV-GL. Another difference between the tests included PNNL flowing solution in their experiments, in some cases, directed at the notch of the sample whereas experiments performed by SNL/DNV-GL were performed in a large volume containing (6 L) with CO_2 scrubbed air bubbling constantly in the solution. Flow at the crack tip could have implications on both crack tip chemistry and electrochemistry. Either way, the oxygen concentration should have maintained saturated conditions in the NaCl solutions. Next, different lots of material were used. The PNNL lot used in their preliminary tests has a lower yield strength and hardness in comparison to the lot utilized here (Table 31) while the compositions are nominally similar (Table 32). Finally, slightly different procedures were used to transition to a constant-K state. In the case of PNNL, the last frequency used before constant-K was 10^{-4} while SNL/DNVGL had a final frequency of 1.14 x 10^{-5}.

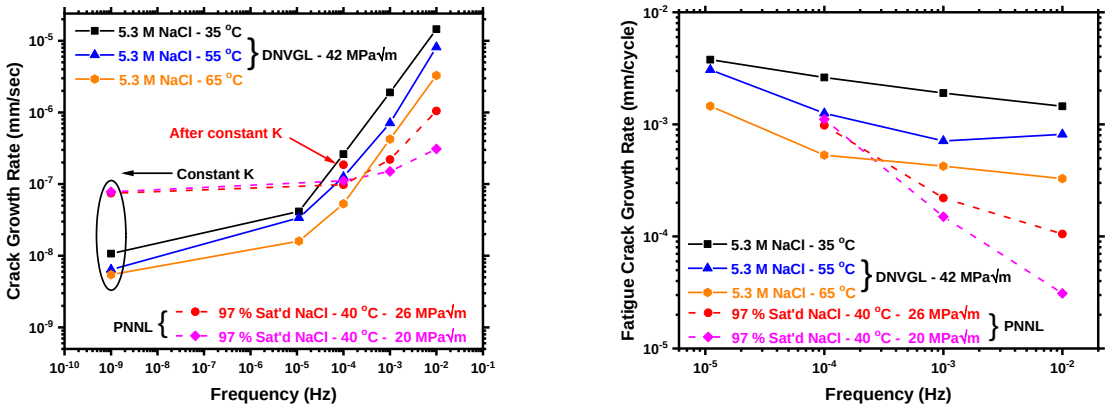

Figure 151. Comparison of SNL/DNVGL and PNNL (a) crack growth rate and (b) corrosion fatigue crack growth rate vs. frequency as a function of temperature and stress intensity. PNNL results were obtained from (Toloczko et al., 2020). It is noted that results presented here were performed with zero air while results from PNNL were in O_2 saturated air.

Results obtained at SNL/DNV-GL and PNNL are plotted with obtained literature results from Bryan and Enos (Bryan and Enos, 2016) as shown in Figure 152. It is noted that the CGR in $MgCl_2$ at 55 and 75 ˚C did not undergo transitioning. Rather the temperature was changed while under constant-K and the crack growth was observed. Preliminary tests in CO_2 scrubbed air did not display a dependence on temperature, potentially indicative of the occurrence of crack bifurcation. Post-mortem failure analysis and fractography are planned for FY21. Overall, the CGR obtained at SNL/DNV-°GL falls within the scatter of the literature CGR for austenitic SS.

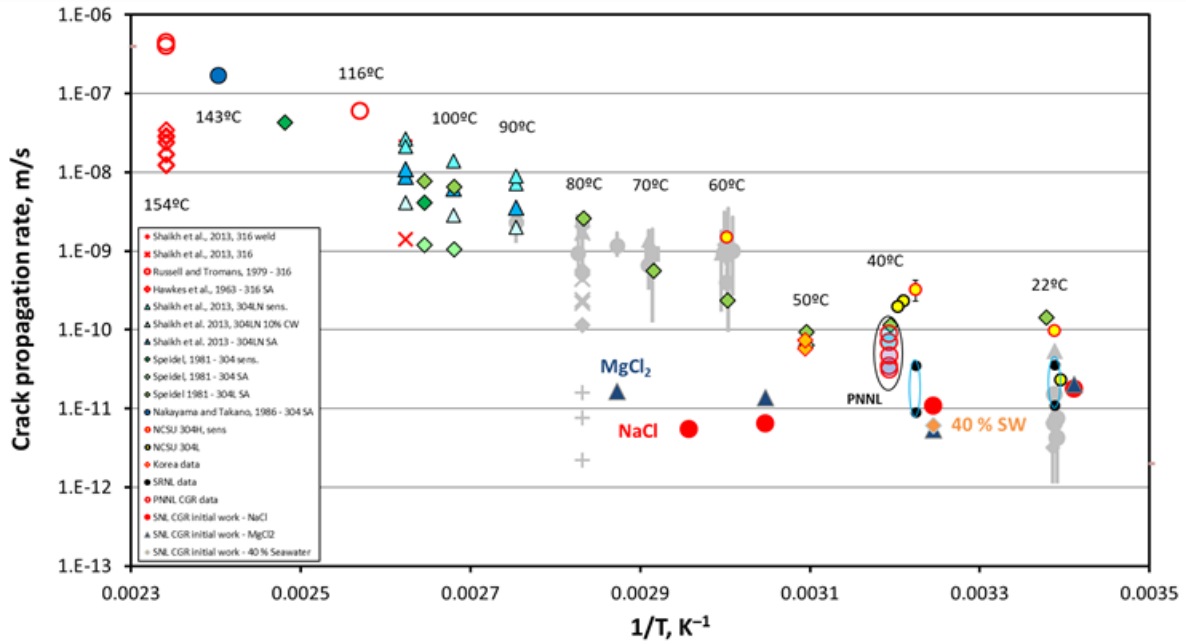

Figure 152. Current SNL/DNV-GL (in solid red and solid blue) and PNNL (in solid orange) CGR data added to SNL literature compilation (Bryan and Enos, 2016). SNL compilation in gray are from atmospheric evaluations while immersed are outlined colored.

4.9 CGR Initial Conclusions

In FY20, the set-up and installation of 4 DCPD systems at SNL was completed. Initial CGR was completed at SNL/DNV-GL and focused on solution composition and temperature variation. Procurement and characterization of multiple lots of 304L and 316L commenced in FY20. The SS lots that were procured by PNNL have a very low sulfur content; to cover the entire potential range that might be relevant for dry storage canisters, a slightly higher sulfur content stainless steel, still within the ASTM specifications for 304L SS, was also procured. SS304L with a higher sulfur content will potentially form more MnS inclusions, which generally serve to enhance corrosion. The SCC response of this material will also be evaluated.

CGR as a function of solution composition and temperature was obtained in FY20 for a non-program lot of SS304L. Saturated NaCl and $MgCl_2$ solutions were used in addition to seawater brines at two different relative humidities. CGR was measured using high fidelity DCPD systems in a temperature-controlled solution ranging from 20 to 75 ˚C with CO_2 scrubbed air. In the single trial of each solution and temperature that were presented within this study, there was minimal dependence of CGR in the CO_2 scrubbed brines. Additionally, a dependence of CGR on temperature was not observed, potentially indicative of crack bifurcation. Further post-mortem analysis of samples will be carried out in FY21 to better understand these behaviors. Also, these trends are going to be further explored with other material lots and experimental conditions in FY21.

Measured CGR values were compared to literature values of CGR and fell within the scatter as displayed in Figure 152. Results compiled by Bryan and Enos (Bryan and Enos, 2016) were performed using a wide variety of testing methods in many different environments contributing to study-to-study variability. When using high fidelity DCPD systems to study CGR (such as PNNL (Toloczko et al., 2020)) an order-of-magnitude variability in CGR exists between the two studies. The difference between the obtained CGRs highlights the importance of testing procedures (including air bubbled into the testing environment, flow of solution, and transitioning procedure) as well as the lot of material that is used.

In FY21, CGR testing will continue at SNL and SNL/DNV-GL, enabling the determination of CGR on roughly 6 frames. As described in Section 4.7.2, the main focus for FY21 will be centered around the testing environment. The role of solution composition, solution concentration and temperature will be evaluated. Additionally, the role of stress intensity will be explored. These different phenomena will first be explored in full immersion testing environments. More importantly in FY21, testing will transition to atmospheric environments. This will include wicking, simulated thin water layers, and salt printing exposed to humid environments. Testing in thin film environments will enable the accurate representation of canister conditions and evaluate potential cathodic control on crack growth rates which could serve to decrease CGR.

5. Conclusions

In FY20, work to define dry storage canister surface environments included several tasks. First, field work at the Maine Yankee ISFSI involved examination of corrosion witness specimens and collection of dust and soluble salt specimens from the vents of in-service dry storage systems. Although not representative of dust on the canisters, the vent samples provided critical information on ambient dust aerosols at the site, allowing a comparison of the ambient dust to that which actually deposits on the canister surfaces as determined by previous sampling efforts at the site. The vent samples contained more chloride than the canister samples, possibly indicating that coarse sea-salt aerosols do not enter the overpack and deposit on the canister surface. This suggests that measurements of ambient salt aerosols at the ISFSI site (e.g., via wet candles) may overestimate the corrosiveness of the canister surface environment.

The predicted evolution of canister surface RH values was estimated using ISFSI site weather data and the horizontal canister thermal model used by the SNL probabilistic SCC model. These calculations determined that for typical ISFSI weather conditions, sea-salt deliquescence to produce $MgCl_2$-rich brines could occur in less than 20 years at the coolest locations on the canister surface. However, RH values rise slowly, and, even after nearly 300 years, conditions for NaCl deliquescence (75% RH) are not reached. This work illustrates the importance of understanding the stability of $MgCl_2$-rich brines on the heated canister surface, and the potential impact of brine composition on corrosion processes, including pitting and stress corrosion cracking.

In an additional study, the description of the canister surface environment was refined in order to define more realistic corrosion testing environments. The aspects of the environment have been evaluated. First, realistic diurnal cycles for evaluating brine wetting and drying cycles were defined; these conditions will eventually occur at all locations on all dry storage canisters. Second, soluble salt chemistries from in-service canister sampling campaigns were evaluated, and a typical salt assemblage was identified for testing purposes. Previous corrosion experiments have been carried out using sea-salts or individual components of sea-salts. However, site sampling has indicated that a mix of marine and continental salt aerosols is commonly present, with high concentrations of sulfate and nitrate as well as chloride; testing using the proposed salt assemblage will determine if these species inhibit canister corrosion or SCC. Finally, inert mineral particle size distributions were determined in canister dust samples. Inert minerals are the most abundant dust particles in samples collected from in-service canisters, and may have a significant impact on corrosion processes by promoting brine spreading on the metal surface, potentially affecting the properties of the cathode supporting pit growth, and/or by creating occluded areas under larger dust grains, resulting in crevice corrosion. The potential impacts of these phenomena on canister corrosion are being evaluated experimentally.

Finally, work over the past few years to evaluate the stability of magnesium chloride brines continued in FY20. $MgCl_2$ degassing experiments were carried out, confirming that $MgCl_2$ brines slowly degas HCl on heated surfaces, converting to less deliquescent magnesium hydroxychloride phases. This process could eventually lead to brine dryout. Corrosion reactions could also result in $MgCl_2$ brine dryout as described below. As part of the work to understand $MgCl_2$-brine stability, development of a thermodynamic model for the complex sequence of magnesium hydroxychloride phases that form at different temperatures and brine concentrations is underway.

In FY20, corrosion testing and modeling was performed in more canister relevant environments. Continued evaluation of pitting observed in large scale exposure tests from FY18/19 and comparison of results to pitting in exposures of varied brine compositions helped elucidate influences of the canister surface environment on pit growth, both size and morphology. In FY20, large scale pitting exposure tests were expanded to include environments based on real site-specific data as described in Section 2.2. A long term (2 year) sample exposure set examining the influence of diurnal temperature and RH fluctuations has been initiated for SS304 and SS316 samples deposited with simulated seawater.

Additionally, initial calibrations are underway for a second large exposure set exploring the influences of inert dust on corrosion in canister relevant exposures (to be started in FY21). Data gained from these exposures will better establish the potentially deleterious factors for corrosion and SCC initiation and help to further parameterize the maximum pit size model. In addition to enhanced experimentation through testing in more relevant scenarios, FY20 also produced expanded modeling efforts for the maximum pit size model. Efforts focused on accounting for non-static brine/corrosion conditions to better predict pitting and SCC initiation, specifically under more relevant brine compositions, i.e. seawater and $MgCl_2$ dominated brines. Two major observations produced from work in FY20 are: 1) $MgCl_2$ brines influence the pit morphology towards the formation of more irregular shapes with near surface microcracks and 2) $MgCl_2$ brines influence the controlling cathodic kinetics through dominance of the HER cathodic reaction and formation of precipitates that lower the predicted maximum pit size. These are both significant findings with respect to canister-relevant environments because brines that form on canister surfaces for the first few hundred years of storage will be $MgCl_2$-dominated brines. Understanding the potentially opposing roles of these two phenomena on SCC initiation will better enhance our determination of the susceptibility of SNF canisters to SCC.

While FY20 saw major advancements with respect to understanding the relationship between canister relevant brine conditions and corrosion, it is still unknown how cracks, once initiated will behave under these conditions. To further the study of this, SNL has installed capabilities (four new load frames) and started initial tests on crack growth rate of SS in canister relevant environments. Testing in FY20 established viable methods for exploring the influence of brine composition and temperature on CGR. Additionally, sample geometries were verified to initiate SCC CGR testing in atmospheric environments, which will become the focus of testing in FY21.

Overall, in FY20, SNL was able to better quantify, and model canister relevant environments present at ISFSI sites. This was applied to inform current and future corrosion tests to explore the effects of relevant brines on corrosion and SCC initiation. Experiments in FY20 elucidated potentially significant influences of $MgCl_2$ dominated brines on corrosion which may also govern crack initiation and crack growth rates. Focus in FY21 will work to further evaluate these more relevant conditions to enhance determination of SCC susceptibility. This will enable better predictions of timing and location of SCC occurrence to minimize inspections and develop and apply enhanced repair and mitigation strategies. Specifically, corrosion work in FY21 at SNL will seek to address:

(1) generation of an expanded statistical pitting data set as function of environment, specifically under more relevant conditions including cyclic conditions, influence of inert dust, and exploring other chemical influences observed at ISFSI locations (i.e. nitrates);

(2) hierarchal identification of features controlling pit-to-crack transitions (environment, material, pit morphology, etc.);

(3) definition of the relationship between surface environmental conditions, cathodic kinetics, and subsequent control of SCC CGR and susceptibility;

(4) initial evaluation and testing of repair and mitigation strategies (including cold spray and other coatings) to determine potential behavior under canister relevant conditions.

6. References

Altmaier, M., Metz, V., Neck, V., Muller, R., Fanghanel, T., 2003. Solid-liquid equilibria of Mg(OH)(2)(cr) and Mg-2(OH)(3)Cl center dot 4H(2)O(cr) in the system Mg-Na-H-OH-O-Cl-H2O at 25 degrees C. *Geochimica Et Cosmochimica Acta*, 67(19): 3595-3601.

Andersen, T.L., 2005. *Fracture Mechanics Fundamentals and Applications*. CRC Press Taylor & Francis Group.

Angeliu, T.M., Andresen, P.L., Hall, E., Sutliff, J.A., Sitzman, S., 2000. *Strain and Microstructure Characterization of Austinitic Stainless Steel Weld HAZS*

NACE International.

ASTM International, 2008. *E1681 – 03 Standard Test Method for*
Determining Threshold Stress Intensity Factor for Environment-Assisted Cracking of Metallic Materials.

ASTM International, 2015a. *A666-15 Standard Specification for Annealed or Cold-Worked Austenitic Stainless Steel Sheet, Strip, Plate, and Flat Bar*. ASTM International.

ASTM International, 2015b. *E647-15 Standard Test Method for Measurement of Fatigue Crack Growth Rates*.

ASTM International, 2015c. *Electrochemical Reactivation (EPR) for Detecting Sensitization of AISI Type 304 and 304L Stainless Steels*, ASTM International. American Society for Testing and Materials, pp. 1-6.

ASTM international, 2016. *E8/E8M-16a Standard Test Methods for Tension Testing of Metallic Materials*.

ASTM International, 2017. *E399 −17 Standard Test Method for Linear-Elastic Plane-Strain Fracture Toughness KIc of Metallic Materials*.

Bethke, C., 2008. *Geochemical and Biogeochemical Reaction Modeling*. Cambridge Press.

Bouchard, P. et al., 2005. Measurement of the Residual Stresses in a Stainless Steel Pipe Girth Weld Containing Long and Short Repairs. *International Journal of Pressure Vessels and Piping*, 82: 299-310.

British Standards Institution, 2015. *BS 8571:2014 Method of test for determination of fracture toughness in metallic materials using single edge notched tension (SENT) specimens*.

Bryan, C., Schindelholz, E., 2018a. *FY18 Status Report: SNL Research into Stress Corrosion Cracking of SNF Interim Storage Canisters*. Milestone # M2SF-18SN010201049, U.S. Department of Energy.

Bryan, C., Schindelholz, E., 2018b. *FY18 Status Report: SNL Research into Stress Corrosion Cracking of SNF Interim Storage Canisters*. In: Energy, U.S.D.o. (Editor).

Bryan, C.R., Enos, D.G., 2016. *Summary of available data for estimating chloride-induced SCC crack growth rates for 304/316 stainless steel*, Sandia National Labs.

Chen, X.-G. et al., 2011. Preparation of magnesium hydroxide chloride hydrate nanowires using calcined dolomite. *Wuji Cailiao Xuebao*, 26(2): 214-218.

Chen, X., Nanstad, R., Sokolov, M., Application of Direct Current Potential Drop for the J-integral Vs. Crack Growth Resistanct Curve Characterization *Materials Science and Technology Division; Oak Ridge National Laboratory*.

Chen, Z.Y., Cui, F., Kelly, R.G., 2008. Calculations of the cathodic current delivery capacity and stability of crevice corrosion under atmospheric environments. *Journal of the Electrochemical Society*, 155(7): C360-C368.

Chen, Z.Y., Kelly, R.G., 2010. Computational modeling of bounding conditions for pit size on stainless steel in atmospheric environments. *Journal of the Electrochemical Society*, 157(2): C69-C78.

Chermak, J.A., Rimstidt, J.D., 1989. Estimating the Thermodynamic Properties (Delta-Gfo and Delta-Hfo) of Silicate Minerals at 298-K from the Sum of Polyhedral Contributions. *American Mineralogist*, 74(9-10): 1023-1031.

Christov, C., 2009. Chemical Equilibrium Model of Solution Behavior and Bishofite (MgCl2 center dot 6H(2)O(cr)) and Hydrogen-Carnallite (HCl center dot MgCl2 center dot 7H(2)O(cr)) Solubility in the MgCl2 + H2O and HCl-MgCl2 + H2O Systems to High Acid Concentration at (0 to 100) degrees C. *Journal of Chemical and Engineering Data*, 54(9): 2599-2608.

Cook, A.J., Padovani, C., Davenport, A.J., 2017. Effect of nitrate and sulfate on atmospheric corrosion of 304L and 316L stainless steels. *Journal of The Electrochemical Society*, 164(4): C148.

Crane, C.B., Gangloff, R.P., 2016. Stress Corrosion Cracking of Al-Mg Alloy 5083 Sensitized at Low Temperature. *NACE - Corrosion*, 72(2).

Crane, C.B., Kelly, R.G., Gangloff, R.P., 2016. Crack Chemistry Control of Intergranular Stress Corrosion Cracking in Sensitized Al-Mg. *NACE - Corrosion*, 72(2).

Crocella, V. et al., 2017. The Importance of Interactions at the Molecular Level: A Spectroscopic Study of a New Composite Sorber Material. *Appl. Spectrosc.*, 71(10): 2278-2285.

de Lima-Neto, P. et al., 2008. Determination of the sensitized zone extension in welded AISI 304 stainless steel using non-destructive electrochemical techniques. *Corrosion Science*, 50(4): 1149-1155.

Dick, J.M., 2019. CHNOSZ: Thermodynamic Calculations and Diagrams for Geochemistry. *Frontiers in Earth Science*, 7.

Dietzel, W., Srinivasan, P.B., Atrens, A., 2011. Testing and evaluation method for stress corrosion cracking (SCC) in metals. In: Raja, S., Tetsuo, S.V. (Ed.), Stress Corrosion Cracking: Theory and Practice. Woodhead Publishing Series in Metals and Surface Engineering Ser. Elsevier Science & Technology, pp. 131-166.

Dong, P., Hong, J., Bouchard, P., 2005. Analysis of residual stresses at weld repairs. *International Journal of Pressure Vessels and Piping*, 82: 258-269.

Dong, P., Zhang, J., Bouchard, P.J., 2002. Effects of Repair Weld Length on Residual Stress Distribution. *Journal of Pressure Vessel Technology*(124): 74-80.

Dorrepaal, R.M., Gowen, A.A., 2018a. Identification of Magnesium Oxychloride Cement Biomaterial Heterogeneity using Raman Chemical Mapping and NIR Hyperspectral Chemical Imaging. *Scientific Reports*, 8.

Dorrepaal, R.M., Gowen, A.A., 2018b. Identification of Magnesium Oxychloride Cement Biomaterial Heterogeneity using Raman Chemical Mapping and NIR Hyperspectral Chemical Imaging. *Sci. Rep.*, 8(1): 1-11.

Duffy, T.S., Meade, C., Fei, Y., Mao, H.-K., Hemley, R.J., 1995. High-pressure phase transition in brucite, Mg(OH)2. *Am. Mineral.*, 80(3-4): 222-30.

Elcoate, C., Dennis, R., Bouchard, P., Smith, M., 2005. Three dimensional multi-pass repair weld simulations. *International Journal of Pressure Vessels and Piping*, 82: 244-257.

Enos, D., Bryan, C., 2016a. *Final Report: Characterization of Canister Mockup Weld Residual Stresses*, Prepared for U.S. Department of Energy

Used Fuel Disposition Program.

Enos, D.G., Bryan, C.R., Understanding the Risk of Chloride Induced Stress Corrosion Cracking of Interim Storage Containers for the Dry Storage of Spent Nuclear Fuel: Residual Stresses in Typical Welded Containers. *SAND2015-8668C*.

Enos, D.G., Bryan, C.R., 2016b. *Characterization of Canister Mockup Weld Residual Stresses* U.S. Department of Energy.

Enos, D.G., Bryan, C.R., 2016c. *Final Report: Characterization of Canister Mockup Weld Residual Stresses*. FCRD-UFD-2016-000064, U.S. DOE.

Fairweather, N., Platts, N., Tice, D., 2008. *Stress-Corrosion Crack Initiation Of Type 304 Stainless Steel In Atmospheric Environments Containing Chloride: Influence Of Surface Condition Relative Humidity Temperature And Thermal Sensitization*, CORROSION 2008. NACE International.

Gangloff, R.P., Ha, H.M., Burns, J.T., Scully, J.R., 2014. Measurement and Modeling of Hydrogen Environment-Assisted Cracking in Monel K-500. *TMMS/ASM Int.*

Garcia, C., de Tiedra, M.P., Blanco, Y., Martin, O., Martin, F., 2008. Intergranular corrosion of welded joints of austenitic stainless steels studied by using an electrochemical minicell. *Corrosion Science*, 50(8): 2390-2397.

George, D., Smith, D., 2005. Through thickness measurement of residual stresses in a stainless steel cylinder containing shallow and deep weld repairs. *International Journal of Pressure Vessels and Piping*, 82: 279-287.

Hanna, R., 1965. Infrared properties of magnesium oxide. *J. Am. Ceram. Soc.*, 48(7): 376-80.

Hebert, K., Alkire, R., 1988. Growth-Rates of Aluminum Etch Tunnels. *Journal of the Electrochemical Society*, 135(10): 2447-2452.

Hofmeister, A.M., Bowey, J.E., 2006. Quantitative infrared spectra of hydrosilicates and related minerals. *Mon. Not. R. Astron. Soc.*, 367(2): 577-591.

Hossain, M., Goudar, D., Truman, C.E., Smith, D.J., 2011. Simulation and measurement of residual stresses in a type 316h stainless steel offset repair in a pipe girth weld. *Materials Science Forum: Trans Tech Publ*: 492-497.

Hossain, S., Truman, C., Smith, D., Bouchard, P., 2006. Measurement of residual stresses in a type 316H stainless steel offset repair in a pipe girth weld. *Journal of pressure vessel technology*, 128: 420-426.

International Standard ISO, 2006. *Corrosion of metals and alloys - Electrochemical potentiokinetic reactivation measruement using the double loop method (based on Cihal's method)*, International Standard, ISO. International Organization for Standardization, pp. 6-7, 14.

Johnson, H.H., 1965. Calibrating the Electric Potential for Studying Slow Crack Growth. *Materials Research Standards*, 5.

Kanesaka, I., Aoyama, S., 2001. Vibrational spectra of magnesia cement, phase 3. *J. Raman Spectrosc.*, 32(5): 361-367.

Katona, R.M., Carpenter, J., Schindelholz, E.J., Kelly, R.G., 2019. Prediction of Maximum Pit Sizes in Elevated Chloride Concentrations and Temperatures. *Journal of the Electrochemical Society*, 166(11): C3364-C3375.

Katona, R.M. et al., 2020a. Importance of the hydrogen evolution reaction in magnesium chloride solutions on stainless steel. *Corrosion Science*, 177: 108935.

Katona, R.M., Kelly, R.G., Bryan, C.R., Schaller, R.F., Knight, A.W., 2020b. Use of in situ Raman spectroelectrochemical technique to explore atmospheric corrosion in marine-relevant environments. *Electrochemistry Communications*, 118.

Katona, R.M. et al., 2020c. Quantitative Assessment of Environmental Phenomena on Maximum Pit Size Predictions in Marine Environments *Electrochimica Acta*, Under Review.

Kokawa, H., Shimada, M., Sato, Y.S., 2000. Grain-boundary structure and precipitation in sensitized austenitic stainless steel. *Jom-Journal of the Minerals Metals & Materials Society*, 52(7): 34-37.

Kondo, Y., 1989. Prediction of fatigue crack initiation life based on pit growth. *Corrosion*, 45(1): 7-11.

Krumgalz, B.S., 2017. Temperature Dependence of Mineral Solubility in Water. Part I. Alkaline and Alkaline Earth Chlorides. *Journal of Physical and Chemical Reference Data*, 46(4).

Lambert, I., Clever, H.L., 1992. Solubilty Data Series, Alkaline Earth Hydroxides in Water and Aqueous Solutions Pergamon Press LTD, Headington Hill Hall, Oxford, England.

Lambourg, A. et al., 2020. Optimization of the DCPD technique for monitoring the crack propagation from notch root in localized plasticity. *International Journal of Fatigue*, 130.

Li, D.D., Gao, D.D., Dong, Y.P., Li, W., 2019. Modeling of phase relations and thermodynamics in the Mg(OH)(2) + MgSO4 + H2O system with implications on magnesium hydroxide sulfate cement. *Calphad-Computer Coupling of Phase Diagrams and Thermochemistry*, 67.

Lin, C.M., Tsai, H.L., Cheng, C.D., Yang, C., 2012. Effect of repeated weld-repairs on microstructure, texture, impact properties and corrosion properties of AISI 304L stainless steel. *Engineering Failure Analysis*, 21: 9-20.

Lin, P., Palumbo, G., Erb, U., Aust, K.T., 1995. Influence of Grain-Boundary-Character-Distribution on Sensitization and Intergranular Corrosion of Alloy-600. *Scripta Metallurgica Et Materialia*, 33(9): 1387-1392.

Linke, W., 1965. *Solubilities Inorganic and Metal-organic Compounds*. American Chemical Society, 1 & 2, Washington.

Macdonald, D.D., Urquidi-Macdonald, M., 1991. A coupled environment model for stress-corrosion cracking in sensitized Type-304 stainless-steel in LWR environments. *Corrosion Science*, 32(1): 51-81.

Martins, M.C., Pereira, C.M., Girault, H.H., Silva, F., 2004. Specific adsorption of tetraalkylammonium cations on the 1,2-dicloroethane/water interface. *Electrochimica Acta*, 50(1): 135-139.

Milad, M., Zreiba, V., Elhalouani, F., Baradai, C., 2008. The effect of cold work on structure and properties of AISI 304 stainless steel. *Journal of Materials Processing Technology*, 203(1-3): 80-85.

Mirshekari, G.R., Tavakoli, E., Atapour, M., Sadeghian, B., 2014. Microstructure and corrosion behavior of multipass gas tungsten arc welded 304L stainless steel. *Materials & Design*, 55: 905-911.

Mostafa, A.T.M.G., Eakman, J.M., Montoya, M.M., Yarbro, S.L., 1996. Prediction of Heat Capacities of Solid Inorganic Salts from Group Contributions *Industrial & Enginnering Chemistry Research*, 35: 343-348.

Murugan, S. et al., 2001. Temperature distribution and residual stresses due to multipass welding in type 304 stainless steel and low carbon steel weld pads. *International Journal of Pressure Vessels and Piping*, 78(4): 307-317.

Newman, J., Raju, I., 1981. An empirical stress-intensity factor equation for the surface crack. *Engineering Fracture Mechanics*, 15(1): 185-192.

Newman, J.C., Raju, I.S., 1979. *Analysis of Surface Cracks in Finite Plates Under Tension or Bending Loads*, NASA, Hampton, VA.

Newman, R.C., 2002. Stress-corrosion cracking mechanisms. *CORROSION TECHNOLOGY-NEW YORK AND BASEL-*, 17: 399-450.

Nikitin, I., Besel, M., 2008. Correlation between residual stress and plastic strain amplitude during low cycle fatigue of mechanically surface treated austenitic stainless steel AISI 304 and ferritic-pearlitic steel SAE 1045. *Materials Science and Engineering a-Structural Materials Properties Microstructure and Processing*, 491(1-2): 297-303.

Nishikata, A. et al., 1995. An electrochemical impedance study on atmospheric corrosion of steels in a cyclic wet-dry condition. *Corrosion science*, 37(12): 2059-2069.

NRC, 2014. *Assessment of Stress Corrosion Cracking Susceptibility for Austenitic Stainless Steels Exposed to Atmospheric Chloride and Non-Chloride Salts*, U.S. Nuclear Regulatory Commission, Washington D.C.

Palumbo, G., Aust, K.T., 1990. Structure-Dependence of Intergranular Corrosion in High-Purity Nickel. *Acta Metallurgica Et Materialia*, 38(11): 2343-2352.

Pannach, M., Bette, S., Freyer, D., 2017. Solubility Equilibria in the System Mg(OH)(2)-MgCl2-H2O from 298 to 393 K. *Journal of Chemical and Engineering Data*, 62(4): 1384-1396.

Paulraj, P., Garg, R., 2016. Effect of welding parameters on pitting behavior of GTAW of DSS and super DSS weldments. *Engineering Science and Technology, an International Journal*, 19(2): 1076-1083.

Phillips, D.H., 2016. *Welding Engineering: An Introduction*. Wiley, Hoboken, New Jersey, 290 pp.

Pitzer, K.S., 1973. Thermodynamics of electrolytes. I. Theoretical basis and general equations *Journal of Physical Chemistry*, 77: 268-277.

Prevey, P.S., Mason, P.W., Hornbach, D.J., Molkenthin, J.P., 1996. Effect of prior machining deformation on the development of tensile residual stresses in weld-fabricated nuclear components. *Journal of Materials Engineering and Performance*, 5(1): 51-56.

Sato, N., 1982. The Stability of Pitting Dissolution of Metals in Aqueous-Solution. *Journal of the Electrochemical Society*, 129(2): 260-264.

Schaller, R., Knight, A., Bryan, C., Schindelholz, E., 2019. *FY19 Status Report: SNL Research into Stress Corrosion Cracking of SNF Dry Storage Canisters*. In: Energy, U.S.D.o. (Editor).

Schindelholz, E., Bryan, C., Alexander, C., 2017a. *FY17 Status Report: Research on Stress Corrosion Cracking of SNF Interim Storage Canisters*. FCRD-UFD-2016-00429, U.S. Department of Energy.

Schindelholz, E., Bryan, C., Alexander, C., 2017b. *FY17 Status Report: Research on Stress Corrosion Cracking of SNF Interim Storage Canisters*. In: Energy, U.S.D.o. (Editor).

Schindelholz, E., Kelly, R.G., 2010a. Application of Ink-Jet Printing for Depositing Salt Prior to Atmospheric Corrosion Testing. *Electrochemical and Solid State Letters*, 13(10).

Schindelholz, E., Kelly, R.G., 2010b. Application of Inkjet Printing for Depositing Salt Prior to Atmospheric Corrosion Testing. *Electrochemical and Solid State Letters*, 13(10): C29-C31.

Shah, B.K., Sinha, A.K., Rastogi, P.K., Kulkarni, P.G., 1990. Effect of Prior Cold Work on Low-Temperature Sensitization Susceptibility of Austenitic Stainless-Steel Aisi-304. *Materials Science and Technology*, 6(2): 157-160.

Shi, E., Wang, A., Ling, Z., 2019. MIR, VNIR, NIR, and Raman spectra of magnesium chlorides with six hydration degrees: Implication for Mars and Europa. *J. Raman Spectrosc.*: Ahead of Print.

Shirai, K. et al., 2011. *SCC evaluation test of a multi-purpose canister. 10-14 April*, 13th International High-Level Radioactive Waste Management Conference (IHLRWMC). American Nuclear Society, Albuquerque, NM, pp. 824-831.

Simoes, M.C., Hughes, K.J., Ingham, D.B., Ma, L., Pourkashanian, M., 2016. Estimation of the Pitzer Parameters for 1-1, 2-1, 3-1, 4-1, and 2-2 Single Electrolytes at 25 degrees C. *Journal of Chemical and Engineering Data*, 61(7): 2536-2554.

Singh, J., Shahi, A.S., 2018. Weld joint design and thermal aging influence on the metallurgical, sensitization and pitting corrosion behavior of AISI 304L stainless steel welds. *Journal of Manufacturing Processes*, 33: 126-135.

SNL, 2007. *In-Drift Precipitates/Salt Model*. In: Laboratories, S.N. (Editor), Albuquerque, New Mexico

Speidel, M.O., 1977. Stress-Corrosion Crack Growth in Austenitic Stainless-Steel. *Corrosion*, 33(6): 199-203.

Srinivasan, J. et al., 2020. Long-Term Effects of Humidity on Stainless Steel Pitting in Sea Salt Exposures. *Journal of The Electrochemical Society*(Under Review).

Srinivasana, P.B., Kumar, M.P.S., 2009. Microstructural and electrochemical characterization of a thin-section dissimilar stainless steel weld joint. *Materials Chemistry and Physics*, 115(1): 179-184.

Steiner, P.J., Burns, J., 2019. *Mechanistic Studies of Intergranular Stress Corrosion Cracking In Al-Mg Alloys under Atmospheric Exposure Conditions*, NACE 2019, Nashville, TN.

Steiner, P.J., Burns, J.T., 2018. Mechanistic Studies of Intergranular Stress Corrosion Cracking in Al-Mg Alloys under Atmospheric Exposure Conditions. *CORROSION*, 74(10): 1117-1131.

Stoenescu, R., Schaublin, R., Gavillet, D., Baluc, N., 2007. Welding-induced microstructure in austenitic stainless steels before and after neutron irradiation. *Journal of Nuclear Materials*, 360(2): 186-195.

Suffield, S., Fort, J.A., Cuta, J.M., Adkins, H.E., 2012. *Thermal Modeling of NUHOMS HSM15 Storage Module at Calvert Cliffs Nuclear Power Station ISFSI*, U.S. Department of Energy.

Toloczko, M.B., Bouffioux, R.A., Colon, F.C., 2020. *Results from PNNL SCC Testing: FY20*, Pacific Northwest National Laboratory.

Tong, J., 2001. Notes on Direct Current Potential Drop Calibration for Crack Growth in Compact Tension Specimens. *Journal of Testing and Evaluation*, 29(4): 402-406.

Travers, A., Nouvel, C.R., 1929. On the solubility of magnesium hydroxide at high temperatures. *Comptes rendus de l'Académie des Sciences*, 188: 499-501.

Turnbull, A., McCartney, L., Zhou, S., 2006. Modelling of the evolution of stress corrosion cracks from corrosion pits. *Scripta materialia*, 54(4): 575-578.

Unnikrishnan, R. et al., 2014. Effect of heat input on the microstructure, residual stresses and corrosion resistance of 304L austenitic stainless steel weldments. *Materials Characterization*, 93: 10-23.

Wagner, W., Pruß, A., 2002. The IAPWS formulation 1995 for the thermodynamic properties of ordinary water substance for general and scientific use. *Journal of Physical and Chemical Reference Data*, 31(2): 387-535.

Weirich, T.D. et al., 2019. Humidity Effects on Pitting of Ground Stainless Steel Exposed to Sea Salt Particles. *Journal of The Electrochemical Society*, 166(11).

Willis, C.F., 1990. *A study of chromium carbide precipitation at interphase boundaries in stainless steel welds*, Berkeley, CA.

Woldemedhin, M.T., Shedd, M.E., Kelly, R.G., 2014. Evaluation of the Maximum Pit Size Model on Stainless Steels under Thin Film Electrolyte Conditions. *Journal of the Electrochemical Society*, 161(8): E3216-E3224.

This page is intentionally left blank.

Appendix A

Katona, R. M., Kelly, R. G., Bryan, C. R., Schaller, R. F., & Knight, A. W. (2020). Use of in situ Raman spectroelectrochemical technique to explore atmospheric corrosion in marine-relevant environments. *Electrochemistry Communications*, *118*, 106768.

Electrochemistry Communications 118 (2020) 106768

Contents lists available at ScienceDirect

Electrochemistry Communications

journal homepage: www.elsevier.com/locate/elecom

Use of *in situ* Raman spectroelectrochemical technique to explore atmospheric corrosion in marine-relevant environments

R.M. Katona[a,b], R.G. Kelly[b], C.R. Bryan[a], R.F. Schaller[a], A.W. Knight[a,*]

[a] Sandia National Laboratories, Albuquerque, NM 87123, USA
[b] Materials Science and Engineering, University of Virginia, Charlottesville, VA 22904, USA

ARTICLE INFO

Keywords:
Atmospheric corrosion
Diffusion boundary layer
Magnesium chloride
Magnesium hydroxide (brucite)
Surface film evolution

ABSTRACT

Here, for the first time, we demonstrate the use of an *in situ* spectroelectrochemical Raman technique to explore simulated atmospheric corrosion scenarios with a variable boundary layer thickness (δ). The effects of solution flow rate on oxygen concentration and δ were explored. It was found solution regeneration is necessary to prevent oxygen depletion in the Raman cell. It was further shown that by increasing the solution flow rate, the effective δ decreases and allows for the investigation of atmospheric corrosion scenarios. Finally, the technique developed was utilized to explore the effect of precipitation on the cathodic behavior of SS304L in dilute $MgCl_2$. During cathodic polarization, evidence supports previous observations that magnesium hydroxide species are kinetically favored over the thermodynamically predicted magnesium carbonate.

1. Introduction

Raman spectroscopy has been used to study the *in situ* formation of surface precipitates on various alloys and solutions [1–4] as well as intermediates for oxygen reduction reactions (ORR) [5]. Although widely used in analysis of electrochemical reactions, *in situ* Raman has not been used to probe the evolution of chemical conditions representative of common exposure conditions. Precipitation of solids resulting from both anodic and cathodic reactions will impact further corrosion, but the small volumes have made assessment of such environments challenging. Raman's ability to speciate solid products could be powerful in obtaining a better understanding of the factors controlling atmospheric corrosion.

Although the method is attractive, there are barriers to its application. First, many Raman cells are characterized by small solution volumes (i.e. several mL) [2]. As ORR is a common cathodic reduction reaction, the oxygen can be depleted, under rates of interest for atmospheric corrosion, and the pH raised, making the chemical composition of the solution under study unrepresentative of the environment of interest. Next, many atmospheric environments are characterized by thin water layers, decreasing the boundary layer thickness (δ) and the diffusion distance for oxygen, which has been proven to be a controlling factor in atmospheric corrosion [6]. As Raman cells may be utilized with various solution flow rates (Q), flow could potentially be used to control δ and thus relate measurements of precipitate chemistry to different water layer thicknesses in atmospheric corrosion [6]. Taking advantage of this capability requires an understanding of the influence of Q on δ and cathodic reduction reactions while performing *in situ* Raman. To determine these effects, cathodic reduction kinetics were explored on stainless steel 304L (SS304L) in an *in situ* Raman cell over a range of flow rates.

SS is often exposed to marine and near-marine atmospheric environments characterized by deliquesced water layers often containing concentrated sea-salt solutions. This chloride-rich deliquesced water layer is highly corrosive and can be detrimental to the overall service lifetime. Various constituents of sea water brines, such as magnesium (Mg) [7,8], have strong thermodynamic driving forces to form stable precipitates at elevated pH [9]. Such precipitates forming on the surface of the alloy have the propensity to limit the environmental severity of corrosion [10].

During corrosion, any anodic reaction must be balanced by a cathodic reduction reaction. Whether the cathodic reduction reaction is ORR or the hydrogen evolution reaction (HER), a product is the hydroxyl anion (OH^-), which causes a rise in the cathode pH. Elevated cathodic pH values have been observed or measured in various solutions and alloys, and the pH can be significantly higher than the bulk solution [11,12]. As a result, the pH in which stable precipitates form can be achieved during corrosion [9]. In Mg-containing environments, which are dominant in sea water brines at low relative humidities (RH) [7], corrosion products of iron-based alloys have shown the presence of hydroxides, hydroxychlorides, and/or hydroxycarbonates as a result of

* Corresponding author.
E-mail address: aknigh@sandia.gov (A.W. Knight).

https://doi.org/10.1016/j.elecom.2020.106768
Received 22 May 2020; Received in revised form 9 June 2020; Accepted 10 June 2020
Available online 16 June 2020

This page is intentionally left blank.

Appendix B

Katona, R. M., Carpenter, J. C., Knight, A. W., Bryan, C. R., Schaller, R. F., Kelly, R. G., & Schindelholz, E. J. (2020). Importance of the hydrogen evolution reaction in magnesium chloride solutions on stainless steel. *Corrosion Science*, *177*, 108935.

Corrosion Science 177 (2020) 108935

Contents lists available at ScienceDirect

Corrosion Science

journal homepage: www.elsevier.com/locate/corsci

Importance of the hydrogen evolution reaction in magnesium chloride solutions on stainless steel

R.M. Katona[a,b], J.C. Carpenter[a], A.W. Knight[a], C.R. Bryan[a], R.F. Schaller[a], R.G. Kelly[b], E.J. Schindelholz[c,*]

[a] Sandia National Laboratories, Albuquerque, NM,87123,USA
[b] Materials Science and Engineering, University of Virginia, Charlottesville, VA,22904,USA
[c] Materials Science and Engineering, The Ohio State University, Columbus, OH,43210,USA

ARTICLE INFO

Keywords:
Cathodic kinetics in marine environments
Oxygen reduction reaction
Atmospheric corrosion
Magnesium chloride electrolyte properties

ABSTRACT

Cathodic kinetics in magnesium chloride ($MgCl_2$) solutions were investigated on platinum (Pt) and stainless steel 304 L (SS304 L). Density, viscosity, and dissolved oxygen concentration for $MgCl_2$ solutions were also measured. A 2-electron transfer for oxygen reduction reaction (ORR) on Pt was determined using a rotating disk electrode. SS304 L displayed non-Levich behavior for ORR and, due to ORR suppression and buffering of near surface pH by Mg-species precipitation, the primary cathodic reaction was the hydrogen evolution reaction (HER) in saturated $MgCl_2$. Furthermore, non-carbonate precipitates were found to be kinetically favored. Implications of HER are discussed through atmospheric corrosion and stress corrosion cracking.

1. Introduction

Stainless steels (SS) are often subjected to marine and near-marine atmospheric environments characterized by hygroscopic sea salt particles which adhere to the alloy surface. Through absorption of moisture from the atmosphere, sea salt particles deliquesce and form a corrosive brine on the surface of the alloy. The chemistry and concentration of the seawater brine varies widely with relative humidity (RH) as seen in Fig. 1 at 25 °C. At high RH values, particularly above the saturation/deliquescence point of NaCl (74% RH), brines are rich in Na^+ and Cl^-. At lower RH values, because of the precipitation of NaCl, the seawater brines composition becomes dominated by Mg^{2+} and Cl^- down to near the saturation/deliquescence point of $MgCl_2 \cdot 6H_2O$ (36% RH). Additionally, the volume of the brine decreases with decreasing RH [1]. In this way, RH along with salt load control the composition, volume and other properties of the resultant brine, impacting anodic and cathodic corrosion kinetics [1,2].

Historically, anodic kinetics of SS have been the main subject of studies related to concentrated seawater or chloride environments and have been summarized elsewhere for localized pitting corrosion [3], a common mode of corrosion degradation for SS's. However, research on the effects of concentrated chloride brines on cathodic kinetics has been lacking with the exception of Alexander et al. [4]. As cathodic kinetics control pit initiation and growth in combination with anodic kinetics, it is critical to understand the effects of concentrated solution chemistries on cathodic behavior.

In dilute chloride solutions [4–9], the oxygen reduction reaction (ORR) has been shown to be the dominant cathodic reaction on SS alloys near the open circuit potential (OCP) and the rate of reaction is diffusion-limited at sufficiently negative potentials. As such, cathodic rates can be predicted through Levich analysis [10]. Numerous studies have explored cathodic kinetics in atmospheric environments across multiple ferrous alloys as a function of solution cation composition [5,7,8,11], dilute chloride concentrations [4,9,12] and surface finish [6,9] and have further shown the dominance of ORR. A detailed chart of ORR in various media and surface finishes is given by Klapper and Goellner and shows that regardless of the conditions explored, ORR is always the dominant cathodic reduction reaction on ferrous alloys [6]. To date, cathodic kinetics literature in highly concentrated $MgCl_2$ brines is lacking. Additionally, minimal information exists on the high-fidelity control of boundary layer thicknesses (δ) as a function of $MgCl_2$ concentration necessary to understand the overall corrosion process at low RH.

Although it has been assumed that ORR is the dominant reduction reaction in chloride-containing environments, various cations have been shown to change the cathodic reduction reaction in other alloy systems and could hold true in SS systems [13,14]. Limited research on Al alloys has shown that Zn^{2+} and Mg^{2+} cations can suppress cathodic

* Corresponding author.
E-mail address: schindelholz.2@osu.edu (E.J. Schindelholz).

https://doi.org/10.1016/j.corsci.2020.108935
Received 19 June 2020; Received in revised form 7 August 2020; Accepted 8 August 2020
Available online 11 August 2020